Search for light sterile neutrinos with the Double Chooz experiment

Von der Fakultät für Mathematik, Informatik und Naturwissenschaften der RWTH Aachen University zur Erlangung des akademischen Grades einer Doktorin der Naturwissenschafen genehmigte Dissertation

vorgelegt von

M. Sc.
Denise Hellwig
aus
Moers

Berichter:
Universitätsprofessor Dr. rer. nat. Christopher Wiebusch
Universitätsprofessor Dr. rer. nat. Achim Stahl

Tag der mündlichen Prüfung: 02.03.2020

Abstract

The Double Chooz (DC) experiment is a reactor antineutrino disappearance experiment located in Chooz, France. It was designed to measure the neutrino mixing angle θ_{13}. The experiment is composed of two liquid scintillator detectors of almost identical design that were able to identify electron antineutrinos from the two Chooz B reactor cores by the unique signal of the inverse beta decay (IBD). The far detector (FD) at an average baseline of 1050 m from the two reactor cores was in operation from April 2011 to the beginning of 2018. The near detector (ND) at an average baseline of 400 m has been operating from the beginning of 2015 to the beginning of 2018. A neutrino oscillation analysis can be setup independently from any theoretical model of the reactor neutrino flux utilizing the different baselines of near and far detector relying only on the comparison of near and far detector data. In doing so, all correlated systematics cancel and the analysis is protected against potential bias due to a mismatch of reactor neutrino prediction and data.
Apart from its original design goal to measure θ_{13}, Double Chooz is sensitive to so called light *sterile neutrinos*. Sterile neutrinos are neutrino states that do not take part in the weak interaction but may lead to additional disappearance of the known neutrino states, if they mix with the latter. That mixing is described by additional neutrino squared mass differences and mixing angles. The *3+1 model* assumes one additional sterile state. Here, Double Chooz is sensitive to the new mixing angle θ_{14} depending on the new squared mass difference Δm^2_{41} if it is in the range of $0.003\,\mathrm{eV}^2 \lesssim \Delta m^2_{41} \lesssim 0.3\,\mathrm{eV}^2$. This work presents the analysis of Double Chooz data with respect to sterile neutrinos. A Poissonian likelihood fit approach not relying on reactor model predictions is used. It is found that the Double Chooz data is with a p-value of 24.7% ± 2.2% consistent with the no-sterile (i.e. $\theta_{14} = 0$) hypothesis. The upper limit on $\sin^2 2\theta_{14}$ at 95% confidence level is given as a function of Δm^2_{41}.

Zusammenfassung

Das Double Chooz Experiment ist ein Reaktor-Antineutrinoexperiment zur präzisen Messung des Neutrinomischungswinkels θ_{13}. Es befindet sich in Chooz, einem kleinem Dorf in Frankreich, auf dem Gelände des dortigen Kernkraftwerkes Chooz-B. Das Experiment besteht aus zwei nahezu identischen Detektoren, welche bis 2018 den Elektronantineutrinofluss der beiden Reaktorblöcke B1 und B2 gemessen haben. Der Nahdetektor wurde in einem mittleren Abstand von 400 m zu den Reaktorblöcken positioniert und war zwischen Anfang 2015 und Anfang 2018 in Betrieb, während der Ferndetektor in einem mittleren Abstand von 1050 m zu den Reaktorblöcken zwischen April 2011 und Anfang 2018 betrieben wurde.

Diese Arbeit präsentiert die Analyse der Double Chooz Daten in Hinblick auf sogenannte *leichte sterile Neutrinos*. Leichte sterile Neutrinos sind Neutrinos, die nicht an der schwachen Wechselwirkung teilnehmen, und eine Masse im Elektronenvoltbereich oder darunter aufweisen. Sie wurden bisher nicht zweifelsfrei nachgewiesen. Falls sterile Neutrinos mit den bekannten Neutrinosorten mischen, besteht die Möglichkeit sie indirekt über Oszillationseffekte der bekannten Sorten nachzuweisen. Das 3+1 Modell sieht die Einführung einer zusätzlichen sterilen Neutrinosorte vor. Dadurch ergeben sich neue Neutrinomischungswinkels und Massenquartsdifferenzen. Double Chooz ist für Massenquartsdifferenzen $0.003\,\mathrm{eV}^2 \lesssim \Delta m^2_{41} \lesssim 0.3\,\mathrm{eV}^2$ auf den neuen Neutrinomischungsparameter $\sin^2 2\theta_{14}$. Die in dieser Arbeit vorgestellte Analyse beruht auf einem Likelihood-Anpassungsverfahren, das possionische Statistik annimmt und auf dem Vergleich der Daten der beiden Detektoren basiert. Es ist daher nahezu vollständig unabhängig von Vorhersagemodellen für die Neutrinoproduktion in den Reaktoren. Auch andere systematische Unsicherheiten kürzen sich heraus, sofern sie zwischen den beiden Detektoren maximal korreliert sind. Es zeigt sich, dass die Double Chooz Daten mit einer Wahrscheinlichkeit von $24.7\% \pm 2.2\%$ mit der Hypothese $\sin^2 2\theta_{14} = 0$ kompatibel sind. Es wird die mit 95% Wahrscheinlichkeit obere Grenze für $\sin^2 2\theta_{14}$ als Funktion von Δm^2_{41} gezeigt.

Contents

List of figures

List of tables

Glossary

AGS Alternating Gradient Synchrotron . . . 1
ANN Artificial Neural Network . . . 38
AW sensitivity Asimov-Wilks sensitivity . . . 83
BEST Baksan Experiment on Sterile Transitions . . . 9
CL confidence level
CPS chimney-pulse-shape . . . 38
CPU central processing unit . . . 98
D2D Data-to-Data . . . 32
D2MC Data-to-Monte Carlo . . . 75
Daya Bay Daya Bay Reactor Neutrino Experiment . . . 8
DC Double Chooz . . . iii
dof degree(s) of freedom . . . 83
DONUT Direct Observation of the NU Tau . . . 1
DUC digital unit of charge . . . 33
EDF Electricité de France . . . 11
EDM estimated distance to minimum . . . 53
FD far detector . . . iii
FD1 far detector in one detector phase (including Off-Off dataset) . . . 29
FD1-On far detector in one detector phase (excluding Off-Off dataset) . . . 29
FD1-Off-Off reactor off data collected in the one detector phase . . . 29
FD2 far detector in double detector phase . . . 29
Fermilab Fermi National Accelerator Laboratory . . . 1
FN fast neutron . . . 23
FNSM fast neutron and stopping muon . . . 72
FV Functional Value . . . 30
GALLEX Gallium Experiment . . . 9
GC gamma-catcher . . . 19
Gd gadolinium . . . 17
Gd++ gadolinium and hydrogen combined selection . . . 33
H hydrogen . . . 17

IBD inverse beta decay ... iii
ID inner detector ... 19
IDLI inner detector light injection ... 22
IOIO inverted mass order standard neutrinos, inverted mass order sterile neutrinos ... 6
IONO inverted mass order standard neutrinos, normal mass order sterile neutrinos ... 6
IV inner veto ... 19
IVLI inner veto light injection ... 21
LED light-emitting diode ... 21
LEP Large Electron–Positron Collider ... 1
Li lithium ... 38
LLH likelihood ... 30
LLH-FF Likelihood Flux Free ... 75
LN Light Noise ... 26
LNL light non-linearity ... 31
linearised PE calibration linearised photo electron calibration ... 30
LSND Liquid Scintillator Neutrino Detector ... 9
MC Monte Carlo ... 15
ND near detector ... iii
NEOS NEutrino Oscillation at Short baseline ... 8
NOIO normal mass ordering standard neutrinos, inverted mass order sterile neutrinos ... 6
NONO normal mass ordering standard neutrinos, normal mass order sterile neutrinos ... 6
NT neutrino target ... 19
OV outer veto ... 20
par. parameter
pdf probability density function ... 99
PMNS matrix Pontecorvo-Maki-Nakagawa-Sakata matrix ... 3
PMT photomultiplier tube ... 19
PWR pressurized water reactor ... 13
QNL charge non-linearity ... 31
RENO Reactor Experiment for Neutrino Oscillation ... 9
RMS Root Mean Square ... 34
SAGE Soviet–American Gallium Experiment ... 9
SM stopping muon ... 25
SNO Sudbury Neutrino Observatory ... 2
TS test statistics ... 82

Chapter 1

Motivation

This chapter describes the basics of neutrino oscillation physics and neutrino properties. Note that I (Denise Hellwig) have written an Double Chooz Collaboration internal password protected non-public single authored technical note on this analysis [74] in order to get blessing from the collaboration. The content of this chapter may be partially identical to content of this document. The same applies to chapter 4. I have made a draft version of this thesis available for Double Chooz Collaboration internal reviewers via the internal documentation system[I] which is password protected and non-public. In the early phase of my PhD studies I have written a proceeding [76]. The proceeding was written by me alone. It is multi-authored for political reasons. However, my sterile analysis has entirely changed after [76] was written.

1.1 History of neutrinos

The existence of neutrinos was theoretically postulated in 1930 by Wolfgang Pauli in order to fulfill the conservation laws in the beta decay [110]. The experimental confirmation was done by utilizing the inverse beta decay and published in 1956 by C. L. Cowan, F. Reines, F. B. Harrison, H.W. Kruse, and A. D. McGuire [46]. Frederick Reines won the 1995 Nobel Prize for *"for the detection of the neutrino"* [97]. A second neutrino type (muon neutrino and muon antineutrino) was detected by studying pion decay at the Alternating Gradient Synchrotron (AGS) and published in 1962 [48]. Leon Lederman, Melvin Schwartz and Jack Steinberger were awarded with the 1988 Nobel Price for the *"for the neutrino beam method and the demonstration of the doublet structure of the leptons through the discovery of the muon neutrino"* [96]. Finally, the *"Observation of tau neutrino interactions"* was published in 2001 using the Direct Observation of the NU Tau (DONUT) experiment at Fermi National Accelerator Laboratory (Fermilab) [84]. The existence of further neutrino states has not been proven so far. In contrast, limits on the number of neutrino states have been set. The number of light neutrino states that take part in the weak interaction may be investigated from the Z production in electron positron collisions. A combination of all four Large Electron–Positron Collider (LEP) experiments yields [100] [121]

$$N_\nu = 2.9841 \pm 0.0083 \quad . \tag{1.1}$$

[I] Double Chooz Document Database 7503

However, this does not constrain the total number of neutrinos but only the number of weakly interacting neutrinos with masses $m_\nu \leq \frac{m_Z}{2}$, where m_Z is the mass of the Z boson. .

Cosmology can set limits on the number of light neutrino states as well, since light neutrinos contribute to the radiation component of the universe; if they interact weakly or not. Taking together Planck and other astrophysical observations gives [108]

$$N_{\text{eff}} = 2.99 \pm 0.17 \quad . \tag{1.2}$$

where N_{eff} is the effective number of relativistic degrees of freedom [12]. The three known neutrino states result in $N_{\text{eff}} = 3.046$ [86]. Any value $N_{\text{eff}} \neq 3.046$ would be a result of non standard neutrino properties, additional neutrino states or other particles (i.e. not photons and not neutrinos) contributing to the radiation density in the early universe [86] . Note that one additional sterile neutrino state does not necessarily lead to an increase in N_{eff} of exactly one. Instead, this is only the case if the state is in thermal equilibrium with the known neutrino states [87]. Indeed, thermal equilibrium of weakly interacting and not weakly interaction neutrino types is not necessarily given and could be suppressed by for instance an initial lepton asymmetry [87] [72] or by a self-interaction of the sterile states [71] [28].

Laboratory limits on the number of neutrino states only apply for the weakly interacting species and cosmological limits eventually can be avoided [87] [72] [71] [28]. Thus, the existence of additional neutrino types is not fully excluded as long as they do not take part in the weak interaction. In contrast, experimental anomalies have been observed that could be explained by such additional neutrino types that do not interact weakly. Those are called *sterile neutrino*. These anomalies will be summarized in section 1.4 after the theory of the phenomena of neutrino oscillation has been explained in the next section, section 1.2. A model containing m sterile neutrino mass states in addition to the three know states will be referred to as *3+m model*, where this work focuses on the 3+1 model.

1.2 Neutrino oscillations

The first hint towards neutrino oscillations was a discrepancy between the predicted neutrino rate and the measured neutrino rate from the Sun [33]. This effect named *solar neutrino problem* was first reported by the *Homestake* experiment in 1968 [49] and later confirmed by several experiments [33]. The solar neutrino problem [111] is solved by neutrino oscillations which were experimentally confirmed in 2001 by the Sudbury Neutrino Observatory (SNO) experiment [17]. Evidence for muon neutrino oscillations was firstly reported by the Super-Kamikande collaboration in 1998 [82]. Neutrino oscillations require neutrinos to have a non vanishing mass which was not foreseen in the original standard model. Thus, Takaaki Kajita from the Super-Kamikande collaboration and Arthur B. McDonald from the SNO collaboration were awarded with the 2015 Nobel Prize *"for the discovery of neutrino oscillations, which shows that neutrinos have mass."* [98].

Neutrino oscillations arise because the neutrino flavor eigenstates are not identical to the mass eigenstates. Instead, the flavor eigenstates are a linear combination of the mass eigenstates [106]:

$$|\nu_{\text{flavor}}\rangle = \mathrm{U}^* \, |\nu_{\text{mass}}\rangle \text{ which means in components } |\nu_\alpha\rangle = \sum_j \mathrm{U}^*_{\alpha j} \, |\nu_j\rangle \quad . \tag{1.3}$$

This is called neutrino mixing. In the 3+1 model it is a convention to write flavor and mass states as:

$$|\nu_{\text{flavor}}\rangle = \begin{pmatrix} \nu_e \\ \nu_\mu \\ \nu_\tau \\ \nu_s \end{pmatrix} \quad \text{and} \quad |\nu_{\text{mass}}\rangle = \begin{pmatrix} \nu_1 \\ \nu_2 \\ \nu_3 \\ \nu_4 \end{pmatrix} \quad . \tag{1.4}$$

In the nominal model, the last row of the vectors does not exist; in a model with more than one sterile state the additional states are added below the others. The matrix U is an element of the special unitary group SU(N). U is called Pontecorvo-Maki-Nakagawa-Sakata matrix (PMNS matrix). This matrix will be explained in detail later. The equation of motion is

$$i\frac{d}{dt}|\nu(t)\rangle = \mathrm{H}\,|\nu(t)\rangle \quad , \tag{1.5}$$

assuming $\hbar = c = 1$. H is the Hamiltonian and diagonal in basis of the mass eigenstates

$$\mathrm{H}_{ij} = \delta_{ij}\mathrm{H}_{ii} = \delta_{ij}E_i = \delta_{ij}\sqrt{p_i^2 + m_i^2} \tag{1.6}$$

where E_i, m_i and p_i are energy, mass and momentum of ν_i. $p_j \approx p_i \approx p$, follows from $p_i >> m_i$ as light neutrinos are relativistic. Therefore, H from equation (1.6) can be simplified to

$$\mathrm{H}_{\mathrm{ii}} \approx p_i + \frac{{m_i}^2}{2p_i} \approx p + \frac{{m_i}^2}{2p} \quad . \tag{1.7}$$

With equation (1.7), equation (1.5) can be rewritten as

$$i\frac{d}{dt}|\nu(t)\rangle = i\frac{d}{dt}e^{-ipt}\left|\nu'(t)\right\rangle \quad . \tag{1.8}$$

The global phase e^{-ipt} in equation (1.8) is not relevant for observable probabilities $|\,\langle\nu(t=0)|\nu(t=t')\rangle\,|^2$. Hence, it is conventionally dropped. With this convention, $x = c{\cdot}t$, $p \approx E$ and equation (1.6) the equation of motion (equation (1.5)) is given by

$$i\frac{d}{dx}|\nu_{\text{mass}}\rangle = \frac{1}{2E}\cdot \mathrm{M}\,|\nu_{\text{mass}}\rangle \tag{1.9}$$

in the basis of the mass eigenstates. Here, M is a diagonal matrix of the squared masses:

$$\mathrm{M}_{ij} = \delta_{ij}\mathrm{M}_{ii} = \delta_{ij}m_i^2 \quad . \tag{1.10}$$

As shown above, adding constants to M has no impact on $|\,\langle\nu(t=0)|\nu(t=t')\rangle\,|^2$. Therefore, M may be for instance defined as

$$\mathrm{M}_{ij} = \delta_{ij}\cdot(m_i^2 - m_1^2) \tag{1.11}$$

equivalently. The notation

$$\Delta m_{ij}^2 := m_i^2 - m_j^2 \tag{1.12}$$

is common and will be used in the following.

Equation (1.9) is solved by

$$|\nu_j\rangle = \left|\nu_j(\vec{0})\right\rangle e^{-im_j^2 L/2E} \quad , \tag{1.13}$$

which implies due to equation (1.3)

$$|\nu_\alpha\rangle = \sum_j \mathrm{U}_{\alpha j}^*\left|\nu_j(\vec{0})\right\rangle e^{-im_j^2 L/2E} \quad . \tag{1.14}$$

The so called appearance probability $P(\alpha \to \beta)$ to tag a neutrino which was in flavor state α at the starting point as flavor β later at point $\vec{x}$ is calculated using:

$$P(\alpha \to \beta) = \left|\left\langle \nu_\alpha(\vec{0}) \middle| \nu_\beta(\vec{x}) \right\rangle\right|^2 = \left|\left\langle \nu_\alpha(\vec{0}) \middle| \nu_\beta(L) \right\rangle\right|^2 \tag{1.15}$$

where the start point has w.l.o.g. been set to $\vec{0}$ and L is the travel distance i.e. $L = |\vec{x}|$. With equation (1.14) [64]

$$P(\alpha \to \beta) = \left| \sum_j \mathrm{U}^*_{\alpha j} \mathrm{U}_{\beta j} e^{-i m_j^2 L/2E} \right|^2 \tag{1.16}$$

follows, which can be rewritten as [68]:

$$P(\alpha \to \beta) = \delta_{\alpha\beta} - 4 \sum_{i>j} \mathrm{Re}(\mathrm{U}^*_{\alpha i} \mathrm{U}_{\beta i} U_{\alpha j} \mathrm{U}^*_{\beta j}) \sin^2(\Delta_{ij}) + 2 \sum_{i>j} \mathrm{Im}(\mathrm{U}^*_{\alpha i} \mathrm{U}_{\beta i} \mathrm{U}_{\alpha j} \mathrm{U}^*_{\beta j}) \sin(2\Delta_{ij}) \tag{1.17}$$

where

$$\Delta_{ij} := \frac{\Delta m^2_{ij} L}{4E} \approx 1.27 \frac{\Delta m^2_{ij}[\mathrm{eV}^2] L[\mathrm{km}]}{4E[\mathrm{GeV}]} \quad . \tag{1.18}$$

For antineutrinos, all matrix elements in equation (1.17) have to be replaced by the their complex conjugate, in other words, the last term changes it sign [64] [68]. Now, for numerical calculations of equation (1.16) the parametrization of the PMNS matrix U is important. As already mentioned, U is part of the SU(N) which is defined by $\mathrm{SU}(N) = \{\, \mathrm{U} \in \mathbb{C}^{(N\times N)} \,|\, \mathrm{U} \cdot \mathrm{U}^\dagger \equiv \mathrm{U} \cdot \mathrm{U}^{*\mathrm{T}} = \mathbb{1}\,(\text{Unitarity}) \wedge \det(\mathrm{U}) = 1 \,\}$. This means that U can be parameterized by $\frac{N(N-1)}{2}$ free real parameters and $\frac{N(N+1)}{2}$ phases. In case neutrinos are Dirac particles, only $\frac{(N-1)(N-2)}{2}$ of these phases are physically relevant; in case neutrinos are Majorana particles $\frac{(N-1)(N-2)}{2} + (N-1)$ are [100]. From equation (1.16) follows that CP-violating phases do not enter $P(\alpha \to \beta)$ if $\alpha = \beta$. Thus, both Majorana and Dirac CP-violating phases are unobservable for disappearance experiments, because $\mathrm{U}^*_{\alpha i}\mathrm{U}_{\beta i}\mathrm{U}_{\alpha j}\mathrm{U}^*_{\beta j} = \mathrm{U}^*_{\alpha i}\mathrm{U}_{\alpha i}\mathrm{U}_{\alpha j}\mathrm{U}^*_{\alpha j} = |\mathrm{U}_{\alpha i}|^2 |\mathrm{U}_{\alpha j}|^2$ for $\alpha = \beta$ in equation (1.17). The real parameters are usually referred to as mixing angles θ_{ij} because U can be parameterized as a product of rotation matrices R_{ij}:

$$(\mathrm{R}_{ij}(\theta_{ij}))_{kl} = \begin{cases} 1 & k = l \wedge k \neq i, j \\ \cos(\theta_{ij}) & k = l \wedge (k = i \vee k = j) \\ -\sin(\theta_{ij}) e^{-\delta} & k = j \wedge l = i \\ \sin(\theta_{ij}) e^{\delta} & k = i \wedge l = j \\ 0 & else \end{cases} \tag{1.19}$$

The order of the multiplication is relevant, because rotation matrices do not commute in general.

Conventionally, in the standard no sterile scenario

$$\begin{aligned}
\mathrm{U} = \begin{pmatrix} \mathrm{U}_{e1} & \mathrm{U}_{e2} & \mathrm{U}_{e3} \\ \mathrm{U}_{\mu 1} & \mathrm{U}_{\mu 2} & \mathrm{U}_{\mu 3} \\ \mathrm{U}_{\tau 1} & \mathrm{U}_{\tau 2} & \mathrm{U}_{\tau 3} \end{pmatrix} &= \mathrm{R}_{23}(\theta_{23}, 0) \cdot \mathrm{R}_{13}(\theta_{13}, \delta) \cdot \mathrm{R}_{12}(\theta_{12}, 0) \cdot \mathrm{V}(e^{i\cdot 0.5\cdot \alpha_{21}}, e^{i\cdot 0.5\cdot \alpha_{31}}) \\
&= \begin{pmatrix} 1 & 0 & 0 \\ 0 & c_{23} & s_{23} \\ 0 & -s_{23} & c_{23} \end{pmatrix} \begin{pmatrix} c_{13} & 0 & s_{13}e^{i\delta} \\ 0 & 1 & 0 \\ -s_{13}e^{-i\delta} & 0 & c_{13} \end{pmatrix} \\
&\quad \begin{pmatrix} c_{12} & s_{12} & 0 \\ -s_{12} & c_{12} & 0 \\ 0 & 0 & 1 \end{pmatrix} \begin{pmatrix} 1 & 0 & 0 \\ 0 & e^{i\alpha_{21}/2} & 0 \\ 0 & 0 & e^{i\alpha_{31}/2} \end{pmatrix} \\
&= \begin{pmatrix} c_{12}c_{13} & s_{12}c_{13} & s_{13}e^{-i\delta} \\ -s_{12}c_{23} - c_{12}s_{23}s_{13}e^{i\delta} & c_{12}c_{23} - s_{12}s_{23}s_{13}e^{i\delta} & s_{23}c_{13} \\ s_{12}s_{23} - c_{12}c_{23}s_{13}e^{i\delta} & -c_{12}s_{23} - s_{12}c_{23}s_{13}e^{i\delta} & c_{23}c_{13} \end{pmatrix} \begin{pmatrix} 1 & 0 & 0 \\ 0 & e^{i\alpha_{21}/2} & 0 \\ 0 & 0 & e^{i\alpha_{31}/2} \end{pmatrix}
\end{aligned} \tag{1.20}$$

is used, where [106]

$$s_{ij} = \sin(\theta_{ij}) \quad \text{and} \quad c_{ij} = \cos(\theta_{ij}) \quad . \tag{1.21}$$

In models with N>3 neutrino states U gets extended to NxN dimensions. In doing so, U has to transform in the nominal convention if additional mixing angles are set to zero -otherwise the physical meaning of the mixing angles may change. Usually

$$\mathrm{U} = \mathrm{R}_{34}\mathrm{R}_{24}\mathrm{R}_{23}\mathrm{R}_{14}\mathrm{R}_{13}\mathrm{R}_{12} = \mathrm{R}_{34}\mathrm{R}_{24}\mathrm{R}_{14}\mathrm{R}_{23}\mathrm{R}_{13}\mathrm{R}_{12} \tag{1.22}$$

is used in the 3+1 model. With this definition the elements of U are[II] [104]

$$\mathrm{U}_{e1} = \cos\theta_{14}\cos\theta_{13}\cos\theta_{12} \tag{1.23}$$
$$\mathrm{U}_{e2} = \cos\theta_{14}\cos\theta_{13}\sin\theta_{12} \tag{1.24}$$
$$\mathrm{U}_{e3} = \cos\theta_{14}\sin\theta_{13} \tag{1.25}$$
$$\mathrm{U}_{e4} = \sin\theta_{14} \tag{1.26}$$

where all CP-violating phases have been set to zero, because the focus of this work is on electron antineutrino disappearance and disappearance experiments can not observe any CP-violation a already mentioned (cf. equation (1.16)). With equations (1.23) to (1.26) and equation (1.17) the electron (anti-) neutrino survival probability is:

$$\begin{aligned}
P_{ee} =& 1 - c_{14}^4 s_{12}^2 \sin^2 2\theta_{13} \sin^2 \Delta_{32} - c_{14}^4 c_{12}^2 \sin^2 2\theta_{13} \sin^2 \Delta_{31} && \text{(1.27a)} \\
& - c_{14}^4 c_{13}^4 \sin^2 2\theta_{12} \sin^2 \Delta_{12} && \text{(1.27b)} \\
& - s_{13}^2 \sin^2 2\theta_{14} \sin^2 \Delta_{43} - c_{13}^2 s_{12}^2 \sin^2 2\theta_{14} \sin^2 \Delta_{42} - c_{13}^2 c_{12}^2 \sin^2 2\theta_{14} \sin^2 \Delta_{41} \quad . && \text{(1.27c)}
\end{aligned}$$

Using $\Delta m_{21}^2 << |m_{32}^2|$ and $\cos^2(x) + \sin^2(x) = 1 \, \forall x \in \mathbb{C}$ equation (1.27) simplifies to:

$$\begin{aligned}
P_{ee} \approx& 1 - c_{14}^4 s_{12}^2 \sin^2 2\theta_{13} \sin^2 \Delta_{31} - c_{14}^4 c_{12}^2 \sin^2 2\theta_{13} \sin^2 \Delta_{31} && \text{(1.28a)} \\
& - s_{13}^2 \sin^2 2\theta_{14} \sin^2 \Delta_{43} - c_{13}^2 s_{12}^2 \sin^2 2\theta_{14} \sin^2 \Delta_{41} - c_{13}^2 c_{12}^2 \sin^2 2\theta_{14} \sin^2 \Delta_{41} && \text{(1.28b)} \\
=& 1 - c_{14}^4 \sin^2 2\theta_{13} \sin^2 \Delta_{31} - s_{13}^2 \sin^2 2\theta_{14} \sin^2 \Delta_{43} - c_{13}^2 \sin^2 2\theta_{14} \sin^2 \Delta_{41} && \text{(1.28c)}
\end{aligned}$$

[II] This has been confirmed with Maple.

Table 1.1: Global best fit values of the standard neutrino mixing parameters [107]. For the CP-violating phase δ no global best fit value is provided in [107].

parameter	value $\pm 1\sigma$
$\Delta m^2_{21}/10^{-5}\,\mathrm{eV}^2$	7.53 ± 0.18
$\Delta m^2_{32}/10^{-3}\,\mathrm{eV}^2$	-2.53 ± 0.05
	$+2.444 \pm 0.034$
$\sin^2\theta_{12}$	0.307 ± 0.013
$\sin^2\theta_{13}$	0.0218 ± 0.0007
$\sin^2\theta_{23}$	$0.536^{+0.023}_{-0.028}$

which may be further approximated to:

$$P_{ee} \approx 1 - c_{14}^4 \sin^2 2\theta_{13} \sin^2 \Delta_{31} - \sin^2 2\theta_{14} \sin^2 \Delta_{41} \tag{1.29}$$

or

$$P_{ee} \approx 1 - c_{14}^4 \sin^2 2\theta_{13} \sin^2 \Delta_{ee} - \sin^2 2\theta_{14} \sin^2 \Delta_{41} \quad , \tag{1.30}$$

where

$$\Delta_{ee} := \frac{\Delta m^2_{ee} L}{4E} \approx 1.27 \frac{\Delta m^2_{ee}[\mathrm{eV}^2] L[\mathrm{km}]}{4E[\mathrm{GeV}]} \tag{1.31}$$

and

$$\Delta m^2_{ee} := \cos^2(\theta_{12}) \Delta m^2_{31} + \sin^2(\theta_{12}) \Delta m^2_{32} \quad . \tag{1.32}$$

The current global best fit values for Δm^2_{21}, Δm^2_{32}, $\sin^2\theta_{12}$, $\sin^2\theta_{13}$ and $\sin^2\theta_{23}$ are summarized in table 1.1.

1.3 Neutrino masses

Solar oscillation experiments proofed that the solar mass squared difference Δm^2_{21} is positive. However, the sign of Δm^2_{32} is not known yet; experiments to answer this question are currently under construction [20]. Sterile neutrinos could be lighter or heavier than the know states i.e. $\Delta m^2_{41} > 0$ or $\Delta m^2_{41} < 0$ is both possible - as long as all masses are positive. Figure 1.1 illustrates all possible mass orderings in the 3+1 model; a) is referred to as normal mass ordering standard neutrinos, normal mass order sterile neutrinos (NONO), b) as inverted mass order standard neutrinos, normal mass order sterile neutrinos (IONO), c) as inverted mass order standard neutrinos, inverted mass order sterile neutrinos (IOIO) and d) as normal mass ordering standard neutrinos, inverted mass order sterile neutrinos (NOIO).

Neutrino oscillations may only occur if neutrinos have a non zero mass. Therefore, neutrino oscillations are not foreseen in the original standard model physics because neutrinos have no mass in it. However, only squared mass differences are relevant for neutrino oscillations. The only requirement is that all masses have to be positive. This results in an upper limit of:

$$\min(m_\nu) > \sqrt{\Delta m^2_{32} - \Delta m^2_{21}} \text{ (IH)} \tag{1.33}$$

$$\min(m_\nu) > \sqrt{\Delta m^2_{32} + \Delta m^2_{21}} \text{ (NH)} \tag{1.34}$$

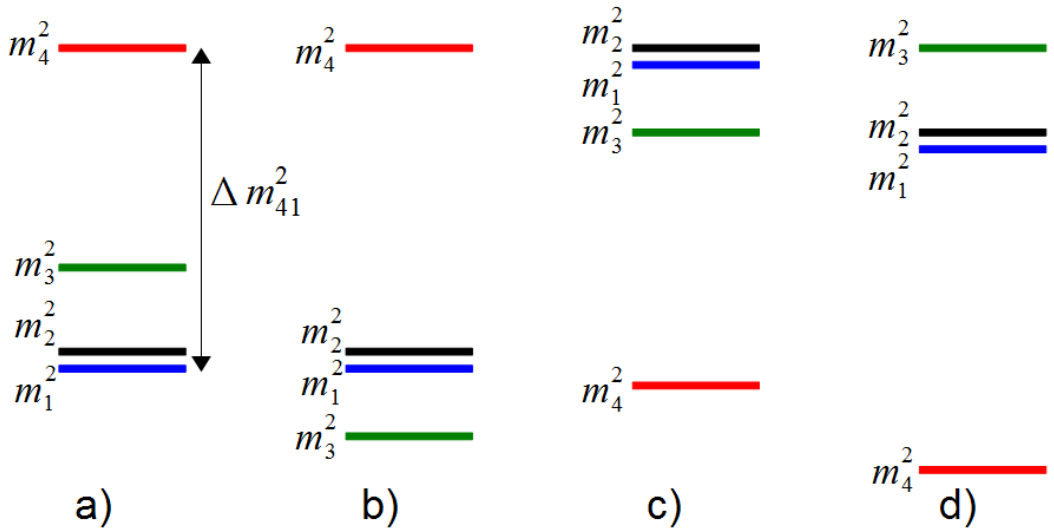

Figure 1.1: Illustration of possible neutrino mass orderings in the 3+1 model: a) is referred to as normal mass ordering standard neutrinos, normal mass order sterile neutrinos, b) as inverted mass order standard neutrinos, normal mass order sterile neutrinos, c) as inverted mass order standard neutrinos, inverted mass order sterile neutrinos and d) as normal mass ordering standard neutrinos, inverted mass order sterile neutrinos.

Laboratory experiments set a limit on the mass of the electron antineutrino $m_{\bar{\nu}_e}$ by measuring the electron β-decay spectrum at its end point. The most precise laboratory measurement is from the Troitsk experiment and obtained an upper limit [100] [29]:

$$m_{\bar{\nu}_e} < 2.05\,\text{eV}\ (95\%\ \text{CL})\ . \tag{1.35}$$

Cosmology yields even more stringent limits; An upper limit on the sum of neutrino masses $\sum_i m_i$ of

$$\sum_i m_i < 0.12\,\text{eV}\ (95\%\ \text{CL}) \tag{1.36}$$

is found by the Planck collaboration by combining their results with other cosmological measurements [108] (see [108] for details).

1.4 Anomalies

Several anomalies hint to or allegedly hint to the existence of further neutrino states. These anomalies are summarized briefly in the following. However, while sterile neutrinos are able to explain some of the anomalies individually the do not manage to describe all of them consistently.

1.4.1 Reactor antineutrino anomaly

The neutrino rate normalization observed by reactor neutrino experiments used be consistent with predictions. However, in 2011, the predictions were recalculated resulting in an increase by about 3.5% [93]. At the same time, the cross section of the inverse beta decay has been corrected down. Suddenly, all reactor neutrino experiments observed a neutrino rate normalization smaller than predicted [91]. This mismatch is named *reactor antineutrino anomaly*.

On the one hand, the oscillation signature observed by reactor neutrino experiments washes out when the oscillation signature becomes smaller than the energy resolution. Therefore, the mismatch could be explained by a sterile neutrino with a mass squared difference in the eV range [91]. Indeed, this is one of the motivations to induce sterile neutrino. However, it can not be excluded that the mismatch is due to a wrong prediction of the initial oscillated reactor flux.

Daya Bay Reactor Neutrino Experiment (Daya Bay) is a θ_{13} experiment similar to Double Chooz. The collaboration has analyzed the reactor antineutrino rate deficit as a function of fuel composition. Daya Bay data indicates that an incorrect antineutrino prediction related to the isotope uranium-235 might be the main source of the reactor antineutrino anomaly. An explanation by a sterile neutrino only is disfavored by 2.6σ [23].

Several dedicated experiments have been designed to investigate the reactor antineutrino anomaly measuring the spectral shape of the reactor antineutrino flux at various baselines of O(10 m) [19][30][38]. The best fit of $\sin^2\theta_{14}$, Δm^2_{41} from the reactor antineutrino anomaly [91] is excluded by more than 95% C.L. by each of the experiments DANSS [19], PROSPECT [30] and STEREO [38]. Also, the *NEutrino Oscillation at Short baseline* (NEOS) experiment disfavors the best fit from the reactor antineutrino anomaly by more that 90% C.L. [83]. Moreover, these experiments exclude significant amounts of the allowed regions from the reactor antineutrino anomaly [91]. However, the reason for the mismatch could not be ascertained without doubt so far.

The global deficit observed with Double Chooz is $\approx 8.6\%$ [101]. A oscillation analysis with Double Chooz data is not able to solve the question whether this is due to washed out oscillations related to a sterile neutrino. Therefore, the predicted global reactor flux normalization is not used in this analysis[III].

[III] The Double Chooz experiment in general has small handle to distinguish if the mismatch between predicted and observed global reactor flux normalization is due to the reactor. However, note that by plotting the global reactor flux normalization versus uranium-235 fraction in the reactor (which changes during the reactor circle (cf. section 2.2)) a dependence on the reactor composition could be detected in general. Unfortunately, only in case of an observed dependence conclusions could be drawn. Additionally, the expected sensitivity for such an analysis is not enough to finally solve the question.

1.4.2 Gallium anomaly

The solar neutrino experiments *Gallium Experiment* (GALLEX) and *Soviet–American Gallium Experiment* (SAGE) used gallium target detectors to identify electron neutrinos by the inverse beta decay reaction $\nu_e + {}^{71}\mathrm{Ga} \rightarrow e + {}^{71}\mathrm{Ge}$. Both experiments investigated radioactive ${}^{51}\mathrm{Cr}$ sources placed inside the detectors [1, 25, 70]. Moreover, the SAGE collaboration investigated a ${}^{37}\mathrm{Ar}$ source [2]. The measured rates from the sources were smaller than expected with a combined significance of 3.0σ [2]. This mismatch could be explained by a sterile neutrino with $\Delta m^2_{41} > 0.35\,\mathrm{eV}^2$, $\sin^2 2\theta_{14} > 0.07$ at 99% CL [67]. However, short baseline reactor experiments have excluded significant amounts of the allowed region from the combined fit of gallium and reactor antineutrino anomaly [19, 30, 38]. Recent recalculations of cross sections based on shell models reduce the significance of the gallium anomaly to 2.3σ [85]. The gallium experiment *Baksan Experiment on Sterile Transitions* (BEST) is going to further investigate the gallium anomaly [34].

1.4.3 LSND and MiniBooNe anomaly

The *Liquid Scintillator Neutrino Detector* (LSND) at the *Los Alamos Meson Physics Facility* measured $\nu_\mu \rightarrow \nu_e$ oscillations utilizing ν_μ beam from π^+ decay in flight and $\bar{\nu}_\mu \rightarrow \bar{\nu}_e$ oscillations from μ^+ decay at rest. The ν_e appearance was detected by the reaction $\nu_e + C \rightarrow e^- + X$ while the $\bar{\nu}_e$ appearance was detected by the inverse beta decay $\bar{\nu}_e + p \rightarrow e^- + n$. The data measured in both channels could not be explained by oscillations among the three known neutrino states [32] [31].

MiniBooNe is a neutrino oscillation experiment at *Fermi National Accelerator Laboratory* (Fermilab) build to investigate the $\nu_\mu \rightarrow \nu_e$ and $\bar{\nu}_\mu \rightarrow \bar{\nu}_e$ oscillations. Historically, the experiment was build to revise the LSND results [15]. The results for both the $\nu_\mu \rightarrow \nu_e$ and $\bar{\nu}_\mu \rightarrow \bar{\nu}_e$ show an excess of electron (anti-)neutrinos [16]. The excess is consistent with the results from LSND. Combination of data from both experiments yield a significance of 6.0σ [16]. The LSND and MiniBooNe data can be explained in the 3+1 model [27]. However, this explanation is rejected by measurements from disappearance experiments [52]. The experiment *MicroBooNE* is intended to further investigate the excess observed with MiniBooNe [27].

1.4.4 Spectral distortion

The Double Chooz Collaboration has observed a mismatch of the reactor neutrino prediction and their measured data in the visible energy region around 5-6 MeV [7]. The mismatch has been confirmed by the *Daya Bay Reactor Neutrino Experiment* (Daya Bay) [22], the *Reactor Experiment for Neutrino Oscillation* (RENO) [114] and the *NEutrino Oscillation at Short baseline* (NEOS) [83]. All these experiments have different baselines to the reactor cores. Moreover, Daya Bay, RENO and Double Chooz even have more than one detector and see the distortion with all of their detectors. Figure 1.2 illustrates the data-MC ratio seen by Daya Bay, RENO, NEOS and Double Chooz (near detector) [50]. One may come to the conclusion that the 4-6 MeV region is remarkably spotty. However, data has been normalized [50] and the region of best agreement depends on that normalization. The distortion can hardly be explained by sterile neutrinos since those would not

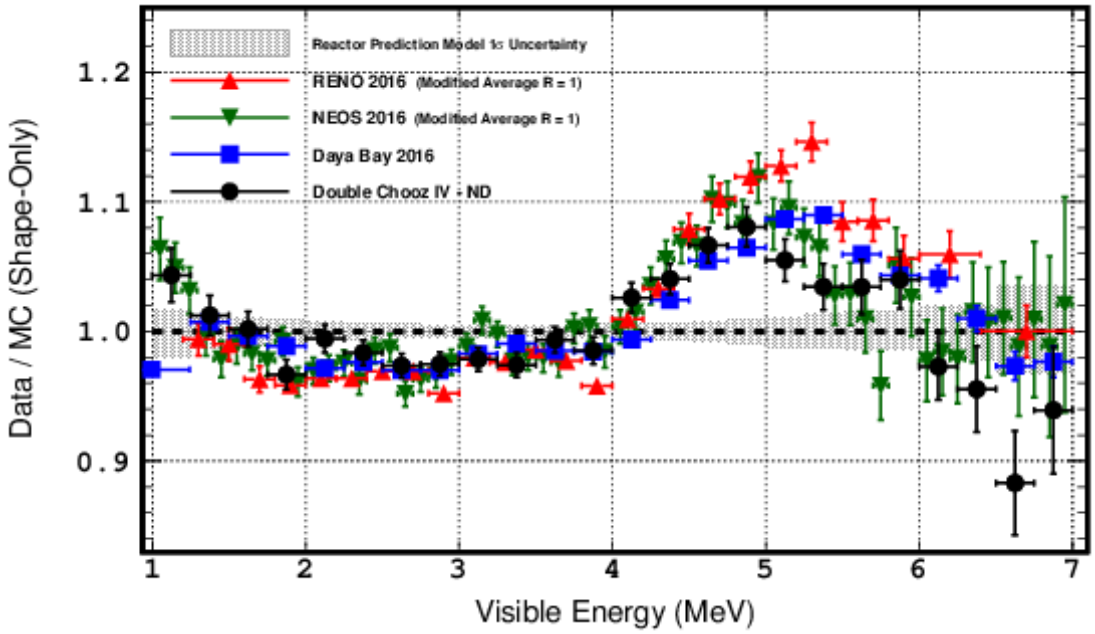

Figure 1.2: Data-MC ratio for neutrino events as a function of visible energy from Daya Bay (blue squares) [24], RENO (red triangles) [18], NEOS (green triangles) [83] and Double Chooz (near detector, black circles) [50]. The normalization from RENO and NEOS has been modified w.r.t. the publications of this experiments. This plot has been taken from [50] .

cause the same pattern at different baselines. Furthermore, the Double Chooz collaboration obtained indication that the distortion is proportional to the thermal power of the reactors [43]. Currently, the spectral distortion seems likely to originate from an imprecise reactor flux prediction. Although there is no indication that it is due to sterile neutrino, the setup of this analysis should avoid any potential bias by the spectral distortion. Therefore, this analysis does not rely on reactor flux prediction but only compares data to other data. More on this is explained in the following chapters.

Chapter 2

The Double Chooz experimental setup

This chapter describes the experimental setup of the Double Chooz Experiment.

2.1 Overview

The Double Chooz experiment is a reactor antineutrino disappearance experiment designed in order to measure the neutrino mixing angle θ_{13}. The experiment is located in a small French city in the Ardennes named Chooz. The Double Chooz experiment has measured the neutrino flux from the two nuclear reactors B1 and B2 until 2018. The Chooz-B nuclear power plant site is located at the *Nucléaire de Chooz* operated by *Electricité de France* (EDF) with two almost identical liquid scintillator detectors. The near detector located at a distance of about 400 m to the nuclear reactors was operating from January 2015 until the beginning of 2018, the far detector located at a distance of about 1050 m to the nuclear reactors was operating between April 2009 until the beginning of 2018. The Chooz-B power plant site and the position of the detectors are shown in figure 2.1. The detailed distances are given in figure 2.2. Importantly, the detectors are almost located at the isoflux curve i.e. at the curve where both detectors measure the same fraction of events from B1 and B2. The far detector is installed under an rock overburden of around 300 m water equivalent [3], the near detector is installed under an rock overburden of around 120 m water equivalent [78].

Figure 2.1: Illustration of the site of the Chooz-B nuclear power plant including the Double Chooz detectors [60]. The insert in the lower left shows the location of Chooz in France. The map has been taken from [126] and been modified.

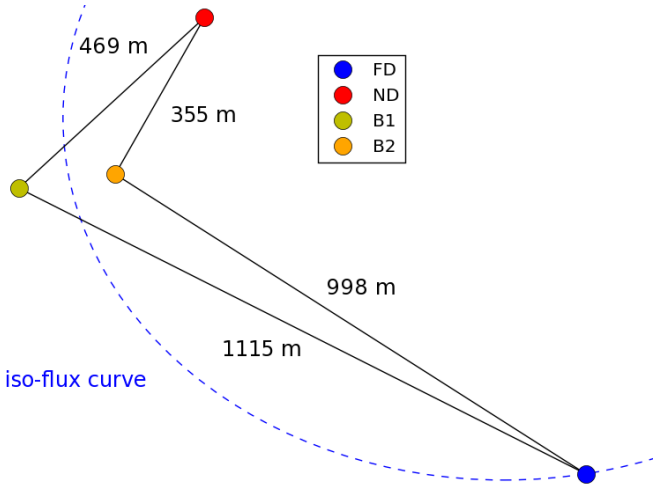

Figure 2.2: Experimental configuration of the Double Chooz experiment. The dashed blue line indicates the far detector isoflux curve i.e. positions at which the ratio of events from both reactors is constant. Altitude differences are not shown in this plot. The far detector is about 31 m below the altitude level of the reactors and the near detector is about 42 m below the altitude level of the reactors. The noted distances between detectors and reactors account for the differences in altitude. Therefore, they do not correspond exactly to the length of the particular line in this plot. The iso-flux curve was calculated assuming all reactors and detectors were at the same altitude. Distances have been taken from [122]. Own illustration.

2.2 Neutrino source

Chooz B1 and B2 are N4 type pressurized water reactor (PWR) cores yielding a nominal power output of 4.25 GW_{th} each [4]. The main process in the reactor cores is the controlled exothermic fission chain reaction:

$$n + {}^{235}\mathrm{U} \rightarrow {}^{236}\mathrm{U}^* \rightarrow {}^{A}\mathrm{X} + {}^{B}\mathrm{Y} + C \cdot n\,, \quad A + B + C = 236, A, B, C \in \mathbb{N} \quad . \tag{2.1}$$

A neutron is captured by an uranium-235 atom, which transforms into an exited uranium-236 atom. Then it breakes into two other atoms X and Y plus neutrons as illustrated in figure 2.3. Exemplary for this is [88]:

$$n + {}^{235}U \rightarrow {}^{236}U^* \rightarrow {}^{140}\mathrm{Xe} + {}^{94}\mathrm{Sr} + 2n + 200\,\mathrm{MeV} \quad . \tag{2.2}$$

The resulting neutrons may induce other interactions of this type. The fission fragments X and Y produce anti electron neutrinos by undergoing a series of beta minus decays since they are unstable due to a large number of neutrons compared to the number of proton in these atoms [88]. For example, in equation (2.2) the decays lines are [88]:

$${}^{140}\mathrm{Xe} \xrightarrow{\beta} {}^{140}\mathrm{Cs} \xrightarrow{\beta} {}^{140}\mathrm{Ba} \xrightarrow{\beta} {}^{140}\mathrm{La} \xrightarrow{\beta} {}^{140}\mathrm{Ce} \text{ and } {}^{94}\mathrm{Sr} \xrightarrow{\beta} {}^{94}\mathrm{Y} \xrightarrow{\beta} {}^{94}\mathrm{Zr} \quad . \tag{2.3}$$

In fact, the total neutrino flux results from decay and fissions of more than 1000 daughter isotopes [62].

The number of neutrinos produced by a nuclear reactor is roughly proportional to its thermal power. Nuclear reactors usually produce an anti electron neutrino rate of about [91]

$$R_{\bar{\nu}_e} \approx 10^{20}\,\mathrm{s}^{-1} \text{ per GW thermal power} \,. \tag{2.4}$$

Three isotopes other than ^{235}U contribute significantly to this number: ^{238}U, ^{239}Pu and ^{241}Pu [91]. The reason for these isotopes being present in the reactor is explained in the following. Typical reactor fuel mostly consists of uranium, where the ^{235}U abundance has been increased artificially to a few percent. The rest of the uranium is almost entirely ^{238}U. The fraction of ^{235}U in the reactor decreases during operation (since it is used for the controlled fission chain reaction) and the reactor accumulates ^{239}Pu due to the reaction [88]:

$$n + {}^{238}\mathrm{U} \rightarrow {}^{239}\mathrm{U} \xrightarrow{\beta} {}^{239}\mathrm{Np} \xrightarrow{\beta} {}^{239}\mathrm{Pu} \quad . \tag{2.5}$$

The ^{239}Pu may capture an other neutron and become ^{240}Pu if it is not fissioned. ^{240}Pu is again able to capture a neutron and become ^{241}Pu [88]. This is illustrated in figure 2.4. The burned ^{235}U must be refilled. Therefore, each reactor is powered off after about one year of operation for several weeks in order to exchange about one third of the fuel [4]. Thus, Double Chooz has taken data with both reactors on but also with only one reactor on. The fuel exchange in a reactor core is usually done while the other reactor core is running. Figures 2.5 and 2.6 show the neutrino candidate rate versus time for near and far detector. The expected rate being roughly proportional to the reactor power (cf. equation (2.4)) is shown in red. It was calculated assuming no-oscillation. The observed rate is shown in blue (near detector) and black (far detector). The plots show that the observed rate is proportional to the reactor power as well as the expected rate and that expected and observed rate are proportional to each other. The bottom plots presents the ratio 2(MC - Data)/(Data + MC) versus time where *Data* is the experimental data and

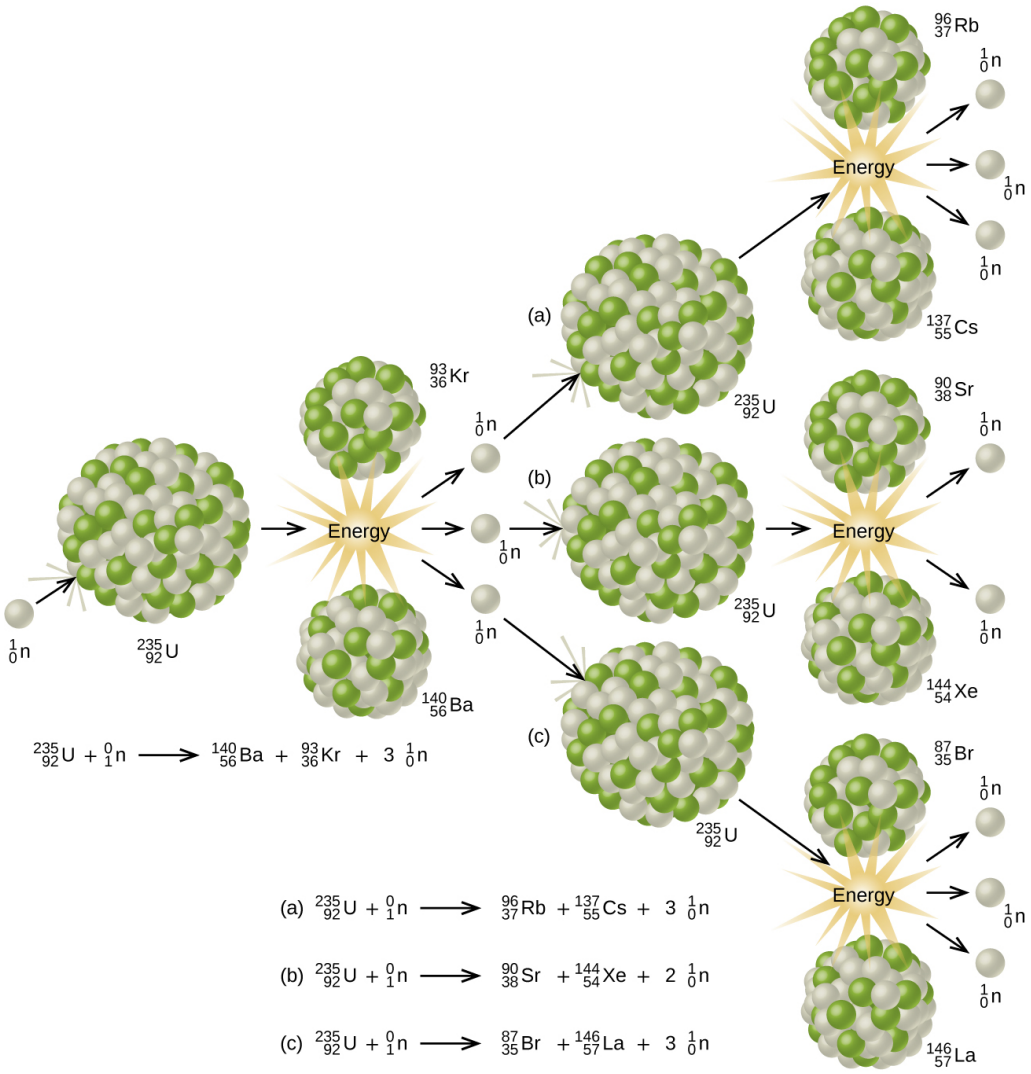

Figure 2.3: Illustration of the fission chain reaction of ^{235}U (cf. equation (2.1)) [103]. As shown here, the uranium may produce several different fission fragments. An example is given in equation (2.2). Note, that if the fission chain reaction is controlled, usually not all of the neutrons induce other fissions. Instead, if for instance the reaction rate is intended to be constant, exactly one neutron on average induces an other fission.

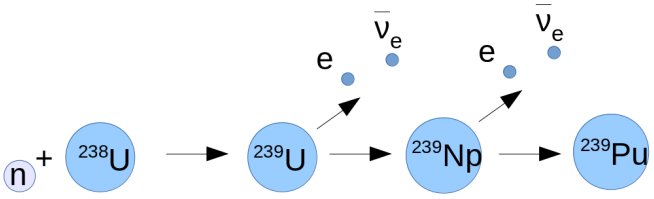

Figure 2.4: Illustration of the ^{239}Pu creation in a nuclear reactor (see equation (2.5)).

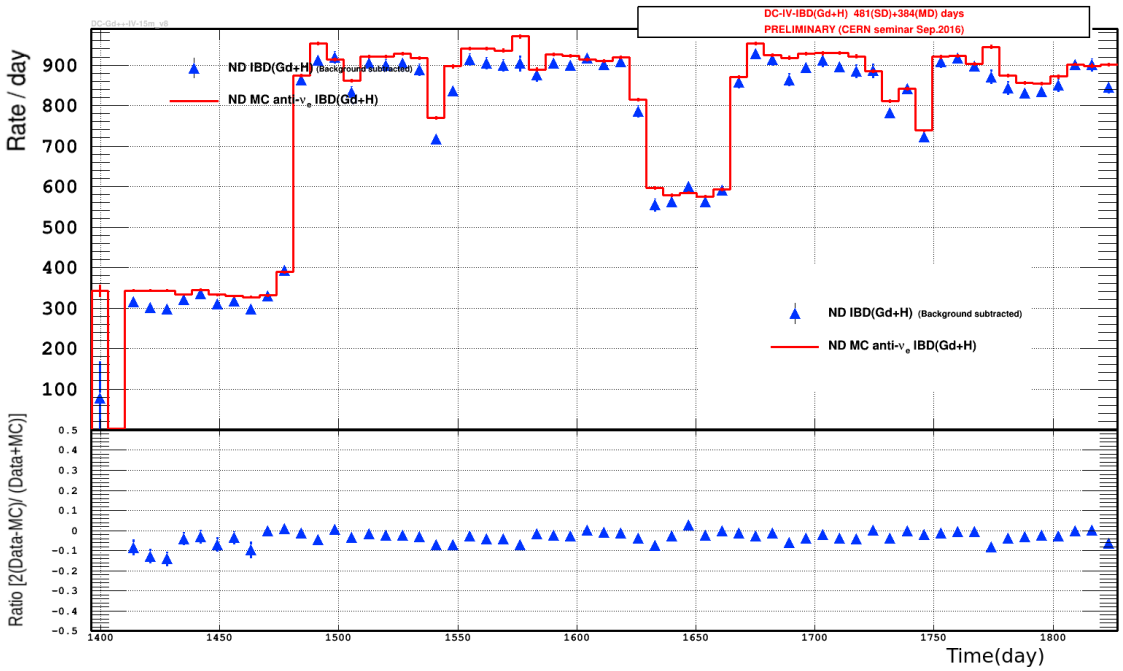

Figure 2.5: Rate of neutrino candidates in the near detector rate versus time. The expected rate is shown in red while the observed rate is shown in blue. The bottom plot presents 2(MC - Data)/(Data + MC) versus time. Here, *Data* means the experimental data and *MC* means the expected rate from Monte Carlo without oscillation [58] (modified).

MC is the expected rate from Monte Carlo (MC) simulations without oscillation. Since oscillation was not included in the expected rate, the ratio 2(MC - Data)/(Data + MC) is smaller than 1 in particular in the far detector. More precisely there is a deficit of ≈ 0.9 due to the oscillation effects related to $\sin^2 2\theta_{13}$.

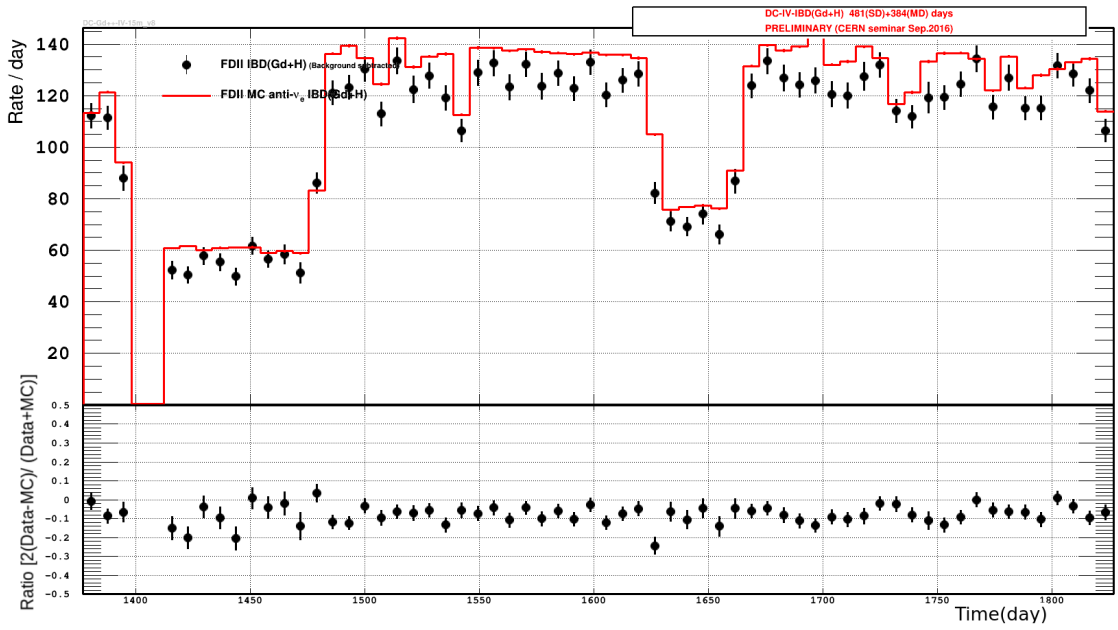

Figure 2.6: Rate of neutrino candidates in the near detector rate versus time. The expected rate is shown in red while the observed rate is shown in black. The bottom plot presents 2(MC-Data)/(Data + MC) versus time. Here, *Data* means the experimental data and *MC* means the expected rate from Monte Carlo without oscillation [59] (modified).

2.3 Neutrino detection

Section 2.3.1 introduces the physical process utilized for the neutrino detection. After that section 2.3.2 goes more into detail abut the Double Chooz detectors.

2.3.1 Detection principle

The neutrino detection is done by inverse beta decay (IBD):

$$\bar{\nu}_e + p \rightarrow n + e^+ \quad . \tag{2.6}$$

The energy threshold for the inverse beta decay process is $m_n - m_p + m_e = 1.8\,\text{MeV}$. The reaction of the inverse beta decay is illustrated in figure 2.7, the corresponding Feynman diagram is shown in figure 2.8. The antineutrino exchanges a W^- boson with a proton producing a neutron and a positron (cf. figure 2.7, figure 2.8). Inverse beta decay produces a characteristic prompt delayed coincidence in the detector as explained in the following.

Prompt signal The positron promptly annihilates with an electron producing two photons. Importantly, the energy deposit of this *prompt event* depends on the neutrino energy E_ν. The positron energy E_{e^+} is approximately [123]:

$$E_{e^+} = E_\nu - (m_n - m_p) - O(E_\nu/m_n) \quad , \tag{2.7}$$

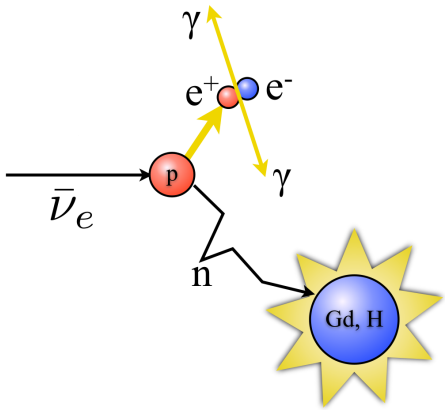

Figure 2.7: Illustration of the inverse beta decay [78].

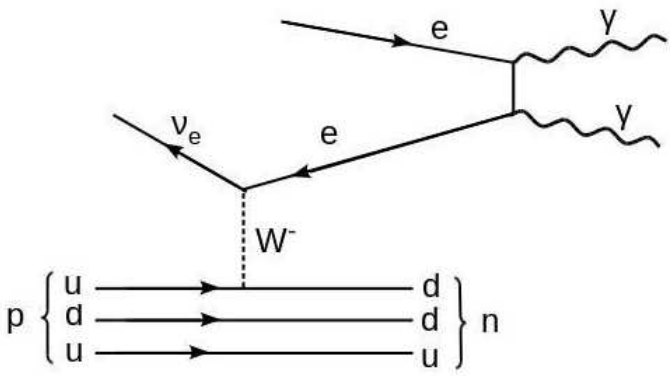

Figure 2.8: Feynman diagram of the inverse beta decay. Time axis is the x-axis. Own illustration.

where m_n and m_p are the rest masses of the neutron and the positron. The visible energy deposited by the photons in the detector E_{vis} is the sum of the total positron energy plus the rest mass of the electron m_{e^-}:

$$E_{\text{vis}} = E_{e^+} + m_{e^-} \approx E_\nu - (m_n - m_p) + m_{e^-} \quad . \tag{2.8}$$

Thus, the energy of the antineutrino can be calculated from the visible energy by

$$E_\nu \approx E_{\text{vis}} - (m_n - m_p) + m_{e^-} \quad . \tag{2.9}$$

As illustrated in figure 2.9, the final reactor neutrino spectrum is a product of the neutrino flux from the reactors (solid line) and the cross section of the inverse beta decay (dashed line). The resulting spectrum is indicated by the light blue area. It reaches from 1.8 MeV to ≈ 8 MeV where the maximum is around 4 MeV (cf. figure 2.9).

Delayed signal The delayed signal is produced when the neutron has been thermalized and is captured by either a gadolinium (Gd) or a hydrogen (H) nucleus afterwards. The neutron capture results in a characteristic energy deposit of 8.0 MeV for gadolinium [128] respectively 2.2 MeV [37] for hydrogen. The delayed event is named after the delay due to the required thermalization process. The precise delay time depends on the fluid in which the interaction occurs, namely on its thermalization properties and its neutron capture cross section. The characteristic energy of the delayed event and the delay time allow a reliable identification of inverse beta decay events. The hydrogen capture energy is closure to typical energy deposit of background reactions caused by natural radioactivity which usually deposit relatively small amounts of energy. Thus, the selection of inverse beta decay events on hydrogen capture suffers more from natural radioactivity induced background than the selection of inverse beta decay events on gadolinium capture. A small fraction of neutrons is also captured by carbon atoms where the characteristic energy deposit is about 5 MeV [50]. Further details on backgrounds and the neutrino candidate selection can be found in section 2.5 and 3.5.

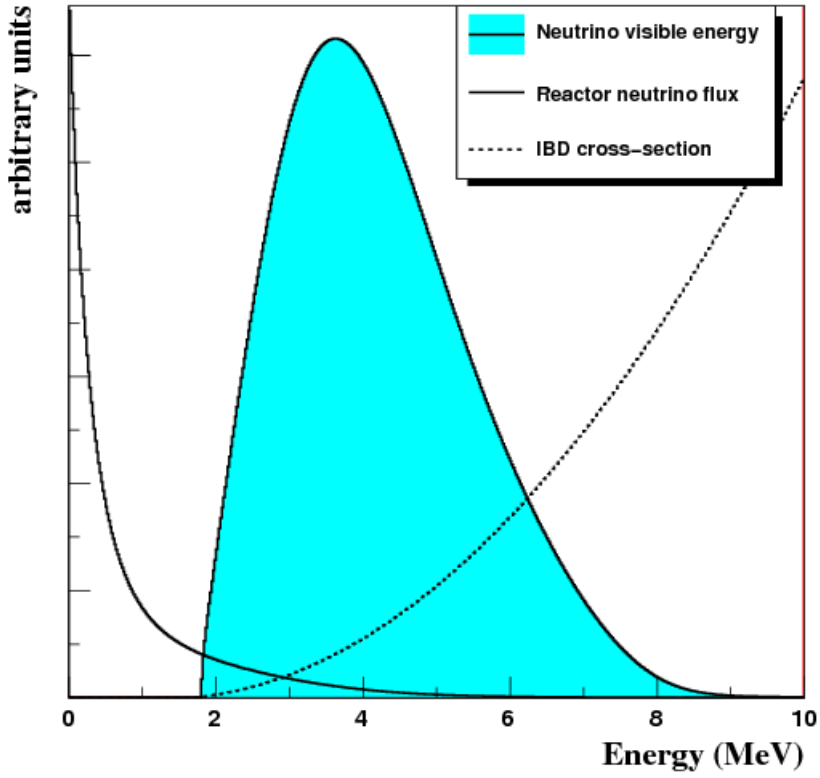

Figure 2.9: Illustration of the reactor neutrino spectrum versus (visible) neutrino energy as a product of detection cross section and reactor flux [99].

2.3.2 Detector

Figure 2.10 shows a schematic illustration of the Double Chooz detectors. The Double Chooz detectors are liquid scintillator detectors made of four con-centric cylindrical vessels inside each other (onion structure). These four vessels hold the *neutrino target* (NT), the *gamma-catcher* (GC), the *buffer* and the *inner veto* (IV) (from inside to outside). All of these volumes will be explained in the following. The outer vessel holding the inner veto volume has a diameter and a height of 7 m.

Inner detector

Neutrino target, gamma-catcher and buffer form the *inner detector* (ID). The buffer fluid is contained in a stainless steel tank holding 390 10-inch photomultiplier tubes (PMTs) while neutrino target and gamma-catcher and buffer are separated by transparent acrylic vessels. The term inner detector includes these PMTs [4].

Neutrino target The neutrino target is the innermost volume inside the inner transparent acrylic vessel filled with 10.3 m^3 liquid scintillator. It is doped with 1 g Gd /liter corresponding to a gadolinium fraction of 0.123% by weight[4]. The neutrino target is the only volume in which neutron captures on gadolinium capture are possible, because the other volumes do not contain gadolinium. Further information about all liquid scintillators used in the experiment can be found in [11] and [10].

Gamma-catcher As mentioned in the previous section, the prompt event consists of two photons produced by annihilation of the positron from the inverse beta decay with an electron inside the detector. In order to obtain the energy of the prompt event it is essential to detect both photons. Therefore, the neutrino target is surrounded by the gamma-catcher a 55 cm thick liquid scintillator layer inside the outer transparent acrylic vessel. The gamma-catcher volume is 22.5 m^3 [4].

Buffer In order to shield against photons from PMTs and the surrounding rock, Neutrino target and gamma-catcher are surrounded by a 105 cm thick layer of non-scintillating mineral oil, the buffer. The 110 m^3 of buffer mineral oil are filled into a stainless steel tank equipped 390 10-inch Hamamatsu R7081 PMTs [35] [4].

Veto-systems

Inner veto The inner detector is surrounded by the inner veto, a 50 cm thick layer of liquid scintillator with 78 8-inch PMTs mounted in the 15 cm thick steal shielding around it; 24 PMTs are mounted in the top, 12 in the side walls and 42 on the bottom [4]. In addition to being an active veto for cosmic ray muons the IV also works as a shield, in particular against external fast neutrons. The steal shielding further protects against photons from the outside.

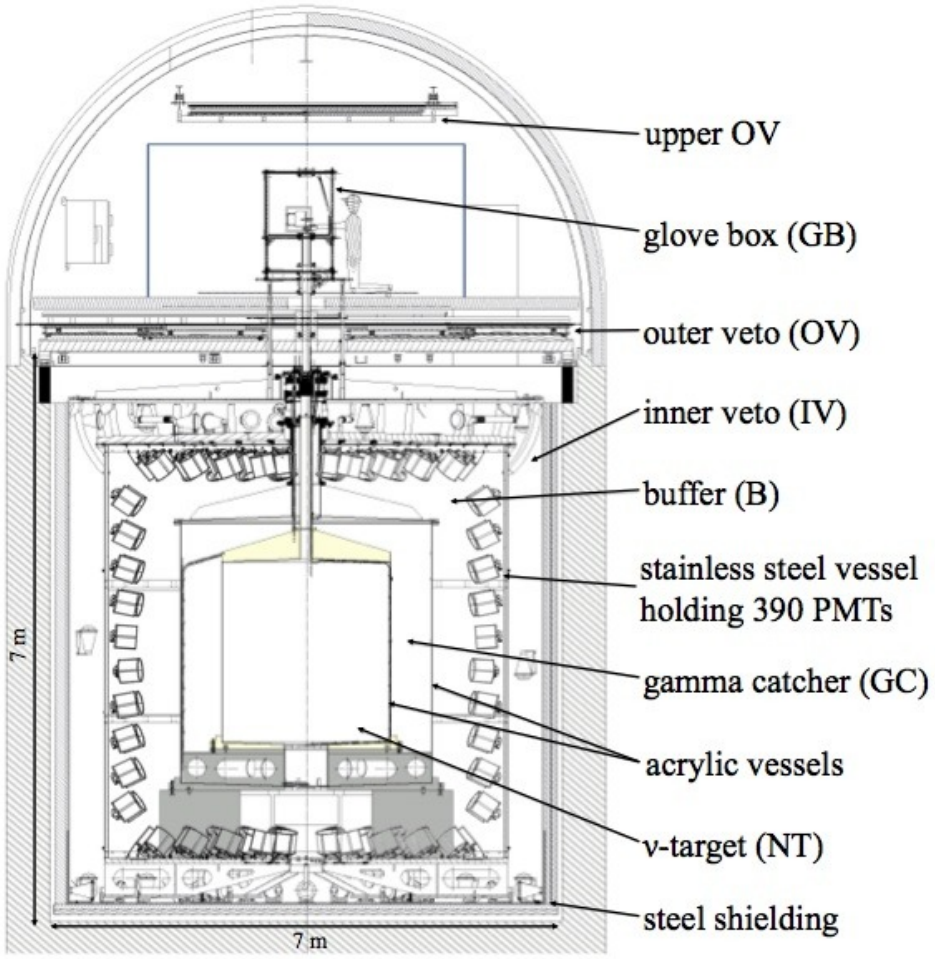

Figure 2.10: Schematic illustration of the Double Chooz detectors [7]. This is the far detector, in the near detector the outer shielding is realized by 1 m of water instead of steel [50].

Outer veto The *outer veto* (OV) covers the top of the detector. The lower outer veto directly above the steel shielding veto consists of plastic scintillator strips mounted in two layers oriented vertically to each other. In the far detector it covers a region of 91 m^2 around the chimney except for 10 cm x 30 cm directly around it [4]. In the near detector the covered area is 47 m^2 [113].

Chimney

The volumes of neutrino target and gamma-catcher are not completely closed in order to allow placing calibration sources in the detector. A vertical shaft called chimney in the center of the detector and a glove box installed at its upper end allow to locate a source in these volumes. There is a clean room around the glove box to avoid contamination.

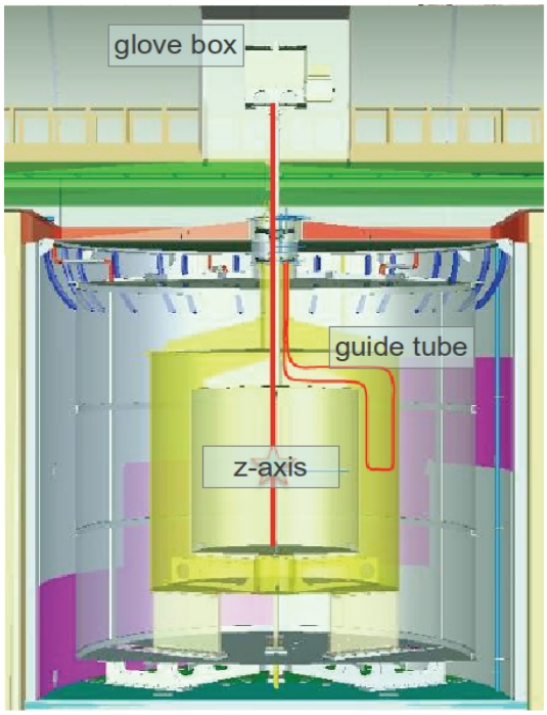

Figure 2.11: Schematic illustration of the calibration systems for deployment of radioactive sources in the Double Chooz detectors, the z-axis system and the guide tube system [89].

2.4 Calibration

In order to reconstruct the neutrino energy a conversion function between charge deposit in the PMTs and visible energy is needed. This conversion function is not constant due to degeneration of detector hardware caused by power cycles or time evolution. Therefore, calibration systems allowing to obtain and to monitor the conversion function over time have been installed in the Double Chooz detectors. They are schematically illustrated in figure 2.11 and described in the following.

2.4.1 Inner veto light injection system

The inner veto light injection (IVLI) system was installed in order to monitor the properties of the inner veto PMT and the liquid scintillator. For this purpose, light-emitting diodes (LEDs) illuminate optical quartz fibers that are attached to the inner veto PMTs (at least one fiber per PMT) and therefore guide the light into the inner veto. Six of the in total 96 LEDs are ultra violet (365 nm wavelength), 78 of them are blue (475 nm). All of the LEDs are placed on one compact board mounted outside the detector on the wall of the laboratories. With this setup, single PMTs can be illuminated. It allows to measure gain and number of p.e. of the PMTs as well as the light yield of the liquid scintillator [61]. Further details can be found in [61].

2.4.2 Inner detector light injection system

The inner detector light injection (IDLI) system is very similar to the inner veto light injection system, except that it monitors the inner detector instead of the inner veto. The inner detector light injection system consists of optical quartz fibers attached to LEDs. These LEDs have wavelength of 385, 425 and 470 nm. In contrast to the IVLI system, the IDLI system can not illuminate single PMTs. Instead, diffuse beams in 32 different configurations or focused beams in 14 different configurations beams through the detector. In doing so, PMTs an scintillator properties may be measured [124]. Further details can be found in [124].

2.4.3 Guide tube system

The guide tube system allows the deployment of radioactive sources in the gamma-catcher. It can be accessed through the chimney and consists of a steel tube loop and a wire being able to guide sources through the tube since it is connected to a computer controlled stepper motor. Thereby, the position of the source along the tube is known to 1 cm precision.

2.4.4 Z-axis system

The z-axis system is used to deploy sources along the central symmetry axis of the detector (z-axis) in the neutrino target volume. Similar to the guide tube system, the z-axis system is accessed through the chimney and the lowering of the source into the neutrino target volume is guided by a wire connected to a computer controlled step motor. The position on the z-axis is known to 1 mm precision.

2.5 Backgrounds

There are several background processes that create a signal similar to the IBD event. All unneglatible types of background processes are explained in the following.

2.5.1 Correlated background

The correlated backgrounds mimic both the prompt and the delayed event. Correlated backgrounds are due to atmospheric muon, i.e. muons that are produced in cosmic ray air showers. These atmospheric muons may enter the detector or the nearby rock. Although through going muons themselves are easily identified by their huge energy deposit atmospheric muons may cause different processes that mimic an inverse beta decay signal as described in the following.

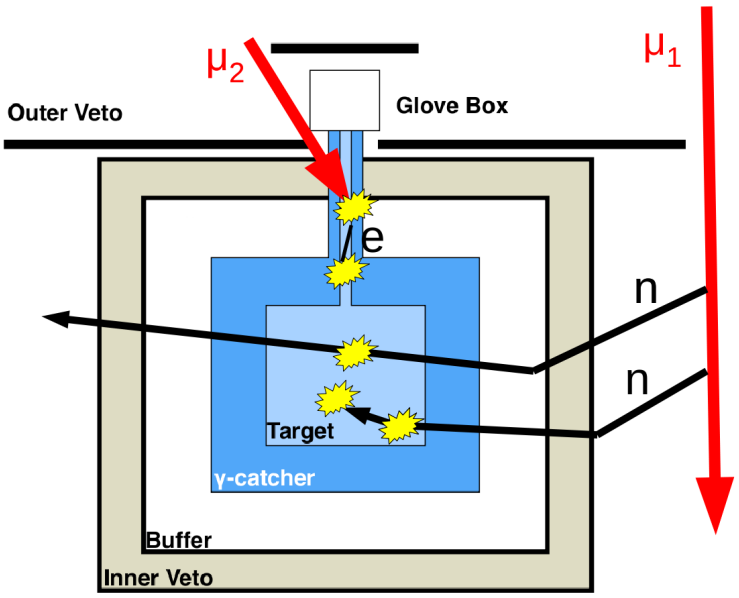

Figure 2.12: Schematic illustration of the fast neutron and stopping muon background process. Muon μ_1 causes fast neutrons, muon μ_2 is a stopping muon. Detector illustration has been taken from [78] and background process illustrations have been added.

Fast neutron background

Muon μ_1 in figure 2.12 sketches the fast neutron (FN) background process. Spallation of carbon atoms in the rock around the detector by atmospheric muons may produce fast neutrons which can enter the detector due to there large interaction length. Proton recoils by a fast neutrons inside the detector may produce an apparently prompt signal followed by the delayed capture of that neutron which got decelerated due to the recoil and thermalization or capture of a different neutron.

Cosmogenic isotope background

Organic liquid scintillators as used in Double Chooz are by definition vulnerable to spallation of carbon atoms by atmospheric muons because of their carbon fraction. The cosmogenic isotope background process is illustrated in figure 2.13. Spallation processes inside the detector induced by cosmogenic muons entering the detector produce several spallation products, in particular ^{9}Li and ^{8}He. ^{9}Li and ^{8}He undergo β-n decay, i.e. beta decay followed by neutron emission. Figure 2.14 illustrates the decay chain and the relevant branching ratios for ^{9}Li, figure 2.15 for ^{8}He. β-n decay can not be distinguished from an inverse beta decay because the Double Chooz detector is not able to distinguish an electron from a positron. Additionally, the ^{9}Li and ^{8}He is challenging because of the long live times of 257 ms respectively 172 ms which do not allow for vetoing on the primary muon event [4] [9].

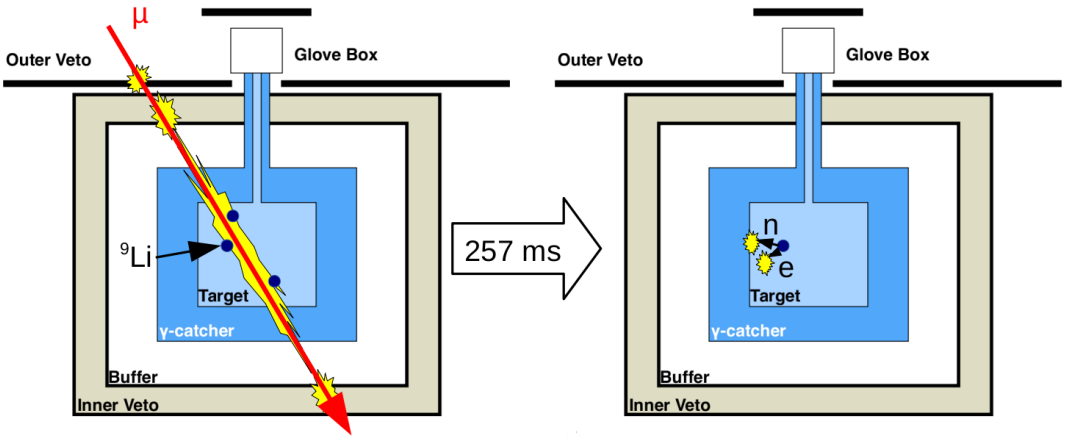

Figure 2.13: Schematic illustration of the cosmogenic isotope background process. The muon at the left handside creates ^{9}Li by spallation. This ^{9}Li decays via $\beta - n$ decay after 257 ms and causes a fake inverse beta decay signal as illustrated at the right handside. Detector illustration has been taken from [78].

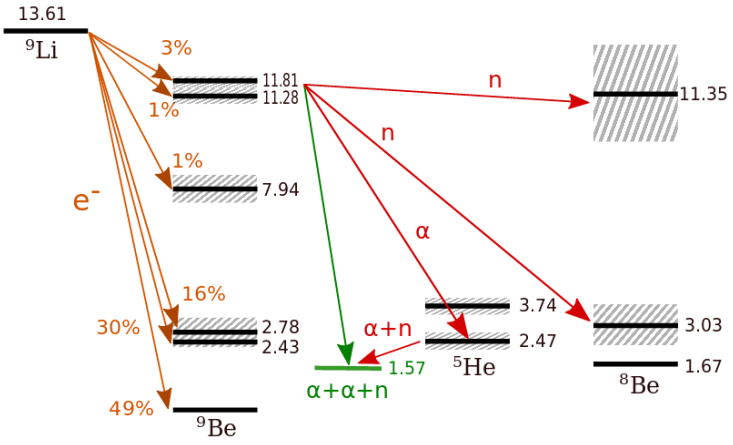

Figure 2.14: Relevant branching ratios of the β-n decaying isotope ^{9}Li (normalized to 100%) [116].

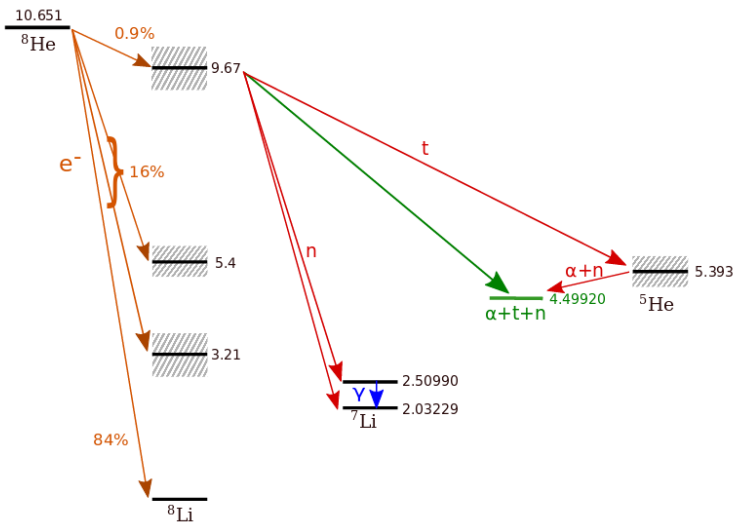

Figure 2.15: Relevant branching ratios of the β-n decaying isotope ^{8}He (normalized to 100%) [116].

Stopping muon background

The stopping muon (SM) background process is illustrated by muon μ_2 in figure 2.12. Muons entering the detector with relatively high energy can easily be identified by their large energy deposit but muons entering the detector with less energy can not. Those muons with few energy usually enter through the chimney and stop inside the detector. In this case, the short muon track and the following Michel electron can be mistaken as prompt delayed coincidence.

2.5.2 Uncorrelated background

The uncorrelated backgrounds produce only one signal. Nevertheless, this signal can be misinterpreted as inverse beta decay event if there is a random coincidence with an other background event.

Accidental background

Accidental background is caused by random coincidence that satisfy the selection criteria. The main source is random association of two energy deposits caused by natural radioactivity or random association of an energy deposit caused by natural radioactivity and a background signal of different type. The mainly responsible isotopes are ^{40}K, ^{60}Co, ^{232}Th, ^{238}U (potassium-40, cobalt-60, thorium-232, uranium-238) and their decay products [105]. In particular the long half-lifetimes of ^{40}K, ^{232}Th and ^{238}U of more than 10^{9}years [63] [36] [112] cause a small unavoidable concentration of them in the detector - mainly in the non-fluid detector components like PMTs, vessels and shielding. Moreover, there is some small amount of natural radioactivity in the rock around the detectors. A schematic illustration can be found in figure 2.16. The energy deposit of radioactive decays is typically below

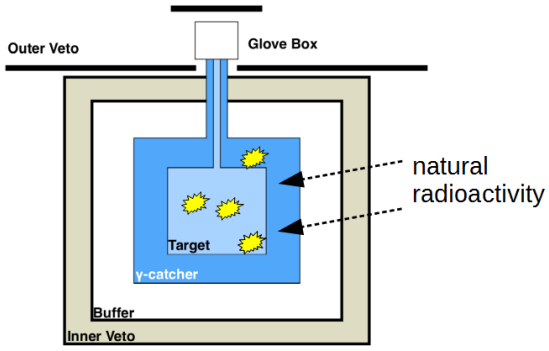

Figure 2.16: Schematic illustration of the accidental background process. Detector illustration has been taken from [78].

3 MeV. Thus, the accidental background is mainly present at low prompt energies and the contamination of neutron captures on hydrogen is bigger than on gadolinium [9].

Light Noise background

Unexpectedly, a high rate >100 Hz of spontaneous light emission by the PMTs themselves was detected during the commissioning of the far detector as illustrated in figure 2.17. This background was named Light Noise (LN) and turned out to be connected to the epoxy used to cover the PMT bases. A possible explanation is that it is caused by discharge of gas in bubbles in the epoxy used to cover the PMT bases [8]. Fortunately, for Light Noise events most of the light is firstly seen by the PMT producing the light, and secondly by the nearby PMTs. In contrast, for an inverse beta decay event the light is more broadly distributed in the inner detector. Furthermore, Light Noise events consist of relatively long sequences of pulses emitted by the PMT base producing a wide range of photon arrival times, while for a single inverse beta decay signal all photons have comparable arrival times. Hence, Light Noise can be efficiently rejected by the charge and arrival time distributions [8]. The PMTs bases in the near detector were masked with a black radiopure polyester film [8] in order to reduce Light Noise. This black film was indeed suppressing the PMT Light Noise successfully.

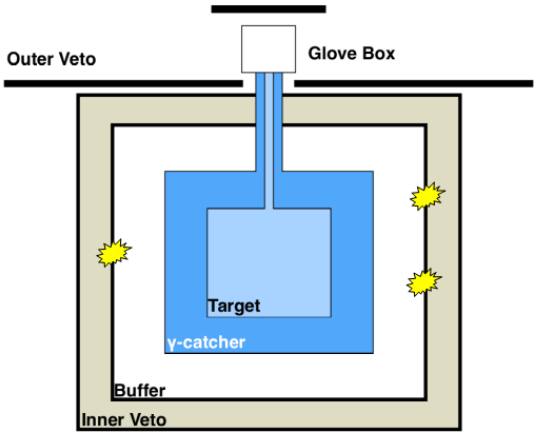

Figure 2.17: Basic schematic illustration of the Light Noise background process. Detector illustration has been taken from [78].

Chapter 3

Datasets

This chapter describes the dataset used in this work. After an introduction in section 3.1 the energy calibration is described in section 3.3. Next, the reactor neutrino prediction is explained in section 3.4. Finally, the selection is described in section 3.5. The dataset is identical to the dataset in [50].

3.1 Overview

The dataset is divided into the following subdatasets:

- FD1-On: Far detector in single detector phase with at least one reactor on
- FD1-Off-Off: Far detector in single detector phase with no reactor on
- FD1: union of FD1-On and FD1-Off-Off
- FD2 (also: FD-II, FDII): Far detector in two detector phase
- ND (also: ND-I): Near detector in two detector phase (i.e. all near detector data)

The most remarkable change in the experimental was the start of data taking with the near detector in 2015 (cf. chapter 2). Thus, the far detector data is divided into data taken in parallel with the near detector and not taken in parallel with the near detector called *FD2* and *FD1* data. The flux observed with both detectors is almost fully correlated only in the parallel data taking period. There are 7.16 days of lifetime with all reactors off taken in 2011 and 2012 during the FD1 period. This so called *FD1-Off-Off* data is mostly background dominated (although a small number of residual reactor neutrinos is expected). The FD1-On data consists of 455.21 days of lifetime [50] [44][I] collected between April 2011 and January 2013, the FD2 and ND datasets have 362.97 respectively 257.96 days of lifetime taken from January 2015 until April 2016 [50] [44]. Table 3.1 summarizes this information about the datasets.

[I] Runtime and lifetime are not identical due to a dead-time after muon events of 1.25 μs (s. section 3.5)

Table 3.1: Data taking period summary table [50] [44]

dataset	FD1-On	FD1-Off-Off	FD2	ND
period	single det.	single det.	two det.	two det.
when taken	04/2011-01/2013	2011+2012	01/2015-04/2016	01/2015-04/2016
lifetime/days	455.21	7.16	362.97	257.96
meas. IBD	48147	68	42660	210480

3.2 Event vertex reconstruction

The vertex of the events is reconstructed by applying a likelihood (LLH) fit approach which uses charge and time information of all PMTs and assumes that events are point like. Consequently, the likelihood $\mathcal{L}(\vec{x})$ of the event vertex being at $\vec{x} = (x, y, z, t, \phi)$ in the five dimensional space of the three spatial coordinates x, y, z, time t and light intensity per unit solid angle ϕ is given as [7]:

$$\mathcal{L}(\vec{x}) = \prod_{i \text{ PMTs with } q_i=0} f_q(q_i, q_i'(\vec{x})) \prod_{j \text{ PMTs with } q_j>0} f_q\left(q_j, q_j'(\vec{x})\right) \cdot f_t\left(t_j, t_j'(\vec{x})\right) \quad . \tag{3.1}$$

Here, the index i runs over all inner detector PMTs that did not see a charge while j runs over all of them which did. q_j and t_j are the charge and the arrival time being seen by PMT j. Correspondingly, $q_j'(\vec{x})$ and $t_j'(\vec{x})$ are charge and time expected to be seen by PMT j for an event at $\vec{x}$ [7]. The algorithm minimizes the negative log likelihood function for $\vec{x}$ where the value of the negative log likelihood function at the best fit position $\hat{\vec{x}}$ is called Functional Value (FV)

$$FV = -\ln\left(\mathcal{L}(\hat{\vec{x}})\right) \quad . \tag{3.2}$$

3.3 Energy calibration

Before any neutrino candidate selection, oscillation analysis or other high level analysis can be done, the raw data must be processed. First, the low level electronic readout must be processed, i.e. the PMT signal has to be digitized and processed. In particular, the PMT charge signal is obtained. This is a non-trivial process, which is further described in [6]. Second, the PMT charge signal is converted into information about visible energy. This process referred to as energy calibration includes several steps described in the following.

3.3.1 Linearized PE calibration

The term *linearised photo electron calibration* (linearised PE calibration) refers to the conversion of the integrated waveform charges of the PMTs to the number of photo electrons N_{pe} [7]:

$$N_{\text{pe}}^m = \sum_i \frac{q_i}{g_i^m(q_i, t)} \quad , \tag{3.3}$$

where the index m denotes either Monte Carlo or experimental data. q_i is the integrated waveform charge of PMT i and $g_i(q_i, t)$ is its gain, i.e. the conversion factor between charge

and number of photo electrons. g_i is a function of time t[II] [7] [53]. Moreover, the gain depends on the charge ($g_i = g_i(q_i, t)$) due to limited sampling effects for small charges [7] [53]:

$$g_i(q_i, t) = \begin{cases} g_i + l_i(q_i - c_i) & q_i < c_i \\ g_i & q_i \geq c_i \end{cases} , \tag{3.4}$$

where the parameters g_i, l_i and c_i are obtained from measured calibration data with constant light yield obtained from the inner detector light injection system [53]. Further details on the linearised PE calibration can be found in [53].

3.3.2 Uniformity calibration

The number of observed photo electrons for an event with given energy depends on the position of the corresponding vertex in the detector. More precisely, it depends on its coordinates in a cylindrical coordinate system (ρ and z) because of the geometry of the detectors. The uniformity calibration $f_u(\rho, z)$ corrects on this position dependence. $f_u(\rho, z)$ is derived utilizing neutron captures from hydrogen which provide a sharp peak at 2.2 MeV [7]. Apart from the precisely known energy deposit, neutron captures on hydrogen provide high statistics all over the detector because all liquids in the detector contain hydrogen.

3.3.3 Energy scale calibration

The energy scale calibration translates the number of photo electrons into an absolute energy information. A ^{252}Cf neutron source is deployed in the center of the detector for this purpose and provides neutron captures on hydrogen with high statistics. The energy scale can be obtained by the position of the narrow peak since the energy deposit of this reaction is almost fixed [7].

3.3.4 Stability calibration

The visible energy information obtained from linearised PE calibration, uniformity calibration and energy scale calibration is corrected for time variation by the so called *stability calibration*. The stability calibration function is obtained from neutron captures of neutrons from muon-induced spallations on gadolinium and hydrogen and α-decay data from ^{212}Po deployment during calibration campaigns [7].

3.3.5 Non-linearity calibrations

The energy of Monte Carlo generated events has to be corrected for discrepancies between real data and simulation. This correction function is non-linear and therefore referred to as *energy non-linearity*. By definition, it is applied to the Monte Carlo events only. Energy non-linearity may be further decomposed into *charge non-linearity* (QNL) and *light non-linearity* (LNL) which will be explained hereinafter.

[II] in particular due to power cycling of the hardware, cf. section 2.4

Charge non-linearity

The *charge non-linearity* (QNL) is due to limited accuracy of the simulation of the readout system and charge integration algorithm. Hence, it is applied to the visible energies of Monte Carlo events of any type. Calibration data taken during deployment of a ^{252}Cf neutron source at the center of the detector is used in order to measure the charge non-linearity correction [7].

Light non-linearity

The *light non-linearity* (LNL) is caused by the modeling of the scintillator properties or more precisely of light yield and quenching. The light yield depends on the ratio of Cherenkov light emission to scintillation light emission. Thus, the LNL correction is particle type depended in contrast to the charge non-linearity correction. Therefore it is not applied to all particles during the common energy calibration but only to the prompt Monte Carlo signals [7]. This is done during the final fit analysis in order to allow for handling the light non-linearity correction parameters as nuisance parameters. For estimation of the light non-linearity correction, simulation parameters quantifying the quenching effects are varied (in particular Birks' constant that allows to calculate the light yield using Birks' formula [41] [7]). The light yield in the Double Chooz detector including its measurement is described in more detail in [11] and [10].

3.4 Reactor neutrino prediction

The expected number of neutrinos in dataset d = FD1-On, FD2 or ND is given by [4]:

$$N_{\bar{\nu}_e}^{\exp,d} = \sum_{r=B1,B2} \frac{1}{4\pi L_{r,d}^2} N_p^d \epsilon_d \frac{P_r^{th}}{\langle E_{f,r}\rangle} \langle \sigma_{f,r}\rangle \quad , \tag{3.5}$$

where $L_{r,d}$ is the distance between the detector corresponding to dataset d and reactor r, N_p is the number of protons in the fiducial volume for dataset d, ϵ_d is the detection efficiency for dataset d and P_r^{th} is the thermal power of reactor r.

$$\langle E_{f,r}\rangle = \sum_k \alpha_{k,r} \langle E_f\rangle_k \tag{3.6}$$

is the mean energy per fission. It is the sum of the $\langle E_f\rangle_k$ where $\langle E_f\rangle_k$ is the mean energy per fission for the mother isotope k present in the reactor and $\alpha_{k,r}$ is the number of fissions originating from the mother isotope k relative to the total number of fissions in reactor r. The index k runs over all mother isotopes present in the reactor.

$$\langle \sigma_{f,r}\rangle = \sum_k \alpha_{k,r} \int_0^\infty S_k(E)\sigma_{\mathrm{IBD}}(E)dE \tag{3.7}$$

is the mean cross section per fission in reactor r where $S_k(E)$ is the reference spectrum of isotope k, $\sigma_{\mathrm{IBD}}(E)$ is the cross section of the inverse beta decay and E the neutrino energy.

The sterile analysis is based on a Data-to-Data (D2D) fit, i.e. a priori information about the reactor is not used. Therefore, the calculation of the reactor neutrino flux prediction is

not of major importance here. The Double Chooz Collaboration used to use the results of the Bugey4 rate measurement [51] in order to normalize the reactor neutrino predictions [4]. This normalization is referred to as *Bugey4 anchor point*. However, the data from the Bugey4 experiment is not used for the prediction used in the sterile analysis. That is because the measurement of the Bugey4 experiment itself would have been affected by sterile neutrino oscillation.

3.5 Neutrino candidate selection

Historically, the data selection used to only aim on selecting inverse beta decay events with the neutron captured by a gadolinium atom. Natively, neutrons can only be captured by Gd-atoms in volumes that contain gadolinium - which is the neutrino target only. The active volume of this so called *Gd selection* is sketched in green on the left in figure 3.1. However, the neutron produced in the inverse beta decay interaction may also be captured by a hydrogen- atom. Using these events significantly increases the statistics, as inverse beta decay events on hydrogen capture may not only occur in the neutrino target but also in the gamma-catcher. Thus, nowadays the Double Chooz Collaboration selects inverse beta decay-events on hydrogen and on gadolinium capture in both neutrino target and gamma-catcher. IBD-events on carbon capture are selected as well, but the contribution is negigable. This selection is used for the dataset used in this work and referred to as Gd++ selection. Its active volume is sketched in green in figure 3.1 on the right. The Gd++ selection results in an increase of the statistics by a factor of 2.5 compared to the Gd selection.

The approximate neutrino rate expected for the far detector is about 130/day and for the near detector is about 800/day (cf. figure 2.5, figure 2.6). The trigger rate in the far detector is more than several hundred Hertz with the Gd++ selection. Thus, a neutrino candidate selection with a low background rate is necessary.

3.5.1 Single event selection

The coincidence of prompt and delayed signal from an inverse beta decay event is the characteristic signal caused by a neutrino in the Double Chooz detector (cf. section 2.3.1). However, before prompt delayed coincidences can be identified raw data cleaning is required. The cuts used for raw data cleaning are described in the following [79].

- The trigger system identifies low energetic background triggers and high energy background online by requiring $0.3\,\text{MeV} < E_{\text{vis}} < 100\,\text{MeV}$.
- Muons are tagged by an energy deposit of E_{vis}>100 MeV in the inner detector or an inner veto deposit of $Q_{\text{IV}} > 30\,000$ digital unit of charge (DUC) in the FD1, $Q_{\text{IV}} > 50\,000$ DUC in the FD2 and $Q_{\text{IV}} > 30\,000$ DUC in the ND.
- A lot of backgrounds is reduced by rejecting all events less than ΔT_{μ}= 1.25 ms after a muon since muons induce fast neutrons and long lived cosmogenic isotopes (cf. section 2.5.1).

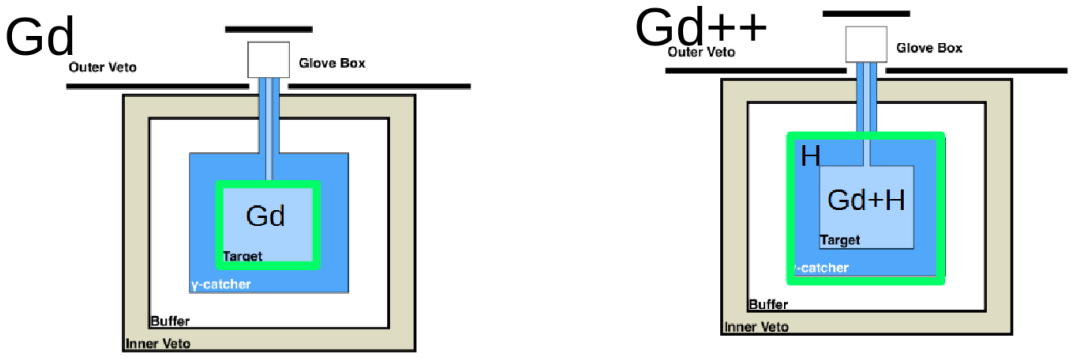

Figure 3.1: Illustration of the approaches for the inverse beta decay candidate selection utilizing a very simple sketch of the detector and highlighting the effective target volume in green. The classical gadolinium selection illustrated on the right aims on inverse beta decay candidates with the neutron captured by gadolinium only. These events only occur in the only volume that contains gadolinium, the neutrino target. Therefore, the effective target volume is the neutrino target as indicated by the green box. In contrast, the Gd++ selection aims on inverse beta decay candidates with the neutron captured by gadolinium, hydrogen or carbon, as illustrated on the left. Consequently, the effective target volume consists of neutrino target and buffer as again indicated by the green box.

- As discussed in section 2.5.2 there is a large background contamination of several hundred Hertz due to undesired light emission by the PMTs themselves, the Light Noise. Light Noise can be identified by inhomogeneous light distribution in the detector, since the light emitting PMT observes most of the light. This is done requiring $\frac{Q_{\max}}{Q_{\text{tot}}} < 0.12$ for FD1 and $\frac{Q_{\max}}{Q_{\text{tot}}} < 0.20$ for FD2 and ND where $Q_{\max}$ is the maximum integrated charge observed by a single PMT. Q_{tot} is the sum of all integrated charges in the inner detector. For further quantification of the homogeneity of the charge distribution in the detector the quantity Q_{diff} is introduced. It is defined as the Root Mean Square (RMS) of the charges observed by the PMTs within a sphere S with a radius of 1 m around the PMT which saw the maximum charge:

$$Q_{\text{diff}} = \frac{1}{N_{\text{PMT},S}} \sum_{i \epsilon S} \frac{(Q_i - Q_{\max})^2}{Q_i^2} \tag{3.8}$$

  where $N_{\text{PMT},S}$ denotes the number of PMTs inside the 1 m radius square around the PMT having seen the maximum charge, Q_i the integrated charge observed by PMT i and $Q_{\max}$ the maximum integrated charge observed by a single PMT. $Q_{\text{diff}} <$ 30000 DUC respectively $Q_{\text{diff}} <$ 100000 DUC is demanded for FD1 respectively FD2 and ND. Finally, there is a third cut making use of the smoothness of the charge distribution. In this case the RMS of the charge distribution $\varsigma(Q)$ is exploited as quantifier. Moreover, the RMS of the pulse start times $\varsigma(T_s)$ is utilized, since Light Noise is characterized by a rather big spread of start times (cf. section 2.5.2 and [8]). $\varsigma(T_s)/\text{ns} < 36$ or RMS(Q) $<$ 464 - 8$\varsigma(T_s)$/ns is claimed for FD1, $\varsigma(T_s) < 36$ ns or $\varsigma(Q) <$ 1680 - 28$\varsigma(T_s)$/ns is claimed for FD2 and ND.

All event that satisfy these conditions (cf. above text: not a muon, $\Delta T_\mu =$ 1.25 ms, not a Light Noise event, 0.3 MeV$< E_{\text{vis}} <$ 100 MeV) and are not a random trigger are kept as valid single triggers.

3.5.2 Inverse beta decy event selection

After the raw data has been reduced to the valid single triggers, the selection of inverse beta decay candidates i.e. pairs of prompt - delayed signal candidates can be done.

First, there is a cut on the visible energies: For prompt event candidates a visible energy $\boldsymbol{E_{\mathrm{vis}}}$ between 1.0 and 20.0 MeV is required. For delayed event candidates a visible energy E_{vis} satisfying 1.3 MeV $< E_{\mathrm{delayed,vis}} <$ 10 MeV is required [50].

Next, there are cuts on the relation between prompt and delayed candidate which are listed in the following.

- The time difference between prompt and delayed signal ΔT has to meet the condition 0.5 μs $<\Delta T <$ 800 μs.
- There is a cut on the distance between the vertex positions ΔR forcing $\Delta R <$ 1.2 m [50]. It reduces accidental background since the distance between a the vertexes of a prompt-delayed signal pair is shorter than for two random coincided signals.
- Muons induce plenty of neutrons rather than single neutrons. Therefore, fast neutron background is considerably suppressed by not allowing for any other valid trigger within 800 μs before the prompt candidate and no valid trigger within 0.5 μs to 900 μs after the prompt candidate except the delayed candidate. These background rejection conditions are referred to as **unicity** conditions and the corresponding cut is referred to as multiplicity cut or unicity cut. These selection conditions are illustrated in figure 3.2. Figure 3.3 provides some examples for accepted and rejected coincidences.

Moreover several vetos are applied [79]. They are explained in the following and summarized in table 3.2.

- Prompt candidates are rejected if there is a coincidence with an **outer veto** signal within 224 ns reducing the fast neutron and stopping muon background. The outer vetos do not always take good data. Therefore the outer veto veto condition is only applied for data for which good outer veto data exists.
- **Inner Veto** veto conditions are slightly different for prompt respectively delayed candidates. Events with an inner veto PMT multiplicity >1 are vetoed (i.e. at least two PMTs must observe a signal to trigger the veto) if the total charge in the inner veto is bigger than 400 DUC (FD1) resp. 300 DUC (FD2 and ND) and if the distance between inner veto and inner detector vertex is <3.7 m. For prompt candidates the veto only applies if the time difference ΔT satisfy -100 ns $< \Delta T <$ -10 ns (FD1) resp. -40 ns $< \Delta T <$ 70 ns (FD2 and ND). For delayed candidates -100 ns $< \Delta T <$ -30 ns (-30 ns $< \Delta T <$ 60 ns) is required in the FD1 (FD2 and ND) phase to meet the veto conditions. Additionally, delayed events are only rejected, if the visible energy in the inner detector is smaller than 3 MeV.
- The so called **Functional Value** veto mainly suppresses the stopping muon background but also Light Noise background not rejected by the Light Noise cut. For that purpose, the Functional Value veto investigates the negative log-likelihood value of the vertex reconstruction algorithm for its best fit hypothesis called Functional

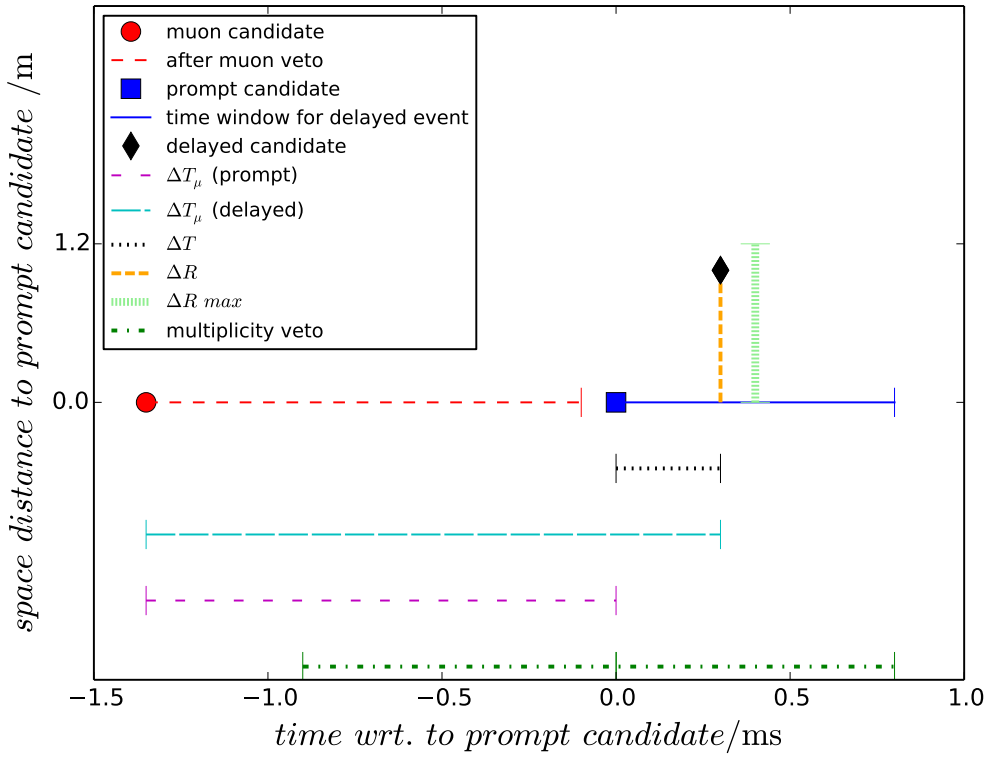

Figure 3.2: Illustration of the inverse beta decay selection conditions that have to be fulfilled by the prompt delayed coincidence.

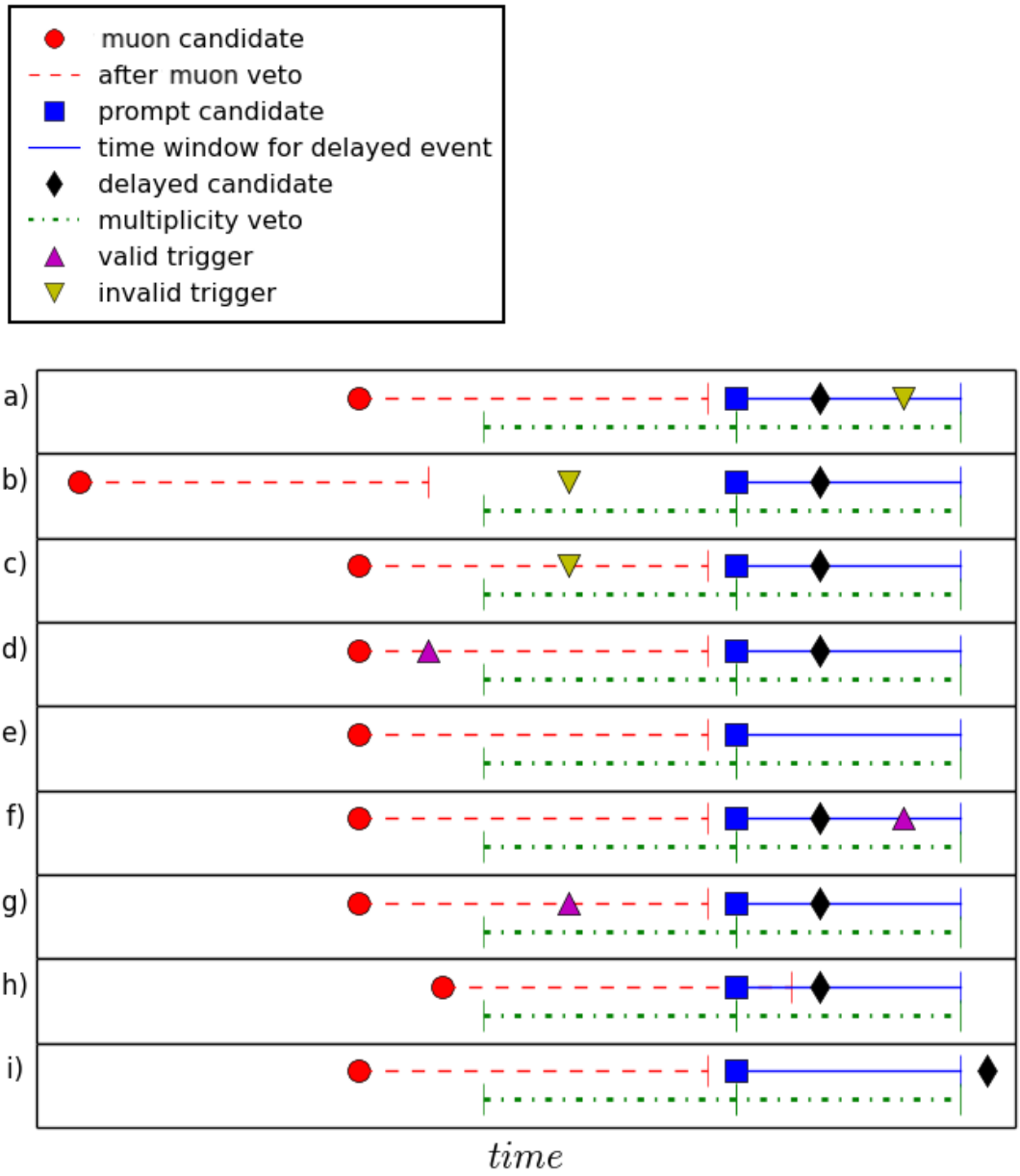

Figure 3.3: Illustration of several examples for accepted and rejected prompt-delayed coincidences. Examples a) - d) are accepted while e) - i) are rejected for the following reasons. e) is rejected because there is no delayed candidate. f) and g) are rejected because the multiplicity cut is not passed, h) is rejected because the prompt candidate comes to shortly after a muon and i) is rejected because the time difference between delayed and prompt candidate is to big.

Value (cf. section 3.2). Large Functional Values, indicating bad reconstruction, occur for non point like events (typically stopping muons) since the algorithm assumes point like events. Thus, stopping muons usually have large Functional Values. The Functional Value cut is a function of the visible energy E_{vis} as the quality of the vertex reconstruction depends on the energy deposit: $E_{\text{vis}}/\text{MeV} > 0.36 \cdot \exp(\text{FV}/2.4)$ and $E_{\text{vis}}/\text{MeV} > 0.06 \cdot \exp(\text{FV}/1.2)$ is required for all delayed candidates in the FD1 dataset, $E_{\text{vis}}/\text{MeV} > 0.2 \cdot \exp(\text{FV}/1.8)$ and $E_{\text{vis}}/\text{MeV} > 0.05 \cdot \exp(\text{FV}/1.2)$ is required for all delayed candidates in the FD2 dataset and $E_{\text{vis}}/\text{MeV} > 0.32 \cdot \exp(\text{FV}/2.1)$ and $E_{\text{vis}}/\text{MeV} > 0.07 \cdot \exp(\text{FV}/1.2)$ is required for all delayed candidates in the ND dataset.

- The **lithium (Li)** veto rejects background from cosmogenic β-n isotopes. The *lithium likelihood* quantifies the probability of each event to be a β-n decay background event. It takes into account the distance between signal vertex position to the next muon track and the number of neutron candidates within 1 ms after this muon. The probability density function for evaluating the lithium likelihood are obtained from ^{12}B because ^{12}B yields more statistics than ^{9}Li. Agreement of the probability denisty functions from lithium and boron has been confirmed [7]. Prompt candidates are rejected if the maximum lithium likelihood $\mathcal{L}_{\text{Li}}$ w.r.t. all preceding muons within 700 ms meets the condition $\mathcal{L}_{\text{Li}} \geq 0.4$. Further details on the lithium likelihood can be found in [45].

- The so called **ANN** is a multivariate analysis grounded on an Artificial Neural Network (ANN) intending for accidental background rejection. Input variables are the distance between the event vertexes ΔR, the time between the events ΔT and the visible delayed energy $E_{\text{vis,delayed}}$. Although preselective cuts have already been applied to this variables, the combination of them allows for major accidental background reduction. The ANN was trained with a Monte Carlo data sample of inverse beta decay events and an accidental background candidate sample obtained from data using the offtime method (cf. section 3.7.1) [9]. The implementation of the ANN cut increased the signal to accidental background ratio by more than a factor of seven from publication [5] to [9] while the detection efficiency only decreased by around six percent [9].

- The **chimney-pulse-shape (CPS)** veto is aiming on further reducing the contamination with stopping muons. The pulse shape of stopping muons is usually distorted due to poor vertex reconstruction. Those events are very often reconstructed more or less in the middle of the upper part of the inner detector, although in reality the muon was decaying in the chimney. For those events, the pulse shape does not get significantly worse if the originally reconstructed vertex is replaced by the position of the chimney [92]. Thus, the stopping muon background can be suppressed be comparing the negative log likelihood of the pulse shape with vertex in the chimney L_{chimney} to the likelihood of the pulse shape with the originally reconstructed vertex L_{vertex} and requiring $L_{\text{chimney}}/L_{\text{vertex}} > 0.95$. The chimney-pulse-shape veto is explained in detail in [92].

- The $\boldsymbol{\Delta BJ - FV^*}$ cut is a cut aiming on stopping muons utilizing the usually unstable vertex reconstruction of these events. As mentioned in [77] there are two vertex reconstruction algorithms: RecoBAMA and RecoJapan. Both algorithms agree well for most of the events. However, for stopping muons the position of the reconstructed

vertex tents to differ [III]. Hence, the variable $\Delta BJ = Z_{\mathrm{JP}} - Z_{\mathrm{BAMA}}$ is defined where Z_{JP} and Z_{BAMA} are the z-coordinates of the vertex from RecoJapan and RecoBAMA respectively. The rejection power of ΔBJ can be improved further if combined with the so called **F**unctional **V**alue **T**ime **Lik**elihood (FV_{tlk}). The FV_{tlk} is the negative log likelihood of the RecoBAMA vertex reconstruction where only the hit time information is used [IV]. High energetic events are easier to reconstruct due to more light emission. Hence, FV_{tlk} is smaller than for low energetic events. Therefore, FV_{tlk} is corrected for the energy depended effect by defining [77]:

$$FV^* = FV_{\mathrm{tlk}} + \begin{cases} 0.110 \cdot E_{\mathrm{vis}}/\mathrm{MeV} & \text{(FD1)} \\ 0.120 \cdot E_{\mathrm{vis}}/\mathrm{MeV} & \text{(FD2)} \\ 0.097 \cdot E_{\mathrm{vis}}/\mathrm{MeV} & \text{(ND)} \end{cases} . \tag{3.9}$$

The cut was finally optimized to

$$FV_{\mathrm{tlk}} > 4.3 \wedge \begin{cases} \frac{(FV^*-4.00)^2}{0.14^2} + \frac{(\Delta BJ+0.03)^2}{0.21^2} \geq 4^2 & \text{(FD1)} \\ \frac{(FV^*-4.00)^2}{0.15^2} + \frac{(\Delta BJ-0.01)^2}{0.21^2} \geq 5^2 & \text{(FD2)} \\ \frac{(FV^*-4.00)^2}{0.14^2} + \frac{(\Delta BJ-0.01)^2}{0.19^2} \geq 5^2 & \text{(ND)} \end{cases} \tag{3.10}$$

Several distributions before and after cuts are exemplary presented in the following. Figure 3.4 shows the ΔR distribution of the FD2 dataset. One can see that the selected events are characterized by a smaller ΔR. For the rejected events the distribution is mostly given by the detector geometry. This is due to the large contamination with accidental background before cuts. Figure 3.5 shows the distribution of the time difference between prompt and delayed event ΔT. One can take from the plot, that the rejected events are basically given by two groups. First, there is a concentration of rejected events at small ΔT. These are mostly fast neutron background events. The second group is characterized by a flat ΔT distribution [54]. These are accidental background events. There is no preferred time difference since they are just random coincidence.

[III] This is because in contrast to RecoBAMA, RecoJapan does not force vertices inside the detector. Moreover, the pull term strategy differs [77].

[IV] Indeed, FV_{tlk} yields a better rejection power than the Functional Value using charge information as well [77].

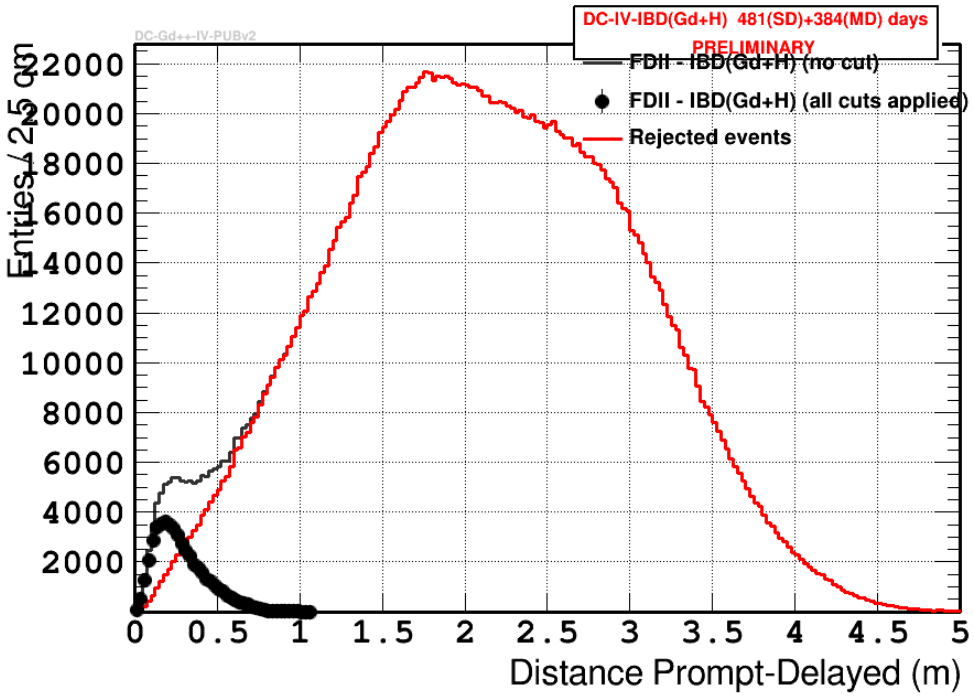

Figure 3.4: ΔR distribution of the FD2 dataset where ΔR is the distance between prompt and delayed vertex in 3 dimensional space. Black dots are used to show the data after all cuts have been applied, all data before cuts is shown as black solid line. The rejected events are shown as red line [54].

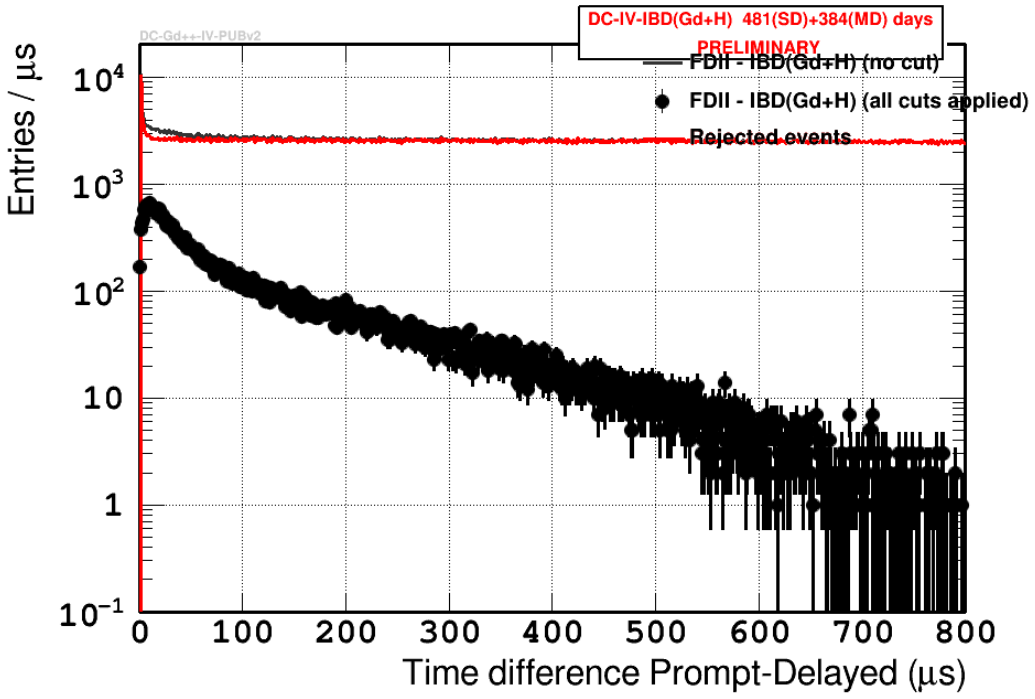

Figure 3.5: ΔT distribution of the FD2 dataset where ΔT is the time between prompt and delayed trigger. Black dots are used to show the data after all cuts have been applied, all data before cuts is shown as black solid line. The rejected events are shown as red line [54].

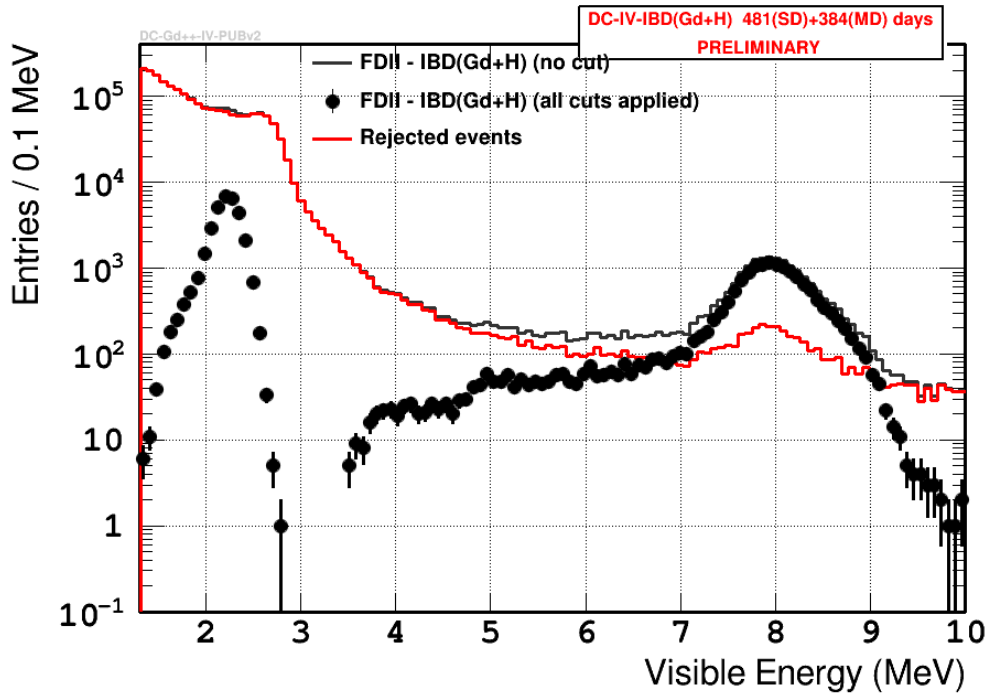

Figure 3.6: Visible delayed energy distribution of the FD2 dataset. Black dots are used to show the data after all cuts have been applied, all data before cuts is shown as black solid line. The rejected events are shown as red line. The accumulation of events around 2.2 MeV arises from neutron captures on hydrogen while the accumulation of events around 8 MeV arises from neutron captures on gadolinium [54].

Table 3.2: Summary of veto conditions for the inverse beta decay selection [79]. Events meeting any of the listed criteria are rejected. If more than one condition is listed in one field and they are not separated by a dashed line all of them have to be fulfilled in order to veto the event. More details can be found in the text.

name	target	FD1	FD2	ND
E_{vis}	p	$E_{\text{vis}} \leq 1.0\,\text{MeV}$		
		$E_{\text{vis}} \geq 20.0$ MeV		
E_{vis}	d	$E_{\text{vis}} \leq 1.3\,\text{MeV}$		
		$E_{\text{vis}} \geq 10.0\,\text{MeV}$		
ΔT	p+d	$\Delta T \leq 0.5\,\mu\text{s}$		
		$\Delta T \geq 800\,\mu\text{s}$		
ΔR	p+d	$\Delta R \geq 1.2\,\text{m}$		
ΔT_μ	p+d	$\Delta T_\mu \leq 1.25\,\text{ms}$		
μ-IV	p+d	Q_{IV} >30000 DUC	$Q_{\text{IV}} > 50000\,\text{DUC}$	$Q_{\text{IV}} > 30000\,\text{DUC}$
		Trigger-Word (TW) = "IV-muon"		
μ-ID	p+d	$E_{\text{vis}} > 100\,\text{MeV}$		
LN	p+d	$Q_{\text{max}}/Q_{\text{tot}} > 0.12$	$Q_{\text{max}}/Q_{\text{tot}} > 0.20$	
		$Q_{\text{diff}} > 30000\,\text{DUC}$	$Q_{\text{diff}} > 100000\,\text{DUC}$	
		$\varsigma(T_{\text{s}}) > 36$ ns	$\varsigma(T_s) > 36$ ns	
		$\frac{\varsigma(Q)}{\text{DUC}} > 464 - 8\frac{\varsigma(T_{\text{s}})}{\text{ns}}$	$\frac{\varsigma(Q)}{\text{DUC}} > 1680 - 28\frac{\varsigma(T_{\text{s}})}{\text{ns}}$	
unicity	p+d	valid trigger within 800 μs before prompt cand.		
		valid trigger 0.5 μs to 900 μs after prompt cand. (except delayed cand.)		
ANN	p	ANN≤0.86		ANN≤0.85
IV	d	IV PMT multiplicity >1		
		distance IV-ID vertex <3.7 m		
		E_{vis}<3 MeV		
		Q>300DUC	Q>400 DUQ	
		-30 ns < ΔT < 60 ns	-100 ns < ΔT < -30 ns	
IV	p	IV PMT multiplicity >1		
		distance IV-ID vertex <3.7 m		
		Q>300 DUC and	Q>400 DUC	
		-40 ns < ΔT < 70 ns	-100 ns < ΔT < -10 ns	
OV	p	OV coincidence within 224 ns (if good OV data exists)		
Li	p	$\mathcal{L}_{\text{Li}} \geq 0.4$		
FV	d	$\frac{E_{\text{vis}}}{\text{MeV}} < 0.36e^{(FV/2.4)}$	$\frac{E_{\text{vis}}}{\text{MeV}} < 0.20e^{(FV/1.8)}$	$\frac{E_{vis}}{\text{MeV}} < 0.32e^{(FV/2.1)}$
		$\frac{E_{\text{vis}}}{\text{MeV}} < 0.06e^{(\overline{FV}/1.2)}$	$\frac{E_{\text{vis}}}{\text{MeV}} < 0.05e^{(\overline{FV}/1.2)}$	$\frac{E_{\text{vis}}}{\text{MeV}} < 0.07e^{(\overline{FV}/1.2)}$
ΔBJ	d	$FV_{\text{tlk}} > 4.3$		
vs. FVt		$\frac{(FV^*-4.00)^2}{0.14^2}$	$\frac{(FV^*-4.00)^2}{0.15^2}$	$\frac{(FV^*-4.00)^2}{0.14^2}$
		$+\frac{(\Delta BJ+0.03)^2}{0.21^2} \geq 4^2$	$+\frac{(\Delta BJ-0.01)^2}{0.21^2} \geq 5^2$	$+\frac{(\Delta BJ-0.01)^2}{0.19^2} \geq 5^2$
CPS	d	$L_{\text{chimney}}/L_{\text{vertex}} \leq 0.95$		

3.6 Efficiencies

The Double Chooz data acquisition system is background free and the trigger efficiency is 100% with negligible uncertainty at 0.5 MeV [7]. Thus, the detection efficiency for the prompt event is almost 100%. In contrast, for the delayed event there are several physics aspects that lead to a smaller detection efficiency.

3.6.1 Inverse beta decay candidate selection

The efficiency of the inverse beta decay selection is defined as [94]:

$$\epsilon_{\text{inc}} = \frac{\#\text{IBD} \cap \text{ANN} > k}{\#\text{IBD} \cap \text{ANN} > 0.1} \begin{cases} k = 0.85 & \text{FD1, FD2} \\ k = 0.86 & \text{ND} \end{cases} \tag{3.11}$$

Here, #IBD is the number of inverse beta decay candidates fulfilling the criteria

- prompt energy E_{prompt} fulfilling $1\,\text{MeV} < E_{\text{prompt}} < 8.5\,\text{MeV}$
- time between prompt and delayed event ΔT fulfilling $0.5\,\mu\text{s} < \Delta T < 800\,\mu\text{s}$
- delayed energy E_{delayed} fulfilling $1.3\,\text{MeV} < E_{\text{delayed}} < 10.0\,\text{MeV}$
- space distance ΔR between prompt and delayed event fulfilling $0.0\,\text{m} < \Delta R < 1.2\,\text{m}$
- passing all other vetos except for the ANN cut

Monte Carlo data studies have been investigating if a small gadolinium contamination in the buffer changes the neutron detection efficiency. For that purpose, four different near detector Monte Carlo datasets with four different gadolinium concentrations of 2.40, 1.55, 1.00 and $0.00\,\mu\text{g/cm}^3$ (standard) in the buffer have been used. The detection efficiencies for near detector Monte Carlo datasets are in agreement [94].

Calibration data with the 252-Cf source located at different positions along the central z-axis is used to measure the inverse beta decay selection efficiency.

3.6.2 Spilling

Neutrons produced in inverse beta decay processes in the buffer might propagate into the neutrino target and neutrons produced in inverse beta decay processes in the neutrino target might propagate into the buffer. This effects are referred to as spill in and spill out. Since in the classical gadolinium analysis the fiducial volume is only the neutrino target, spilling is an important systematical effect in that analysis. In contrast, in the Gd++ analysis the fiducial volume is given by neutrino target and buffer. Thus, spilling is almost irrelevant, as it is only a propagation of the signal inside the fiducial volume.

3.6.3 Boundary effects

The neutron occupancy is almost the same for the flat top respectively bottom lid of the cylindrical vessel and the curved lateral walls of the cylindrical vessel.

Table 3.3: Percentage of neutrino events surviving each background rejection cut for the inverse beta decay selection[79].

name	target	FD1	FD2	ND
ΔT_μ	p+d	$94.57\pm < 0.01$		$74.48\pm < 0.01$
LN	p+d	$99.99\pm < 0.01$	$100.00\pm < 0.01$	$100.00\pm < 0.01$
unicity	d+p	$97.29\pm < 0.01$	$96.20\pm < 0.01$	$96.86\pm < 0.01$
IV	d	99.94 ± 0.01	99.95 ± 0.01	99.93 ± 0.01
IV	p	$100.00\pm < 0.01$	$100.00\pm < 0.01$	$99.99\pm < 0.01$
OV	p	$99.94\pm < 0.01$	$99.94\pm < 0.01$	$99.99\pm < 0.01$
Li	p	$99.48\pm < 0.01$	99.47 ± 0.01	$99.88\pm < 0.01$
CPS	d	$99.99\pm < 0.01$	99.85 ± 0.01	$99.93\pm < 0.01$
ΔBJ vs. FVt	d	99.87 ± 0.02	99.90 ± 0.02	99.97 ± 0.01
FV	d	99.95 ± 0.01	99.92 ± 0.02	99.96 ± 0.01

3.6.4 Background rejection inefficiency

Although background rejection cuts aim on background reduction they might also reject some small amount of real neutrino events. This is referred to as background rejection inefficiency. Table 3.3 presents the percentage of neutrino events surviving each background rejection cut [79]. Values typically range from $\sin 99.5\% - 100.0\%$ except for the unicity conditions ($\sim 96\% - 97\%$) and the ΔT_μ cut. The ΔT_μ cut reduces the livetime in the near detector more significantly than in the far detector due to less overburden (cf. section 2.1, table 3.1).

3.7 Background estimation

The background rejection cuts (cf. section 3.5) reject through going muon events and Light Noise events with almost hundred percent efficiency. However, a rest contamination with accidental, lithium, fast neutron and stopping muon background events can not be avoided[V]. The top plot in figure 3.7 shows the number of inverse beta decay candidates as a function of the visible energy of the prompt event for the near detector dataset with blue triangles. The red line indicates the prediction from reactor models assuming no oscillation and background templates. Background templates are plotted as shaded areas. The middle and bottom plot in figure 3.7 display the save distributions for the FD1-On respectively FD2 dataset. The signal to background ratio is ~ 10 in the far detector and ~ 20 in the near detector. This section describes how the background templates that are shown in figure 3.7 are obtained.

3.7.1 Accidental background

The accidental background is estimated with the *offtime method* [7]: The original time difference of $0.5\,\mu\text{s} < \Delta T < 800\,\mu\text{s}$ in the selection is replaced by a time window in which no delayed events are expected while other section criteria remain unchanged. Therefore,

[V] Light Noise events passing all cuts are automatically accounted for by the accidental background estimation as described in the next subsection (section 3.7.1).

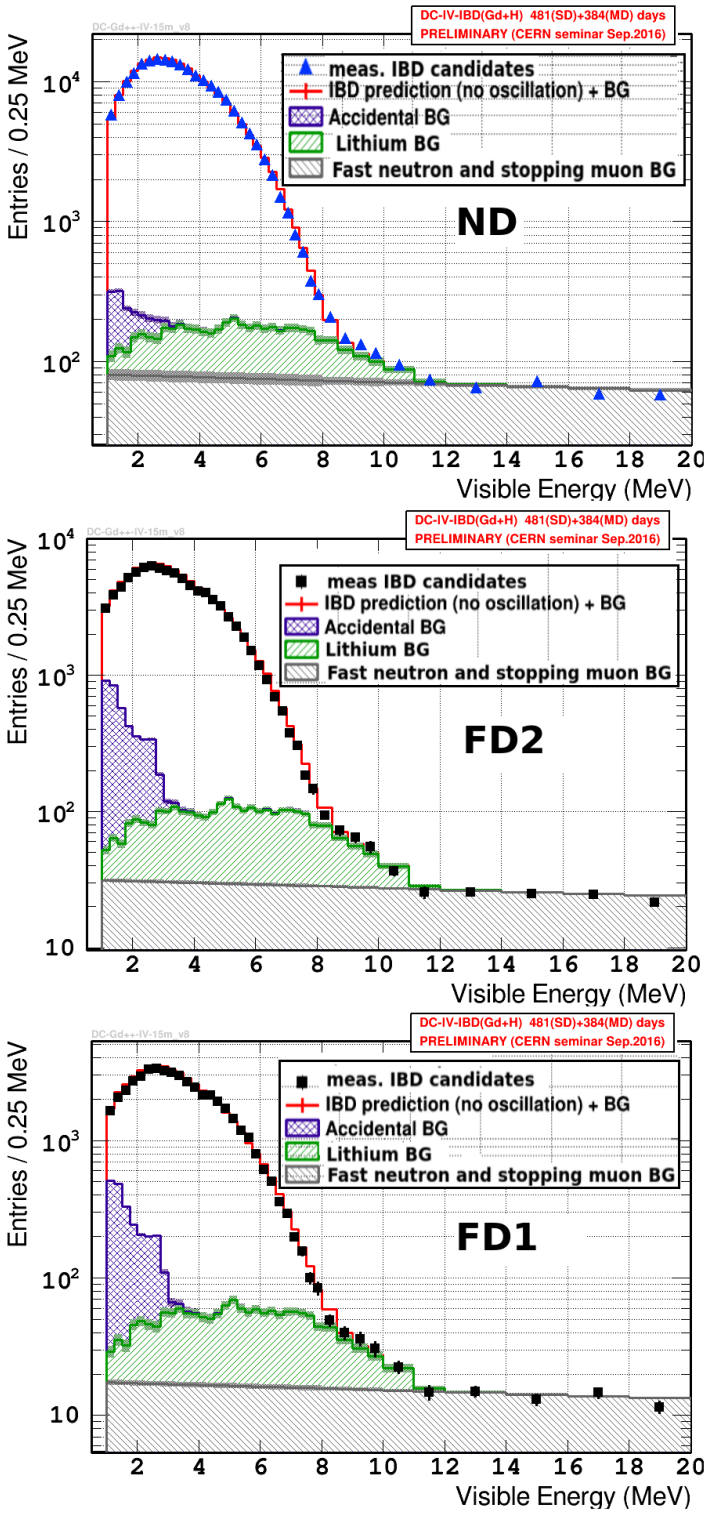

Figure 3.7: Visible energy distributions of the prompt events in the final inverse beta decay dataset. Entries versus visible energy are shown. The experimental data from the near detector is plotted in the top plot with blue diamonds. The distributions for the FD2 and the FD1-On experimental dataset are displayed the middle and bottom plot (black squares). The red line indicates the prediction from reactor models assuming no oscillation background templates. Those are represented by the shaded areas where green indicates the lithium background template, blue the accidental background template and gray the fast neutron and stopping muon background template [55] (modified).

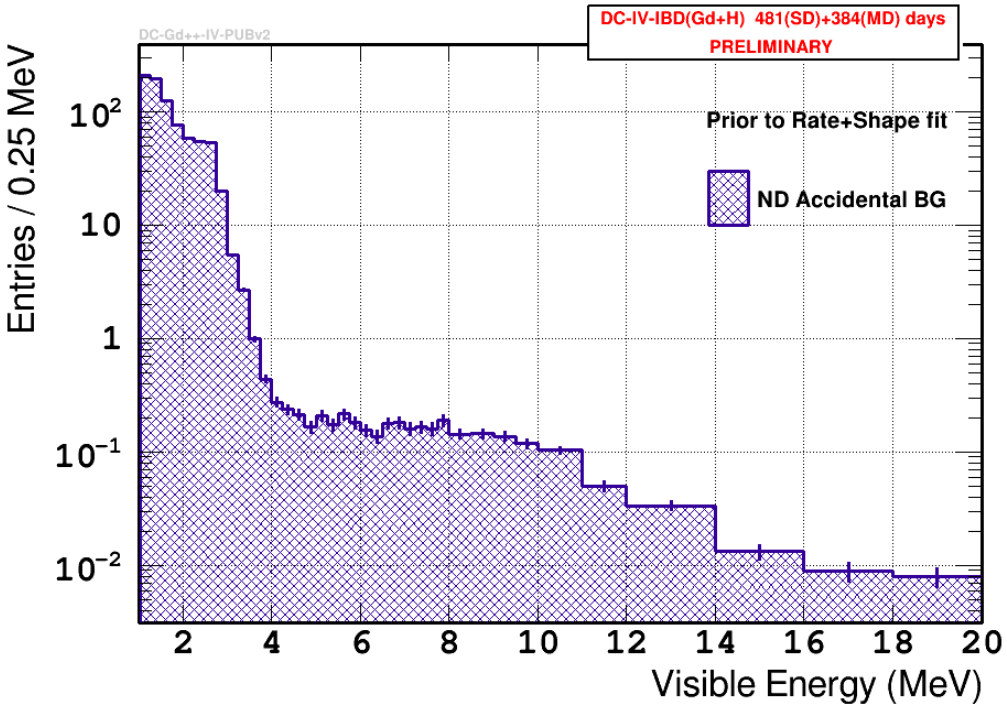

Figure 3.8: Data sample of the accidental background in the near detector obtained with the offtime method as explained in the text[56]. Entries versus visible energy are shown.

the remaining events in that time window are mostly accidental background events. In that way, the accidental background rate is measured using 200 consecutive time slots where the first one begins 1 s after the prompt candidate. Moreover, an accidental background sample is obtained by putting all of the 200 time slots in a row. Figure 3.8 shows the accidental background sample for the near detector in dependence of the visible energy in the detector. Figure 3.9 and 3.10 show it for the far detector. The accidental background is characterized by small energies (cf. figure 3.8, figure 3.9 and figure 3.10). The distributions for FD1 and FD2 are not a priory assumed to be the same since there have been changes in the data readout system from the FD1 to the FD2 period. However, the shapes are comparable and the order of magnitude is the same (see figure FD1, cf. figure FD2).

Figure 3.11 presents the covariance matrix of the data sample for the FD2 accidental background obtained with the offtime method. The corresponding plots for near detector and FD1 data sample can be found in figure A.2 and figure A.1.

3.7.2 Lithium background

The shape of the lithium background is measured with a lithium background sample. This sample contains events passing all selection criteria except for having a lithium likelihood $\mathcal{L}_{Li} \geq 0.4$ (cf. section 3.5.2). The lithium background dataset is complementary to the final inverse beta decay candidate dataset because the final inverse beta decay candidate dataset only contains events with $\mathcal{L}_{Li} < 0.4$ (cf. section 3.5.2). Furthermore, there is a Monte Carlo simulation of the lithium background taking into account feasible branches considering α and neutron emissions as well [7] [116]. Monte Carlo simulation and real

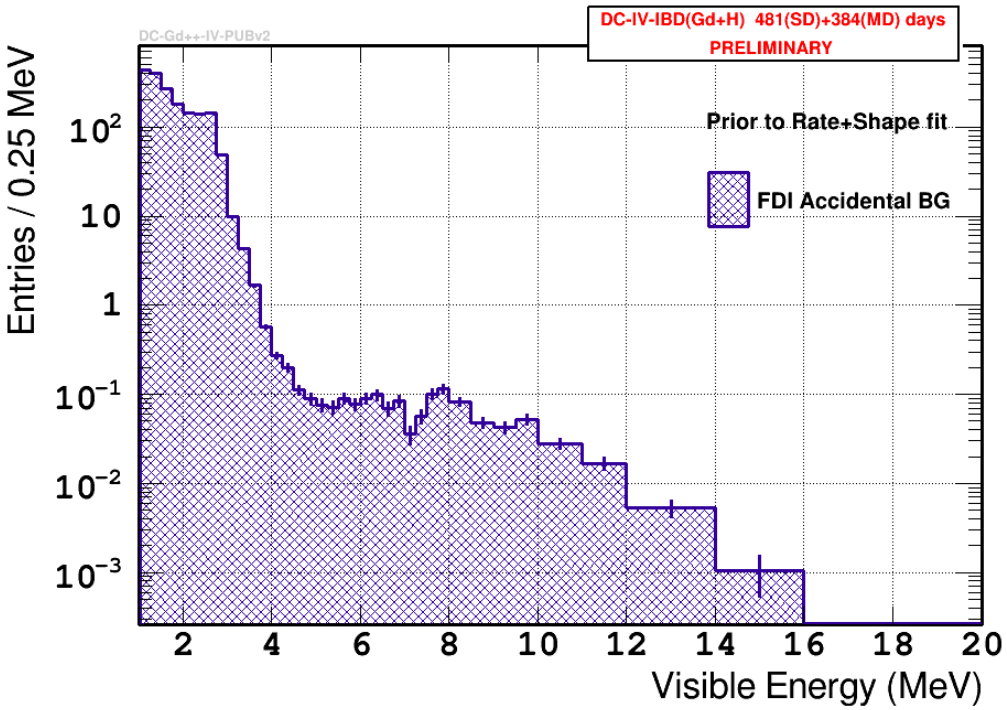

Figure 3.9: Data sample of the accidental background for the FD1 dataset obtained with the offtime method as explained in the text [56]. Entries versus visible energy are shown.

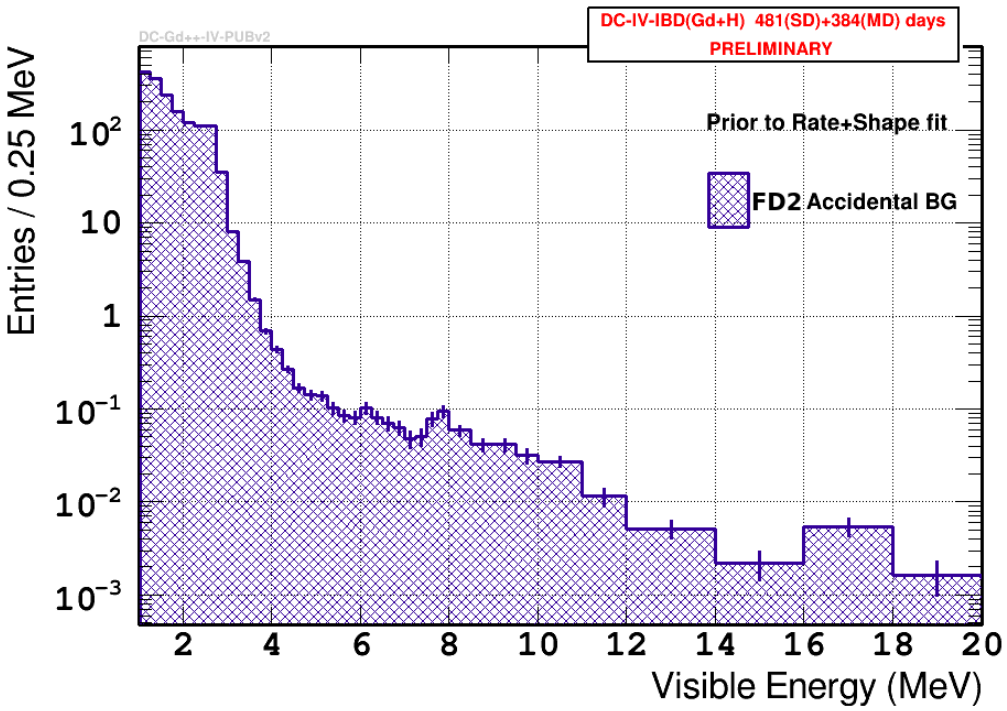

Figure 3.10: Data sample of the accidental background for the FD2 dataset obtained with the offtime method as explained in the text [56] (modified). Entries versus visible energy are shown.

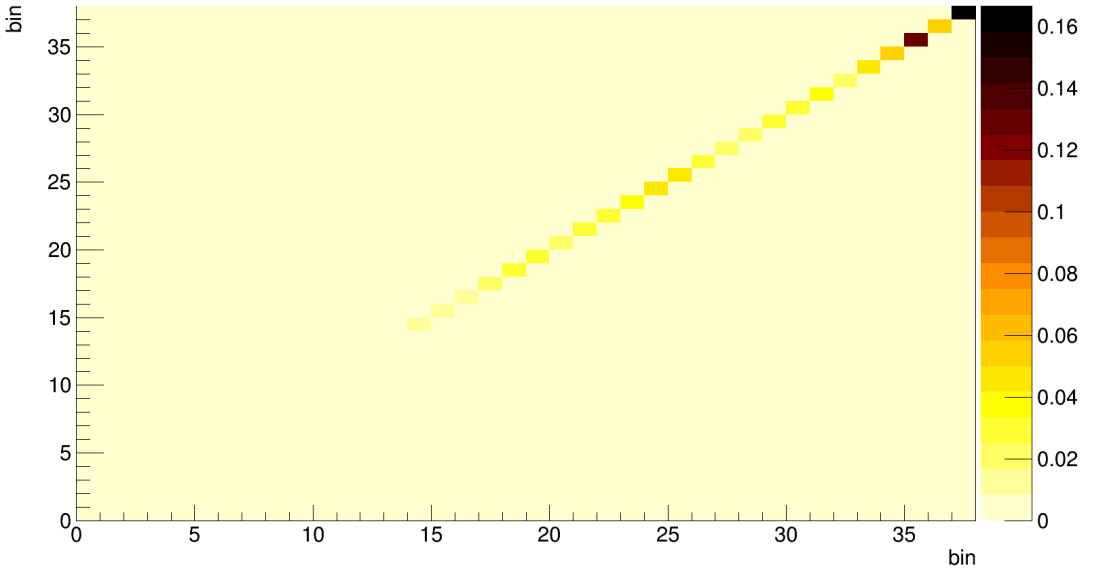

Figure 3.11: Covariance matrix for the FD2 accidental background obtained with the offtime method as explained in the text.

background data energy distributions agree within the uncertainty [116]. Figures 3.12, 3.13 and A.3 show the energy distributions of the lithium data samples used in this work for ND, FD2 and FD1. The absolute lithium rate is a free parameter in the final fit. However, an independent estimate can be done by fitting the time difference of the inverse beta decay-candidates to the previous muons ΔT_μ since random coincidence of muons and inverse beta decay candidates yield a flat distribution while the lithium contamination is falling with ΔT_μ. In doing so, time and space distance to the previous muons and the visible energy of these muons is taken into account. The results of this external estimate from [116] can be found in table 4.5. There is no physical reason to assume a different lithium background shape between FD2, ND and FD1. This is confirmed by experimental data (cf. figure 3.12, figure 3.13 and figure A.3). The matrix of the correlations among bins of the cosmogenic isotope background is displayed in figure 3.14.

3.7.3 Fast neutron and stopping muon background

Most of the correlated fast neutron and stopping muon background can be sorted out by the inner veto. Thus, events that did not pass the inner veto veto conditions but all other cuts can be used for a shape measurement of the fast neutron and stopping muon background. These events are referred to as inner veto tagged events. Figure 3.15 presents entries versus visible energy exemplary for the FD2 dataset, figure 3.16 and A.4 show it for FD2 and FD1. The fast neutron and stopping muon background shape is consistent to be identical in all datasets and parameterized by an empirical function

$$f_{\mathrm{FNSM}}(E_{\mathrm{vis}}) = p_0 \cdot \exp(-p_1 \cdot E_{\mathrm{vis}}) + p_2 \cdot E_{\mathrm{vis}} \quad . \tag{3.12}$$

The fast neutron and stopping muon rate is estimated using the fact that these background events are dominating at high energies. The rate is higher in the near detector due to

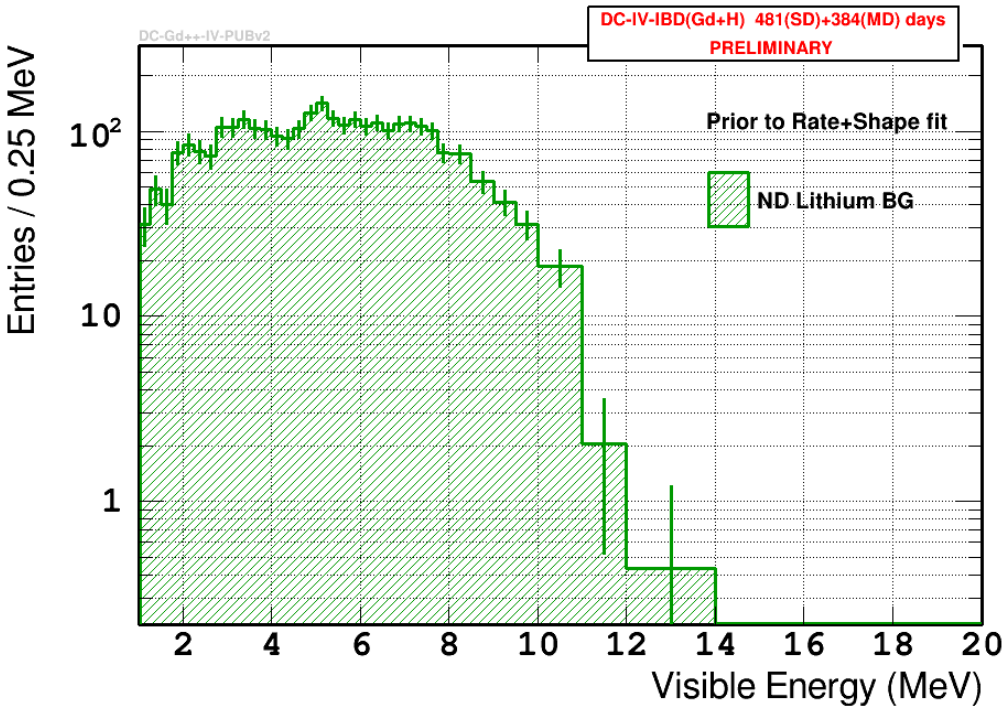

Figure 3.12: ND lithium background data sample obtained based on the lithium likelihood as explained in the text [56]. Entries versus visible energy are shown.

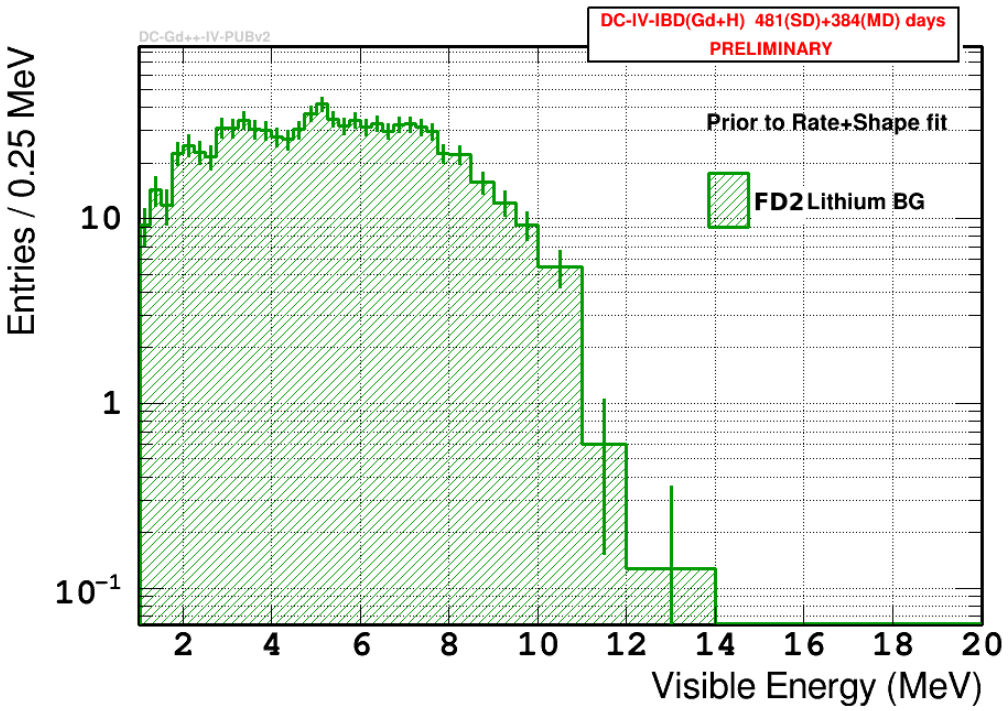

Figure 3.13: FD2 lithium background data sample obtained with the offtime method based on the lithium likelihood as explained in the text [56] (modified). Entries versus visible energy are shown.

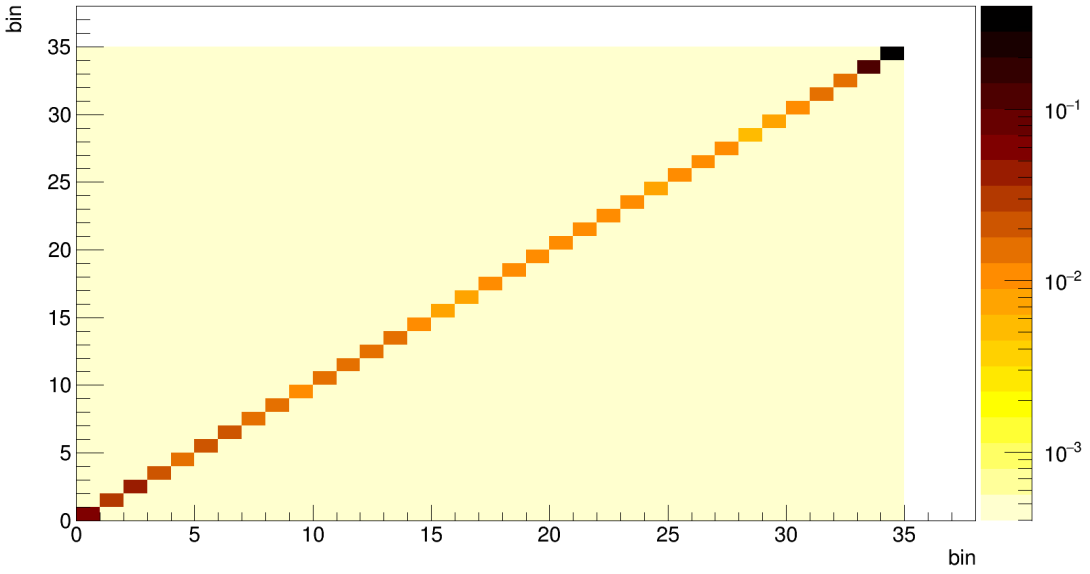

Figure 3.14: Covariance matrix for cosmogenic isotopes generated using the cosmogenic isotope sample obtained as described in the text.

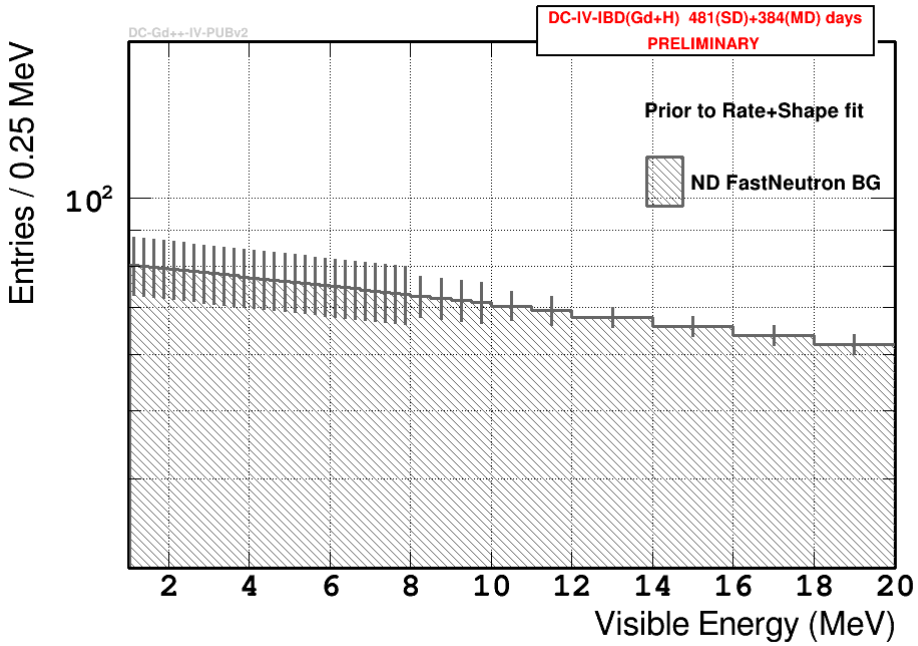

Figure 3.15: Fast neutron and stopping muon background data sample for the near detector from inner veto tagged events as explained in the text [56]. Entries versus visible energy are shown.

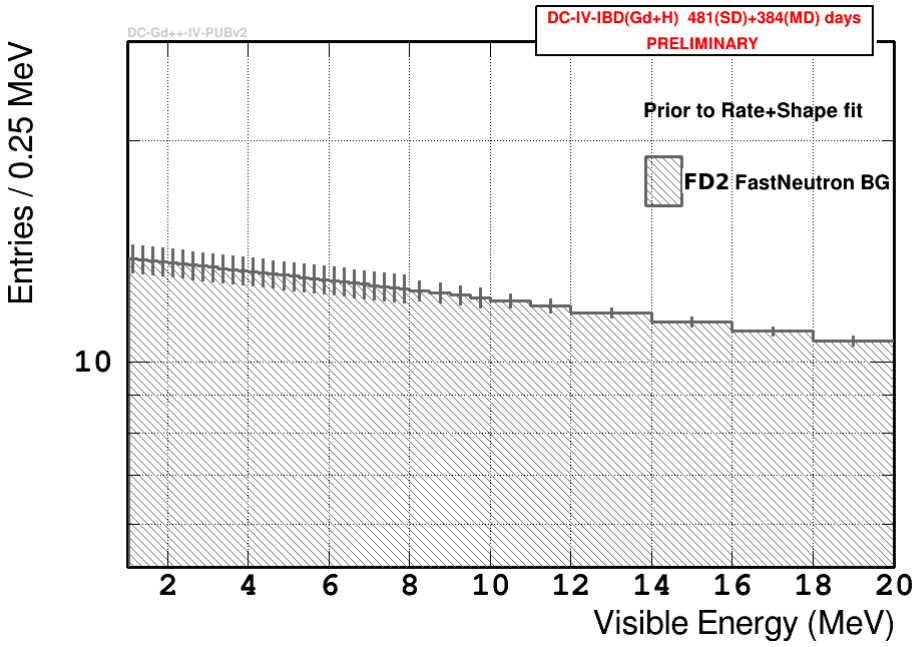

Figure 3.16: FD2 fast neutron and stopping muon background data sample obtained from inner veto tagged events as explained in the text [56] (modified). Entries versus visible energy are shown.

less overburden (cf. figure 3.15, figure 3.16). It is constraint by the inverse beta decay candidates passing all selection criteria except for a visible prompt energy between 20 MeV and 100 MeV. More details about the parameterization of the background are explained in section 4.2.5 where the values of p_0, p_1, and p_2 are as well as the rates listed in table 4.5.

Chapter 4

Sterile oscillation analysis

This chapter describes the oscillation analysis performed in this work.

4.1 General concept

The general concept of this analysis is a Poisson likelihood based approach, which is based on Stefan Schoppmann's [113] analysis. Figure 4.1 illustrates the fitting process. The strategy is not unfolding but one that will be referred to as *forward folding* in the following. At first, a hypothetical measurement is constructed from a simulated reactor neutrino flux, background spectra, detector systematics and oscillation parameters - simultaneously for all datasets (i.e. ND, FD1, FD2). These hypothetical measurements are then simultaneously compared to the real measurements. These two steps are repeated for another set of initial parameters. This is done until the point of best agreement between real and hypothetical measurement is found. This point is mathematically identified by the smallest negative logarithmic likelihood. Technically, the algorithm calculates the estimated distance to minimum (EDM) and aborts the minimization if the EDM is below a threshold (i.e. a fixed value that depends on the desired accuracy). Figure 4.2 provides an other illustration of the fit principle.

4.1.1 Statistical method

This section summarizes the statistical method used in this analysis. The analysis is based on the minimum negative logarithmic likelihood which is equivalent to the maximum likelihood approach as described in the following.

A set of measurements $\vec{n}$ may consist of $N \in \mathbb{N}$ single measurements:

$$\vec{n} = (n_1, n_2, \ldots, n_N) \quad . \tag{4.1}$$

The parameters of primary interest (i.e. the oscillation parameters $\sin^2 2\theta_{13}$, $\sin^2 2\theta_{14}$ and Δm^2_{41}) as well as so called nuisance parameters may be contained in a vector $\vec{a}$:

$$\vec{a} = (a_1, a_2, \ldots, a_M),\ M \in \mathbb{N} \tag{4.2}$$

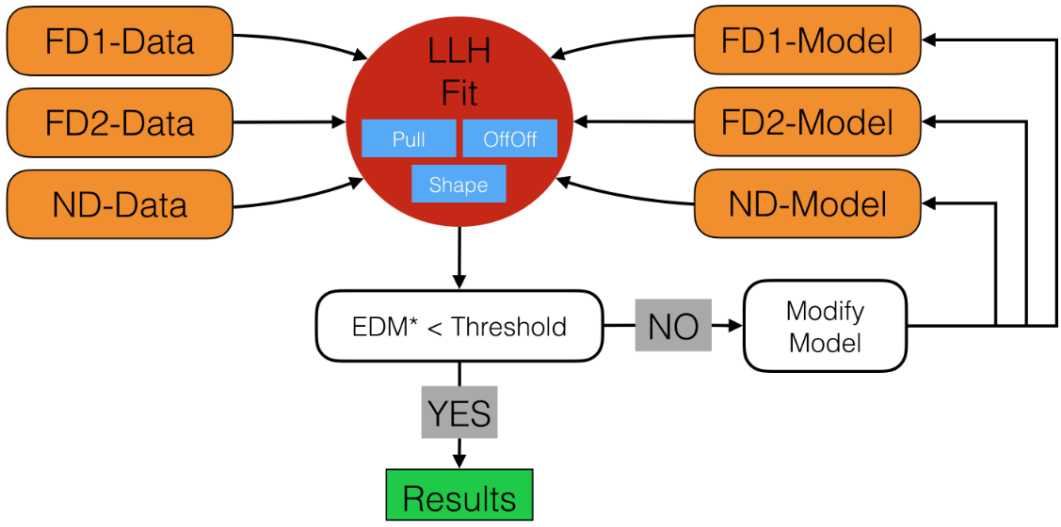

Figure 4.1: Illustration of the general fit idea following a so-called *forward folding* approach which is explained in the text. As illustrated, the likelihood formula consists of a shape part, an OffOff part and pulls. These parts will be explained in further detail hereinafter [117].

where nuisance parameters are parameters that are not of primary interest but needed in order to construct a prediction (the nuisance parameters used in this analysis will be listed below).

The likelihood to observe the measurements $\vec{n}$ under the assumption that $\vec{a}$ contains the true values is the so called likelihood function $\mathcal{L}(\vec{n}|\vec{a})$. If the measurements in $\vec{n}$ are uncorrelated, the likelihood function is a product of the probabilities $f_i(n_i|\vec{a})$ to observe the measurement n_i under the condition that $\vec{a}$ contains the true values:

$$\mathcal{L}(\vec{n}|\vec{a}) = \prod_{i=1}^{N} f_i(n_i|\vec{a}) \quad . \tag{4.3}$$

If L external measurements $\vec{x} = (x_1, x_2, \ldots, x_L)$ independently from the measurement $\vec{n}$ constrain components of $\vec{a}$, this knowledge may be included by extending equation (4.3) to

$$\mathcal{L}(\vec{n}, \vec{x}|\vec{a}) = \prod_{i=1}^{N} f_i(n_i|\vec{a}) \prod_{j=1}^{L} g_j(x_j|\vec{a}) \quad . \tag{4.4}$$

Equation (4.4) can be understood as a function of $\vec{a}$ if $\vec{n}$ is given:

$$\mathcal{L}(\vec{n}, \vec{x}|\vec{a}) = \prod_{i=1}^{N} f_i(\vec{a}, n_i = const.) \prod_{j=1}^{L} g_j(\vec{a}, x_j = const.) = \prod_{i=1}^{N} \tilde{f}_i(\vec{a}) \prod_{j=0}^{L} \tilde{g}_j(\vec{a}) = \mathcal{L}(\vec{a}) \quad . \tag{4.5}$$

Thus, the vector containing the most likely parameters $\hat{\vec{a}}$ may be obtained by maximizing equation (4.5). This is the so called maximum likelihood approach.

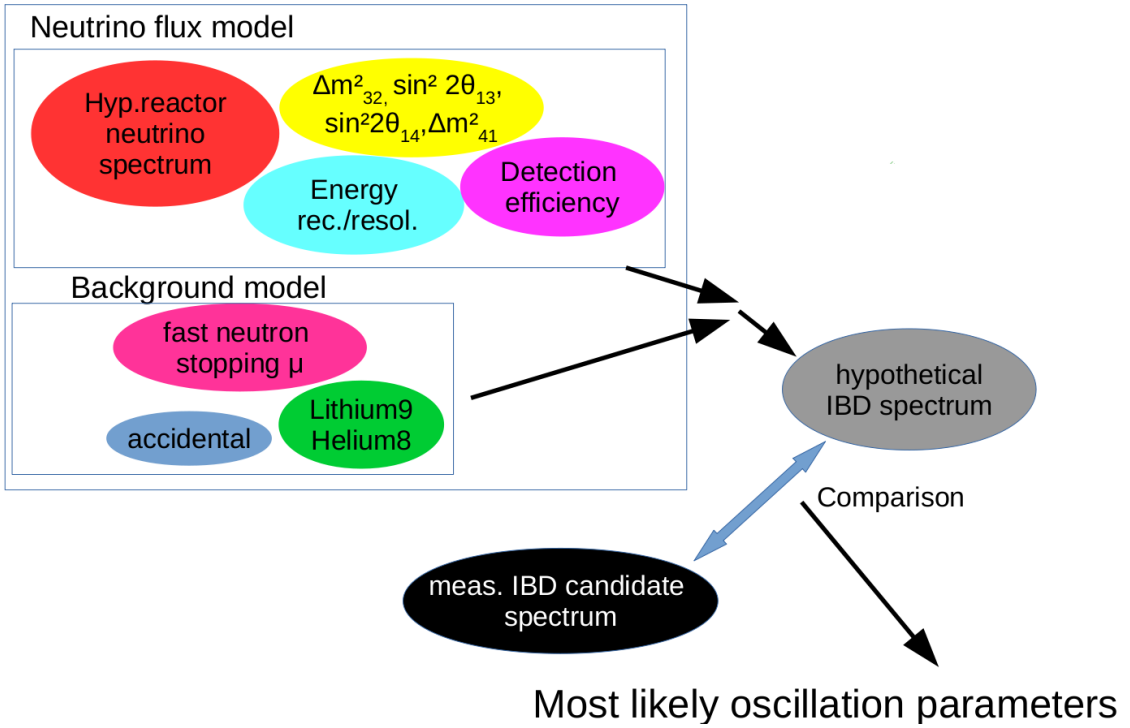

Figure 4.2: Illustration of the general fit idea following a so called *forward folding* approach which is explained in the text. As illustrated a model for the measured energy distribution of neutrino events is constructed using oscillation parameter, energy reconstruction and resolution parameters, detection systematics and the hypothetical initial reactor flux. The backgrounds are added in the next step. The resulting total model of energy spectrum of the inverse beta decay candidates is then compared to the data. As pointed out in the text and illustrated in figure 4.1, after the comparison the model parameters are changed using the gradient method *Minuit2* [80] [26] [81]. The whole process is repeated until the point of best agreement is found.

The minimum negative logarithmic likelihood approach is equivalent but includes two modifications induced for technical reasons. $\mathcal{L}(\vec{n},\vec{x}|\vec{a})$ can be replaced by $2\ln(\mathcal{L}(\vec{n},\vec{x}|\vec{a}))$ as the natural logarithm is a strictly monotonically increasing function:

$$\mathcal{L}(\hat{\vec{a}}) = max. \Leftrightarrow 2\ln\left(\mathcal{L}(\hat{\vec{a}})\right) = max. \tag{4.6}$$

By doing so, the product in equation (4.5) transforms into a sum:

$$\mathcal{L}(\vec{a}) = \prod_{i=1}^{N} \tilde{f}_i(\vec{a}) \prod_{j=0}^{L} \tilde{g}_j(\vec{a}) \Leftrightarrow 2\ln\left(\mathcal{L}(\hat{\vec{a}})\right) = 2\sum_{i=1}^{N} \ln\left(\tilde{f}_i(\vec{a})\right) + 2\sum_{j=0}^{L} \ln\left(\tilde{g}_j(\vec{a})\right) \quad . \tag{4.7}$$

In particular the $\tilde{g}_j(\vec{a})$, which are included in order to account for a priori knowledge of components of $\vec{a}$, usually do not depend on all components of $\vec{a}$. Thus, a separation of variables is usually done by the logarithm. A minimization is technically easier to do than a maximization. Therefore, $\ln(\mathcal{L}(\vec{a})) \cdot -2$ is minimized instead of maximizing $2\ln(\mathcal{L}(\vec{a}))$ since it is equivalent:

$$2\ln\left(\mathcal{L}(\hat{\vec{a}})\right) = max. \Leftrightarrow -2\ln\left(\mathcal{L}(\hat{\vec{a}})\right) = min. \quad . \tag{4.8}$$

If the measurement values are Gaussian distributions,

$$-2\ln(\mathcal{L}(\vec{n}|\vec{a})) = \sum_{i=1}^{n} \frac{(n_i^{\text{meas}} - n_i^{\text{exp}}(\vec{a}))^2}{\sigma_i^2} \tag{4.9}$$

follows. The right side of equation (4.9) is well known as the so called *Chi-square* [95].

In this work, the measurements are the number of events in visible prompt energy bins for FD1-On, FD2 and ND. They are assumed to follow a Poisson distribution. For Poisson distributions

$$\mathcal{L}(\vec{n}|\vec{a}) = \prod_i \frac{n_i^{\text{exp}}(\vec{a})^{n_i^{\text{meas}}}}{n_i^{\text{meas}}!} \cdot e^{-n_i^{\text{exp}}(\vec{a})} \Rightarrow \tag{4.10}$$

$$-2\ln(\mathcal{L}(\vec{n}|\vec{a})) = -2\left(\sum_i n_i^{\text{meas}} \cdot \ln(n_i^{\text{exp}}(\vec{a})) - n_i^{\text{exp}}(\vec{a}) - \ln(n_i^{\text{meas}}!)\right) \tag{4.11}$$

applies.

The binning in this work consists of 38 bins between 1 and 20 MeV with custom bin sizes. Only the region up to about 8 MeV is IBD dominated. The bin size is 0.25 MeV in this region. The fit region has been extended to background dominated energy regions in order to allow a background constraint in the fit itself. In doing so, more bins have been added. In order to optimize for the lower statistics in the background dominated regions the bin size is increasing; in the lithium background dominated region between 8 and 10 MeV the bin width is 0.5 MeV, followed by two bins from 10-12 MeV with a width of 1.0 MeV each. Finally, the bin size is 2.0 MeV in the region between 12 and 20 MeV which is dominated by fast neutron and stopping muon background (cf. figure 3.7). A summary of the binning can be found in table 4.1.

Table 4.1: Binning of the visible prompt energy spectrum (identical to the binning used in the θ_{13} analysis [39]).

characteristics	range [MeV]	bin width [MeV]	number of bins
IBD dominated	[1.0, 8.0)	0.25	28
lithium bckgr. dominated	[8.0, 10)	0.5	4
intermediate	[10.0, 12.0)	1.0	2
FNSM bckgr. dominated	[12.0, 20.0)	2.0	4
total	[1.0, 20.0)	0.25 - 2.0	38

Thus, assuming Poisson statistics for the measurement the negative log likelihood function is given by:

$$-2\ln\mathcal{L}(\vec{a}) = \tag{4.12a}$$

$$\sum_{d\,\epsilon\,\{\text{FD1-On, ND, FD2}\}} \left[-2\sum_i n_i^{\text{meas},d} \cdot \ln\Big(n_i^{\text{exp},d}(\vec{a})\Big) - n_i^{\text{exp},d}(\vec{a}) \right] \tag{4.12b}$$

$$+\, n_{\text{OffOff}}^{\text{meas}} \cdot \ln\big(n_{\text{OffOff}}^{\text{exp}}(\vec{a})\big) - n_{\text{OffOff}}^{\text{exp}}(\vec{a}) \tag{4.12c}$$

$$+ \sum_{j\,\epsilon\,\{\text{constraint input par./vectors}\}} \begin{cases} \text{pull}_{\text{corr}}(j) & j \text{ vector of correlated par.} \\ \text{pull}(j) & j \text{ single par. (uncorrelated)} \end{cases} \tag{4.12d}$$

where $n_i^{\text{meas},d}$ is the measured number of inverse beta decay-candidates in energy bin i and dataset d (FD1-On, FD2 or ND). $n_i^{\text{exp},d}(\vec{a})$ is the expected number of IBD candidates in energy bin i and dataset d under the condition that the input parameters are given by vector $\vec{a}$. $n_{\text{OffOff}}^{\text{meas}}$ is the number of measured inverse beta decay-candidates during the reactor off FD1 period, $n_{\text{OffOff}}^{\text{exp}}(\vec{a})$ is the number of expected reactor off candidates. The parts (4.12b) and (4.12c) account for the measurement compared to the expectation assuming Poisson statistics. The terms in equation (4.12d) are Gaussian priors on those input parameters which are constraint in the fit. The Gaussian prior is given by:

$$\text{pull}(j) = \left(\frac{a_j - \hat{a}_j}{\sigma_j} \right)^2 \tag{4.13}$$

for those constraint parameters which are not correlated to others. For those constraint parameters that are correlated to others, the correlations are accounted for by a correlated Gaussian prior:

$$\text{pull}_{\text{corr.}}(j) = \left(\vec{j} - \hat{\vec{j}}\right)^{\text{T}} \cdot \text{V}_{\text{j}}{}^{-1} \cdot \left(\vec{j} - \hat{\vec{j}}\right) \tag{4.14}$$

where $\vec{j}$ is the vector of parameters that are correlated to each other and V_j is the corresponding covariance matrix. The parameters not constraint by a prior are referring to:

- $\sin^2 2\theta_{14}$, Δm^2_{41}- the parameters of major interest
- $\sin^2 2\theta_{13}$

  It is important to have no constraints on θ_{13} as all values provided by any experiment were either obtained under the no sterile assumption or in a sterile analysis. It should be considered that the best fit θ_{13} value can actually be different if $\theta_{14} \neq 0$ which does not allow to have a θ_{13} constraint. Also the result of a similar analysis should not be inserted into this analysis (unless a combination of both analysis is aimed.)

- correlated reactor flux normalization in all energy bins,
- lithium background rates.

The reactor flux normalization in all energy bins are nuisance parameters. In principle, they could be constraint in the fit as predictions for the reactor flux exist. However, it turns out that the currently existing reactor predictions do not describe the observations by reactor neutrino experiments sufficiently (cf. sections 1.4.1 and 1.4.4). Thus, the rate and shape of the reactor prediction is not used and a *Data-to-Data* fit approach is done.

The parameters that are constraint by a prior in the fit are related to:

- Δm^2_{ee}
- several background attributes:
  - accidental background rates
  - spectral shape of the accidental background
  - spectral shape of the lithium background
  - fast neutron and stopping muon background rates
  - spectral shape of the fast neutron and stopping muon background
- energy reconstruction
- detection efficiencies
- number of neutrino events during the reactor off period
- uncorrelated reactor neutrino flux in all energy bins

Thus, equation (4.12) may be expressed as:

$$
\begin{aligned}
-2\ln\mathcal{L}(\vec{a}) = & && \text{(4.15a)}\\
& \sum_{d\,\epsilon\ \text{FD1-On, ND, FD2}} \left[-2 \sum_i N_i^{\text{meas},d} \cdot \ln\Big(N_i^{\text{exp},d}(\vec{a}) \Big) - N_i^{\text{exp},d}(\vec{a}) \right] && \text{(4.15b)}\\
& + N^{\text{meas}}_{\text{OffOff}} \cdot \ln\big(N^{\text{exp}}_{\text{OffOff}}(\vec{a}) \big) - N^{\text{exp}}_{\text{OffOff}}(\vec{a})) && \text{(4.15c)}\\
& + \text{pull(acc. rate FD1)} + \text{pull(acc. rate FD2)} + \text{pull(acc. rate ND)} && \text{(4.15d)}\\
& + \sum_i \text{pull(spectral acc. bin i FD1)} + \sum_i \text{pull(spectral acc. bin i FD2)} \\
& \qquad + \sum_i \text{pull(spectral acc. bin i ND)} && \text{(4.15e)}\\
& + \text{pull(FNSM rate FD)} + \text{pull(FNSM rate ND)} && \text{(4.15f)}\\
& + \sum_k \text{pull(FNSM spectral parameter k)} && \text{(4.15g)}\\
& + \sum_i \text{pull(spectral lithium bin i)} && \text{(4.15h)}\\
& + \text{pull}_{\text{corr}}\text{(uncorr. reactor flux in all energy bins)} && \text{(4.15i)}\\
& + \text{pull}_{\text{corr}}\text{(energy parameters)} && \text{(4.15j)}\\
& + \text{pull}_{\text{corr}}\text{(detection efficiency parameters)} && \text{(4.15k)}\\
& + \text{pull(OffOff neutrino rate)} && \text{(4.15l)}\\
& + \text{pull}(\Delta m^2_{ee}) \quad . && \text{(4.15m)}
\end{aligned}
$$

The treatment of the systematics effects is explained in further detail in the following.

The likelihood function is minimized using the Minuit2 algorithm [80].

4.2 Input model

This section describes the input model i.e. how the $n_i^{\mathrm{exp},d}(\vec{a})$ in equation (4.12) are calculated.

4.2.1 Correlation handling

Several model parameters such as the reactor flux, detection efficiencies, energy parameters and background parameters are correlated among ND, FD1-On and FD2 and/or other parameters of the same dataset. Minimizer algorithms do not a priori assume correlations unless this is forced despite that they usually can calculate posterior correlations of parameters based on the function to be minimized. How correlations are forced in this work is explained in the following. This section describes the general method of correlation handling used in this work, while further information about the correlation coefficients can be found in the following sections.

Covariance matrices (a_{ji}) are always quadratic real symmetric matrices ($a_{ij} = a_{ji} \in \mathbb{R}\, i, j = 0, 1, .., n$). Thus, they always have exactly n eigenvalues and n orthogonal eigenvectors. Furthermore, all of the eigenvalues are non negative real numbers (i.e. covariance matrices are *positive definite*). Correlated variables can not only be expressed in the given coordinate system in which they are correlated but also in the eigenbasis of the covariance matrix in which they are uncorrelated. Since the parameters used by the minimizing algorithm are preferrably uncorrelated, they necessarily need to be collinear to the eigenvectors of the covariance matrix requiring a variable transformation into that eigenbasis. This transformation of a vector in the eigenbasis of a matrix M (the so called *eigenvector decomposition*) can be done with the matrix U defined by:

$$\mathrm{M} = \mathrm{U}\Lambda\mathrm{U}^T \tag{4.16}$$

where Λ is the n dimensional diagonal matrix with the eigenvalues on the diagonal axis. Since the eigenvalues are always non-negative equation (4.16) can also be written as

$$\mathrm{M} = \mathrm{L}\mathrm{L}^T \text{ with } \mathrm{L} = U\sqrt{\Lambda} \quad . \tag{4.17}$$

That is the so called Cholesky decomposition [42]. It transforms into a coordinate system in which the matrix M is the unit matrix. In doing so, multiplication of U with a vector can be understood as a rotation of the coordinate system while multiplication of $\sqrt{\Lambda}$ with a vector can be understood as a stretching or shrinking of it. Speaking in terms of correlated variables, the Cholesky decomposition matrix transforms a vector of correlated variables into the coordinate system in which the variables are uncorrelated and all variances are exactly equal to one. Figure 4.3 illustrates the coordinate systems. The eigenbasis of the covariance matrix (obtained by applying matrix U) is illustrated in the top, the transformation in the scaled eigenbasis in which the covariance matrix (obtained by applying matrix L) is the unit matrix is shown in the bottom.

In this work, the Cholesky decomposition is used to substitute correlated variables by their representation in the coordinate system in which the covariance matrix is the unit matrix. Namely this is applied to the energy treatment parameters, the reactor flux parameters, the detection efficiency parameters and background shape parameters.

4.2.2 Energy

The energy reconstruction parameters are correlated among FD1, FD2 and ND.

The light non-linearity correction is applied only to the prompt Monte Carlo events in the final fit process. All other corrections related to energy are already implemented in the Monte Carlo simulation. The energy $E_{\text{vis, MC}}$ in the final fit is modeled as

$$E_{\text{vis, MC}} = E'_{\text{vis, MC}} \cdot f_{\text{LNL}} \cdot f_{\text{St/U}} \cdot f_{\text{QNL}} \tag{4.18}$$

where f_{LNL}, $f_{\text{St/U}}$ and f_{QNL} are correction functions accounting for light non-linearity, stability plus uniformity respectively charge non-linearity:

$$f_{\text{LNL}} = \frac{a_{\text{LNL}}}{E'_{\text{vis, MC}}} + b_{\text{LNL}} \tag{4.19a}$$

$$f_{\text{St/U}} = b_{\text{St/U}} \tag{4.19b}$$

$$f_{\text{QNL}} = b_{\text{QNL}} + c_{\text{QNL}} \cdot E'_{\text{vis, MC}} \tag{4.19c}$$

Here, $E'_{\text{vis, MC}}$ is the visible energy of the prompt event from the Monte Carlo simulation. (4.18) may be written as:

$$E_{\text{vis, MC}} = a' + b' \cdot E'_{\text{vis, MC}} + c' \cdot (E'_{\text{vis, MC}})^2 \tag{4.20}$$

where

$$a' = a_{\text{LNL}} \cdot b_{\text{St/U}} \cdot b_{\text{QNL}} \tag{4.21}$$

$$b' = a_{\text{LNL}} \cdot b_{\text{St/U}} \cdot c_{\text{QNL}} + b_{\text{LNL}} \cdot b_{\text{St/U}} \cdot b_{\text{QNL}} \tag{4.22}$$

$$c' = b_{\text{LNL}} \cdot b_{\text{St/U}} \cdot c_{\text{QNL}} \quad . \tag{4.23}$$

a', b' and c' are optimized in the final oscillation analysis instead of a_{LNL}, b_{LNL}, $b_{\text{St/U}}$, b_{QNL} and c_{QNL} in order to avoid ambiguity induced by an unnecessary amount of degrees of freedom. Table B.2 (see section B.2) presents the values of a_{LNL}, b_{LNL}, $b_{\text{St/U}}$, b_{QNL} and c_{QNL}. The correlations between these parameters can be found in table B.1 (see section B.2). The correlation matrix is assumed to be identical for FD1, FD2 and ND. a_{LNL} and b_{LNL} are entirely anti-correlated and the correlation correlation between b_{QNL} and c_{QNL} of the same detector is -0.45 while light non-linearity, charge non-linearity and stability and uniformity corrections are fully uncorrelated to each other. a_{LNL} and b_{LNL} are completely correlated between FD1, FD2 and ND while $b_{\text{St/U}}$, b_{QNL} and c_{QNL} are not correlated between FD1, FD2 and ND.

a', b' and c' can be calculated to the values presented in table 4.2 with the given information from table B.2 and the functional dependence from equation (4.21) . The correlations of the parameters have been calculated using a simulation of 15 000 random Gaussian distributed values [102]. The results can be found in table 4.3.

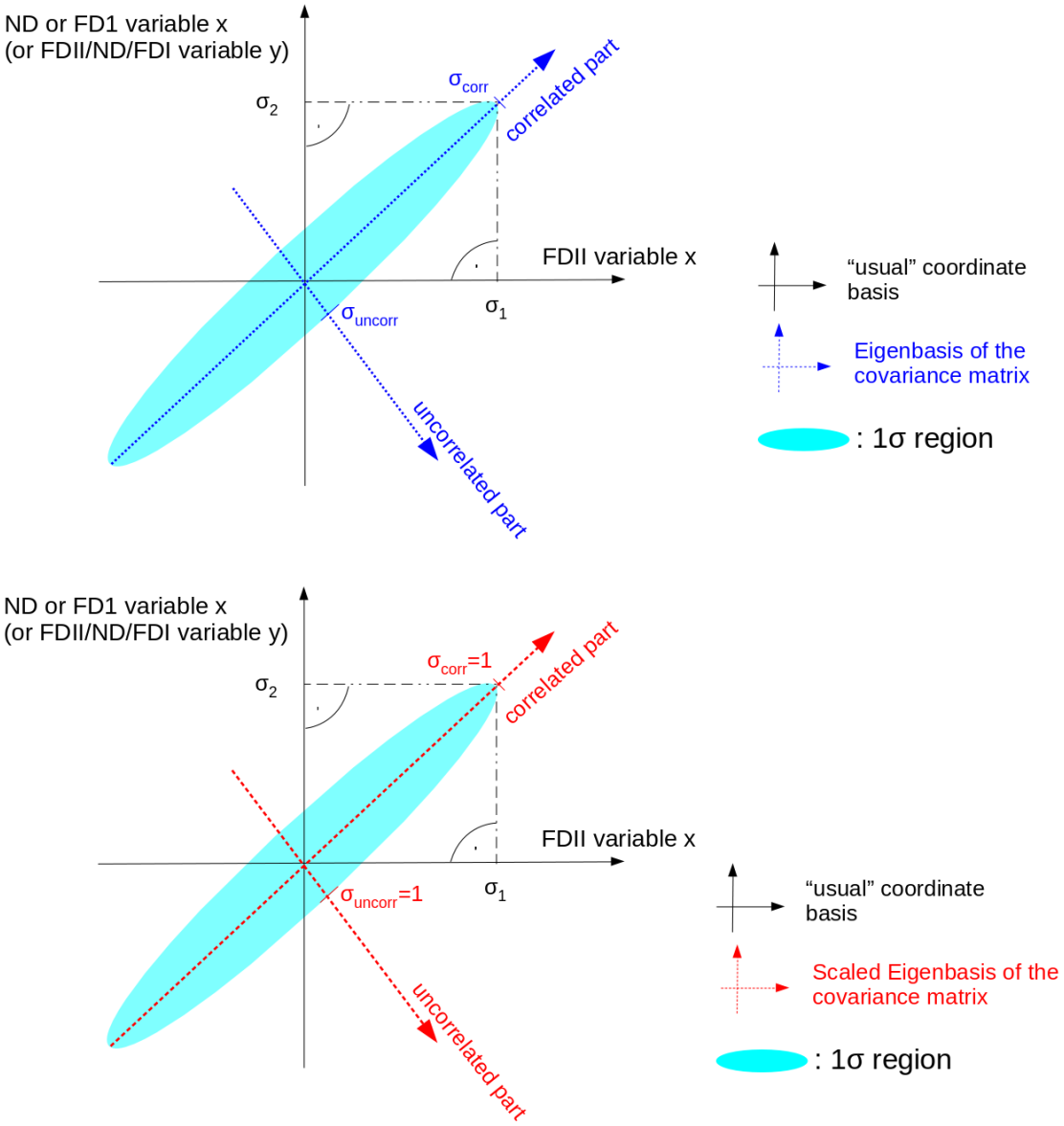

Figure 4.3: Illustration of the different coordinate systems used in this work for two example variables called FD2 variable x and ND variable x. Note that this is only an example and the variables could also belong to the same dataset or be different variables of different datasets. The eigenbasis system of two correlated variable is shown in the top (blue fine dashed coordinate system), the coordinate system in which the covariance matrix is the unit matrix is shown in the bottom (red dashed coordinate system). The second coordinate system can not be obtained from the original coordinate system (black solid) by a rotation. Additionally, a stretching of the axis is needed. In this work, a variable substitution from the original coordinate system into the coordinate system in which the covariance matrix is the unit matrix (bottom plot, red dashed coordinate system) is done. For further information see text.

Table 4.2: Values of the energy calibration parameters and their uncertainties in terms of the parameters a', b' and c' used in the final fit. All values are identical to the values used in the θ_{13} fit [44].

parameter	FD1	FD2	ND
a'	0.009 ± 0.016		
b'	0.9959 ± 0.0083	0.9959 ± 0.0085	0.9959 ± 0.0093
c'	0.00000 ± 0.00053	0.00000 ± 0.00069	0.00000 ± 0.00048

Table 4.3: Correlations of the energy calibration parameters in terms of the parameters a', b' and c' used in the final fit. The values are identical to the values used in the θ_{13} fit [44].

parameter	a	b' FD1	b' FD2	b' ND	c' FD1	c' FD2	c' ND
a'	1	-0.85	-0.83	-0.76	0.00	0.00	0.00
b' FD1	-0.85	1	0.71	0.65	-0.07	0.00	0.00
b' FD2	-0.83	0.71	1	0.63	0.00	-0.08	0.00
b' ND	-0.76	0.65	0.63	1	0.00	0.00	-0.05
c' FD1	0.00	-0.07	0.00	0.00	1	0.00	0.00
c' FD2	0.00	0.00	-0.08	0.00	0.00	1	0.00
c' ND	0.00	0.00	0.00	-0.05	0.00	0.00	1

4.2.3 Oscillation model

The theory of neutrino oscillation has been discussed in chapter 1.2. It was shown that the survival probability of electron antineutrinos in the range of baselines relevant for Double Chooz is approximately given by equation (1.30):

$$P_{ee} \approx 1 - c_{14}^4 \sin^2 2\theta_{13} \sin^2 \Delta_{ee} - \sin^2 2\theta_{14} \sin^2 \Delta_{41} \quad .$$

In this section, oscillation signatures observable with the Double Chooz experiment are visualized and further discussed in this section.

Majorana and Dirac CP-validating phases are not observable for disappearance experiments such as Double Chooz in general regardless of the number of neutrino states (see section 1.2, equation (1.17)). Therefore, CP-validating phases are not discussed in the following.

Figure 4.4 illustrates an example for the $\bar{\nu_e}$ neutrino survival probability versus true neutrino energy in MeV for baselines of 400 m (top) and 1050 m (bottom) assuming sterile oscillations. The dotted blue line shows $\sin^2 2\theta_{14}$=0.0, the red dashed line $\sin^2 2\theta_{14}$=0.02, Δm^2_{41}=0.1 eV^2 and the solid green line $\sin^2 2\theta_{14}$=0.02, Δm^2_{41}=0.02 eV^2. The far detector has been placed in such a way that the first minimum due to the $\sin^2 2\theta_{13}$ oscillation is in an observable energy range (cf. $\sin^2 2\theta_{14}$=0.0, dotted blue line in the lower part of figure 4.4). In contrast, the position of the near detector was chosen such that there is mostly no oscillation due to $\sin^2 2\theta_{13}$ yet (cf. $\sin^2 2\theta_{14}$=0.0, dotted blue line in the upper part of figure 4.4). Comparing the dashed dotted blue line to the dashed red and solid green line one can see that in case of $\sin^2 2\theta_{14} \neq 0$ there is basically a superposition of the deficits due to $\sin^2 2\theta_{13}$ and $\sin^2 2\theta_{14}$ oscillation (given that $\sin^2 2\theta_{14} << 1$ and $|\Delta m^2_{41}| \geq |\Delta m^2_{31}|$). The superposition of the deficits due to $\sin^2 2\theta_{13}$ and $\sin^2 2\theta_{14}$ oscillations also follows from

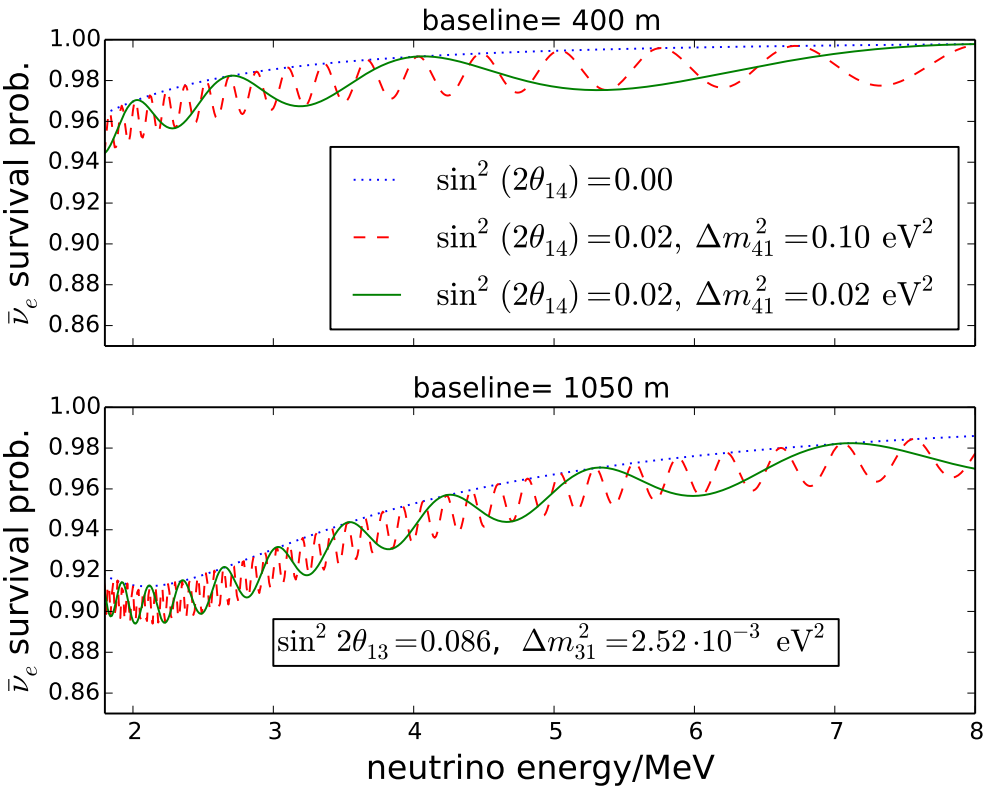

Figure 4.4: $\bar{\nu}_e$ neutrino survival probability versus true neutrino energy in MeV for baselines of 400 m (top) and 1050 m (bottom). The dotted blue line illustrates $\sin^2 2\theta_{14}$=0.0, the red dashed line $\sin^2 2\theta_{14}$=0.02, Δm^2_{41}=0.1 eV^2 and the solid green line $\sin^2 2\theta_{14}$=0.02, Δm^2_{41}=0.02 eV^2. $\theta_{13} = 8.52°$ ($\sin^2 2\theta_{13} = 0.086$) and Δm^2_{31}=0.00252 eV^2 has been used for all probabilities shown in this figure. All probabilities in this plots were calculated with NuCraft [125] assuming full four flavor oscillation.

equation (1.30) since $\cos^4\theta_{14} \approx 0$. $\sin^2 2\theta_{14} > 0$, $|\Delta m^2_{41}| > |\Delta m^2_{31}|$ leads to oscillation patterns in both defectors that are different in near and far detector (cf. figure 4.4). More precisely, the oscillations are around $1050/400 \approx 2.5$ times faster in the far detector. That is because the baseline L appears in the nominator of the term $\sin^2\left(\frac{\Delta m^2_{41}[\mathrm{eV}^2]L[\mathrm{km}]}{4E[\mathrm{GeV}]}\right)$ in equation (1.30). $|\Delta m^2_{41}|$ also appears in the nominator of $\sin^2\left(\frac{\Delta m^2_{41}[\mathrm{eV}^2]L[\mathrm{km}]}{4E[\mathrm{GeV}]}\right)$. Hence, the larger $|\Delta m^2_{41}|$, the faster the oscillations are, as one can see by comparing the lines for $\sin^2 2\theta_{14}$=0.02, Δm^2_{41}=0.02 eV^2 and $\sin^2 2\theta_{14}$=0.02, Δm^2_{41}=0.10 eV^2 in figure 4.4. $\sin^2 2\theta_{14}$ gives the amplitude of the sterile oscillation signature since $\sin^2\left(\frac{\Delta m^2_{41}[\mathrm{eV}^2]L[\mathrm{km}]}{4E[\mathrm{GeV}]}\right)$ is multiplied by the factor $\sin^2 2\theta_{14}$ in equation (1.30).

Neutrinos are oscillated using the approximation (1.30) in the final analysis where $\Delta m^2_{ee} = (2.484 \pm 0.036) \cdot 10^{-3}\mathrm{eV}^2$ is used where Δm^2_{ee} the value is from [44] which used the input from [65] [66]. Figure 4.5 compares the approximation for exemplary sterile parameters of $\sin^2 2\theta_{14} = 0.02$ and $\Delta m^2_{41} = 0.05\,\mathrm{eV}^2$. Hereby, the full four flavor oscillation probability $\Delta m^2_{41} > 0$ and a baseline of 1050 m are assumed. By showing the electron antineutrino survival probability versus true neutrino energy for a far detector baseline of precisely 1050 m, figure 4.6 does the same but assumes $\Delta m^2_{41} < 0$. The solid blue lines show the full four flavor oscillation for $\Delta m^2_{32} > 0$ while the dashed green lines show the full four flavor oscillation for $\Delta m^2_{32} < 0$ and the dashed red lines show the approximation from equation (1.30). The lines for $\Delta m^2_{32} > 0$ and $\Delta m^2_{32} < 0$ are very close to each other and cannot be distinguished experimentally since Double Chooz has no sensitivity to the mass ordering of the known neutrino states. The oscillation probabilities assuming full four flavor oscillation have been calculated using NuCraft [125]. One can see that approximation and full four flavor oscillation probabilities agree to the per-mille level in all cases. The maximum difference between approximation and full four flavor case is 4.5 per-mill. Figure 4.7 shows electron antineutrino survival probability versus energy for all possible mass orderings together in one plot. Figure B.1 is identical to figure 4.7 expect for the sterile mass and shows the same for $\Delta m^2_{41} = 0.02\,\mathrm{eV}^2$.

Figure 4.8 shows an example for so called Asimov[I] inverse beta decay candidate predictions without background relative to the no-oscillation model prediction versus visible prompt energy. Error bars correspond to three years of gadolinium physics data taking from the signal region with example parameters of $\sin^2 2\theta_{13} = 0.085$, $\sin^2 2\theta_{14} = 0.100$ and $\Delta m^2_{41} = 0.02\,\mathrm{eV}^2$. The FD2 plot is shown in the top, FD1-On plot in the middle and the the ND plot in the bottom. A sterile oscillation pattern is observed in all detectors. Figure 4.9 shows the same set of plots for a different sterile squared mass difference of $\Delta m^2_{41} = 1.0\,\mathrm{eV}^2$. For such a big value of $|\Delta m^2_{41}|$ the oscillations become so fast that they can not be resolved anymore due to the finite energy resolution of the detectors. Thus, only a smaller normalization is visible in all detectors to which the analysis will not be sensitive since it does not compare the correlated reactor flux (i.e. the global normalization in all energy bins) to the prediction. Therefore, there is no sensitivity to $\Delta m^2_{41} = O(1.0\,\mathrm{eV}^2)$ or larger. Examples for $\Delta m^2_{41} = 0.0001\,\mathrm{eV}^2$ are shown in figure 4.10. For $|\Delta m^2_{41}| < |\Delta m^2_{ee}|$ no significant sterile oscillation happened yet at both near and far detector baselines. Hence, the sterile analysis will not be sensitive in this mass squared region either.

[I] It has been pointed out in [47] that a sensitivity study on many pseudo experiments (i.e. a so-called ensemble study) can be replaced by a sensitivity study on the expected mean dataset which has infinite statistics. The sensitivity study on this so-called *Asimov Dataset* will give the same result as the median result of the ensemble study. More on this can be found in section 4.3.1

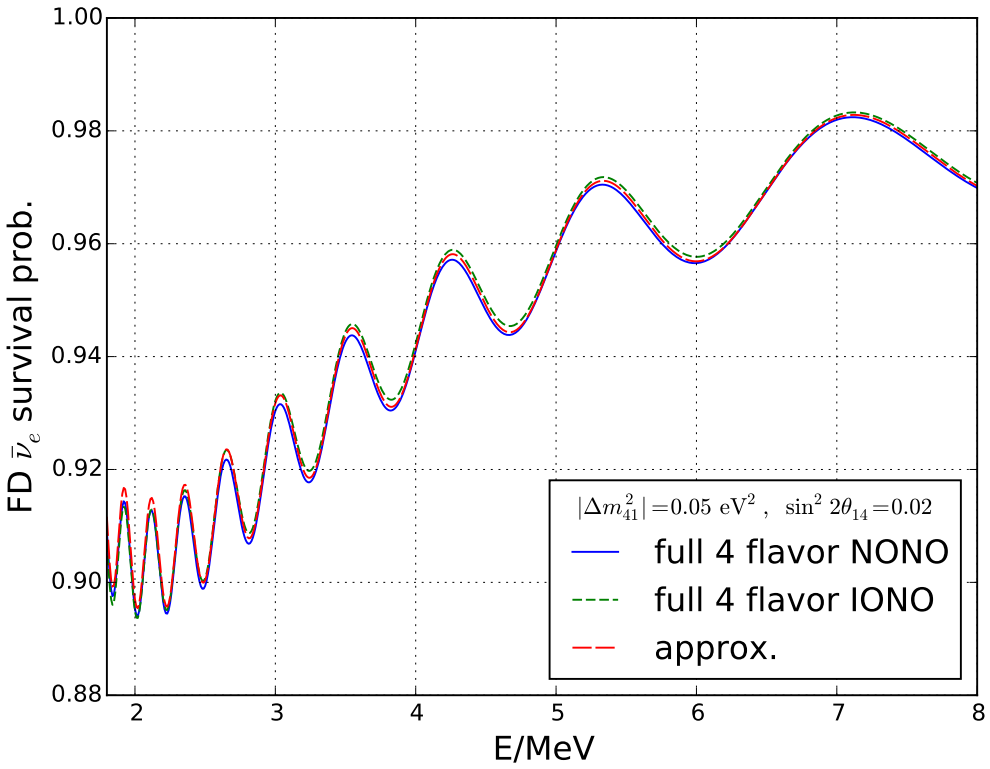

Figure 4.5: Comparison of the approximation for the electron antineutrino survival probability used in this work to the full four flavor oscillation for example parameters of $\sin^2 2\theta_{14} = 0.02$ and $\Delta m^2_{41} = 0.05\,\mathrm{eV}^2$. The electron antineutrino survival probability versus true energy is shown. The approximation used in this work is plotted in dashed red. The full four flavor probability is shown in solid blue for scenario of neutrino mass ordering NONO, and in dashed green for scenario NOIO. The full four flavor oscillation probabilities have been calculated using NuCraft [125]. $\theta_{13} = 8.52\,^\circ$ ($\sin^2 2\theta_{13} = 0.086$) and Δm^2_{31}=0.00252 eV^2 has been used for all probabilities shown in this figure.

4.2.4 Neutrino flux model

This analysis uses the Data-to-Data fit principle. Thus, it does not depend on any specific reactor model since the data of far and near detector is not compared to the MC but only to data of the other detector. The correlation of the reactor flux between ND and FD2 is assumed to be 99.75%, the correction between FD1-On and FD2 is 93.20% and the correlation between FD1-On and ND is 93.10% [44]. These correlations are also summarized in table 4.4. The reactor flux model is only used for corrections to allow for a flux difference due to uncorrelated reactor flux parts. These effects are very small due to a correlation of more than 93%. For these small correction the reactor flux covariance matrices produced without using the Bugey4 anchor point are used (cf. section 3.4) - just as it is done in the θ_{13} Data-to-Data fit. These reactor covariance matrices are displayed in figure 4.11 (ND), figure B.2 (FD1-On) and figure B.3 (FD2).

Despite this analysis does not rely on any reactor flux prediction model, the algorithm internally constructs a hypothetical neutrino flux in order to compare it to data as explained

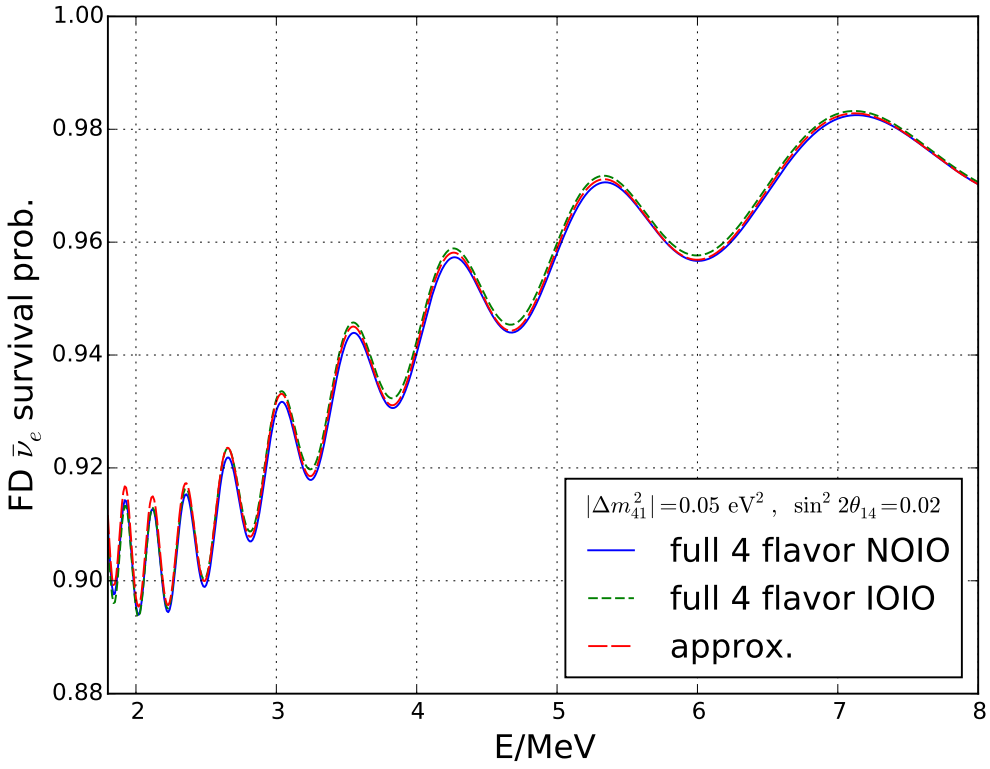

Figure 4.6: Comparison of the approximation for the electron antineutrino survival probability used in this work to the full four flavor oscillation for example parameters of $\sin^2 2\theta_{14} = 0.02$ and $\Delta m^2_{41} = -0.05\,\mathrm{eV}^2$. The electron antineutrino survival probability versus true energy is shown. The approximation used in this work in dashed red. The full four flavor probability is shown in solid blue for the scenario of neutrino mass ordering IONO, and in dashed green for scenario IOIO. The full four flavor oscillation probabilities have been calculated using NuCraft [125]. $\theta_{13} = 8.52^\circ$ ($\sin^2 2\theta_{13} = 0.086$) and Δm^2_{31}=0.00252 eV^2 has been used for all probabilities shown in this figure.

Table 4.4: Correlations of the reactor flux used in this work. All correlations are identical to the correlations used in the θ_{13} fit [44].

correlations	FD1-On	FD2	ND
FD1-On	1	0.932	0.931
FD2	0.932	1	0.9975
ND	0.931	0.9975	1

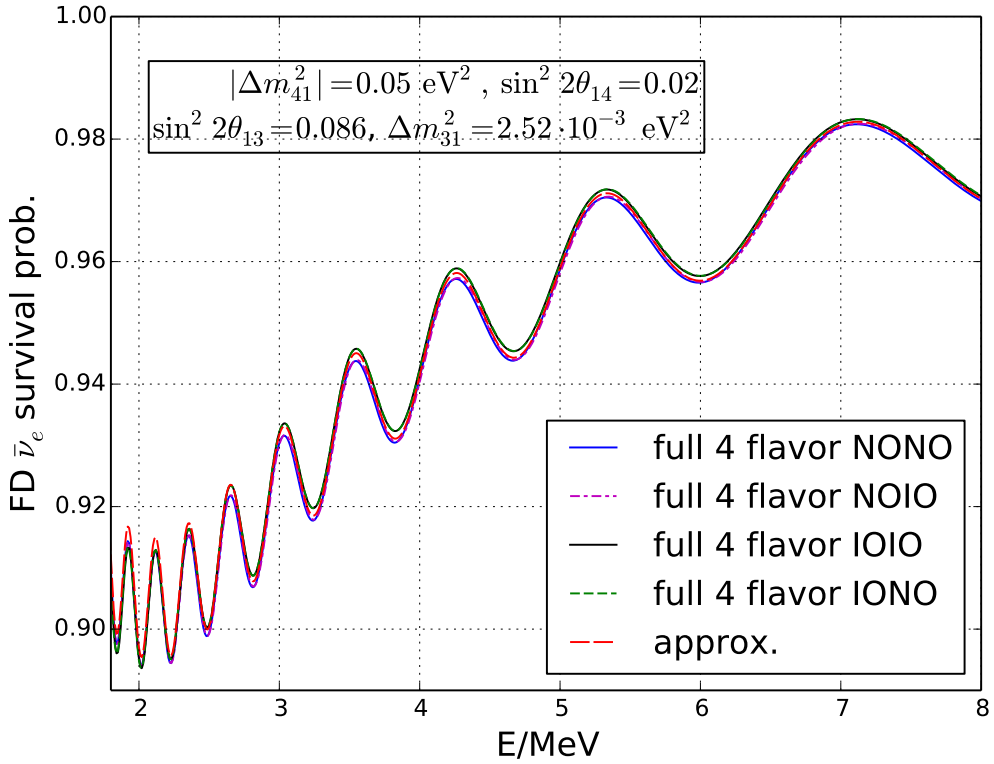

Figure 4.7: Comparison of oscillation formula approximation used in this work to the full four flavor oscillation for example parameters of $\sin^2 2\theta_{14} = 0.02$ and $|\Delta m^2_{41}| = 0.05\,\mathrm{eV}^2$. The electron antineutrino survival probability versus true energy is shown. The approximation used in this work while the full four flavor probability is shown in solid blue for scenario NONO in dashed magenta for scenario NOIO in solid black for scenario IOIO and in dashed green for scenario IONO. The full four flavor oscillation probabilities have been calculated using NuCraft [125]. $\theta_{13} = 8.52^\circ$ ($\sin^2 2\theta_{13} = 0.086$) and Δm^2_{31}=0.00252 eV^2 has been used for all probabilities shown in this figure.

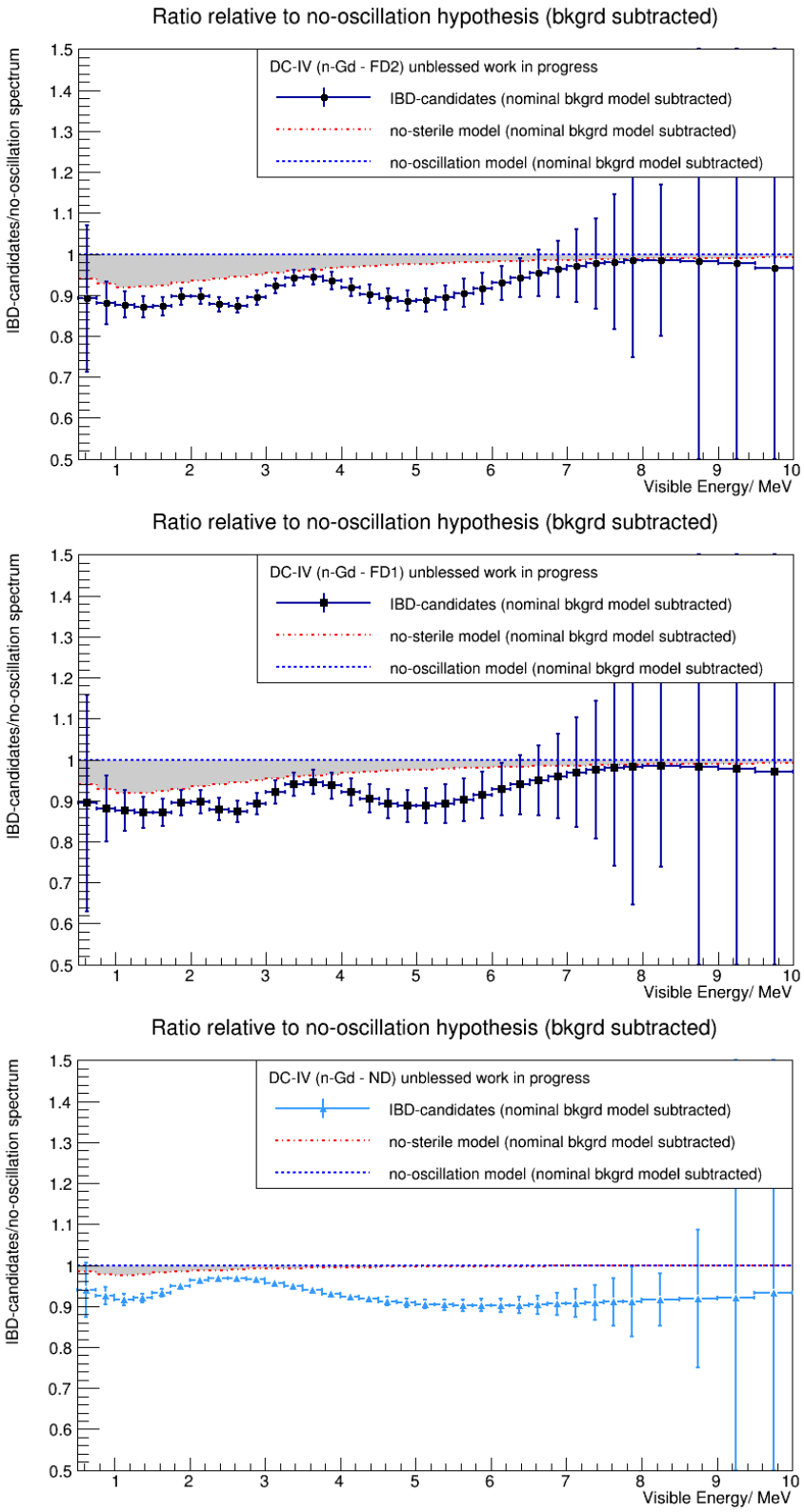

Figure 4.8: Asimov (cf. footnote I) inverse beta decay candidate predictions without background relative to the no-oscillation model prediction versus visible prompt energy where error bars correspond to three years of gadolinium physics data taking. The ratio of the no-sterile prediction to the no-oscillation prediction is shown in dashed red. The FD2 plot is shown in the top, FD1-On plot in the middle and the the ND plot in the bottom. $\sin^2 2\theta_{13} = 0.085$, $\sin^2 2\theta_{14} = 0.100$ and $\Delta m^2_{41} = 0.02\,\mathrm{eV}^2$ have been used.

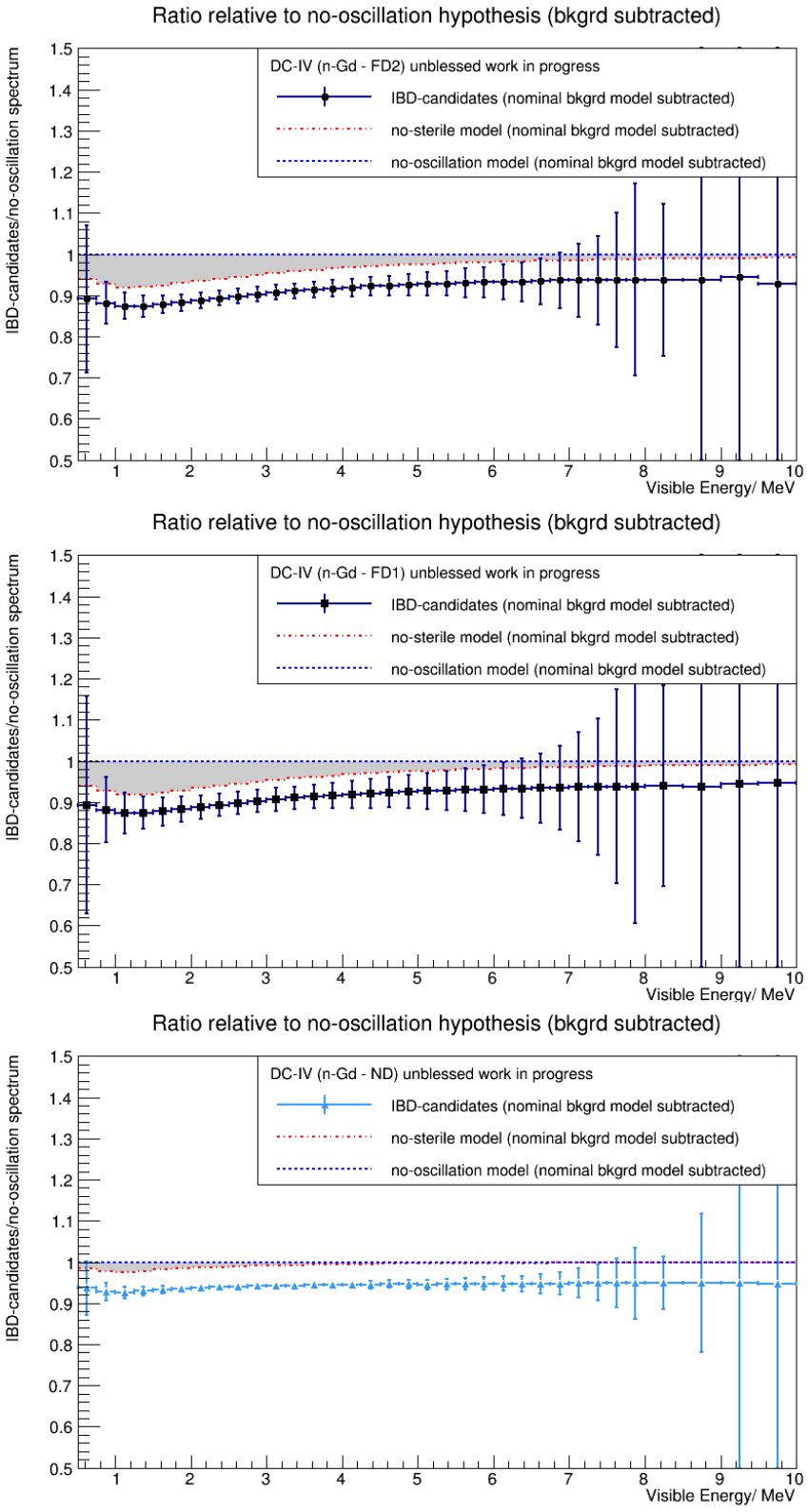

Figure 4.9: Asimov inverse beta decay candidate predictions without background relative to the no-oscillation model prediction versus visible prompt energy where error bars correspond to three years of gadolinium physics data taking. The ratio of the no-sterile prediction to the no-oscillation prediction is shown in dashed red. The FD2 plot is shown in the top, FD1-On plot in the middle and the the ND plot in the bottom. Here, $\sin^2 2\theta_{13} = 0.085$, $\sin^2 2\theta_{14} = 0.100$ and $\Delta m^2_{41} = 1.00\,\mathrm{eV}^2$ have been used.

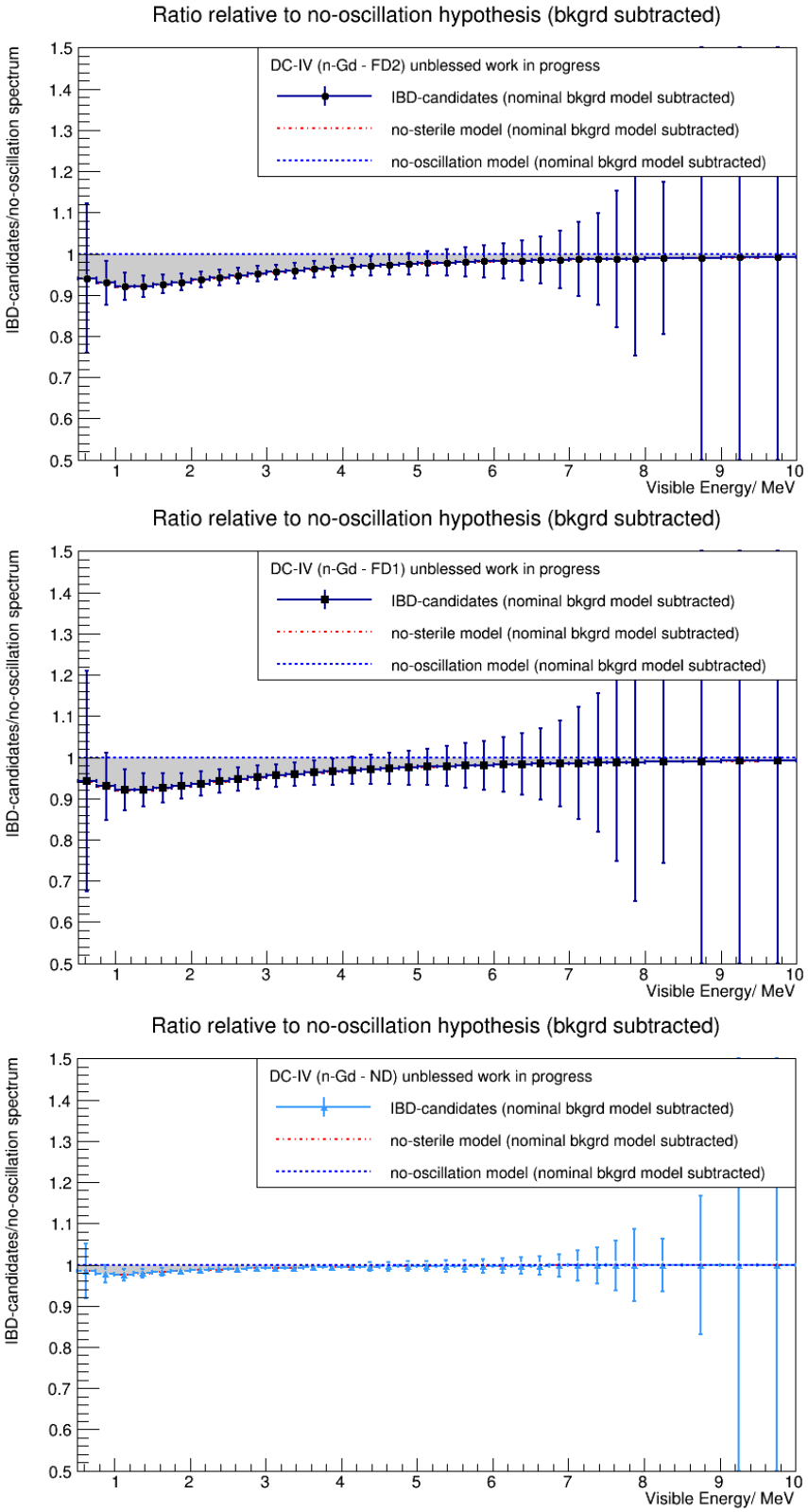

Figure 4.10: Asimov inverse beta decay candidate predictions without background relative to the no-oscillation model prediction versus visible prompt energy where error bars correspond to three years of gadolinium physics data taking. The ratio of the no-sterile prediction to the no-oscillation prediction is shown in dashed red. The FD2 plot is shown in the top, FD1-On plot in the middle and the the ND plot in the bottom. Here, $\sin^2 2\theta_{13} = 0.085$, $\sin^2 2\theta_{14} = 0.100$ and $\Delta m^2_{41} = 0.0001\,\mathrm{eV}^2$ have been used.

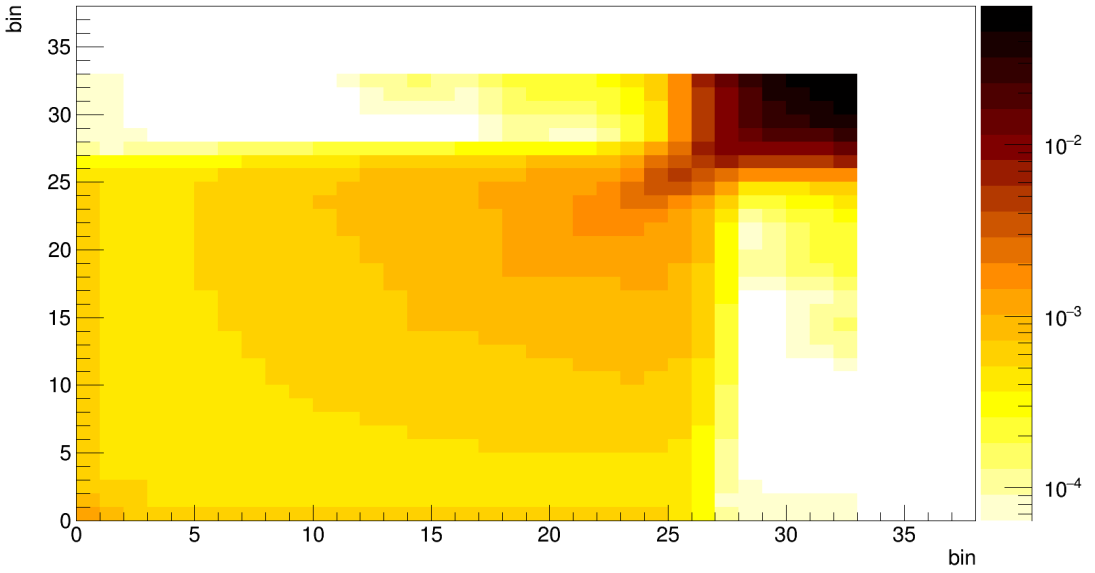

Figure 4.11: Covariance matrix of the reactor flux parameters for the near detector dataset. This matrix has been generated without using the Bugey4 anchor point (cf. section 3.4).

in the introduction of this chapter. This hypothetical spectrum does not have to match any prediction. It is described by 41 reactor flux parameters per detector that are optimized in the fit. These parameters are correlated among the datasets with the correlation factors that can be found in table 2.2. The correlation is technically implemented by a transformation in the eigenbasis of the covariance matrix as described in section 4.2.1. The part that is correlated is efficiently not constraint in the fit, more precisely the Gaussian prior on these parameters is relaxed by a factor of 20 since a soft prior helps the fit to converge. In order to center this weak prior as good as possible, the internally constructed model is re-weighted on number of events w.r.t. the measurement assuming the latest Double Chooz θ_{13} result of $\sin^2 2\theta_{13} = 0.119$ [43].

More precisely, the reactor flux parameters do not refer directly to the absolute reactor flux but to the relative deviation in units of the reactor flux uncertainty from the reference Monte Carlo which is in particular arbitrary. This is useful since for the conversion from true neutrino energy to visible prompt energy a Monte Carlo simulation must be used. For the baseline distribution, a Monte Carlo simulation is necessary as well. The already existing Monte Carlo, which was used for the MC-Data θ_{13} fit [57], is used in order to do the conversion and for the baseline distribution. The true neutrino energy distribution in that Monte Carlo is arbitrary as long as the near - far ratio in the Monte Carlo is conserved. The Monte Carlo which was used for the MC-Data θ_{13} fit was chosen because it is the only existing Monte Carlo. Moreover, it is helpful to use a Monte Carlo which has the most statistics at a reasonable position and is not by several orders of magnitude away from the measurement. Technically, for instance a Monte Carlo having a flat energy distribution could also be used, but this would require much more computing time a large human effort to produce it. By using the Monte Carlo as a reference point for comparison expected differences between near detector and far detector are automatically accounted for. Such expected differences are for instance the different baseline distributions or small non-iso flux corrections in terms of thermal power or fuel composition.

How the construction of the hypothetical neutrino flux is done and why it is independent from the energy shape of the Monte Carlo is explained in further detail in the following.

1. The algorithm iterates over all events in the Monte Carlo and first oscillates them using equation (1.30), true baseline and true energy from the Monte Carlo. Next, it fills them in a histogram according to their visible prompt energy information provided in the Monte Carlo. That histogram covers the energy range of 0-20 MeV with 80 bins of 0.25 MeV width each. The bins are smaller because this allows for more precise energy corrections which are explained in the next steps.

2. The histogram is re-weighted by the reactor flux shift parameters.

3. The histogram from step 2 is interpolated using a linear spline.

4. The linear spline from step 3 is shifted using the energy parameters a', b', c' for the corresponding dataset.

5. The shifted linear spline is converted to a histogram of equidistant 80 bins from 0-20 MeV again by analytic integration.

As mentioned in section 1.4.1 the Double Chooz Experiment observes a global deficit of the total neutrino rate with both near and far detector to the prediction which can not be explained by oscillation. Therefore, the Monte Carlo prediction for the neutrino events is divided by the empirical factor describing the deficit of 8.6% [101].

4.2.5 Background model

Lithium background The lithium background shape is assumed to be the same in FD1, FD2 and ND (i.e. it is fully correlated). It is modeled with 38 shape parameters. The lithium rate is fully correlated between FD1 and FD2 while the FD1 and FD2 lithium rate is not correlated to the lithium rate in the near detector. Therefore, there are two parameters for the lithium rate in total. As mentioned above, the lithium rates are not constrained in the fit.

Fast neutron and stopping muon background The fast neutron and stopping muon (FNSM) background shape is parameterized by the empirical function

$$f_{\mathrm{FNSM}}(E_{\mathrm{vis}}) = p_0 \cdot \exp(-p_1 \cdot E_{\mathrm{vis}}) + p_2 \cdot E_{\mathrm{vis}} \tag{4.24}$$

where E_{vis} is the visible prompt inverse beta decay candidate energy. The values of the parameters p_0 , p_1 and p_2 can be found in table 4.5 and are fully correlated among FD1-On, FD2 and ND. The correlations between p_0, p_1 and p_2 can be found in table 4.6. Equation (4.24) is normalized on integral to one and scaled with the rate parameters. The fast neutron and stopping muon rate is fully correlated between FD1 and FD2 but uncorrelated between far and near detector (i.e. there are two parameters for the fast neutron and stopping muon rates in total).

Table 4.5: Values of the background rate parameters and the shape parameters for the fast neutron and stopping muon background used in the fit in 1/day [44].

parameter	FD1	FD2	ND
acc. bckgr. rate	3.930 ± 0.010	4.320 ± 0.020	3.110 ± 0.004
Li bckgr. rate	2.57 ± 0.61		12.32 ± 2.01
FNSM bckgr. rate	2.54 ± 0.07		20.77 ± 0.43
FNSM bckgr. par. p0	180.723 ± 3.911		
FNSM bckgr. par. p1	0.0153251 ± 0.00102562		
FNSM bckgr. par. p2	-0.296282 ± 0.041220		

Table 4.6: Covariance matrix of the fast neutron and stopping muon background parameters used in the fit in 1/day^2. The matrix is identical to the matrix used in the θ_{13} fit [44].

parameter	p0	p1	. p2
p0	$1.52951 \cdot 10^{1}$	$3.21573 \cdot 10^{-3}$	0.103868
p1	$3.21573 \cdot 10^{-3}$	$1.05219 \cdot 10^{-6}$	$4.04599 \cdot 10^{-5}$
p2	$1.03868 \cdot 10^{-1}$	$4.04599 \cdot 10^{-5}$	0.00169909

Accidental background Since the readout system has changed, the accidental background rates and shapes are fully uncorrelated between FD1, FD2 and ND. There is one rate parameter and 38 shape parameters for each dataset.

A summary of the background rates can be found in table 4.5.

4.2.6 Reactor Off

The expected number of inverse beta decay events with both reactors off is mainly given by the expected number of background events for that period. However, a small number of neutrinos from the reactor cores is expected even when they are off. More precisely, $N^{\nu,\mathrm{exp}}_{\mathrm{OffOff}} = 4.18 \pm 1.25$ neutrinos are expected within the 7.16 days of FD1-Off-Off lifetime with both reactors off resulting in a rate of 0.58 ± 0.17/day. These neutrinos undergo neutrino oscillation with the same neutrino oscillation parameters as neutrinos produced when reactors are running. These neutrinos are oscillated using their mean energy of 2.74 MeV in order to get the off-off expectation. While this is a very good approximation for the θ_{13} fit since the far detector is in the first oscillation minimum, for a sterile analysis this is usually not the case. Thus, using the mean energy is less accurate, since it is not averaged over the energy distribution. As no official energy shape distribution of the neutrinos exists for the Gd++ analysis, the off-off rate is only priored if it is larger than the central value since sterile neutrino oscillation can only reduce and not increase the number of measured electron antineutrinos. Furthermore, only positive rates are allowed and the neutrinos are oscillated using $\theta_{14} = 0$ in order to avoid an unstable behavior of the prediction for large Δm^2_{41} due to fast oscillation.

The background rates are assumed to be independent from the reactor operation. Thus, they are identical to the rates with reactors running and can be used as a background measurement. The values can be found in table 4.5.

Table 4.7: Values and correlations of the MC-data correction factor. All values and correlations are identical to the values and correlations used in the θ_{13} fit [44].

values	FD1	FD2	ND
	0.9076 ± 0.0069	0.8944 ± 0.0069	0.7010 ± 0.0049
correlations	FD1	FD2	ND
FD1	1	0.808	0.743
FD2	0.809	1	0.742
ND	0.743	0.742	1

Table 4.8: List of parameters used in the fit

	number of par.			correlation		
	FD1	FD2	ND	FD1-FD2	FD2-ND	FD1 - ND
detection^{II}	1	1	1	yes	yes	yes
energy a	1			yes	yes	yes
energy b	1	1	1	yes	yes	yes
energy c	1	1	1	yes	yes	yes
Off-Off ν-rate	1	0	0	no	no	no
acc-rate	1	1	1	no	no	no
acc-shape	38	38	38	no	no	no
Li-rate	1		1	yes	no	no
Li-shape	38			yes	yes	yes
FNSM-rate	1		1	yes	no	no
FNSM-shape	3			yes	yes	yes
relative shift of reactor ν	41	41	41	yes	yes	yes
$\sin^2 2\theta_{13}$	1			yes	yes	yes
Δm^2_{ee}	1			yes	yes	yes
$\sin^2 2\theta_{14}$	1			yes	yes	yes
Δm^2_{41}	1			yes	yes	yes

4.2.7 Detection efficiency

The Monte Carlo generation was using the best measurement value of the proton number at that time. However, the Monte Carlo generation was not repeated after a more precise measurement, as it can be rescaled to correct for the difference to the more precise measurement. The proton number correction is applied simultaneously with other effects contributing to the detection efficiency. All corrections are merged in a factor called *Monte Carlo data correction factor*. Table 4.7 presents the values and correlations used in the fit. Note that the contribution fully correlated in all detectors is fixed in the fit in order to avoid ambiguity.

4.2.8 List of parameters

Table 4.8 provides a list of all parameters to summarize the model description in the text above. For details on the usage of the parameters refer to the corresponding subsection.

4.3 Validation of the algorithm

4.3.1 Crosschecking with non-sterile fit

The Poisson likelihood approach used for this analysis has also been used for a θ_{13} analysis [117]. The fit framework and the inputs are identical - except for the electron antineutrino survival probability which is in the θ_{13} analysis calculated for the specific case $\theta_{14} = 0.0$. Thus, the sterile fit results with $\theta_{14} = 0.0$ are always identical with the θ_{13} fit results using the approach developed in Aachen.

The θ_{13} analysis done with the software and inputs of this analysis has been very carefully crosschecked. There are three θ_{13} analysis groups in the Double Chooz collaboration and all of them have been carefully crosschecking each other. Sensitivities as well as the systematics breakdown have been compared before the experimental data fit has been done.

The Aachen Double Chooz group is one of the groups. The fit approach done in Aachen for the θ_{13} analysis and the sterile fit is referred to as Likelihood Flux Free (LLH-FF) fit. The term LLH-D2MC is used for the approach in [117]. It only differs from the LLH-FF by constraining the reactor flux parameters with adding pulls on the reactor flux using the reactor covariance matrix (cf. figure 4.11) correlated with the correlation coefficients in table 4.7.

The two other fit groups have developed Chi-square based fits where each group has a Data-MC fit and a Data-to-Data fit. The approaches of both groups are similar. Details on the Chi-square fits can be found in [39]. In the following, the Chi-square fits are referred to by the names of the people doing the fit for better comparison with Double Chooz internal documentation, Thiago J.C. Bezerra and Tsunayuki Matsubara.

Before the comparison between the tests is shown, the techniques used to compare the systematics breakdown are explained.

- **General technique** The post fit uncertainties are not necessarily symmetric if Poisson statistics are assumed. Moreover, correlations between parameters may in general depend on the values of these parameters themselves. The ROOT framework assumes that uncertainties are symmetric and the statistics is Gaussian when providing post fit uncertainties on default (even if the Minos method is used) [81]. Thus, a precise uncertainty calculation requires a likelihood scan. This is done in the following way: First, the best fit is obtained. Second, the best fit value fit $\sin^2 2\theta_{13}$ is shifted by the root error estimate in positive and negative direction and fixed. Next, a fit at that position is done, $\ln(\mathcal{L})$ is obtained and $-2\Delta\ln(\mathcal{L}) = -2(\ln(\mathcal{L}) - \ln(\mathcal{L}_{\max}))$ is calculated where $\mathcal{L}_{\max}$ is the maximum likelihood value. If $0.99 < |-2\Delta\ln(\mathcal{L})| - 1 < 1.01$, the error estimate is accepted. Otherwise, a two sided parabola is extrapolated (interpolated) to the point $-2\Delta\ln(\mathcal{L}) = 1$ and the difference of the corresponding $\sin^2 2\theta_{13}$ to the best fit $\sin^2 2\theta_{13}$ is taken as new error estimate. The procedure is repeated with the new error estimate if $0.95 < |-2\Delta\ln(\mathcal{L})| - 1 < 1.05$.
- **Asimov approach** All $\sin^2 2\theta_{13}$ sensitivities are calculated with the so called *Asimov approach*. It has been pointed out in [47] that a sensitivity study on many pseudo experiments (i.e. an ensemble study) can be replaced by a sensitivity study on the expected mean dataset which has infinite statistics. The sensitivity study on

this so-called *Asimov Dataset* will give the same result as the median result of the ensemble study. Using the Asimov dataset for sensitivity calculation is refereed to as *Asimov approach*. The Asimov approach usually saves a lot of computing time, provided that - like in this work - the Asimov dataset can be calculated analytically. If this is given, the Asimov dataset is simply given by the calculated expectation without any fluctuations applied.

- **Statistical (only) sensitivity** The statistical (stat.) uncertainty/sensitivity σ_{stat} is defined as the sensitivity obtained with all nuisance parameters fixed at their best fit value (which is the central value if the Asimov approach is used). With this, the systematics sensitivity σ_{sys} is defined as

$$\sigma_{\text{sys}} = \sqrt{\sigma_{\text{tot}}^2 - \sigma_{\text{stat}}^2} \tag{4.25}$$

where σ_{tot} is the total sensitivity i.e. the sensitivity with the default systematics setup.

- **N-1 test** The impact of a systematic quantity is investigated in the so called *N-1 test*. Hereby, the sensitivity assuming that this systematics quantity is known with infinite precision is calculated and compared to the sensitivity with default setup. A handle to estimate the impact of the specific variable is

$$\sigma_{\text{N}-1,\text{X}} = \sqrt{\sigma_{\text{tot}}^2 - \sigma_{\text{N}-\text{X}}^2} \quad , \tag{4.26}$$

where $\sigma_{\text{N}-\text{X}}$ is the sensitivity assuming the quantity X is known with infinite precision and σ_{tot} is the sensitivity in the default setup. Alternatively the quality

$$r_{\text{N}-1,\text{X}} := \frac{\sigma_{\text{N}-1,\text{X}}}{\sigma_{\text{tot}}} = \frac{\sqrt{\sigma_{\text{tot}}^2 - \sigma_{\text{N}-\text{X}}^2}}{\sigma_{\text{tot}}} \quad . \tag{4.27}$$

may be used.

- **Stat+1 test** First of all the statistics only sensitivity is calculated in the so called *Stat+1 test*. Second, one particular systematic effect is enabled (i.e. nuisance parameters describing this systematics effected are unfixed) and the sensitivity is calculated in this setup. Next, the nuisance parameters describing the particular systematic effect are fixed again and the procedure is repeated with the next systematic effect. An estimate of the impact of the specific variable is

$$\sigma_{\text{stat}+1,\text{X}} = \sqrt{\sigma_{\text{stat}+\text{X}}^2 - \sigma_{\text{stat}}^2} \tag{4.28}$$

where σ_{stat+X} is the sensitivity assuming the quantity X is the only systematic effect to be considered and σ_{stat} is the statistics only sensitivity. This quantity may also be used relative to the default sensitivity defining:

$$r_{\text{stat}+1,\text{X}} := \frac{\sigma_{\text{stat}+1,\text{X}}}{\sigma_{\text{tot}}} = \frac{\sqrt{\sigma_{\text{stat}+\text{X}}^2 - \sigma_{\text{stat}}^2}}{\sigma_{\text{tot}}} \tag{4.29}$$

can be used.

The N-1 test provides an estimate on how much the sensitivity can be improved if a certain variable is known better. However, in this test correlations among sets of parameters play a role. Therefore, if the intention is to isolate the impact of a certain variable and to compare it between different fits, the Stat+1 test is better.

Table 4.9 shows the results of the Stat+1 and N-1 test for the LLH-FF approach and the D2D Chi-square fit approach. For the LLH-FF fit approach negative, positive and average sensitivities (σ_- , σ_+ and σ) are given. For the D2D Chi-square fit the sensitivity is symmetric by definition. The quantities $\sigma_{\mathrm{N-1,X}}$ (cf. equation (4.26)), $\sigma_{\mathrm{stat+1,X}}$ (cf. equation (4.28)), $r_{\mathrm{stat+1,X}}$ (cf. equation (4.29)) and $r_{\mathrm{N-1,X}}$ (cf. equation (4.27)) can be found in the table.

The focus of the discussion will be on the Stat+1 test results since in the N-1 test correlations usually play a bigger role as in the Stat+1 test and correlations are respected differently in the likelihood fit and the Chi-square fit.

Figure 4.12 provides a visual comparison of the systematics breakdown for LLH-FF and D2D Chi-square from the Stat+1 test. The top plot shows the N-1 test sensitivity results, the plot in the middle shows $\sigma_{\mathrm{stat+1,X}}$ (cf. equation (4.28)) and the plot in the bottom shows $r_{\mathrm{stat+1,X}}$ (cf. equation (4.28)). The values can be found in table 4.9. The likelihood fit is shown in red, the D2D Chi-square fit in light blue. The error bars correspond to a rounding error of 0.00005 for the Chi-square fit and to 1% of the Stat+1 test results for the likelihood fit.

The default sensitivity is in good agreement between both fits, the statistics only sensitivity is a bit larger for the likelihood fit. This can be possible to the different statistical assumptions. Furthermore, the impact of the atmospheric square mass difference and the background seems consistent. However, the energy seems to be much more important in the likelihood fit. Also, there is a small difference w.r.t. the impact of detection and reactor parameters. The results of the N-1 test are consistent with those of the Stat+1 test. The comparison plot for the N-1 test can be found in figure C.1 in the appendix. A possible explanation for the difference w.r.t. the impact of detection, energy and reactor parameters is that the parameters modeling the correlated reactor flux are not fixed in the likelihood fit for the statistics only sensitivity since they are part of the model. Hypothesis A states that the difference in the systematics breakdown is due to correlation between the correlated reactor flux, energy and detection parameters (which seem to be likely).

In order to test hypothesis A, the Stat+1 test has been repeated using the MC-Data approach for detection, energy and reactor. The outcome is presented in table 4.10 and figure 4.13. The agreement is now remarkably good verifying hypothesis A. The difference in the systematics breakdown between Chi-square and likelihood fit was largest for the energy parameters. Therefore, as an additional test, the post fit correlations of the energy parameters and the correlated reactor flux parameters have been plotted, That plot is displayed in figure C.2 and shows correlations up to 0.58 between energy and reactor flux parameters.

$\mathbf{Sin^2 2\theta_{13}}$ fit results

The LLH-FF $\sin^2 2\theta_{13}$ fit has been run on experimental data. Table 4.11 summarizes the $\sin^2 2\theta_{13}$ fit results of the three fits that are based on comparing experimental near and far detector only. The agreement between Thiago's fit and the likelihood fit is within a quarter of the uncertainty and the agreement to Tsunayukis fit is also within a half of the uncertainty on $\sin^2 2\theta_{13}$. It is remarkable that the LLH-FF fit which has both lithium rates unconstrained fits a around two sigma larger lithium rate for both near and far detector.

Table 4.9: Comparison of the systematic breakdown w.r.t. $\sin^2 2\theta_{13}$ between the LLH-FF fit approach used in this work and the D2D Chi-square fit approach for $\sin^2 2\theta_{13} = 0.1$. For the LLH-FF fit approach negative, positive and average sensitivity (σ_- , σ_+ and σ) are given. For the D2D Chi-square fit the sensitivity is symmetric by definition. Therefore, only σ is given. σ_{sys} denotes σ_{sys} in the stat only row, $\sigma_{\text{N}-1,\text{X}}$ (cf. equation (4.26)) in the N-1 test rows and $\sigma_{\text{stat}+1,\text{X}}$(cf. equation (4.28)) in the stat+1 test rows. Similarly, r either stands for $\sigma_{\text{sys}}/\sigma_{\text{tot}}$ in the stat only row, $r_{\text{N}-1,\text{X}}$ (cf. equation (4.27)) or $r_{\text{Stat}+1,\text{X}}$ (cf. equation (4.29)). Visualizations of this table can be found in figure C.1 and 4.12.

$\sin^2 2\theta_{13}$ systematics breakdown								
	LLH-FF					D2D Chi-square [40]		
	σ_+	σ_-	σ	σ_{sys}	r	σ	σ_{sys}	r
default	0.0162	0.0164	0.0163			0.0164		
stat only	0.0092	0.0092	0.0092	0.0135	0.82	0.0084	0.0141	0.86
N-Detection	0.0137	0.0137	0.0137	0.0089	0.55	0.0136	0.0092	0.56
N-BG	0.0155	0.0157	0.0156	0.0047	0.29	0.0155	0.0054	0.33
N-Reactor	0.0149	0.0150	0.0149	0.0066	0.40	0.0138	0.0089	0.54
N-Energy	0.0129	0.0130	0.0130	0.0099	0.61	0.0139	0.0087	0.53
N-Δm^2	0.0161	0.0164	0.0163	0.0012	0.07	0.0163	0.0018	0.11
Stat+Detection	0.0114	0.0116	0.0115	0.0068	0.42	0.0117	0.0081	0.50
Stat+BG	0.0096	0.0096	0.0096	0.0026	0.16	0.0087	0.0023	0.14
Stat+Reactor	0.0106	0.0106	0.0106	0.0052	0.32	0.0116	0.0080	0.49
Stat+Energy	0.0106	0.0108	0.0107	0.0054	0.33	0.0087	0.0023	0.14
Stat+Δm^2	0.0093	0.0093	0.0093	0.0013	0.08	0.0085	0.0013	0.08
Stat+En+Reactor	0.0126	0.0127	0.0127	0.0087	0.53			

Table 4.10: Comparison of the systematic breakdown w.r.t. $\sin^2 2\theta_{13}$ between the LLH-D2MC fit approach and the D2MC Chi-square fit approach for $\sin^2 2\theta_{13} = 0.1$. For the LLH-D2MC fit approach negative, positive and average sensitivity (σ_- , σ_+ and σ) are given. For the D2MC Chi-square fit the sensitivity is symmetric by definition. Therefore, only σ is given. σ_{sys} denotes s_{sys} in the stat only row and $\sigma_{\text{stat}+1,\text{X}}$(cf. equation (4.28)) in the stat+1 test rows. Similarly, r either stands for $\sigma_{\text{sys}}/\sigma_{\text{tot}}$ or $r_{\text{Stat}+1,\text{X}}$ (cf. equation (4.29)).

$\sin^2 2\theta_{13}$ MC-data $\sin^2 2\theta_{13}$ systematics breakdown								
	LLH-D2MC					D2MC Chi-square [40]		
	σ_+	σ_-	σ	σ_{sys}	r	σ	σ_{sys}	r
default	0.0136	0.0140	0.0138			0.0141		
stat only	0.0054	0.0054	0.0054	0.0127	0.92	0.0054	0.0130	0.92
Stat+Detection	0.0090	0.0091	0.0091	0.0072	0.52	0.0091	0.0073	0.52
Stat+Reactor	0.0098	0.0099	0.0098	0.0082	0.59	0.0097	0.0081	0.57
Stat+Energy	0.0057	0.0057	0.0057	0.0017	0.12	0.0057	0.0018	0.13

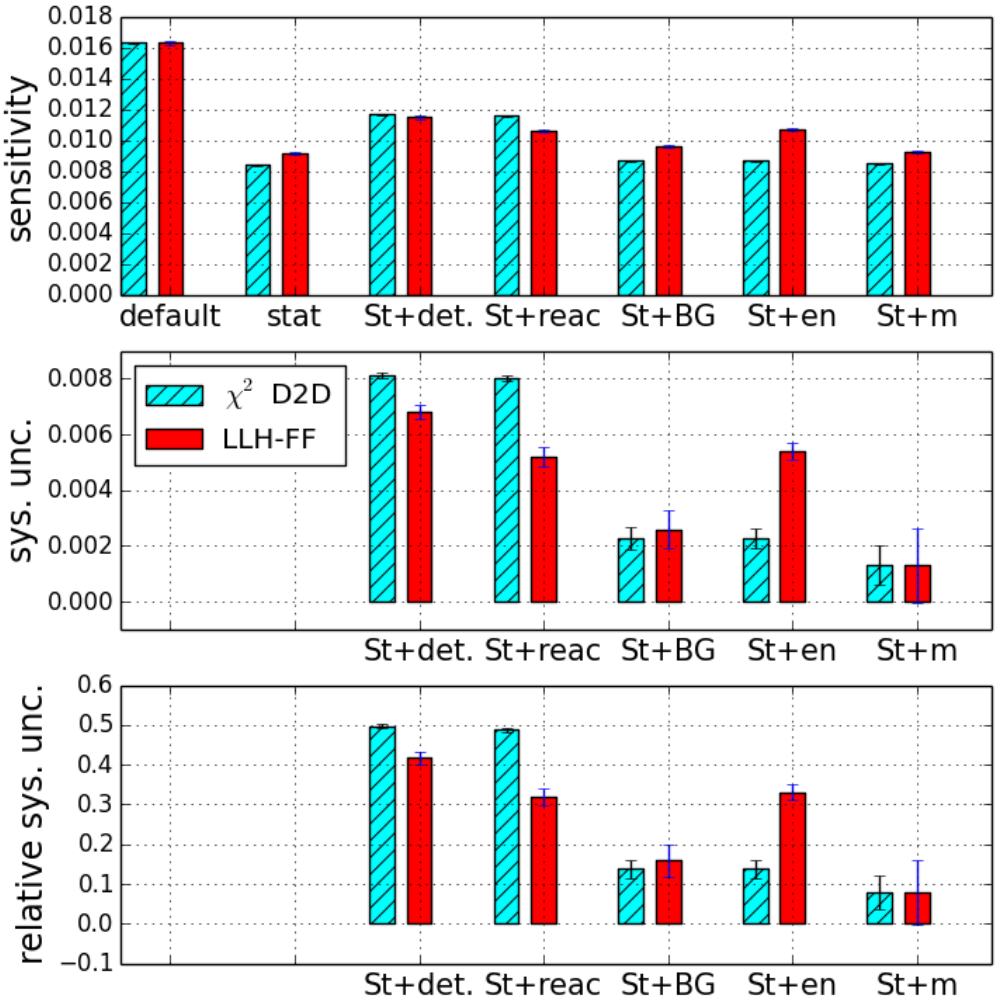

Figure 4.12: Comparison of the LLH-FF fit and D2D Chi-square fit (Thiago) for a breakdown of the systematics for $\sin^2 2\theta_{13}$ from the Stat+1 test. The top plot shows the Stat+1 test sensitivity results, the plot in the middle shows $\sigma_{\text{stat+1,X}}$ (cf. equation (4.28)) and the plot in the bottom shows $r_{\text{Stat+1,X}}$ (cf. equation (4.29)). The values can be found in table 4.9. The error bars correspond to a rounding error of 0.00005 for the Chi-square fit and to 1% of the Stat+1 test results for the likelihood fit. The error bars correspond to a rounding error of 0.00005 for the Chi-square fit and to 1% of the Stat+1 test results for the likelihood fit.

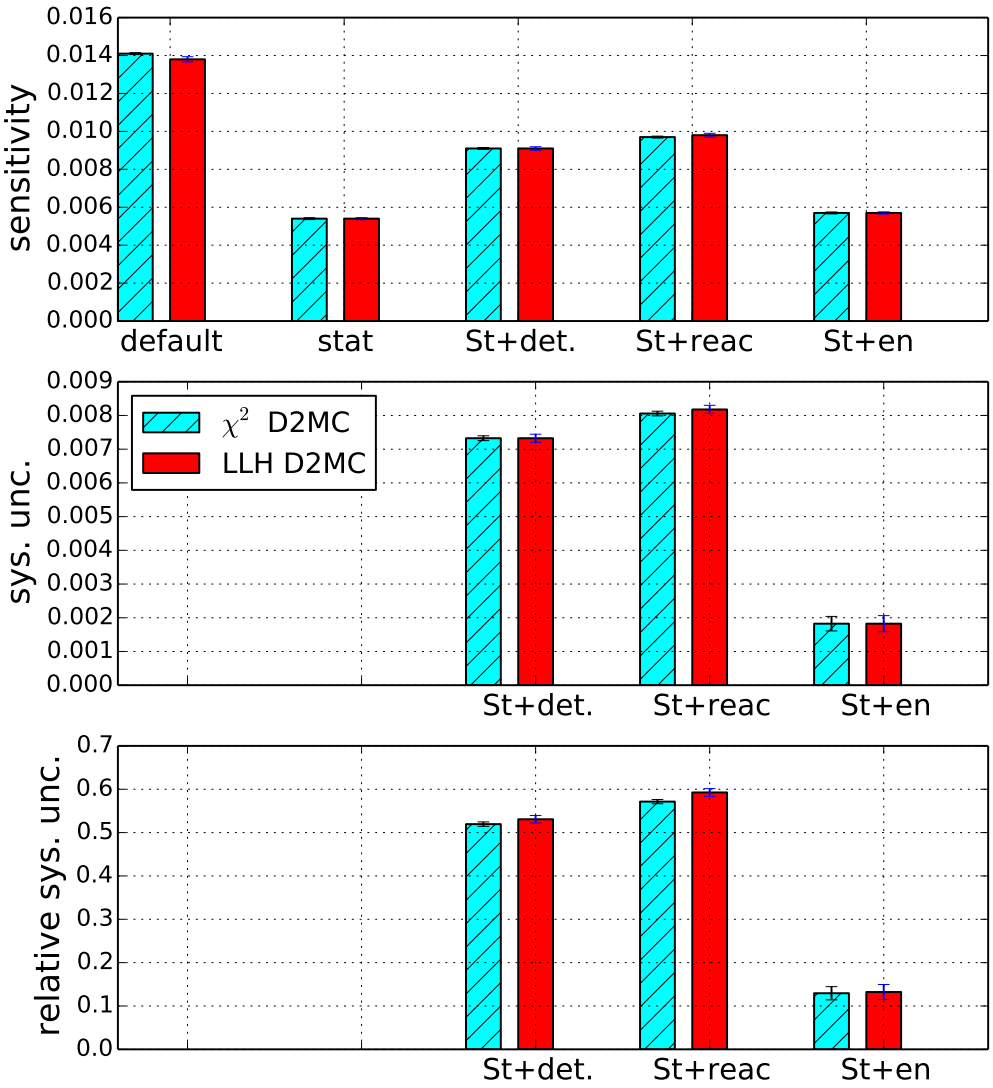

Figure 4.13: Comparison of the likelihood D2MC fit and D2MC Chi-square fit (Thiago) for a breakdown of the systematics for $\sin^2 2\theta_{13}$ from the Stat+1 test. The top plot shows the Stat+1 test sensitivity results, the plot in the middle shows $\sigma_{\text{stat+1,X}}$ (cf. equation (4.28)) and the plot in the bottom shows $r_{\text{Stat+1,X}}$ (cf. equation (4.29)). The values can be found in table 4.9. The error bars correspond to a rounding error of 0.00005 for the Chi-square fit and to 1% of the Stat+1 test results for the likelihood fit. The error bars correspond to a rounding error of 0.00005 for the Chi-square fit and to 1% of the Stat+1 test results for the likelihood fit.

Table 4.11: Comparison of final fit results on experimental data between the three fits that are based on near-far comparison. Values for the Chi-square fits have been taken from [40]. The degrees of freedom given for the likelihood fit are calculated by *number of data points* minus *number of parameters in the fit that are not constraint with a Gaussian prior*

fit	LLH-FF (Li-unconst)	LLH-FF (Li-const)	χ^2 D2D (Thiago)	χ^2 D2D (Tsunayuki)
$\sin^2 2\theta_{13}$	0.1075	0.1069	0.1034	0.0987
σ_+	0.0161		0.0170	0.0164
σ_-	0.0172		0.0170	0.0164
χ^2(Pearson)	78.2			
χ^2(Neyman)	79.1			
Li-FD (1/day)	$3.109^{+0.298}_{-0.274}$	3.005	2.612±0.347	2.588± 0.315
Li-ND (1/day)	$16.752^{+1.898}_{-1.805}$	14.865	12.558 ±1.909	13.221 ± 1.797
dof	71	73	37	38

4.3.2 Wilks' theorem

The so called Wilks' theorem [127] is useful to compare two different hypothesis and applied in many physics cases. May H_0 be a hypothesis to be compared to another hypothesis H_1 given a measurement $\vec{x}$ with high statistics. H_0 (H_1) may be that some physics is described by $\vec{\theta_0}$ ($\vec{\theta_1}$). Correspondingly, $\sup(\mathcal{L}(\vec{\theta_0}|\vec{x})$ ($\sup(\mathcal{L}(\vec{\theta_1}|\vec{x}))$ is the supremum of the likelihood function given hypothesis H_0 (H_1) described by θ_0 (θ_1) given the measurements $\vec{x}$. In other words, $\sup(\mathcal{L}(\vec{\theta_0}|\vec{x})$ ($\sup(\mathcal{L}(\vec{\theta_1}|\vec{x}))$ is the likelihood function for hypothesis H_0 (H_1) evaluated at the best fit θ_0 (θ_1).

H_0 may be a *simple* version of hypothesis H_1. This means that H_0 is that one or more parameters describing H_1 have a given constant value. In case H_0 is true, the theorem states for the likelihood ratio

$$\lambda(\vec{x}) = \frac{\sup(\mathcal{L}(\vec{\theta_0}|\vec{x}))}{\sup(\mathcal{L}(\vec{\theta_1}|\vec{x}))} \tag{4.30}$$

that $-2\ln(\lambda)$ follows a Chi-square distribution with $m-n$ degrees of freedom, where m and n are the number of dimension of $\vec{\theta_1}$ and $\vec{\theta_0}$, i.e.

$$-2\ln(\lambda(\vec{x})) = \chi^2_{m-n} \tag{4.31}$$

if *optimum estimates of the θ_j exist.* The existence of optimum estimates requires that the matrices of the mathematical expectations of the partial derivative $||c^k_{ij}|| := ||< \frac{\partial^2 \ln(\mathcal{L}(\vec{\theta_k}|\vec{x}))}{\partial\theta_{ki}\partial\theta_{kj}} >||$ with $k = 1, 2$ is positive definite [127]. Here, $\theta_k i$ ($\theta_k j$) is component i (j) of θ_k. Correspondingly $\frac{\partial}{\theta_k i}$ is the partial derivative with respect to $\theta_k i$. i and j run over all dimensions of θ_0 and θ_1.

In the context of this thesis H_0 could be that $\sin^2 2\theta_{14}$ and Δm^2_{41} have given values:

$$H_0 : \{\sin^2 2\theta_{14} = X, \Delta m^2_{41} = Y\,\mathrm{eV}^2 | X, Y \in \mathbb{R}, 0 \leq X \leq 1\} \quad . \tag{4.32}$$

The alternative, less simple hypothesis H_1 could be:

$$H_1 : \{0 \leq \sin^2 2\theta_{14} \leq 1, |\Delta m^2_{41}| \geq 0\,\mathrm{eV}^2\} \quad . \tag{4.33}$$

These definitions result in the test statistics (TS) [14]:

$$TS_{2\mathrm{D}} := -2\ln\lambda(\vec{x}) = -2\ln\left(\frac{\sup\mathcal{L}(\sin^2 2\theta_{14} = X, \Delta m^2_{41} = Y\,\mathrm{eV}^2|\vec{x})}{\sup\mathcal{L}(\sin^2 2\theta_{14}, \Delta m^2_{41}|\vec{x})}\right) \quad . \tag{4.34}$$

The hypothesis H_0' : $\{\ \sin^2 2\theta_{14} = 0 \vee \Delta m^2_{41} = 0\}$ is particular interesting and is compared to H_1': $\{\sin^2 2\theta_{14} \neq 0 \wedge \Delta m^2_{41} \neq 0\}$. In this situation $m - n = 2$ holds.

Δm^2_{41} and $\sin^2 2\theta_{14}$ are degenerate in ($\Delta m^2_{41} = 0.$, $\sin^2 2\theta_{14} = 0.$). This implies that Wilks' theorem is not strictly fulfilled [14] but in most of physics cases the later issue is no problem, in particular as Double Chooz is hardly sensitive to $|\Delta m^2_{41}| \lesssim |\Delta m^2_{31}|$.

The negative logarithmic function is a function of the electron antineutrino survival probability (cf. equation (4.12)). The survival probability of an electron antineutrino is approximately given by equation (1.30). Nyquist-Shannon sampling theorem says that a signal with a certain frequency (which is the additional oscillation pattern due to sterile in this case) can always be described by a series of higher frequencies [115]. Therefore, $-2\Delta\ln(\mathcal{L})$ always includes several minima in Δm^2_{41}. Several minima imply that $< \frac{\partial^2 \ln\left(\mathcal{L}(\vec{\theta_1}|\vec{x})\right)}{\partial\Delta m^2_{41}\partial\Delta m^2_{41}} >$ must be zero at some point in parameter space in between. Thus, the conditions for Wilks' theorem are not given in $\Delta m^2_{41}, \sin^2 2\theta_{14}$ space i.e. the behavior of $-2\ln(\lambda(\vec{x})) = -2\Delta\ln(\mathcal{L})$ is a priori unknown and must be obtained from pseudo experiments.

However, Wilks' theorem holds in $\sin^2 2\theta_{14}$ space for a fixed specific Δm^2_{41} in the region in which Double Chooz is sensitive [14]. Hereby, the simple hypothesis is

$$H_0 : \{\sin^2 2\theta_{14} = X', \Delta m^2_{41} = Y'\,\mathrm{eV}^2|X', Y' \in \mathbb{R}, 0 \leq X \leq 1\} \quad , \tag{4.35}$$

while the alternative hypothesis H_1 is

$$H_1 : \{0 \leq \sin^2 2\theta_{14} \leq 1, \Delta m^2_{41} = Y', \mathrm{eV}^2|Y' \in \mathbb{R}\} \quad . \tag{4.36}$$

Here, H_1 and H_0 yield the test statistics:

$$TS_{1\mathrm{D}} := -2\ln\lambda(\vec{x}) = -2\ln\left(\frac{\sup\mathcal{L}(\sin^2 2\theta_{14} = X', \Delta m^2_{41} = Y'\,\mathrm{eV}^2|\vec{x})}{\sup\mathcal{L}(\sin^2 2\theta_{14}, \Delta m^2_{41} = Y'\,\mathrm{eV}^2|\vec{x})}\right) \quad . \tag{4.37}$$

TS_{1D} follows a Chi-square distribution with one degree of freedom if H_1 is true [127] [14]. Examples are shown in section 4.4.1.

4.3.3 Sterile Asimov-Wilks sensitivity

The so called *signal exclusion sensitivity* describes the parameter space that is expected to be excluded assuming that the null hypothesis (i.e. $\sin^2 2\theta_{14} = 0.0$) is true. If the distribution of the TS is known, it can be obtained by utilizing a two dimensional scan of -2 $\ln(\mathcal{L})$ in $\sin^2 2\theta_{14}$ and Δm^2_{14} on Asimov data (cf. section 4.3.1) with $\sin^2 2\theta_{14} = 0.0$. It follows a Chi-square distribution if Wilks' theorem holds. 95% confidence level corresponds to $-2\Delta\ln(\mathcal{L})$ =3.84 for one degree(s) of freedom resp to $-2\Delta\ln(\mathcal{L})$ =5.99 for two degree(s) of freedoms concerning a two sided parameter space centered around the central value. However, Wilks' theorem does not hold if Δm^2_{41} is free (cf. section 4.3.2, cf. [14]) and the

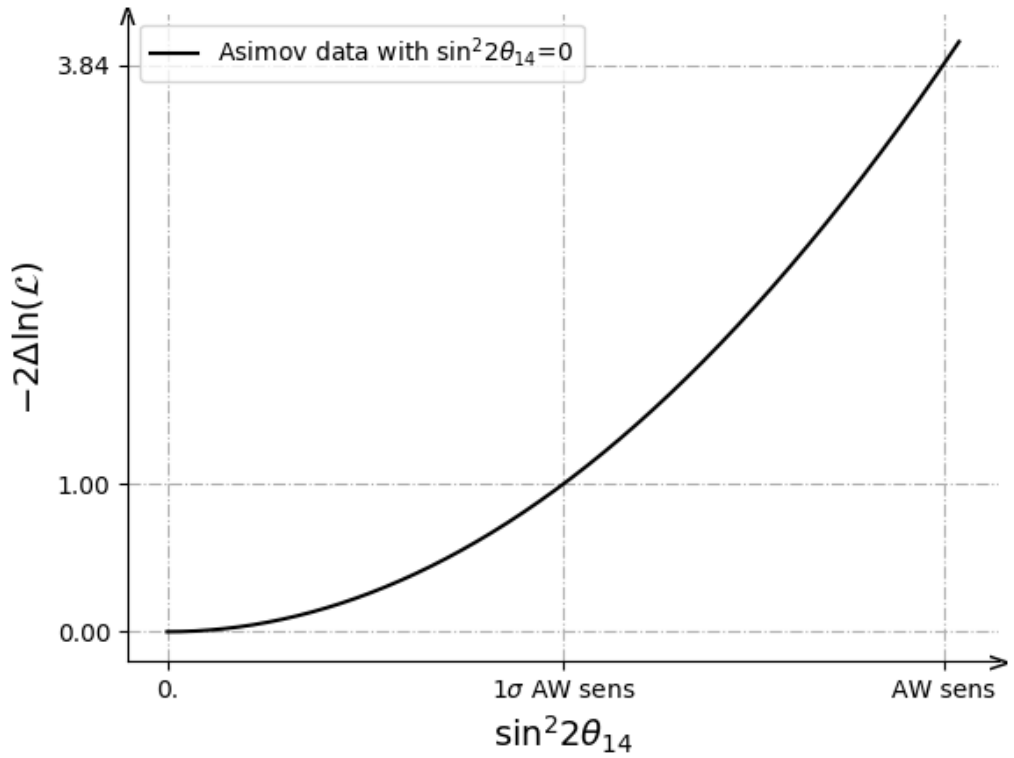

Figure 4.14: Sketch of scan of $-2\ln(\mathcal{L})$ for Asimov data with $\sin^2 2\theta_{14} = 0$: $-2\Delta\ln(\mathcal{L})$ versus $\sin^2 2\theta_{14}$ where $-2\Delta\ln(\mathcal{L})$ is the difference between $-2\ln(\mathcal{L})$ for the given $\sin^2 2\theta_{14}$ and the minimum of $-2\ln(\mathcal{L})$. The 1σ AW sensitivity is that $\sin^2 2\theta_{14}$ for which $-2\Delta\ln(\mathcal{L}) = 1$ and the AW sensitivity at 95% confidence level is that $\sin^2 2\theta_{14}$ for which $-2\Delta\ln(\mathcal{L}) = 3.84$, as indicated on the x-axis.

distribution of the test statistics is only known a priori if Δm^2_{41} is fixed [14]. Nevertheless, it will be shown later, that the actual sensitivity indeed is proportional to a quantity refereed to as *Asimov-Wilks sensitivity* (AW sensitivity) in the following. The AW sensitivity is defined as that value of $\sin^2 2\theta_{14}$ for which a scan of $-2\ln(\mathcal{L})$ on Asimov data with true $\sin^2 2\theta_{14} = 0$ yields $-2\Delta\ln(\mathcal{L})$ =3.84. Similarly, the term 1σ AW sensitivity is used for that value of $\sin^2 2\theta_{14}$ for which an likelihood scan on Asimov data with true $\sin^2 2\theta_{14} = 0$ yields $-2\Delta\ln(\mathcal{L})$ =1. Both definitions are sketched in figure 4.14[III]. As the calculation of the actual sensitivity is too computing expensive to be done for all systematics studies, the AW sensitivity will be used for validation instead.

Figure 4.15 shows the AW sensitivity at 95% confidence level. The AW sensitivity for one degree(s) of freedom (dof) is shown in solid black, while the 1σ AW sensitivity for one dof is shown in solid green. The $\sin^2 2\theta_{14}$ steps in the grid used for the scan have a width of

[III]The AW sensitivity is rather a discovery potential with extremely low confidence level than the actual sensitivity, following the definition by [109]. One can also understand the AW sensitivity as the expected 95% allowed region around the central value $\sin^2 2\theta_{14} = 0$, which would only make sense to give if the existence of a sterile neutrino was known from external input. Otherwise an upper limit will be provided in case the measurement is consistent with the no sterile hypothesis.

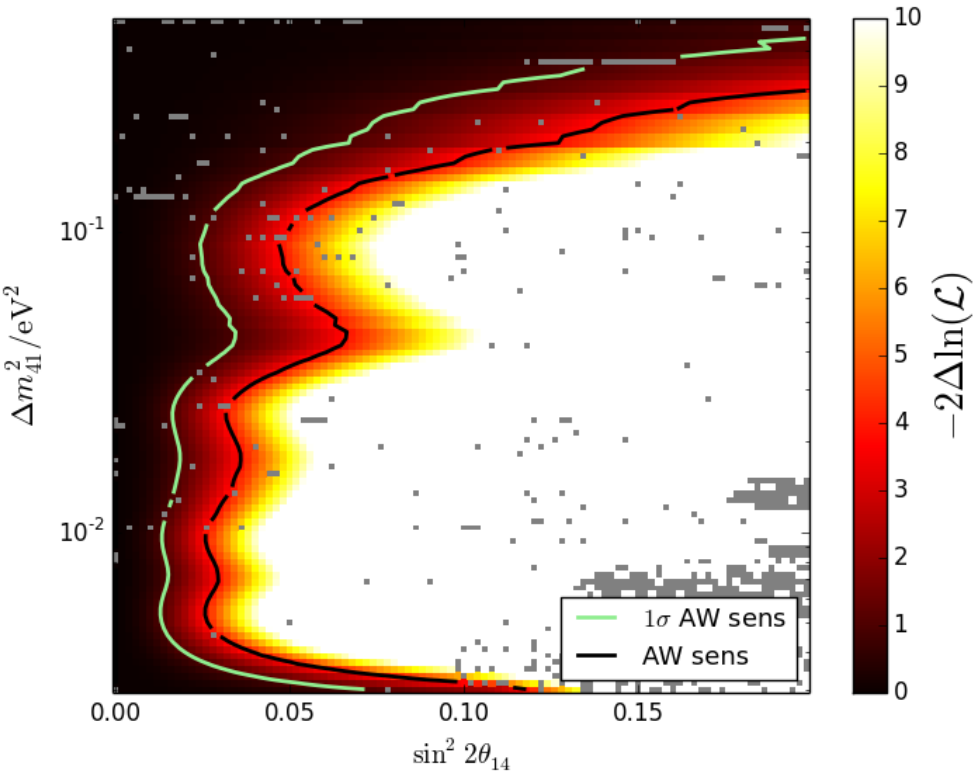

Figure 4.15: AW sensitivity at 95% confidence level with the LLH-FF approach. The black solid line shows the AW sensitivity for one degree of freedom, the solid green line the $1\,\sigma$ AW sensitivity for one degree of freedom (see text, figure 4.14). The color scale shows $-2\Delta\ln(\mathcal{L})$ w.r.t. the minimum $-2\ln(\mathcal{L})$ from this plot. Gray shaded areas mark missing data[a].

[a]Isolated missing data points are due to technical not fit related computing issues (such as that the machine on which a fit was running got switched off). The number of fits that did not converge due to EDM above max is around 0.3% and clustered at large $\sin^2 2\theta_{14}$ and small Δm^2_{41}.

0.002. The color scale represents $-2\Delta\ln(\mathcal{L})$ w.r.t. the minimum $-2\ln(\mathcal{L})$ from this plot. Gray shaded areas mark missing data[IV].

The lack of sensitivity around $\Delta m^2_{41} \approx m^2_{ee}$ is due to ambiguity between $\sin^2 2\theta_{41}$ and $\sin^2 2\theta_{13}$, below Double Chooz is not sensitive because the oscillation baselines are to large for both detectors (cf. section 4.2.3). For high $\Delta m^2_{41} \gtrsim 0.3\,\mathrm{eV}^2$ the fast oscillations get washed out by limited energy resolution in both detectors. Thus, Double Chooz is not sensitive here. It is clearly not intended to apply the MC-Data fit to the sterile analysis in the near or intermediate future due to the reactor neutrino anomaly (cf. section 1.4.1) and the spectral distortion (cf. section 1.4.4). The AW sensitivity for the MC-Data fit approach is plotted with a solid red line in figure 4.16. It is compared to the AW sensitivity for the MC-Data fit approach (solid black line). One can see that the AW sensitivity for the MC-Data fit approach is always better than for the LLH-FF approach. That is because the MC-Data fit approach has the ability to compare the predicted neutrino rate in near and far detector to the measurements. Therefore, the LLH-FF approach does not provide any sensitivity for large $\Delta m^2_{41} \geq 0.3\,\mathrm{eV}^2$ since the sterile signature is only a global deficit in all detectors (cf. section 4.2.3). In contrast, the MC-Data approach has the ability to compare that constant global deficit to the prediction. Hence, it provides a constant sensitivity for $\Delta m^2_{41} \geq 0.3\,\mathrm{eV}^2$. Both approaches are not sensitive for $\Delta m^2_{41} \approx |\Delta m^2_{31}|$ due to the ambiguity between $\sin^2 2\theta_{13}$ and $\sin^2 2\theta_{14}$.

It was shown in [73] that the shape of the AW sensitivity is well understood by the cross correlation $\mathrm{corr}_{\mathrm{cross}}(\theta_{14}, \Delta m^2_{41})$ between near and far detector defined as

$$\mathrm{corr}_{\mathrm{cross}}(\theta_{14}, \Delta m^2_{41}) = \frac{\sum_i \Delta N_{\mathrm{ND},i}(\theta_{14}, \Delta m^2_{41}) \cdot \Delta N_{\mathrm{FD},i}(\theta_{14}, \Delta m^2_{41})}{\sqrt{\sum_i [\Delta N_{\mathrm{ND},i}(\theta_{14}, \Delta m^2_{41})]^2}\sqrt{\sum_i [\Delta N_{\mathrm{FD},i}(\theta_{14}, \Delta m^2_{41})]^2}} \tag{4.38}$$

where i runs over all energy bins and

$$\Delta N_{\mathrm{JD},i}(\theta_{14}, \Delta m^2_{41}) = N_{\mathrm{JD},i}(\theta_{14}, \Delta m^2_{41}) - N_{\mathrm{JD},i}(\theta_{14} = 0., \Delta m^2_{41}) \tag{4.39}$$

and $N_{\mathrm{JD},i}(\theta_{14}, \Delta m^2_{41}), \mathrm{J} = \mathrm{N}, \mathrm{F}$ is the mean expected number of inverse beta decay candidates in energy bin i [73]. This cross correlation may be identified as a quantity related to the inner product of to vectors $\vec{x}$ and $\vec{y}$. For the angle between those two vectors $\cos(\phi) = \frac{\vec{x}\cdot\vec{y}}{|\vec{x}||\vec{y}|}$ applies.

In order to identify the systematics due to interference of the two reactor baselines, the AW sensitivity was calculated where the baseline of all neutrinos detected in the near (far) detector from reactor B1 was changed to the near (far) detector B2 baseline in the oscillation progress of pseudo data generation and fit. Total number of neutrinos and unoscillated neutrino energy spectrum were not modified. Figure 4.17 shows the corresponding scan of $-2\ln(\mathcal{L})$ and the AW sensitivity. Compared to the nominal AW sensitivity the dip around $\Delta m^2_{41} \approx 0.05\,\mathrm{eV}^2$ is not present anymore (see figure 4.17, cf. figure 4.15). The overall AW sensitivity is better in this hypothetical situation. However, this does not mean that the overall sensitivity would be better if there was only one reactor at Chooz power plant since that would also reduce the overall statistics in the usual dataset but probably also increase the statistics in the Off-Off dataset.

[IV] cf. footnote *a* for text in caption of figure 4.15

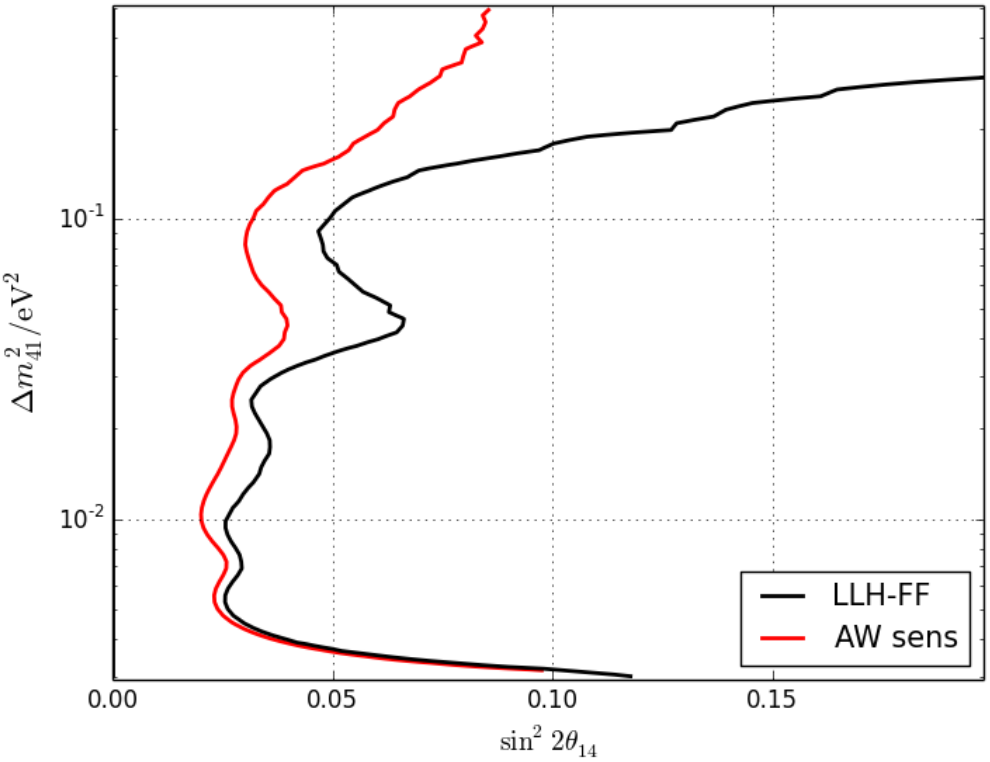

Figure 4.16: Comparison of AW sensitivity at 95% CL between MC-Data approach and LLH-FF approach. Δm^2_{41} is plotted versus $\sin^2 2\theta_{14}$. The black solid line shows the AW sensitivity for the LLH-FF approach, the red line for the LLH MC-Data approach. Note that no fit of experimental data with the MC-Data fit is planned.

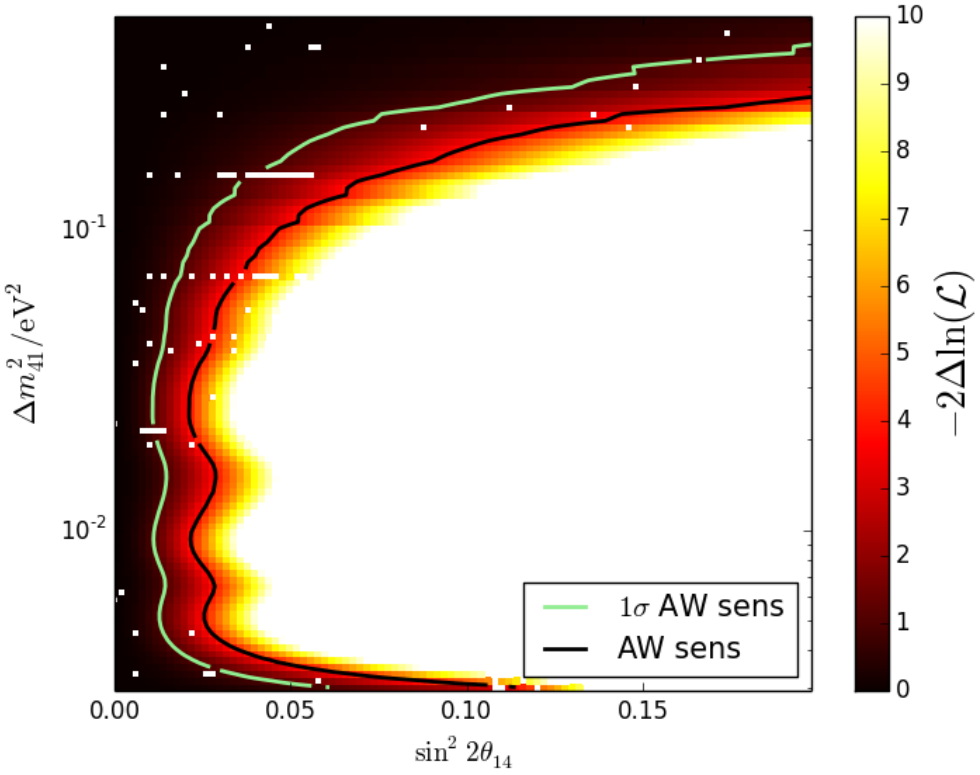

Figure 4.17: Two dimensional scan of $-2\ln(\mathcal{L})$ in $\sin^2 2\theta_{14}$ (x-axis) and Δm^2_{41} (y-axis) on Asimov data where the baseline of neutrinos from B1 was changed to the B2 baseline (i.e. the measured number of neutrinos in near and far detector was conserved (see text)). The color scale shows the $-2\Delta\ln(\mathcal{L})$ w.r.t. to the minimum of $-2\Delta\ln(\mathcal{L})$. The 1σ AW sensitivity is solid green line. The solid black line marks the AW sensitivity at 95% confidence level. Gray shaded areas mark missing data.

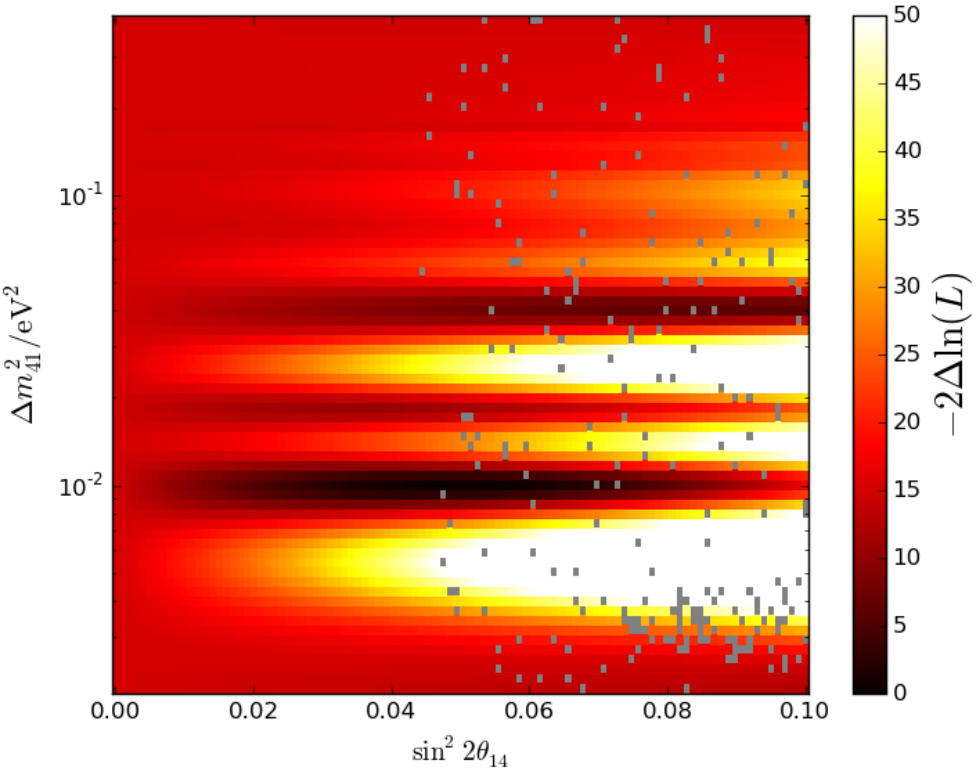

Figure 4.18: Two dimensional scan of $-2\ln(\mathcal{L})$ in $\sin^2 2\theta_{14}$(x-axis) and Δm^2_{14}(y-axis) of Asimov data with $\sin^2 2\theta_{14} = 0.05$ and $\Delta m^2_{14} = 0.01\,\mathrm{eV}^2$. $-2\Delta\ln(L)$ is represented by the color bar where $\Delta\ln(L) = \ln(\mathcal{L}) - \ln(\mathcal{L}_{\max})$ is the difference of the natural logarithm of the likelihood to the natural logarithm of the maximum likelihood. Gray shaded areas mark missing data. Figure 4.19 shows the same data with a different color scale such that the minimum is more obvious.

4.3.4 Data challenges

A so called *data challenge* is a method to test the full chain of analysis in a representative computer experiment. For a *data challenge* pseudo data is calculated using known input values. This pseudo data is inserted in the fit algorithm in order to test if the algorithm can recover the inserted values. Instead of mock data Asimov data may be inserted as well. The fit should recover the inserted values exactly except for a negligible deviation due to limited numerical accuracy.

Figure 4.18 shows an example of such a data challenge with Asimov data. Here, Asimov data with $\sin^2 2\theta_{14} = 0.05$ and $\Delta m^2_{14} = 0.01\,\mathrm{eV}^2$ has been generated. Figure 4.19 displays the same scan on $-2\ln(\mathcal{L})$ with different scaling of the z-axis. Figures 4.18 and 4.19 illustrate that the inserted values are recovered. Moreover, it can be seen in figure 4.18 that there are several local minima. Indeed, due to the Nyquist-Shannon sampling theorem there are always local minima in the signal region [115] (cf. section 4.3.2).

The data challenge presented above has two disadvantages: First, the Asimov data is calculated by the same software that does the fit. Second, the person running the fit knows the true value. Thus, a blind data challenge has been done, i.e. the datasets were

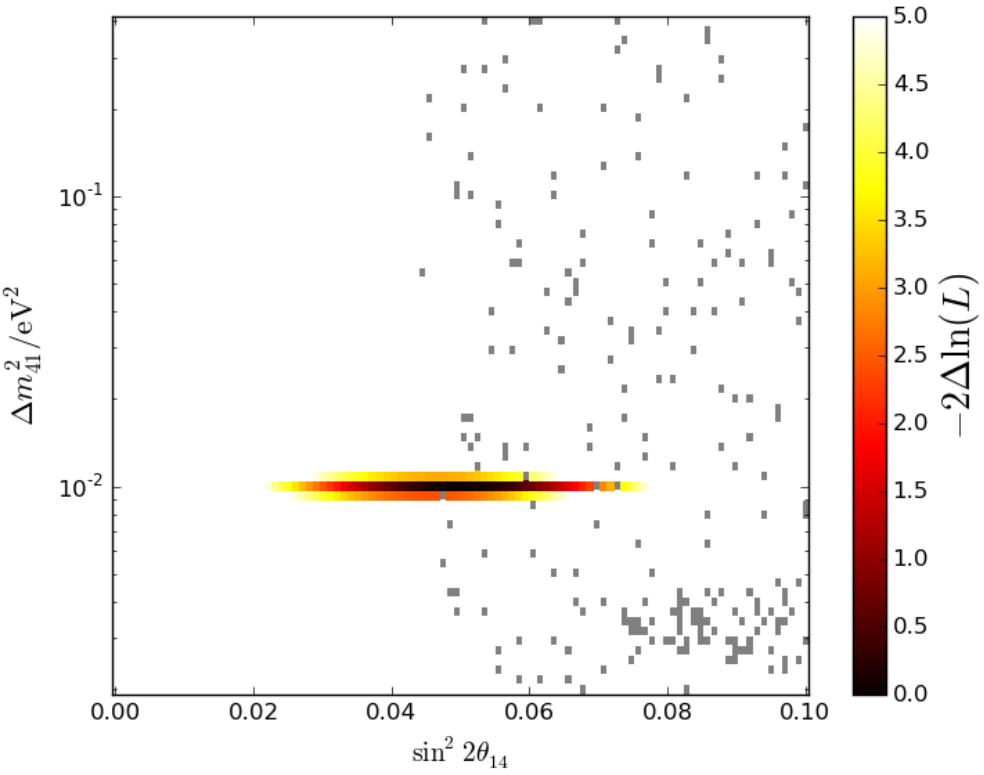

Figure 4.19: Two dimensional scan of $-2\ln(\mathcal{L})$ in $\sin^2 2\theta_{14}$(x-axis) and Δm^2_{14}(y-axis) of Asimov data with $\sin^2 2\theta_{14} = 0.05$ and $\Delta m^2_{14} = 0.01\,\mathrm{eV}^2$. $-2\Delta\ln(\mathcal{L})$ is represented by the color bar where $\Delta\ln(\mathcal{L}) = \ln(\mathcal{L}) - \ln(\mathcal{L}_{\max})$ is the difference of the natural logarithm of the likelihood to the natural logarithm of the maximum likelihood. Gray shaded areas indicate missing data. Figure 4.18 shows the same data with a different color scale.

Table 4.12: Summary of the blind data challenge. The first column indicates the number of the dataset, the second the indicates which figures show the result of the corresponding $-2\ln(\mathcal{L})$ scan, the third one the best fit value of $\sin^2\theta_{13}$, the fifth the bin width in $\sin^2\theta_{13}$, the sixth one the fitted $\Delta m^2_{41}/\mathrm{eV}^2$ and the last one the true $\Delta m^2_{41}/\mathrm{eV}^2$.

#	plots	$\sin^2\theta_{14,\mathrm{fit}}$	bin width	$\sin^2\theta_{14,\mathrm{true}}$	$\Delta m^2_{41,\mathrm{fit}}\mathrm{eV}^2$	$\Delta m^2_{41,\mathrm{true}}\mathrm{eV}^2$
1	C.4, C.3	0.0394	0.0010	0.040	0.050	0.0500
2	C.6, C.5	0.0808	0.0010	0.080	0.16	0.1600
3	4.20, C.7	0.0807	0.0010	0.080	0.012	0.0120
4	C.9, C.8	0.0285	0.0020	0.030	0.0055	0.0055
5	C.11, C.10	0.0806	0.0010	0.080	0.045	0.0450

provided by another person[V] without letting the analyzing person know which values were inserted. This has been done with an algorithm which is independent from the likelihood fit in this work (i.e. the datasets are not generated in the same way as they are produced). Five Asimov datasets with unknown parameters have been provided. Two dimensional scans of $-2\ln(\mathcal{L})$ have been performed on these Asimov datasets since there is usually more than one local minimum (cf. previous paragraph).

Here, dataset 3 is taken as an example. A first scan was used to identify local minima (cf. figure C.7), second a scan with a finer binning has been done around the deepest local minimum and is shown in figure 4.20. $\sin^2 2\theta_{14}$ is on the x-axis, Δm^2_{41} on the y-axis the difference in $2\ln(\mathcal{L})$ is shown by the color scale. The minimum was found at $\sin^2 2\theta_{14} = 0.0807$ with a bin width of 0.0010 and $\Delta m^2_{41} = 0.012\,\mathrm{eV}^2$ and is marked with a green star. The true inserted values were $\sin^2 2\theta_{14} = 0.080$ and $\Delta m^2_{41} = 0.012\,\mathrm{eV}^2$. Thus, they have been recovered. All true values used in the blind data challenge are indicated by a star in figure 4.21 and numbered. All of these points have been recovered as summarized in table 4.12. The corresponding plots of the scans of $-2\ln(\mathcal{L})$ can be found in figures C.4, C.3, C.6, C.5, 4.20, C.7, C.9, C.8, C.11 and C.10. Table 4.12 indicates which plots belong to which dataset.

4.3.5 Spectral distortion bias testing

As mentioned in section 1.4.4, the shape of the reactor flux observed with reactor flux experiments does not meet the theoretical prediction very well.

In order to test the independence of the fit result from the original reactor Monte Carlo, Asimov data with artificial distortions have been created. Next, a two dimensional raster scan in $\sin^2 2\theta_{14}$ and Δm^2_{41} has been done with those datasets.

The modeled spectral distortion was officially used in order to probe the stability of the $\sin^2 2\theta_{13}$ fits. It was modeled by fitting two Gaussians to the spectral distortion observed by Daya Bay. The datasets were provided by Tsunayuki Matsubara. Figures 4.22, 4.23 and 4.24 show the distorted Asimov datasets for FD1-On, FD2 and ND.

Figure 4.25 shows the result of the two dimensional raster scan of these datasets, where $\sin^2 2\theta_{14}$ is on the x-axis, Δm^2_{41} is on the y-axis and $-2\Delta\ln(\mathcal{L}) = 2\cdot(\ln(\mathcal{L}) - \ln(\mathcal{L}_{\max}))$ is

[V] Thiago J.C. Bezerra

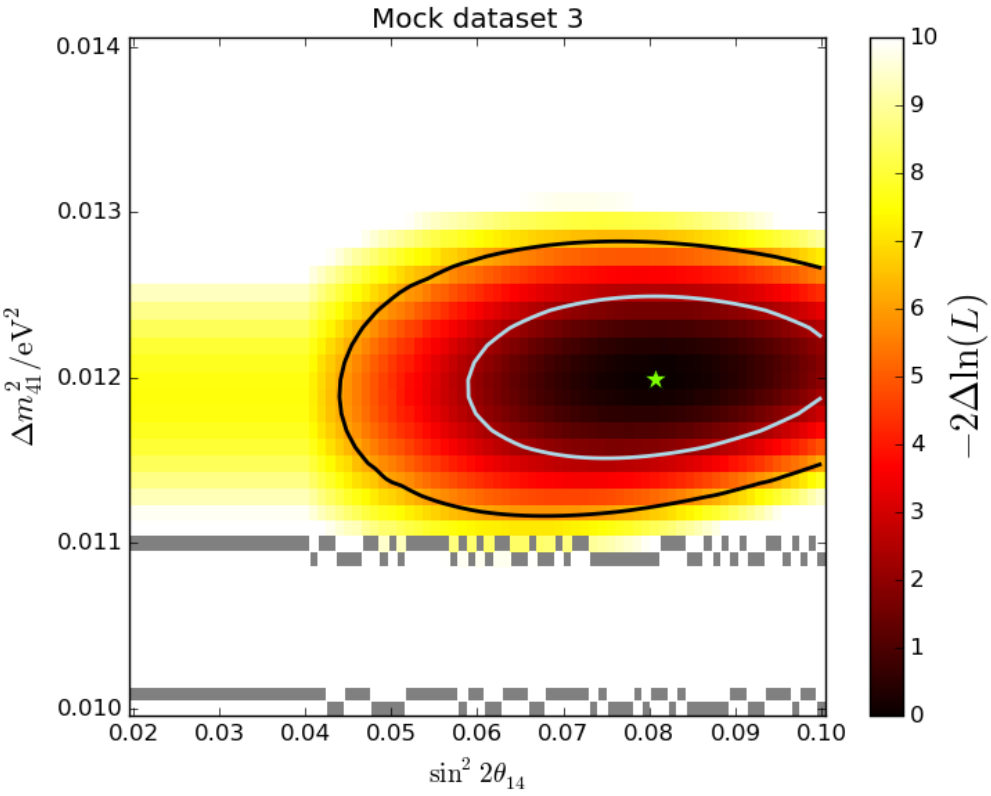

Figure 4.20: Two dimensional scan of $-2\Delta\ln(\mathcal{L})$ in $\sin^2 2\theta_{14}$ (x-axis) and Δm^2_{41} (y-axis) of the third Asimov data sample. where $-2\Delta\ln(L)$ is represented by the color bar. $\Delta\ln(L) = \ln(\mathcal{L}) - \ln(\mathcal{L}_{\max})$ is the difference of the natural logarithm of the likelihood to the natural logarithm of the maximum likelihood. The 1σ (2σ) region for the local ($\sin^2 2\theta_{14}$, Δm^2_{41}) range in which Wilks' theorem holds is marked by the light blue (black) line.

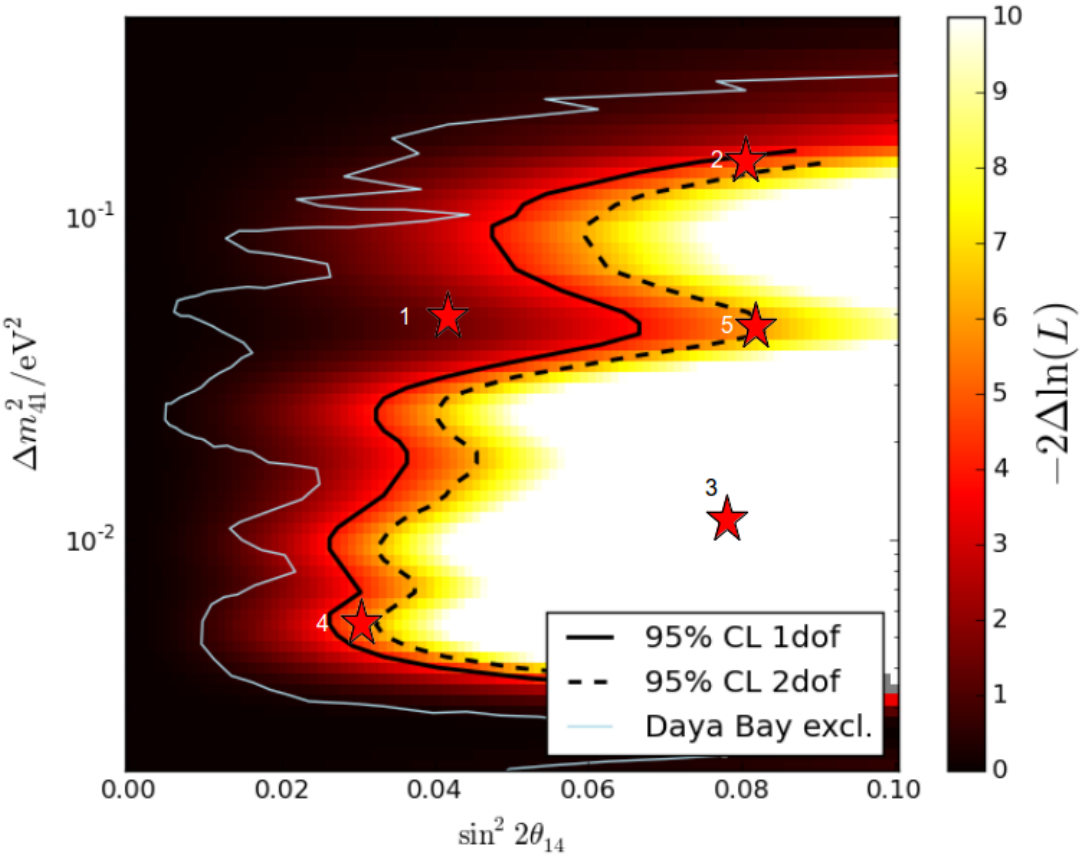

Figure 4.21: AW sensitivity at 95% confidence level with the LLH-FF approach. The black solid line shows the one degree of freedom case, the dashed line the two degree of freedom case. The Daya Bay 95% C.L. exclusion limit from [21] is shown in light blue for comparison. The true values inserted in the blind data challenge are marked with starts and numbered. The results of the blind data challenge are summarized in table 4.12.

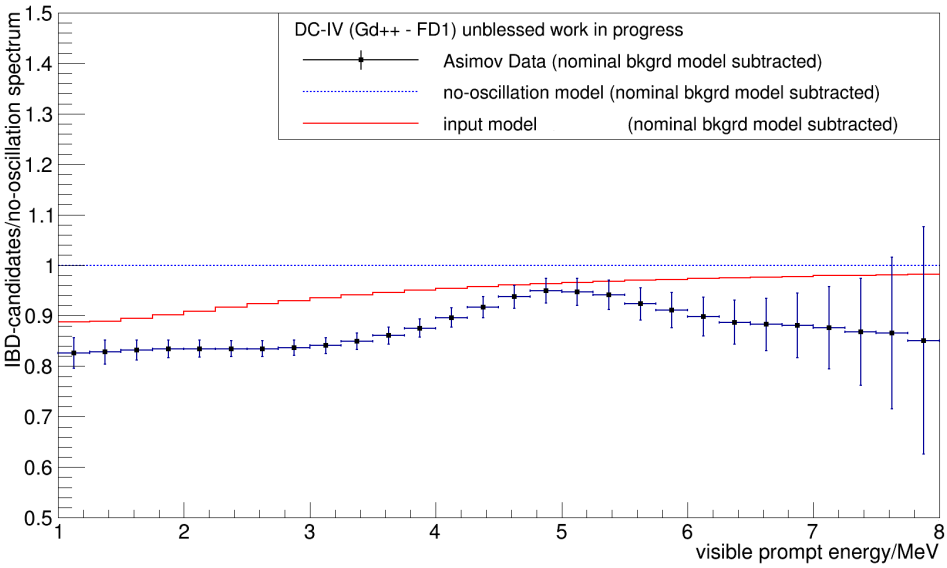

Figure 4.22: FD1-On Asimov data with the spectral distortion used to test the θ_{13} fit and the sterile fit. The nominal background subtracted number of inverse beta decay candidates in this dataset is shown relative to the nominal prediction (without neutrino oscillation and spectral distortion) versus visible energy of the prompt event by the data points. The red line indicates the nominal model assuming $\sin^2 2\theta_{14} = 0$ and $\sin^2 2\theta_{13} = 0.119$.

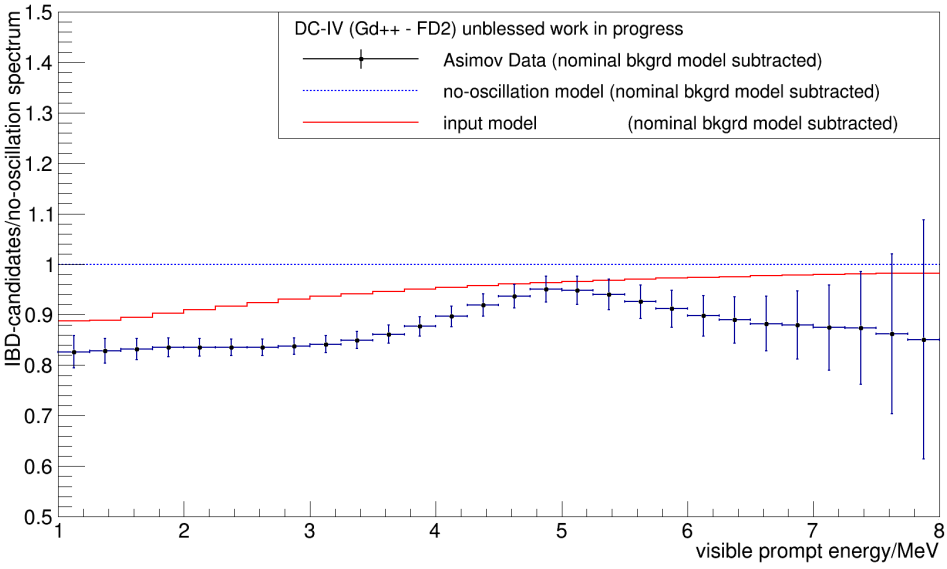

Figure 4.23: FD2 Asimov data with the spectral distortion used to test the θ_{13} fit and the sterile fit. The nominal background subtracted number of inverse beta decay candidates in this dataset is shown relative to the nominal prediction (without neutrino oscillation and spectral distortion) versus visible energy of the prompt event by the data points. The red line indicates the nominal model assuming $\sin^2 2\theta_{14} = 0$ and $\sin^2 2\theta_{13} = 0.119$.

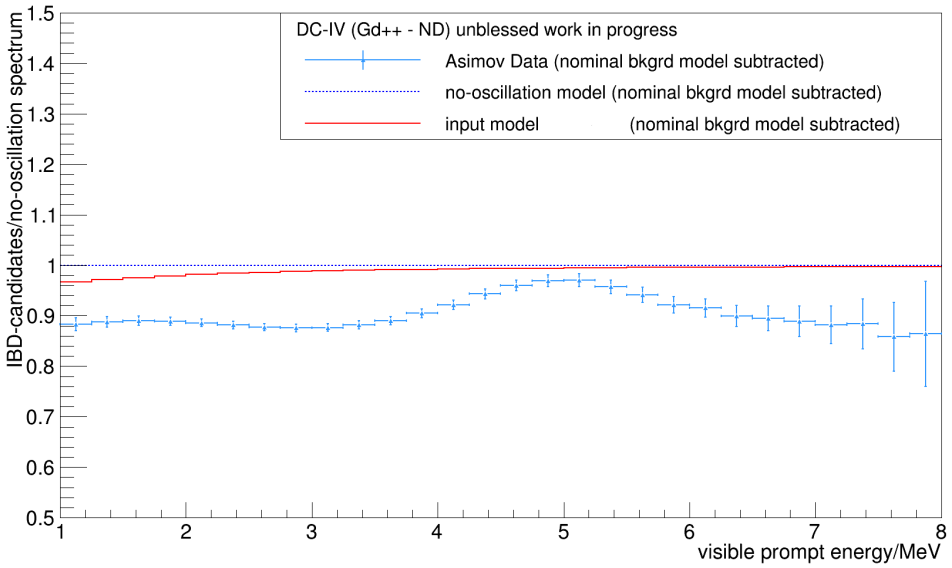

Figure 4.24: ND Asimov data with the spectral distortion used to test the θ_{13} fit and the sterile fit. The nominal background subtracted number of inverse beta decay candidates in this dataset is shown relative to the nominal prediction (without neutrino oscillation and spectral distortion) versus visible energy of the prompt event by the data points. The red line indicates the nominal model assuming $\sin^2 2\theta_{14} = 0$ and $\sin^2 2\theta_{13} = 0.119$.

represented by the color bar. Here, $\mathcal{L}$ is the likelihood value at the specific $\left(\sin^2 2\theta_{14}, \Delta m^2_{41}\right)$ position and $\mathcal{L}_{\max}$ is the maximum likelihood value. One can see that the fit does not a minimum for $\sin^2 2\theta_{14} \neq 0$. Figure 4.26 compares the 95 % confidence level AW sensitivities (1 dof) obtained from the datasets with (dashed green) and without distortion (solid blue) to each other. Both AW sensitivitys match well except for a small difference due to the statistics being slightly different.

4.3.6 Systematics breakdown

Figure 4.27 shows the two dimensional Stat+1 test AW sensitivity at 95% confidence level (1 dof), where Δm^2_{41} is on the y-axis and $\sin^2 2\theta_{14}$ is on the x-axis. Default (solid black), statistics only (solid blue), stat+detection (dashed red), stat+reactor (dashed dotted violet), stat+energy (dashed dotted cyan) and stat+θ_{13} (dashed green) 95% CL AW sensitivity (1 dof) AW sensitivity are plotted.

It can be seen that the statistics only AW sensitivity is very close to the default AW sensitivity in most of the Δm^2_{41} region.

The statistics only AW sensitivity assumes that θ_{13} is known to infinite precision. This is a hypothetical assumption since the Double Chooz experiment cannot measure θ_{13} and θ_{14} independently. Therefore, a sterile analysis should always do a simultaneous fit of θ_{13} and θ_{14}. However, only for $\Delta m^2_{41} \approx \Delta m^2_{31}$ the difference between Stat+θ_{13} and Stat. only sensitivity is significant. The difference between stat only AW sensitivity and Stat+reactor and Stat+detection AW sensitivity is not significant for any Δm^2_{41}. The energy has some

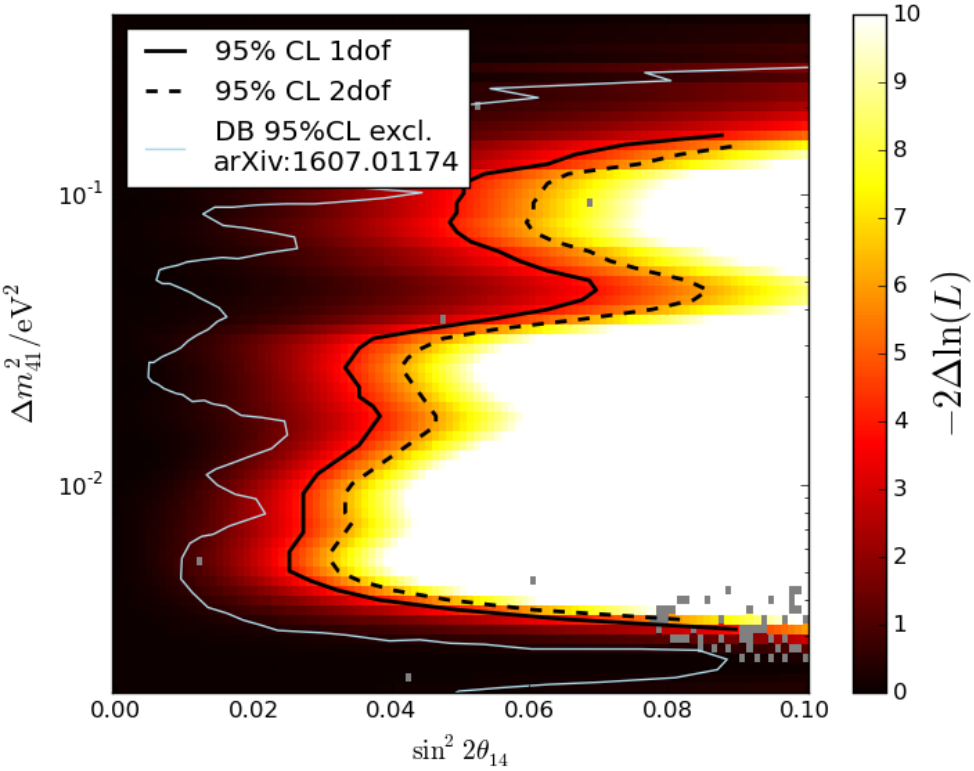

Figure 4.25: Two dimensional scan of $-2\ln(\mathcal{L})$ in $\sin^2 2\theta_{14}$ (x-axis) and Δm^2_{41} (y-axis) of the Asimov data shown in figures 4.22, 4.23 and 4.24 where $-2\Delta\ln(\mathcal{L})$ is represented by the color bar. $\Delta\ln(\mathcal{L}) = \ln(\mathcal{L}) - \ln(\mathcal{L}_{\mathrm{max}})$ is the difference of the natural logarithm of the likelihood to the natural logarithm of the maximum likelihood. The 95% CL AW sensitivity for 1 dof (solid) and 2 dof (dashed) is drawn as well as the Daya Bay 95% C.L. exclusion limit from [21] (solid light blue). Gray shaded areas mark missing data.

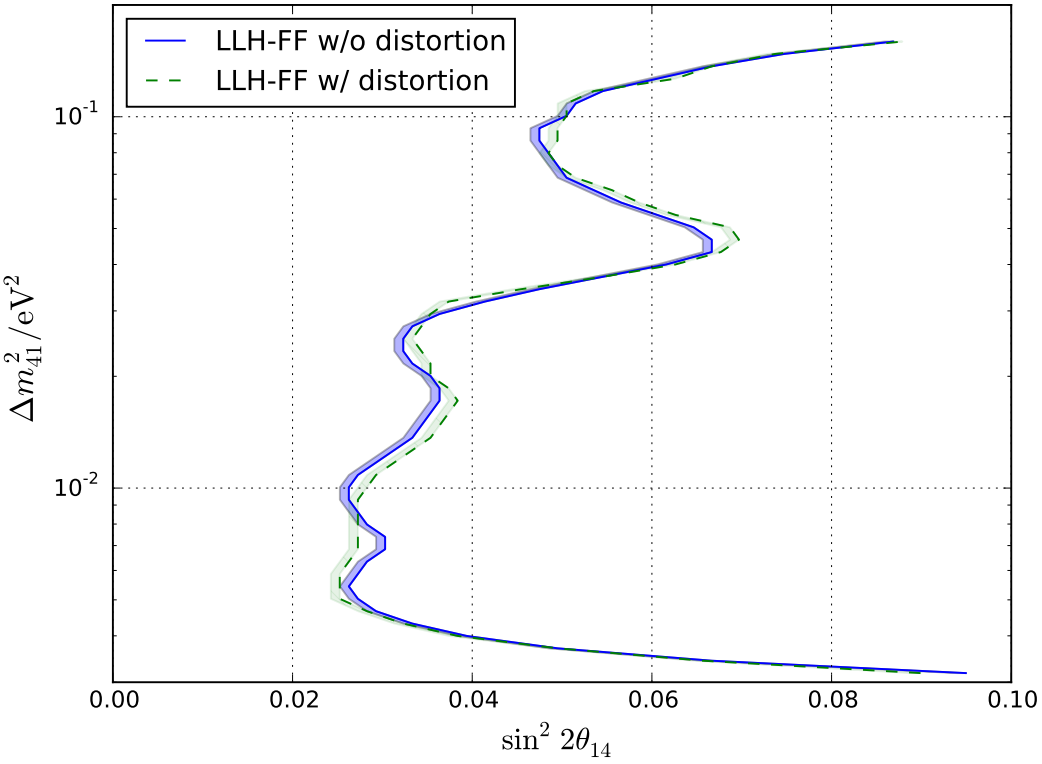

Figure 4.26: AW sensitivity with spectral distortion (dashed green) and nominal AW sensitivity (solid blue). The corresponding Asimov data with distortion is shown in figures 4.22, 4.23 and 4.24. The colored regions indicate the accuracy of the calculation.

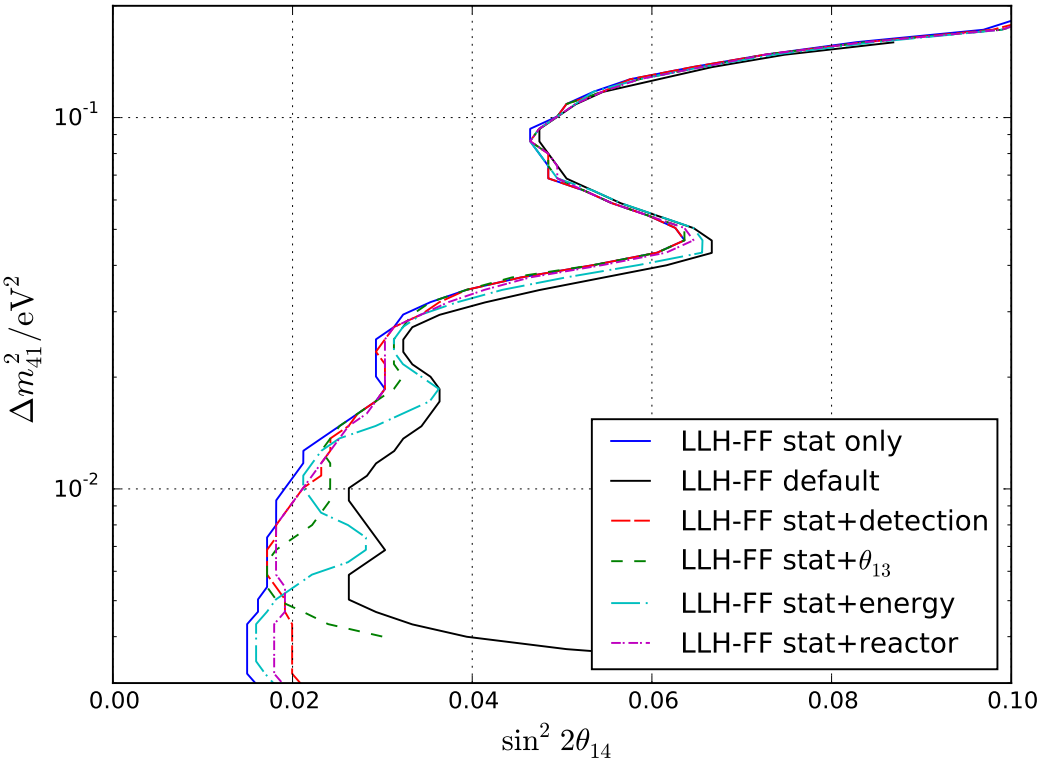

Figure 4.27: Sterile systematics breakdown: Comparison of default (solid black), statistics only (solid blue), stat+detection (dashed red), stat+ reactor (dashed dotted violet), stat+energy (dashed dotted cyan) and stat+ θ_{13} (dashed green) AW sensitivity (1 dof) at 95% confidence level. Plotted is Δm^2_{41} versus $\sin^2 2\theta_{14}$.

impact for $\Delta m^2_{41} < 0.01\,\mathrm{eV}^2$ which can be understood by the correlation between parameters modeling the reactor flux and energy as pointed out in section 4.3.1.

In addition to the two dimensional Stat+1 test, one dimensional Stat+1 and N-1 tests have been done for specific Δm^2_{41} (0.1000, 0.0500, 0.0300, 0.0200, 0.0100 and 0.0073 eV^2). The results are summarized in table 4.13. The calculation of the systematical uncertainties (cf. equation (4.25), table 4.13) shows that the fit uncertainty is statistically dominated for $\Delta m^2_{41} \geq 0.01\,\mathrm{eV}^2$.

In addition to the two dimension stat+1 test, one dimensional stat+1 and N-1 tests have been done for some $\Delta m^2_{41}/\mathrm{eV}^2$ where $\sin^2 2\theta_{14} = 0.1$. The results are presented in table 4.13. Note that the values have an uncertainty of around two percent. One can take from the table that for $\Delta m^2_{41} > 0.01\,\mathrm{eV}^2$ the statistical uncertainty is dominant. This is a direct consequence from the fact, that Double Chooz was optimized for the mass squared difference $\Delta m^2_{ee} \approx 0.0025\,\mathrm{eV}^2$. The one dimensional systematics breakdown also demonstrates that background and Δm^2_{ee} have almost no impact.

Table 4.13: One dimensional systematics breakdown in $\sin^2 2\theta_{14}$ for $\sin^2 2\theta_{14} = 0.1$ and several Δm^2_{41}. The values have a uncertainty of around 2%.

$\sin^2 2\theta_{14}$ AW sensitivity (for $\sin^2 2\theta_{14} = 0.1$)												
$\Delta m^2_{41}/\text{eV}^2$	0.1000	r	0.0500		0.0300	r	0.0200	r	0.0100	r	0.0073	r
1. Default	0.0240	1.00	0.0314	1.00	0.0182	1.00	0.0169	1.00	0.0121	1.00	0.0140	1.00
2. Stat.	0.0237	0.99	0.0305	0.97	0.0161	0.88	0.0143	0.85	0.0085	0.70	0.0077	0.55
3. Sys. :	0.0038	0.16	0.0075	0.24	0.0085	0.47	0.0090	0.53	0.0087	0.71	0.0117	0.84
4. N-1												
4.1 Det.	0.0240		0.0314		0.0182		0.0169		0.0120		0.0139	
4.2 Reactor	0.0238		0.0313		0.0180		0.0168		0.0120		0.0138	
4.3 BG	0.0239		0.0314		0.0181		0.0169		0.0121		0.0139	
4.4 Energy	0.0238		0.0311		0.0172		0.0156		0.0115		0.0105	
4.6 θ_{13}	0.0240		0.0314		0.0181		0.0168		0.0110		0.0135	
4.7 Δm^2_{atm}	0.0240		0.0315		0.0182		0.0169		0.0121		0.0140	
4.8 Δm^2_{41}	0.0240		0.0324		0.0181		0.0169		0.0121		0.0140	
5. Stat+1												
5.1 Det.	0.0237		0.0306		0.0166		0.0144		0.0094		0.0077	
5.2 Reactor	0.0237		0.0308		0.0167		0.0145		0.0093		0.0079	
5.2 BG	0.0237		0.0308		0.0163		0.0145		0.0086		0.0078	
5.3 Energy	0.0238		0.0311		0.0170		0.0167		0.0093		0.0132	
5.5 θ_{13}	0.0237		0.0305		0.0164		0.0148		0.0111		0.0091	
5.6 Δm^2_{atm}	0.0237		0.0306		0.0161		0.0143		0.0086		0.0077	
5.7 Δm^2_{41}	0.0237		0.0306		0.0161		0.0143		0.0086		0.0077	

4.4 Test statistics and sensitivity

This section describes the sensitivity calculation. In order to do so, first the test statistic used to quantify the agreement with the no-sterile hypothesis is discussed. Next, the test statistics with sterile signal is introduced. Finally, the sensitivity calculation is presented.

4.4.1 No-sterile test statistics

As mentioned in section 4.3.2, Wilks' theorem does not hold for the sterile analysis with free parameters $\sin^2 2\theta_{14}$ and Δm^2_{41} in general. This means that the distribution of the test statistics of type TS_{2D} (cf. equation (4.34)) is a priori unknown [14]. In principle, this problem can be solved by Monte Carlo simulations (cf. section 4.3.2). Unfortunately, for each pseudo experiment, a full scan would need to be done while one scan takes at least 100 – 200 central processing unit (CPU)-hours which means that a solution via Monte Carlo simulations becomes practically impossible.

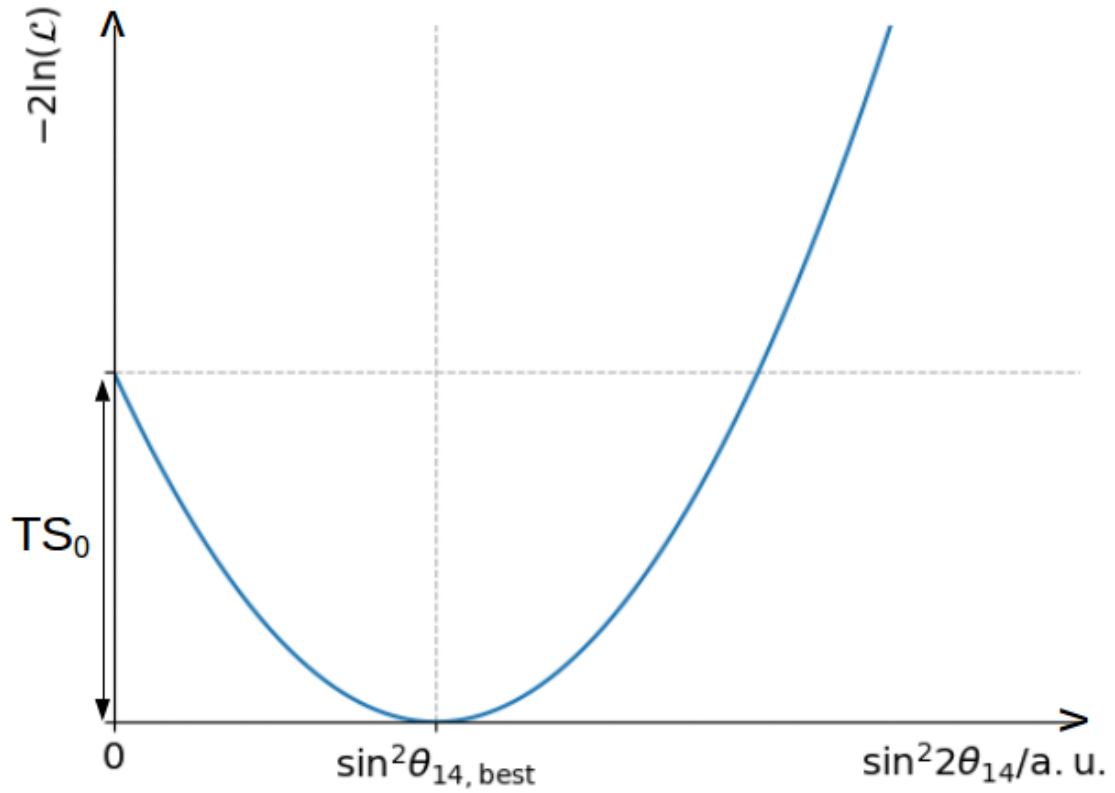

Figure 4.28: Sketch of the definition of the background test statistics from equation (4.40a): $-2\ln(\mathcal{L})$ versus $\sin^2 2\theta_{14}$ in arbitrary units for a given dataset. Here, $-2\ln\big(\mathcal{L}(\sin^2 2\theta_{14})\big) = \ln\sup(\mathcal{L}(\sin^2\theta_{14} \geq 0)$ i.e. all parameters except $\sin^2 2\theta_{14}$ are optimized. $\sin^2 2\theta_{14,\text{best}}$ labels the best fitting $\sin^2 2\theta_{14}$ for this dataset.

In order to quantify the agreement with the no-sterile hypothesis, the test statistics TS_0 is defined as a special case of $TS_{2\text{D}}$ (cf. equation (4.34)):

$$\text{TS}_0 := -2\ln(\lambda) = -2\ln\left(\frac{\sup(\mathcal{L}(\sin^2\theta_{14} = 0., \Delta m^2_{41}))}{\sup(\mathcal{L}(\sin^2\theta_{14} \geq 0, \Delta m^2_{41} \geq 0))}\right) \tag{4.40a}$$

$$= -2\ln\sup(\mathcal{L}(\sin^2\theta_{14} = 0)) + 2\ln\sup(\mathcal{L}(\sin^2\theta_{14} \geq 0)) \tag{4.40b}$$

$$= \min(-2\ln\mathcal{L}(\sin^2\theta_{14} = 0)) - \min(-2\ln\mathcal{L}(\sin^2\theta_{14} \geq 0)) \tag{4.40c}$$

This definition is illustrated in figure 4.28. TS_0 will be referred to as background test statistics.

The background test statistics was obtained from 390 pseudo experiments. Thereby, Δm^2_{41} was scanned with 100 grid points in order to find the best fit while $\sin^2 2\theta_{14}$ was a free parameter in the fit[VI].

The resulting probability density function (pdf) of the background test statistics from equation (4.40a) is plotted in solid blue in figure 4.29. It does neither follow a χ^2 distribution with dof=1 which is plotted in dashed dotted black, nor a χ^2 distribution with dof=2 shown in dashed red. Strikingly, zero is not the most likely value of the TS and values close to zero are extremely unlikely. but This is a mathematical feature of the likelihood-function:

[VI] except that it was required $0 \leq \sin^2 2\theta_{14} \leq 1$

Any fluctuation of the data will always be described better by a sterile oscillation with free amplitude and frequency than by no a non-sterile oscillation. Mathematically this can be explained as follows:

- There is always more than one minimum of $-2\ln(\mathcal{L})$ (cf. section 4.3.2)
- Close to each of this local minima $-2\ln(\mathcal{L})$ follows a Chi-square distribution
- Dicing random numbers from more than one Chi-square distribution and taking the minimum of this numbers does not yield in a Chi-square distribution

One may understand this being similar to the look elsewhere effect [69][90][14]. There are always multiple minima and only the deepest minimum is selected. For further confirmation and illustration a simple test has been done by dicing random numbers from Chi-square distributions with given number of dofs n_{dof} and selecting the minimum, i.e. producing a distribution of

$$Q(x, M, n_{\mathrm{dof}}) = min\left(\overbrace{\chi^2(x, n_{\mathrm{dof}}), \chi^2(x, n_{\mathrm{dof}}), ..}^{M \text{ times}}\right) \tag{4.41}$$

where $\chi^2(n_{dof})$ is a Chi-square distribution with n_{dof} of freedom. The resulting pdf for 100000 pseudo experiments is displayed in figure 4.30. The dashed dotted black line shows the pdf for $Q(M = 6, n_{\mathrm{dof}})$, the solid blue line shows the average pdf of $Q(M = 3, n_{\mathrm{dof}})$ and $Q(M = 9, n_{\mathrm{dof}})$ and the dashed red line shows the average probability density function for $Q(M = 3, n_{\mathrm{dof}})$, $Q(M = 4, n_{\mathrm{dof}})$,..,$Q(M = 9, n_{\mathrm{dof}})$. These three pdfs are not identical and neither of them matches a Chi-square distribution with n_{dof}=2 which is shown in cyan.

$Q(M, n_{\mathrm{dof}})$ can be written down as

$$Q(x, M, n_{\mathrm{dof}}) = M \cdot \chi 2(n_{\mathrm{dof}}, x) \cdot \left(\int_0^x \chi 2(n_{\mathrm{dof}}, y)dy\right)^{(M-1)} \quad . \tag{4.42}$$

The fit of equation (4.42) with free parameters (M, n_{dof}) to the TS_0 probability density function is shown in figure 4.29. It yields $n_{\mathrm{dof}} = 1.79 \pm 0.44, M = 7.52 \pm 3.02$ with a χ^2/dof of 1.23 i.e. is consistent with $n_{\mathrm{dof}} = 2$ and 2σ consistent with $n_{\mathrm{dof}} = 1$. Fits with fixed $n_{\mathrm{dof}} = 2$ ($n_{\mathrm{dof}} = 1$) are shown in dashed cyan (dashed green). The fit with $n_{\mathrm{dof}} = 2$ describes the probability density function quite good and returns $M = 6.22 \pm 0.34$, $\chi^2/dof = 1.15$ while the fit with $n_{\mathrm{dof}} = 1$ is worse than the two other fits. Thus, taken together, the degrees of freedom seem to be close to two.

4.4.2 Sensitivity

By definition the median 95% confidence level sensitivity $\sin^2 2\theta_{14}^{\mathrm{sens}}$ is that value of $\sin^2 2\theta_{14}$ for which in 95% of cases pseudo experiments will result in a larger best fit background test statistics than the median best fit background test statistics for pseudo experiments with true value $\sin^2 2\theta_{14} = 0$ (called $\sin^2 2\theta_{14}^{\mathrm{med}}$). This definition is sketched in figure 4.32 a). Unfortunately, the behavior of the test statistics in two dimensions is not a priori known (cf. section 4.3.2) and fitting a sufficient number of pseudo experiments in every point of ($\sin^2 2\theta_{14}$, Δm^2_{41}) requires an undoable amount of computing time. this work, the sensitivity is given as a function of Δm^2_{41}.

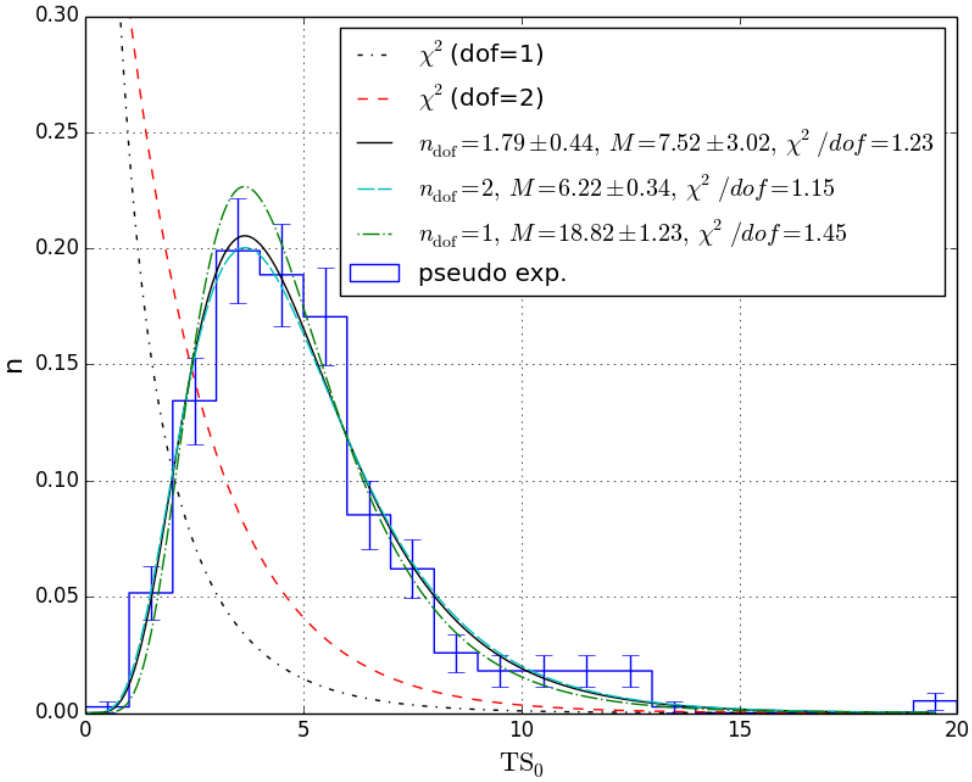

Figure 4.29: Probability density function of the test statistics distribution (cf. equation (4.40a)) for no sterile signal. Plotted are fraction of occurrence versus TS value (cf. equation (4.40a)). The obtained pseudo data is illustrated by the solid blue histogram. The fit of a $Q(M, n_{\rm dof})$ (cf. equation (4.41)) with $n_{\rm dof}$ as an unconstrained fit parameter is shown in solid black, with $n_{\rm dof}$=1 ($n_{\rm dof}$=2) in dashed dotted green (dashed cyan). For comparison Chi-square distributions with 1 (2) dof are shown in dashed dotted black (dashed red). This plot includes 388 pseudo experiments.

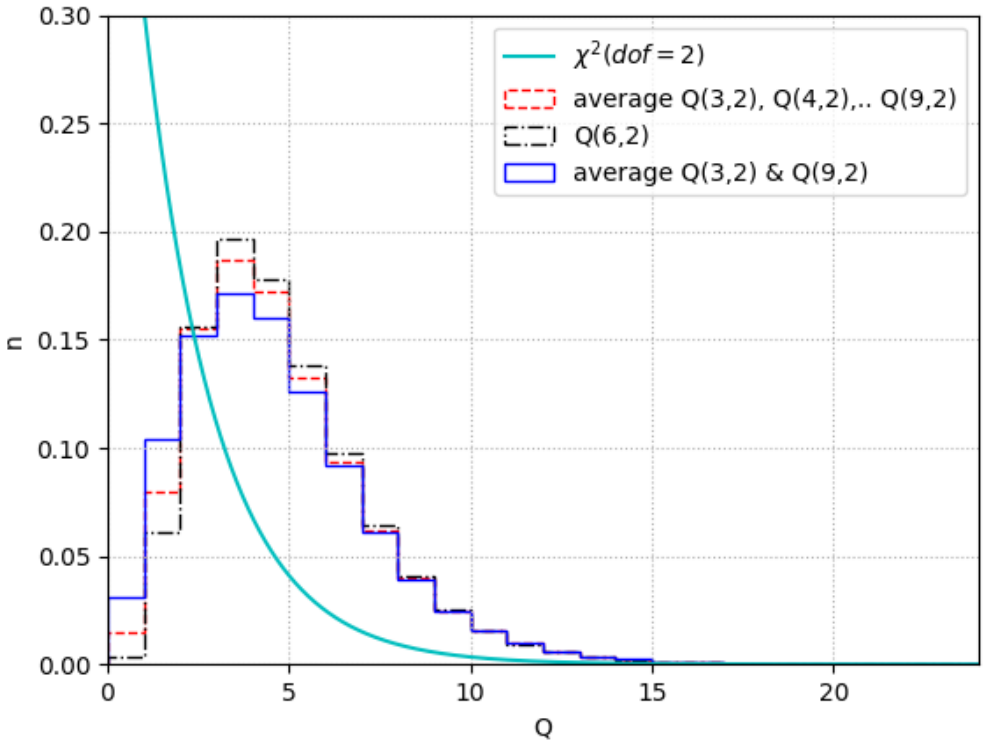

Figure 4.30: Pdf of dicing random numbers from equation (4.41). The dashed dotted black line shows the pdf for $Q(M = 6, n_{\text{dof}})$, the solid blue line shows the average pdf of $Q(M = 3, n_{\text{dof}})$ and $Q(M = 9, n_{\text{dof}})$ and the dashed red line shows the average pdf for $Q(M = 3, n_{\text{dof}})$, $Q(M = 4, n_{\text{dof}})$,..,$Q(M = 9, n_{\text{dof}})$. A Chi-square distribution with $n_{\text{dof}} = 2$ is shown in cyan for comparison.

Accordingly, by definition the median 95% confidence level sensitivity $\sin^2 2\theta_{14}^{\text{sens}}$ for a Δm^2_{41} is that value of $\sin^2 2\theta_{14}$ for that Δm^2_{41} which in 95% of cases pseudo experiments will result in a larger best fit $\sin^2 2\theta_{14}$ for that Δm^2_{41} than the median best fit $\sin^2 2\theta_{14}^{\text{med}}$ for that Δm^2_{41}. For reasons of readability the dependence on Δm^2_{41} is not written out[VII].

$\sin^2 2\theta_{14}^{\text{med}}$ is obtained from pseudo experiments. In detail, 390 pseudo experiments with true $\sin^2 2\theta_{14} = 0$ were generated and $\sin^2 2\theta_{14}$ was fitted for 100 Δm^2_{41} grid points. These pseudo experiments are identical to those used for the background test statistics calculation (cf. section 4.4.1). $\sin^2 2\theta_{14}^{\text{med}}$ is the median fit result and was identified for all 100 Δm^2_{41} grid point independently.

For the sterile distribution, pseudo experiments are not needed as Wilks' theorem holds as long as Δm^2_{41} is fixed.

The red histogram in figure 4.31 displays the probability density function of the test statistics TS_{1D} (cf. equation (4.37)) from 1999 pseudo experiments with $\sin^2 2\theta_{14} = 0.000$ for constant $\Delta m^2_{41} = 0.080\,\text{eV}^2$. The black histogram shows the probability density function of the test statistics from 1999 pseudo experiments with $\sin^2 2\theta_{14} = 0.072$ for constant $\Delta m^2_{41} = 0.280\,\text{eV}^2$. Both histograms match well with the chi-square distribution for one degree of freedom indicated with the dashed blue line.

The test statistics

$$\begin{aligned} TS_S(\Delta m^2_{41}) :=& -2\ln\left(\frac{\mathcal{L}(\vec{x_a}|\sin^2 2\theta_{14}^{\text{med}}, \Delta m^2_{41})}{\mathcal{L}(\vec{x_a}|\sin^2 2\theta_{14}^{\text{best}}, \Delta m^2_{41})}\right) \\ =& -2\ln\Big(\mathcal{L}(\vec{x_a}|\sin^2 2\theta_{14}^{\text{med}}, \Delta m^2_{41})\Big) \\ & -\Big(-2\ln\Big(\mathcal{L}(\vec{x_a}|\sin^2 2\theta_{14}^{\text{best}}, \Delta m^2_{41})\Big)\Big) \end{aligned} \tag{4.43}$$

is defined as illustrated in sketch 4.32 b). Here, $\sin^2 2\theta_{14}^{\text{best}}$ is the best fit $\sin^2 2\theta_{14}$ for the Asimov dataset $\vec{x_a}$ (i.e. $\vec{x_a}$ is a pseudo dataset with infinite statistics, cf. section 4.3.1) and $\mathcal{L}$ is the likelihood function (cf. equation (4.12)). $\sin^2 2\theta_{14,\text{best}}$ is identical to the true $\sin^2 2\theta_{14}$ used to produce the dataset as the statistics is infinite and the fit is unbiased. While the dependence on Δm^2_{41} is explicitly mentioned in equation (4.43) it will not be explicitly written out in the following. The median sensitivity $\sin^2 2\theta_{14,\text{sens}}$ according to Wilks' theorem is that true value of $\sin^2 2\theta_{14}$ for which $TS_S = 2.71$ [100] [127]. This is illustrated in figure 4.32 c). Thus, TS_S is obtained for reasonable $\sin^2 2\theta_{14} > \sin^2 2\theta_{14}^{\text{med}}$ and a spline is used to describe the inverse of the relation $TS_S(\sin^2 2\theta_{14})$ (cf. figure 4.32 d)). That spline evaluated at $TS_S = 2.71$ yields the median sensitivity.

The uncertainty on the sensitivity is calculated similarly. The 1σ area is defined as the area in which 68.2% of experiments should be, where values are added to the area according to their likeliness. This yields an area centered around the median in case of a Gaussian distribution (cf. figure 4.33). However, 1σ and 2σ area might be asymmetric or even share an edge if the probability distribution is not symmetric. Moreover, that edge can even be identical to the median if the probability distribution contains a delta distribution at that edge.

Figure 4.34 shows the pdfs of best fit $\sin^2 2\theta_{14}$ from pseudo experiments with true $\sin^2 2\theta_{14} = 0$ exemplary for for $\Delta m^2_{41} = 0.007\,\text{eV}^2$ (dashed blue line), $\Delta m^2_{41} = 0.017\,\text{eV}^2$

[VII] i.e. one could also use $\sin^2 2\theta_{14}^{\text{sens},\Delta m^2_{41}}$, $\sin^2 2\theta_{14}^{\text{med},\Delta m^2_{41}}$ as symbols

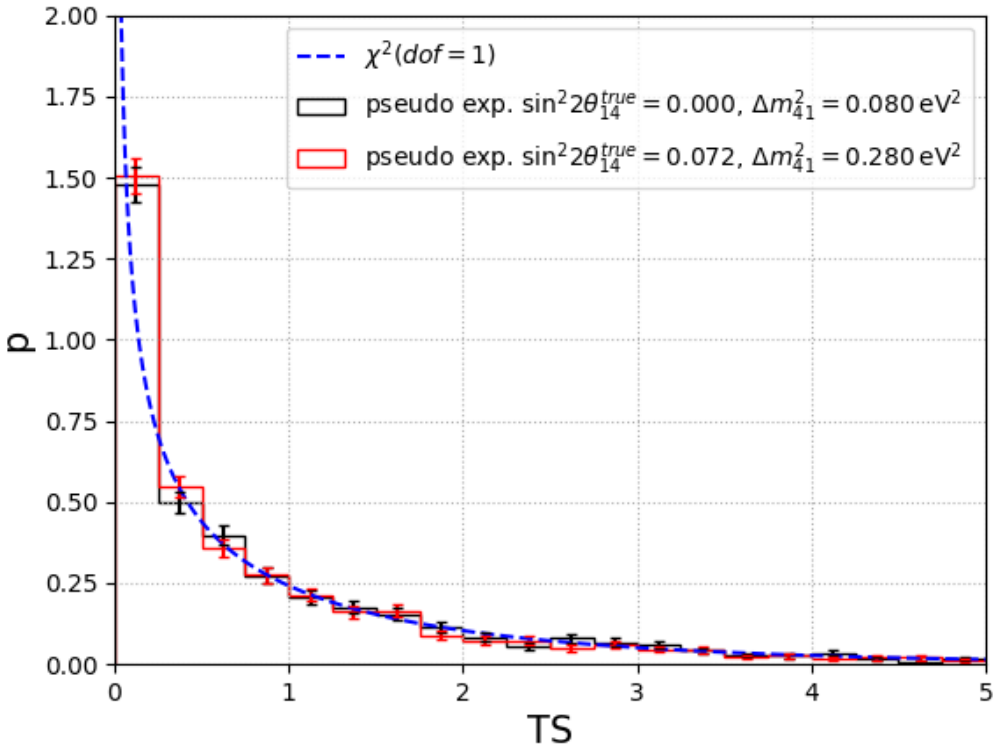

Figure 4.31: Probability density function of the test statistics TS_{1D} (cf. equation (4.37)) with fixed Δm^2_{41} from pseudo experiments. The red histogram shows the probability density function from 1999 pseudo experiments with $\sin^2 2\theta_{14} = 0.000$ for constant $\Delta m^2_{41} = 0.080\,\mathrm{eV}^2$. The red histogram displays the probability density function from 1997 pseudo experiments with $\sin^2 2\theta_{14} = 0.072$ for constant $\Delta m^2_{41} = 0.280\,\mathrm{eV}^2$. The dashed blue line indicates a Chi-square distribution with one degree of freedom.

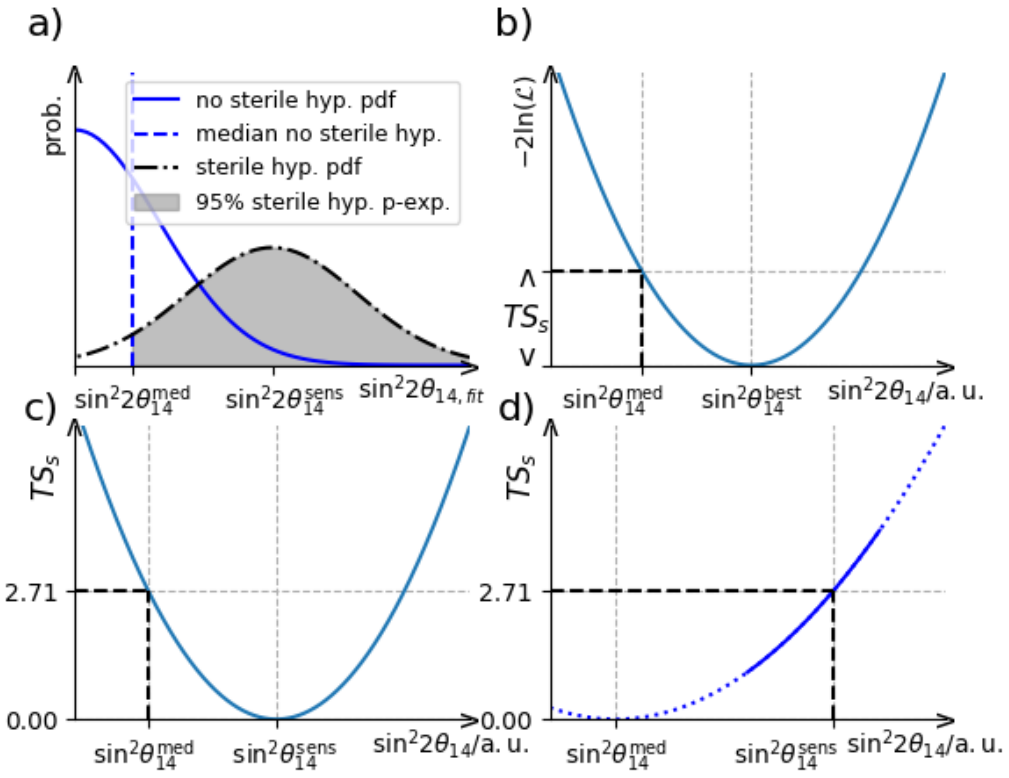

Figure 4.32: Sketches on the sensitivity calculation: Δm^2_{41} is assumed to have the same fixed value in all subplots. $\sin^2 2\theta_{14}^{\text{sens}}$ names the $\sin^2 2\theta_{14}$ sensitivity (which is to be calculated) and $\sin^2 2\theta_{14}^{\text{med}}$ the median best fit $\sin^2 2\theta_{14}$ for pseudo experiments with no signal for that given Δm^2_{41} [a].
a) Definition of the sensitivity [90]: The probability is sketched versus $\sin^2 2\theta_{14}$ in arbitrary units. The solid blue line shows the probability density function of best fit $\sin^2 2\theta_{14}$ for pseudo experiment with true value $\sin^2 2\theta_{14} = 0.0$. The dashed blue line marks the median of this distribution, called $\sin^2 2\theta_{14}^{\text{med}}$. The black dashed dotted line sketches the pdf for pseudo experiments with true value $\sin^2 2\theta_{14} = \sin^2 2\theta_{14}^{\text{med}}$ (i.e. at the sensitivity value). The gray shaded area covers the 95% upper tail of the later distribution.
b) Definition of TS_S from equation (4.43); $-2\ln\mathcal{L}$ for pseudo data with median best fit value $\sin^2 2\theta_{14}^{\text{best}}$ is plotted versus $\sin^2 2\theta_{14}$ in arbitrary units. The definition of the test statistics is marked on the y-axis..
c) Illustration of how the sensitivity is connected to TS_S (cf. equation (4.43)); TS_S versus $\sin^2 2\theta_{14}$ in arbitrary units, $\sin^2 2\theta_{14}^{\text{sens}}$ is marked on the x-axis (for more see text).
d) Sketch on the calculation of the sensitivity. TS_S (y-axis) is obtained for various $\sin^2 2\theta_{14}$ (x-axis, sketched in arbitrary units). A spline is used to describe the inverse function ($\sin^2 2\theta_{14}$ as a function of TS_S) and its value for $TS_S = 2.71$ is given as $\sin^2 2\theta_{14}^{\text{sens}}$. For efficiency reasons and the make the function unique not the whole range of $\sin^2 \theta_{14}$ is scanned but only reasonable values $> \sin^2 2\theta_{14}^{\text{med}}$ as $\sin^2 2\theta_{14}^{\text{sens}}$ is larger than $> \sin^2 2\theta_{14}^{\text{med}}$ by definition.

[a] i.e. $\sin^2 2\theta_{14}^{\text{sens}}$ and $\sin^2 2\theta_{14}^{\text{med}}$ are a functions of Δm^2_{41} which are evaluated at the same fixed point here, for reasons of readability the dependence on Δm^2_{41} is not written out.

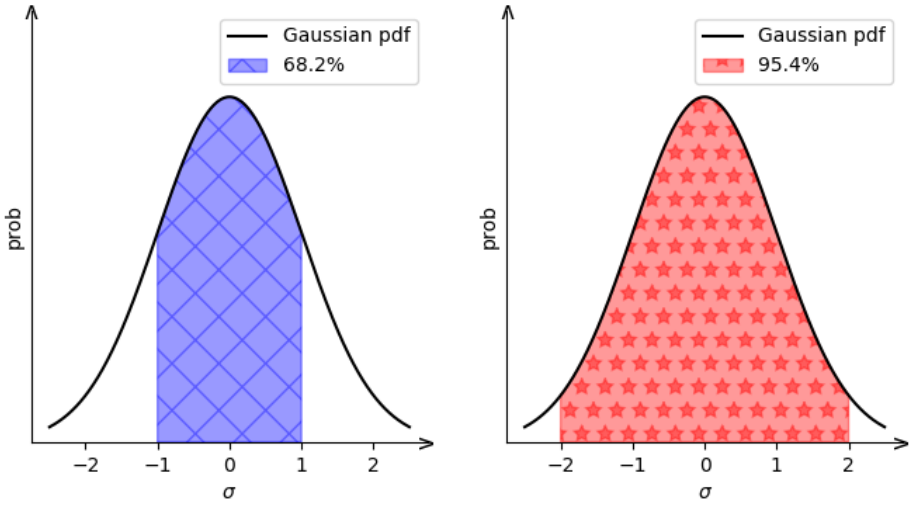

Figure 4.33: 1 (a)) and 2 (b)) σ area from a Gaussian distribution. The 1σ area covers $\approx$68.2%, the 2σ area $\approx$ 95.4%.

(solid cyan line), $\Delta m^2_{41} = 0.040\,\mathrm{eV}^2$ (dashed dotted green line), $\Delta m^2_{41} = 0.096\,\mathrm{eV}^2$ (dotted black line) and $\Delta m^2_{41} = 0.230\,\mathrm{eV}^2$ (dashed red line). In all fits $\sin^2 2\theta_{14}$ was free while Δm^2_{41} was fixed. Each histogram contains around 390 pseudo experiments. Those pseudo experiments are identical to the pseudo experiments used to obtain TS_0 (cf. section 4.4.1). One can see that the probability density functions are maximal in the first bin (i.e. for $\sin^2 2\theta = 0$, cf. figure 4.34). This means that as long as Δm^2_{41} is fixed to the inserted value, $\sin^2 2\theta_{14} = 0$ is the most likely best fit result for true inserted $\sin^2 2\theta_{14} = 0$. In the specific situation given here, the 1σ area is identical to the 68.2% quantile and the 2σ area is identical to the 95.4% quantile since $\sin^2 2\theta_{14} < 0.$ is not allowed.

Figure 4.35 illustrates the definition of the upper edge of the sensitivity uncertainty band following fro that for 1 and 2σ range.

The rest of the calculation works entirely analogy to the calculation of the median sensitivity. Just that $\sin^2 2\theta_{14,\mathrm{med}}$ is exchanged for the 1σ (2σ) quantile $\sin^2 2\theta_{14}^{\mathrm{q}1\sigma}$ ($\sin^2 2\theta_{14}^{\mathrm{q}2\sigma}$).

Figure 4.36 presents median(solid black), Φ(68.2%) quantile(solid red) and Φ(95.4%) quantile (dashed blue) of the best fit $\sin^2 2\theta_{14}$ pdf from null hypothesis pseudo experiments. The median is very close to zero for all Δm^2_{41}. This is expected as the inserted true value was $\sin^2 2\theta_{14} = 0.0 \,\forall\, \Delta m^2_{41}$ unless fluctuations into the $\sin^2 2\theta_{14} < 0.$ region fit better to $\sin^2 2\theta_{14} > 0.$ than to $\sin^2 2\theta_{14} = 0.$. Here, this is not given as Δm^2_{41} is fixed[VIII]. The 1σ AW sensitivity (cf. section 4.3.3) is represented by the dotted black line in figure 4.36. It matches the 68.2% quantile (solid red line) by construction.

The final step for sensitivity calculation is to describe the inverse function $TS(\sin^2 2\theta_{14})$ by a spline and evaluate it at TS=2.71 like it is sketched in figure 4.32 d). This spline interpolation is presented exemplary for several Δm^2_{41} in figure 4.37.

[VIII] Otherwise (if Δm^2_{41} was not fixed), the median best fit $\sin^2 2\theta_{14}$ value would be a non-zero and a positive number

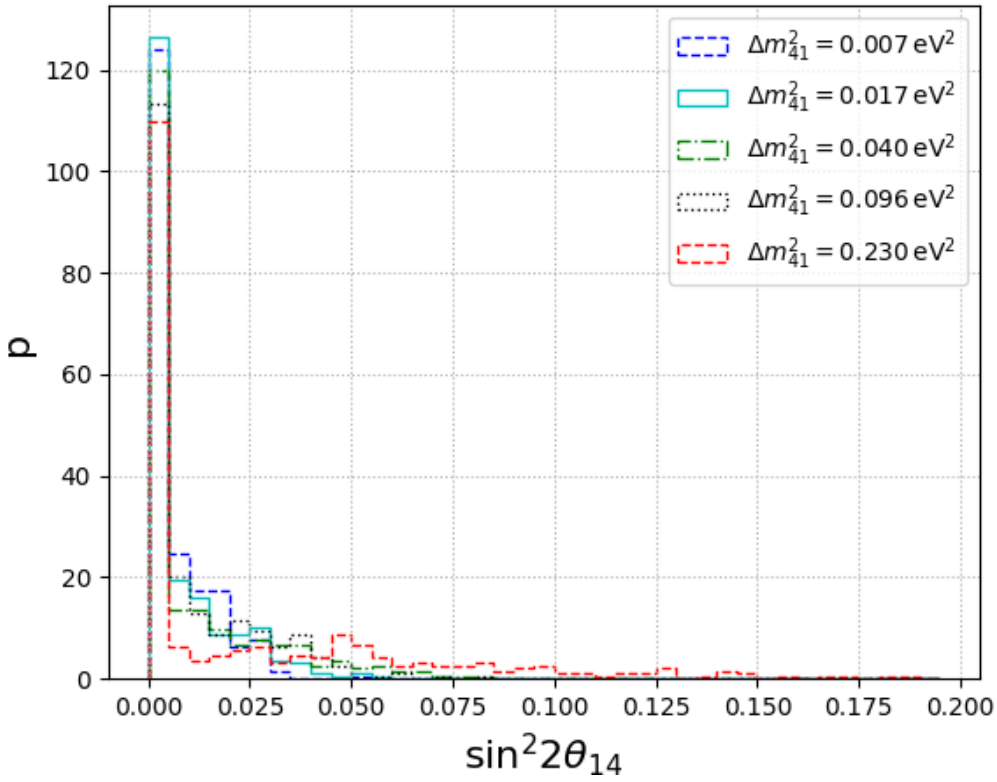

Figure 4.34: Example probability density functions of best fit $\sin^2 2\theta_{14}$ from pseudo experiments with true $\sin^2 2\theta_{14} = 0.0$. The plot shows the probability density p versus best fit $\sin^2 2\theta_{14}$ for $\Delta m^2_{41} = 0.007\,\mathrm{eV}^2$ (dashed blue line), $\Delta m^2_{41} = 0.017\,\mathrm{eV}^2$ (solid cyan line), $\Delta m^2_{41} = 0.040\,\mathrm{eV}^2$ (dashed dotted green line), $\Delta m^2_{41} = 0.096\,\mathrm{eV}^2$ (dotted black line) and $\Delta m^2_{41} = 0.230\,\mathrm{eV}^2$ (dashed red line). Each histogram contains around 390 pseudo experiments. Those pseudo experiments are identical to the pseudo experiments used to obtain TS_0 from equation (4.40a) (cf. section 4.4.1).

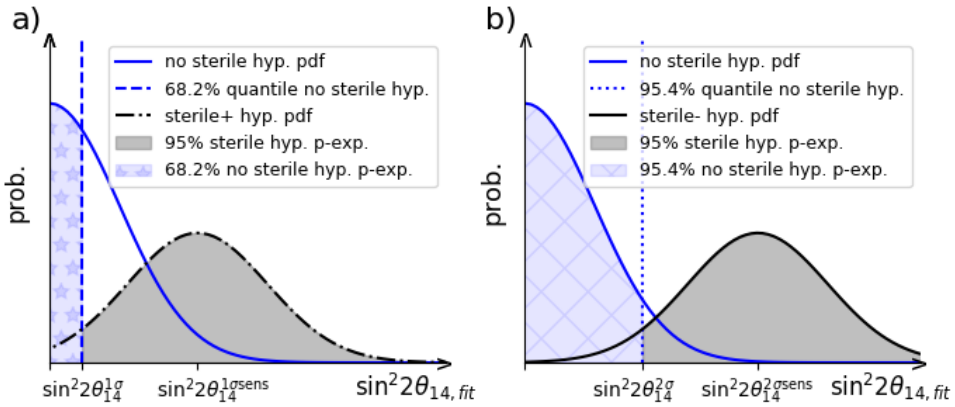

Figure 4.35: Sketches on the definition of the uncertainty of the sensitivity: Δm^2_{41} is assumed to have the same fixed value in all subplots.
a) Definition of the upper 1σ edge of the sensitivity uncertainty error band. The solid blue line shows probability versus best fit $\sin^2 2\theta_{14}$ for the probability density function of best fit $\sin^2 2\theta_{14}$ for pseudo experiments with true value $\sin^2 2\theta_{14} = 0.0$. The dashed blue line marks the 1σ quantile of this distribution, called $\sin^2 2\theta_{14}^{\text{q}1\sigma}$ [a]. The black dashed dotted line represents the probability density function for pseudo experiments with true value $\sin^2 2\theta_{14} = \sin^2 2\theta_{14}^{1\sigma\text{sens}}$ (i.e. at the 1σ edge of the sensitivity uncertainty band). The gray shaded area covers the 95% upper tail of the later distribution.
b) Definition of the upper edge of the 2σ sensitivity uncertainty error band. The solid blue line shows pdf of best fit $\sin^2 2\theta_{14}$ for pseudo with true value $\sin^2 2\theta_{14} = 0.$ in terms of probability versus best fit $\sin^2 2\theta_{14}$ and the dashed blue line marks the 2σ quantile of this distribution, called $\sin^2 2\theta_{14}^{\text{q}2\sigma}$ [b]. The solid black line sketches the pdf for pseudo experiments with true value $\sin^2 2\theta_{14} = \sin^2 2\theta_{14}^{2\sigma\text{sens}}$ (i.e. at the 2σ edge of the sensitivity uncertainty band). The gray shaded area covers the 95% upper tail of the later distribution.

[a] The no-sterile pdf actually almost contains a delta distribution at $\sin^2 2\theta_{14} = 0$ and thus does not look like sketched here.

[b] The no-sterile pdf actually almost contains a delta distribution at $\sin^2 2\theta_{14} = 0$ and thus does not look like sketched here.

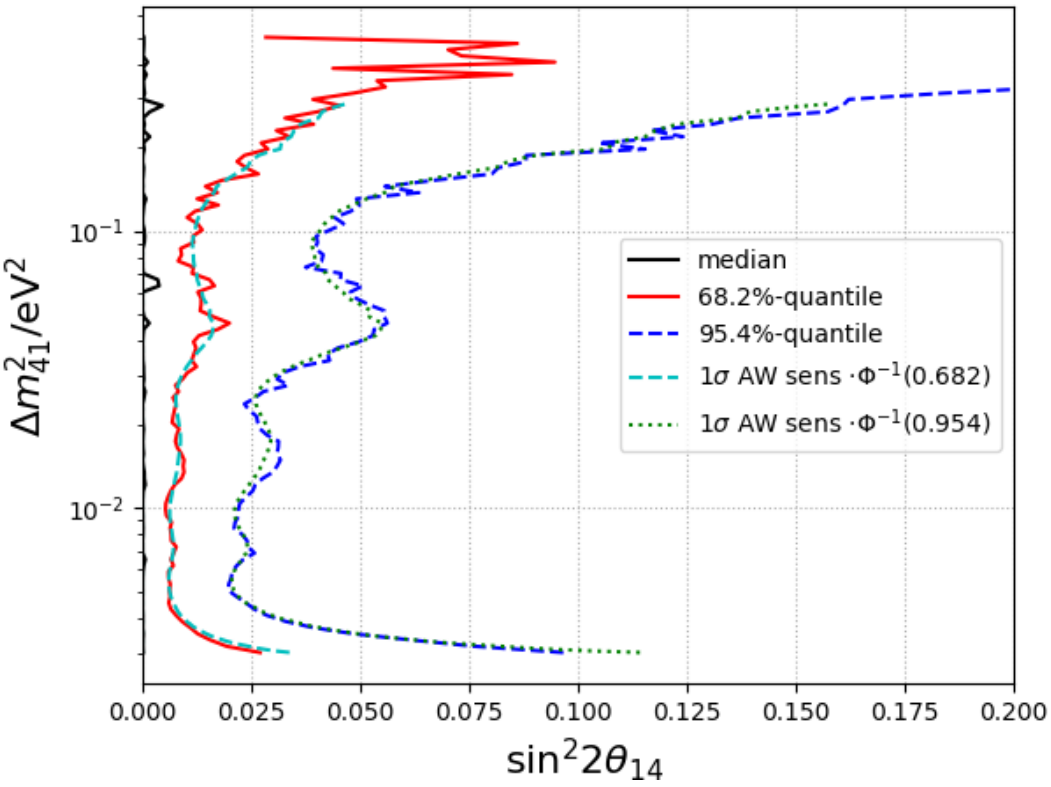

Figure 4.36: Various quantiles of the $\sin^2 2\theta_{14}$ best fit distribution from null hypothesis pseudo experiments; Δm^2_{41} versus $\sin^2 2\theta_{14}$. The median is shown in solid black, the $\Phi(68.2\%)$ quantile in solid red and the $\Phi(95.4\%)$ quantile in dashed blue. The 1σ AW sensitivity (cf. section 4.3.3) is shown in dotted black and matches the $\Phi(1)$ quantile by construction.

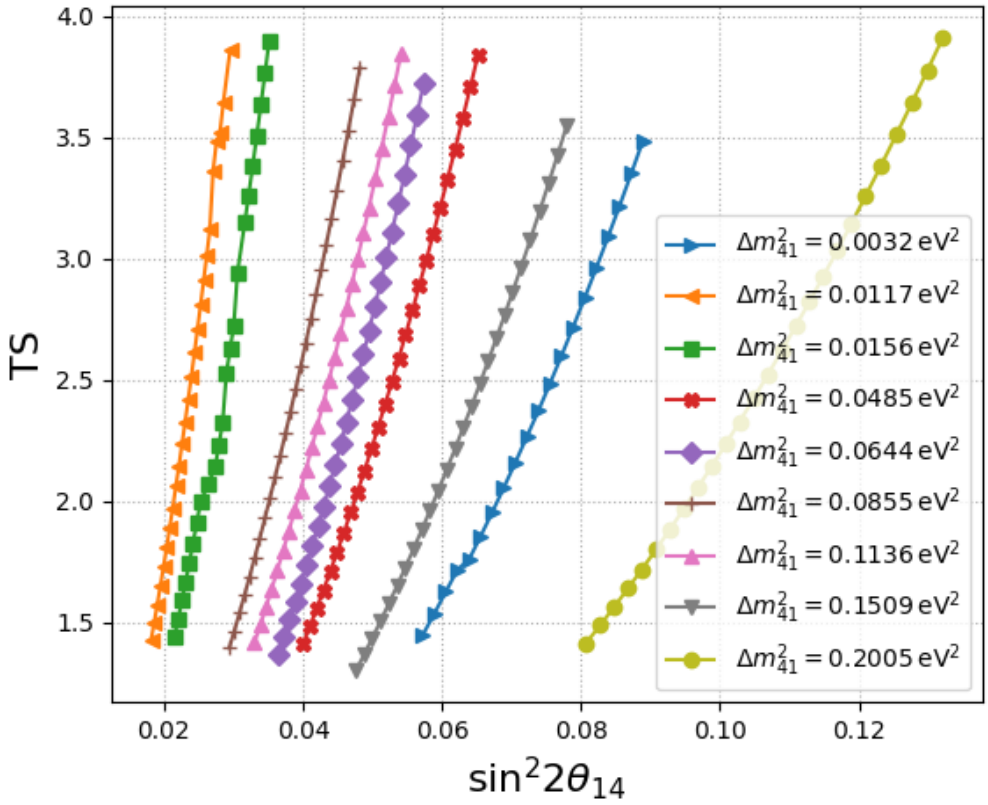

Figure 4.37: TS_S from equation (4.43) (illustrated in figure 4.32 b)) versus $\sin^2 2\theta_{14}$ for Asimov data with true value $\sin^2 2\theta_{14}$ and various Δm^2_{41} (see legend) as sketched in figure 4.32 d). The spline interpolation is indicated by the solid lines.

Figure 4.38 displays the final median sensitivity to $\sin^2 2\theta_{14}$ as a function of $\Delta m^2_{41}/\mathrm{eV}^2$ (y-axis). Its 1σ (2σ) uncertainty area is shaded in green (yellow). As the pdf of best fit $\sin^2 2\theta_{14}$ for no sterile pseudo experiments has its global maximum at $\sin^2 2\theta_{14} = 0$ and is zero for $\sin^2 2\theta_{14} = 0$ values left to the left 1σ uncertainty edge are not possible. The median sensitivity is almost identical to the later. Therefore, best fits on experimental data to the right of the median sensitivity are more likely than to its left since being to the left is not even possible for most of Δm^2_{41}. The AW sensitivity (cf. figure 4.14, section 4.3.3) is indicated with a dashed blue line in figure 4.38. It is almost parallel to the median sensitivity and in the middle of the 1σ area. Thus, all systematical studies done with the AW sensitivity can be transferred to the actual median sensitivity.

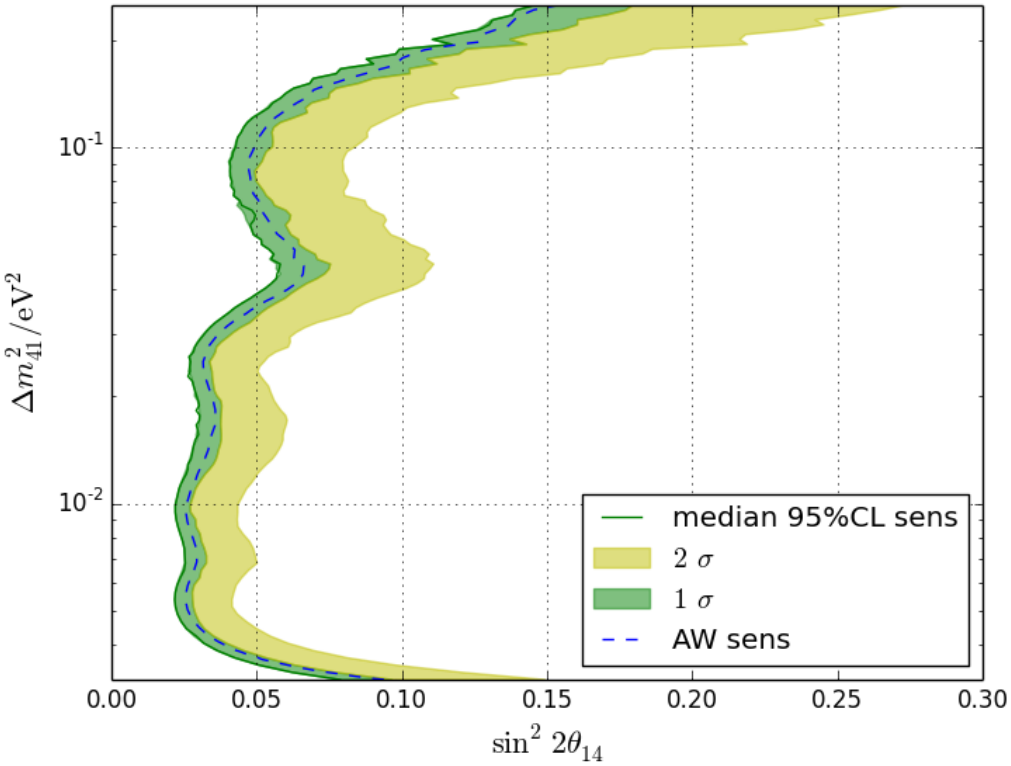

Figure 4.38: Sensitivity to $\sin^2 2\theta_{14}$ (x-axis) as a function of $\Delta m^2_{41}/\mathrm{eV}^2$ (y-axis). The median sensitivity is plotted in solid green, the 1σ area is indicated in green and the 2σ area in yellow. The AW sensitivity (cf. figure 4.14, section 4.3.3) is plotted with a dashed blue line.

Chapter 5

Results

This chapter presents the results of the experimental data fit, the fit validation and the upper limit calculation.

Figure 5.1 shows the results of a two dimensional likelihood scan in $\sin^2 2\theta_{14}$ (x-axis) and $\Delta m^2_{41}/\mathrm{eV}^2$ (y-axis) on experimental data. The color scale shows $-2\Delta\ln(\mathcal{L})$ which is minus two times the difference between the natural logarithm of the likelihood at the grid point and the minimum of $\ln(\mathcal{L})$. The green star marks the global best fit. It was found that $-2\Delta\ln\big(\mathcal{L}(\sin^2 2\theta_{14} = 0 \vee \Delta m^2_{41} = 0)\big) = 6.15$. The main tasks of the sterile analysis are testing whether $-2\Delta\ln\big(\mathcal{L}(\sin^2 2\theta_{14} = 0 \vee \Delta m^2_{41} = 0)\big) = 6.15$ is consistent with no-sterile signal and giving a p-value.

These two tasks will be discussed in section 5.1. The definition of the p-value is sketched in figure 5.2.

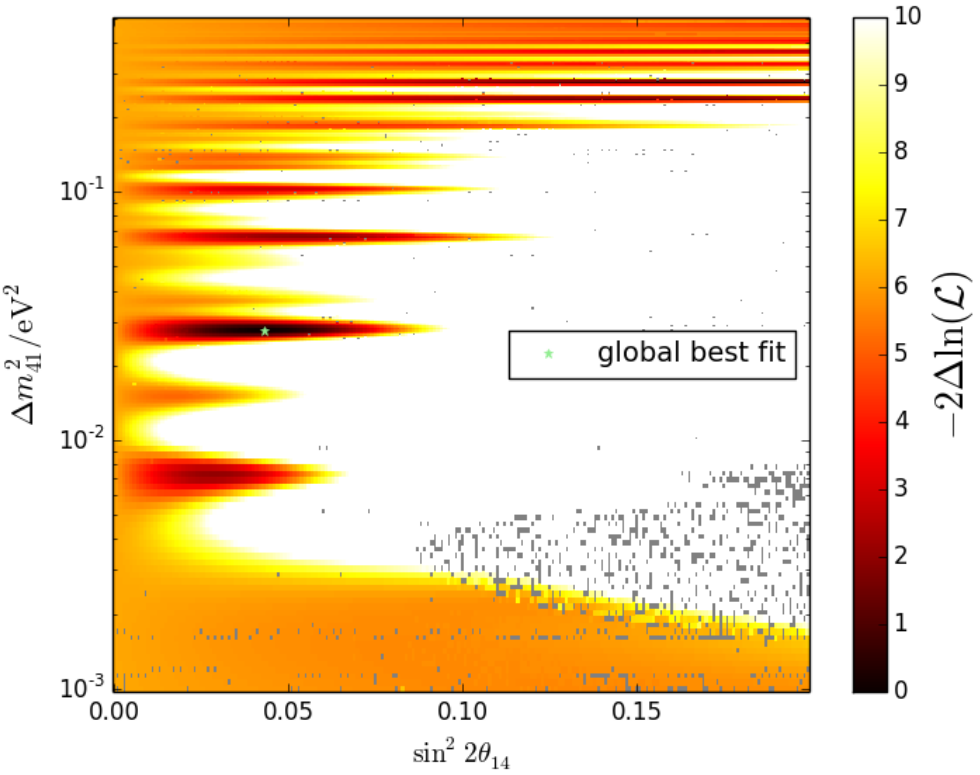

Figure 5.1: Scan of $-2\Delta\ln(\mathcal{L})$ for experimental data in $\sin^2 2\theta_{14}$ (x-axis) and $\Delta m^2_{41}/\mathrm{eV}^2$(y-axis).$-2\Delta\ln(\mathcal{L})$ is represented in the color bar where $\Delta\ln(\mathcal{L}) = \ln(\mathcal{L}) - \ln(\mathcal{L}_{\max})$ is the difference of the natural logarithm of the likelihood to the natural logarithm of the maximum likelihood from this scan. The green star marks the best fit point (i.e. the minimum of $-2\Delta\ln(\mathcal{L})$). Grey shaded areas mark missing data.

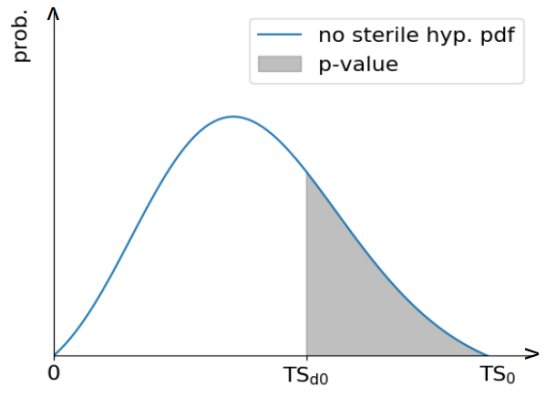

Figure 5.2: Sketch on p-value definition: Probability density function of TS_0 (defined in equation (4.40a), cf. section 4.4.1) for pseudo experiments without sterile signal. The p-value corresponds to the shaded area i.e. to the integral of the pdf from the TS_0 found in actual data, TS_{d0}, to infinity.

5.1 P-value

Figure 5.3 displays test statistics for the null hypothesis (see also figure 4.29). The value of the test statistics from experimental data is indicated by the dashed black vertical line. One can see that the experimental data result is well within the expectation from pseudo experiments. $K = 96$ of the $N = 388$ pseudo experiments of the null hypothesis for figure 5.3 have a test statistics value of $TS_0 > 6.15$. This corresponds to a p-value of 0.247. Assuming a Poisson uncertainty on K results in an uncertainty of 0.025. However, the distribution of the pseudo experiments is a binomial distribution. Therefore giving

$$\sigma_{\text{p-value}} = \frac{\sqrt{K(1-K/N)}}{N} \approx 0.022 \tag{5.1}$$

as uncertainty is more accurate.

As explained in section 4.4.1 the test statistics distribution for no-sterile signal has been fitted with an extreme value function $Q(M, n_{\text{dof}})$ cf. equation (4.41). $Q(M, n_{\text{dof}})$ mathematically describes the superposition of M Chi-square functions with n_{dof} degrees of freedom. The best fit of $Q(x, M, n_{\text{dof}})$ yields $M = 7.52 \pm 3.02$. There are O(10) local minima of $-2\Delta\ln(\mathcal{L})$ visible in the scan of experimental data. This is consistent with $M = 7.52 \pm 3.02$. Also one can see in figure 5.1 that the minima are horizontal, i.e. there is only one minimum per Δm^2_{41}. The p-value may also be calculated via

$$\text{p-value} = \int_{6.15}^{\infty} Q(x, M, n_{\text{dof}})dx \tag{5.2}$$

The p-values for best fit parameters can be found in table 5.1. All of them are consistent with 0.247 ± 0.025 and do not depend on the details on the parametrization of the test statistics. Even more importantly, all values are significantly larger than 5%. Taking all p-values together confirms that the experimental data is consistent with the no-sterile hypothesis.

Thus, giving allowed regions under the signal hypothesis is not meaningful and an upper limit is given. The global best fit is compared to the sensitivity in figure 5.4. One can see that is just outside the 1σ area. This is indeed expected, as fluctuations in a range in which Double Chooz is not sensitive would not be recognized by the fit.

As already mentioned, the best fit was found to be consistent with the no-sterile hypothesis. Thus, it was decided not to give uncertainties under the signal hypothesis. Also, giving uncertainties even on nuisance parameters would require an uneffortable computing effort

Table 5.1: P-values of the no-sterile hypothesis w.r.t. Double Chooz experimental data. Values were obtained from fitting $Q(M, n_{\text{dof}})$ (cf. equation (4.41)) to the test statistics distribution for no sterile signal (cf. equation (5.2)) and from counting pseudo experiments assuming a binomial distribution respectively.

Method	M	n_{dof}	p value
counting pseudo experiments			0.247 ± 0.022
equation (5.2)	7.52	1.79	0.248
equation (5.2)	6.22	2	0.255
equation (5.2)	18.82	1	0.220

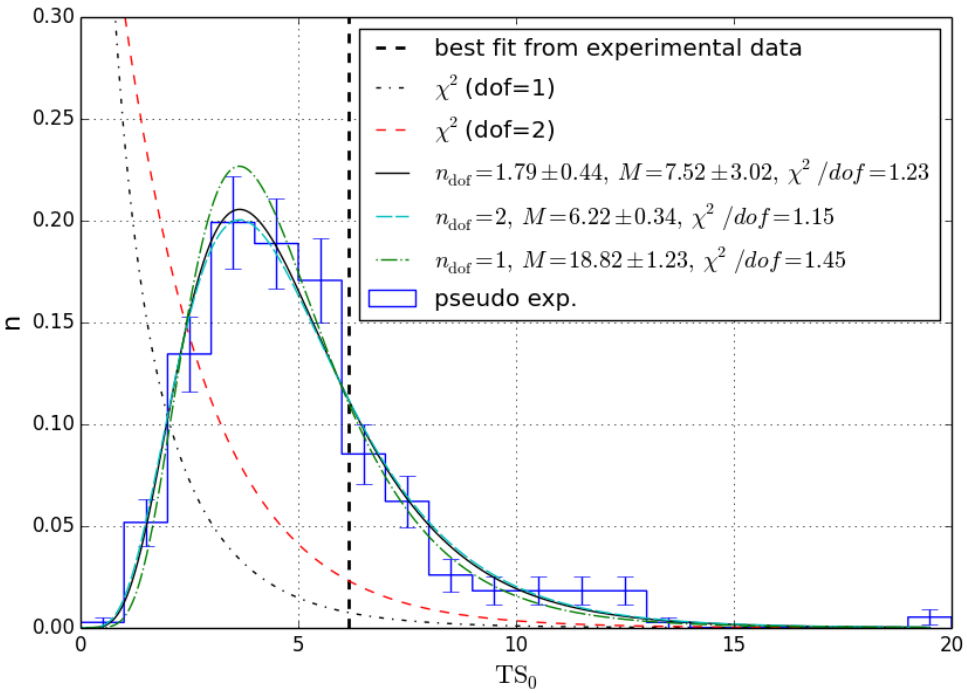

Figure 5.3: Probability density function of the test statistics distribution (cf. equation (4.40a)) for no sterile signal. Plotted are fraction of occurrence versus test statistics value TS_0 (cf. equation (4.40a)). The obtained pseudo data is illustrated by the solid blue histogram. The fit of a $Q(M, n_{\mathrm{dof}})$ (cf. equation (4.41)) with n_{dof} as an unconstrained fit parameter is shown in solid black, with n_{dof}=1 (n_{dof}=2) in dashed dotted green (dashed cyan). For comparison Chi-square distributions with 1 (2) dof are shown in dashed dotted black (dashed red). This plot is identical to figure 4.29 except that the value from experimental data is indicated by the dashed black vertical line. It includes 388 pseudo experiments.

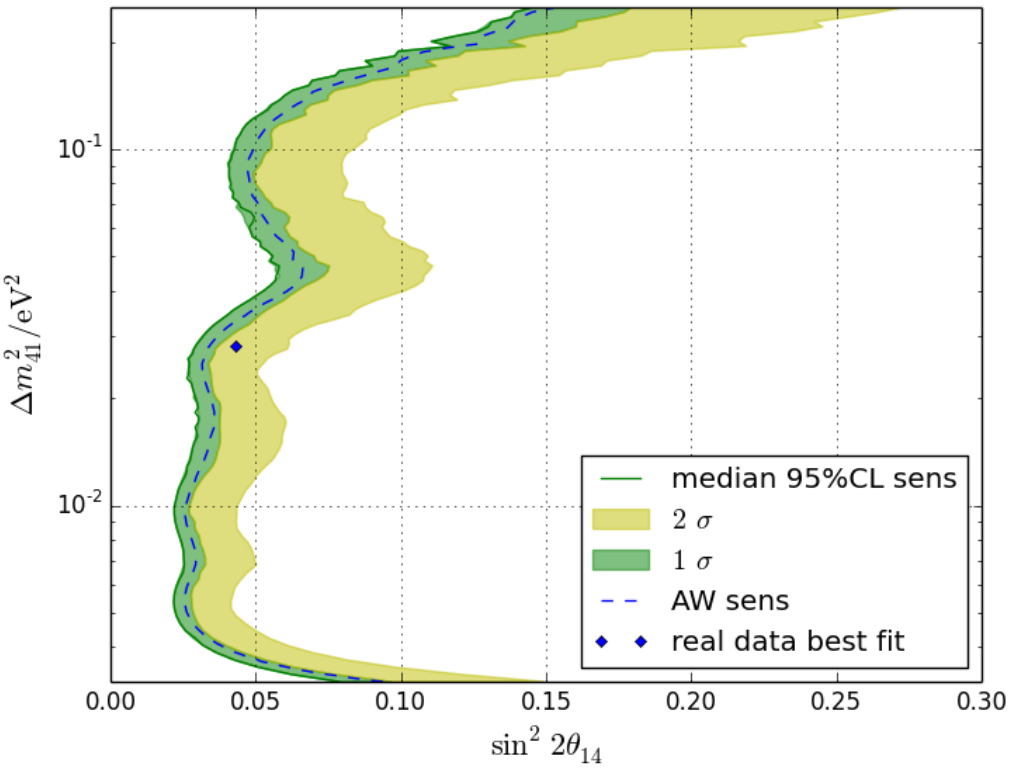

Figure 5.4: Sensitivity to $\sin^2 2\theta_{14}$ (x-axis) as a function of $\Delta m^2_{41}/\mathrm{eV}^2$ (y-axis). The median sensitivity is plotted in solid green, the 1σ area is indicated in green and the 2σ area in yellow. The AW sensitivity (cf. figure 4.14, section 4.3.3) is plotted with a dashed blue line. The global best fit from experimental data is marked with a blue star.

Table 5.2: Sterile and nominal best fit parameter values. For the sterile best fit uncertainties are not provided.

	sterile best fit	nominal best fit
$\sin^2\theta_{14}$	0.043	-
$\Delta m^2_{41}/\mathrm{eV}^2$	0.028	-
$\sin^2\theta_{13}$	0.1077	$0.1075^{+0.0161}_{-0.0172}$
Li-ND/(1/day)	3.14	3.11 ± 0.29
Li-FD/(1/day)	17.17	16.75 ± 1.85

since requiring a scan of $-2\ln(\mathcal{L})$ for each parameter where every point would again require a scan in Δm^2_{41}, $\sin^2 2\theta_{14}$. However, it has been checked that all nuisance parameters stay in the σ allowed range. Table 5.2 summarizes best fit values of the main important parameters for sterile and nominal best fit.

5.2 Fit validation

The next paragraph describes the validation of the data fit. After that, the upper limit and its calculation is explained in section 5.3.

Figure 5.5 shows the best fit spectra of inverse beta decay candidates normalized to the nominal expectation oscillated with $\sin^2 2\theta_{13} = 0.086$ [13]. The sterile best fit spectrum is plotted in solid blue, the no-sterile best fit in dashed black and the data with red points. Note that the dof are significantly less than N=(number of data points-2) since (among others) the reactor flux parameters are free in the fit.

To highlight the difference between the sterile and the no-sterile best fit the Chi-square per energy bin i following the definition by Neyman [95] is used:

$$\chi^2_i(\vec{\zeta}) = \frac{(n_{i,\vec{\zeta}} - n_{i,\mathrm{meas}})^2}{n_{i,\vec{\zeta}}} \quad , \tag{5.3}$$

where $n_{i,\vec{\zeta}}$ is the number of inverse beta decay candidates in bin i expected for the model parameters set $\vec{\zeta}$. $n_{i,\mathrm{meas}}$ is the number of inverse beta decay candidates measured in bin i. $\chi^2_i(\vec{\zeta})$ will be labeled $\chi^2_{\mathrm{sbf},i}$ if $\vec{\zeta}$ is given by the outcome of the sterile best fit and $\chi^2_{\mathrm{nsbf},i}$ if $\vec{\zeta}$ is given by the outcome of the no-sterile best fit. The difference between both quantities will be called:

$$\Delta\chi^2_i := \chi^2_{\mathrm{nsbf},i} - \chi^2_{\mathrm{sbf},i} \quad . \tag{5.4}$$

Figure 5.6 shows the residuum for the no-sterile best fit normalized to the no-sterile best fit as a function of visible energy. The sterile best fit is indicated by the solid blue line. The color scale shows the $\Delta\chi^2_i$ (cf. equation (5.4)) between sterile and no-sterile best fit for each energy bin. For red points (positive values) the sterile fit fits better while for blue points (negative values) the no-sterile best fit matches data better. The ND is shown in the top, the FD1-On in the middle and FD2 in the bottom. Indeed, the sterile best fit seams to fit better. One can identify that the points around 2, 4 and 6 MeV have the largest impact on the fit.

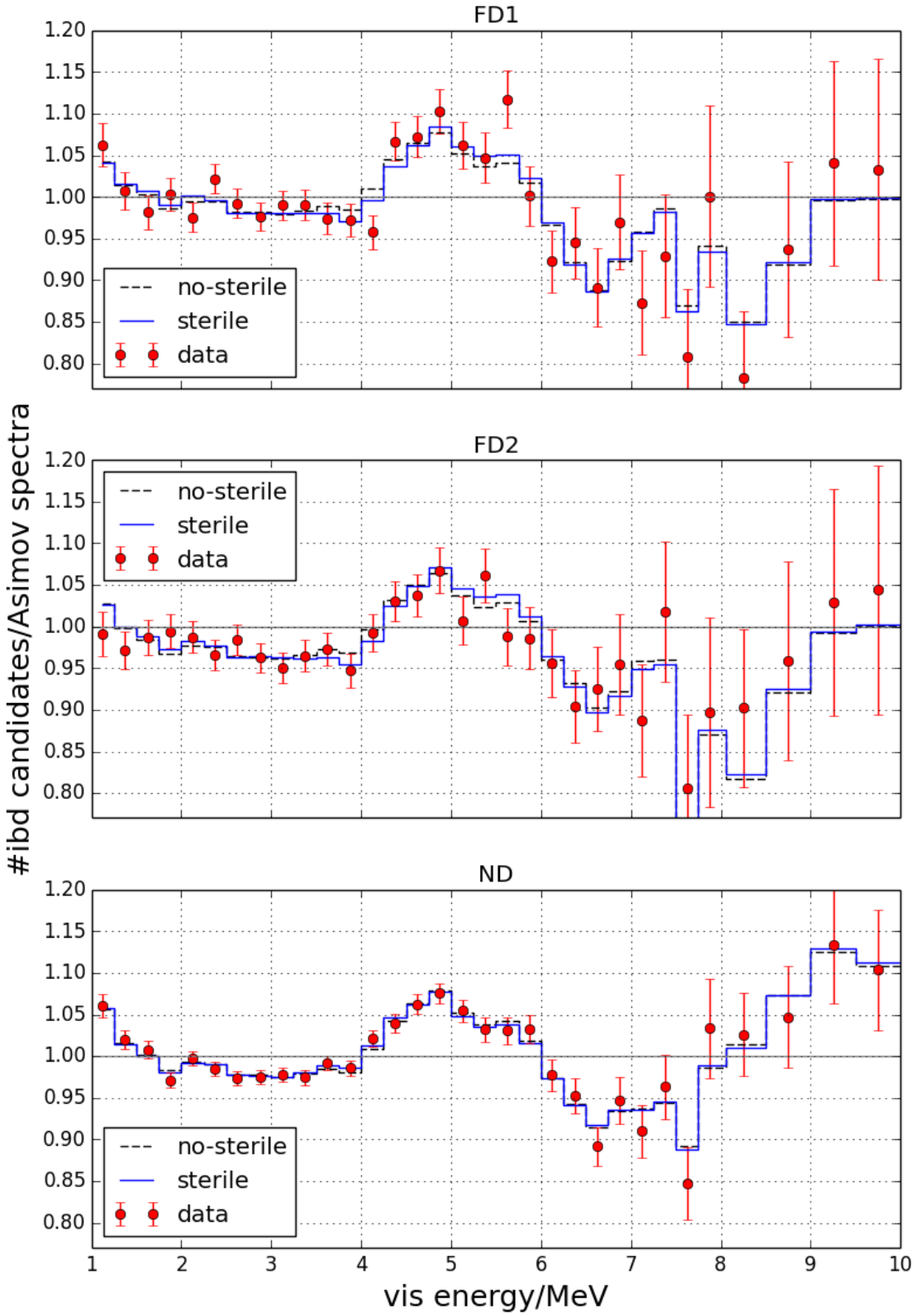

Figure 5.5: Sterile (solid blue) and no-sterile (dashed black) best fit inverse beta decay spectra. FD1-On (top), FD2 (middle) and ND (bottom) number of inverse beta decay candidates normalized to the nominal expectation oscillated with $\sin^2 2\theta_{13} = 0.086$ [13] versus visible energy. The experimental data is plotted with red circles.

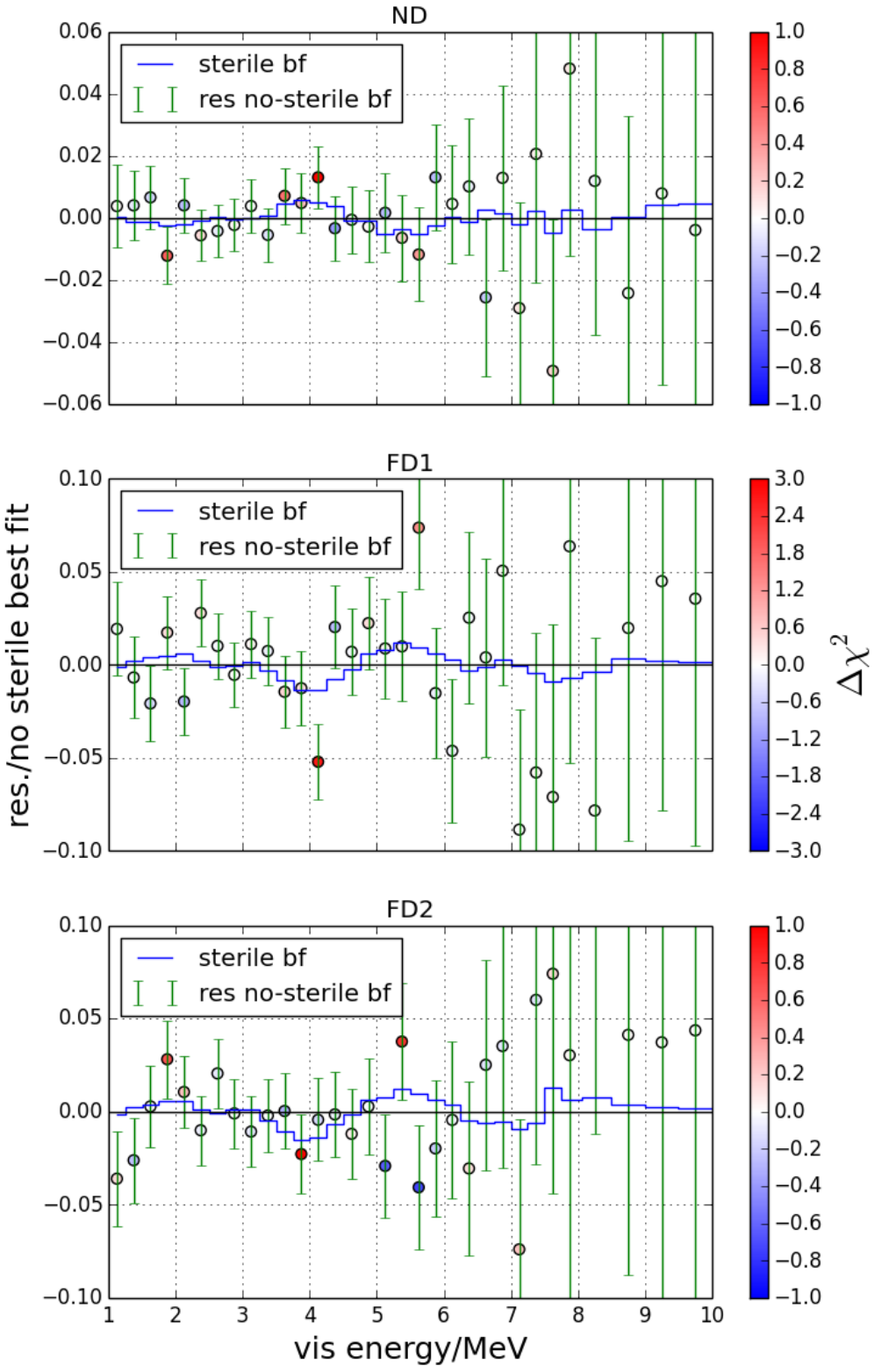

Figure 5.6: Residuum of no-sterile best fit normalized to the no-sterile best fit versus visible energy compared to sterile best fit (blue line) for the ND(top), FD1 (middle) and FD2 (bottom) dataset. The color scale shows the $\Delta\chi_i^2$ (cf. equation (5.4)) between sterile and no-sterile best fit for each energy bin.

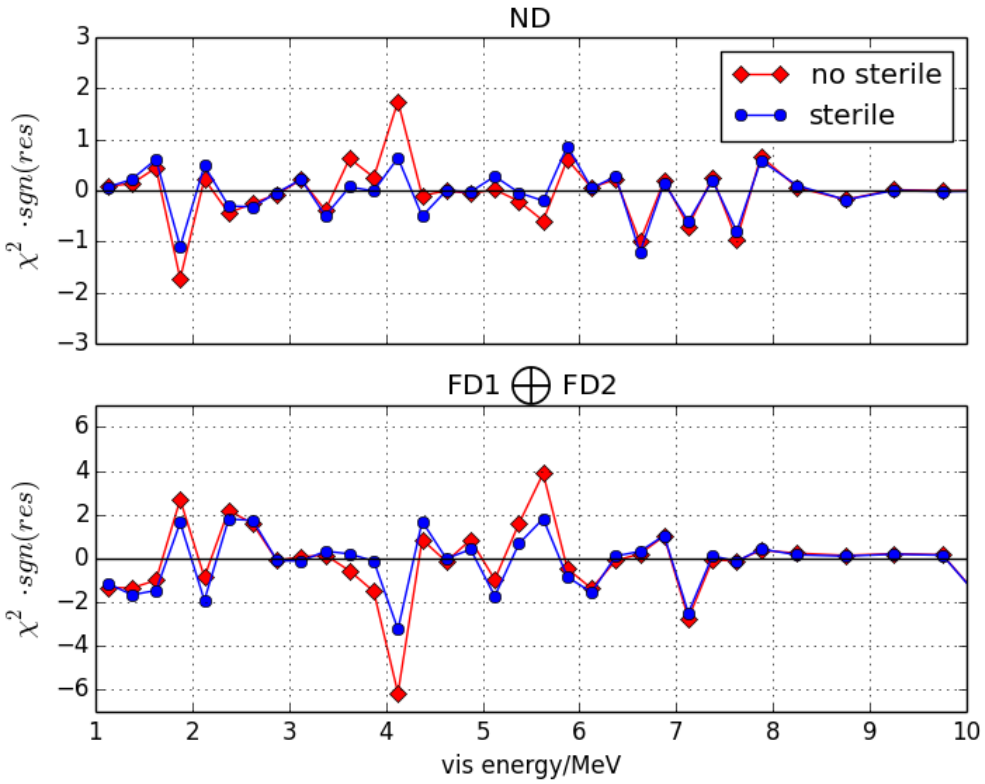

Figure 5.7: Sterile (blue dots) and no-sterile (red squared) best fit $\chi^2 \cdot \text{sign}(residuum)$ versus visible energy for ND(top) and FD1⊕FD2(bottom). FD1⊕FD2 simply means that the terms for FD1($\chi^2_{i,\text{FD1}}$) and FD2($\chi^2_{i,\text{FD2}}$) are added to each other: $\chi^2_{i,\text{FDI}} \bigoplus \chi^2_{i,\text{FD2}} = \chi^2_{i,\text{FDI}} + \chi^2_{i,\text{FD2}}$.

The fit should be rather driven by the combination of FD1 and FD2 period together than any single one of them, i.e. a fluctuation in either of the FD datasets should not be matched by a sterile oscillation. Thus, the quantile $\chi^2_{i,\text{FD1}} \bigoplus \chi^2_{i,\text{FD2}} = \chi^2_{i,\text{FD1}} + \chi^2_{i,\text{FD2}}$ has been plotted as a function of visible energy in the bottom plot of figure 5.7. The top plot shows $\chi^2_{i,\text{ND}}$. In both detectors, one can see the points around 2, 4 and 6 MeV for which the sterile fit is better. One can estimate from figure 5.6, that the Chi-square difference between near and far detector is around six.

Despite the observed sterile best fit is fully consistent with the null hypothesis the Asimov dataset with best fit $\sin^2 2\theta_{14}$ and Δm^2_{41} has been produced andn scan of $-2\ln(\mathcal{L})$ for this dataset is displayed in figure D.1. It does not qualitatively differ much from the experimental data scan.

Taken together, the fit seams robust and no indication for a technical failure of the fit was found.

5.3 Frequentist upper limit

This section focuses on the upper limit as the experimental data fit result was found to be consistent with the no-sterile hypothesis (cf. to the beginning of this chapter). First, the definition and calculation are explained before the result is given later in this section.

The classical frequentist upper limit is defined as that point in parameter space for which one would in 95% of cases observe an effect (i.e. test statistics) larger than actually seen in data [90].

As explained in section 4.3.2, Wilks' theorem does not hold in ($\sin^2 2\theta_{14}$, Δm^2_{41}) space. Therefore, the behavior of the test statistics is a priori unknown. In order to get access to it, pseudo experiments in every point of the ($\sin^2 2\theta_{14}$, Δm^2_{41}) area are needed, which again need to be scanned with a grid. This is due to the fact that the landscape of the negative logarithmic likelihood always has more than one local minimum in Δm^2_{41}. Taking together giving limits in two dimensions includes enormous computing effort and makes giving two dimensional limits technically impossible at current point in time.

As pointed out in section 4.3.2, Wilks' theorem is not violated if Δm^2_{41} is fixed. Hence, the test statistics is known to follow a Chi-square distribution with one degree of freedom and pseudo experiments in every point are not needed. Therefore, the upper limit on $\sin^2 2\theta_{14}$ is given in one dimension as a function of Δm^2_{41}. Thus, the upper limit at 95% confidence level for a given Δm^2_{41} is defined as that $\sin^2 2\theta_{14}$ for which in 95% cases one would observe a larger $\sin^2 2\theta_{14}$ (for that Δm^2_{41}) than seen in experimental data (for that Δm^2_{41}). This definition in sketched in figure 5.8 a).

The following paragraph describes how the upper limit is technically obtained. In doing so, the Asimov approach (cf. section 4.3.1) is used, as the $-2\ln(\mathcal{L})$ landscape is known to have only one minimum in $\sin^2 2\theta_{14}$ and Wilks' theorem holds. Using the Asimov approach is significantly faster than using pseudo experiments and gives a more precise result as the statistics of pseudo experiments would be highly constrained by computing time. The calculation works analogy to the calculation of the sensitivity (cf. section 4.4.2) just that instead of $\sin^2 2\theta_{14,\text{med}}$ the best fit found in experimental data $\sin^2 2\theta_{14,\text{bfd}}$.

More in detail, first, the test statistics is defined as

$$\begin{aligned} TS(\Delta m^2_{41}) := &- \left(-2\ln\big(\mathcal{L}(\vec{x_a}|\sin^2 2\theta_{14,\text{bfd}}, \Delta m^2_{41})\big)\right) \\ &- 2\ln\big(\mathcal{L}(\vec{x_a}|\sin^2 2\theta_{14,\text{true}}, \Delta m^2_{41})\big) \end{aligned} \tag{5.5}$$

where $\mathcal{L}(\vec{x_a}|\sin^2 2\theta_{14,\text{bfd}}, \Delta m^2_{41})$ is the likelihood of Asimov data with parameters ($\sin^2 2\theta_{14,\text{true}}, \Delta m^2_{41}$ ($\vec{x_a}$) evaluated at the experimental data best fit $\sin^2 2\theta_{14}$ for that Δm^2_{41}. This definition is sketched in figure 5.8 b). The upper limit $\sin^2 2\theta_{14,\text{UL}}$ is that $\sin^2 2\theta_{14}$ for which TS=2.71 as illustrated in figure 5.8 c). The test statistics (cf. equation 5.5) is calculated for a set of Asimov datasets with $\sin^2 2\theta_{14} > \sin^2 2\theta_{14,\text{bfd}}$ as $\sin^2 2\theta_{14} > \sin^2 2\theta_{14,\text{bfd}}$ by definition. A spline interpolation between these (TS, $\sin^2 2\theta_{14}$) is performed to extract $\sin^2 2\theta_{14}(\text{TS} = 2.71)$ as sketched in figure 5.8 d).

Figure 5.9 presents the scan of $2\ln(\mathcal{L})$ for experimental data in $\sin^2 2\theta_{14}$ (x-axis) and $\Delta m^2_{41}/\text{eV}^2$ (y-axis). The best fit $\sin^2 2\theta_{14}$ from experimental data for each Δm^2_{41}, $\sin^2 2\theta_{14,\text{bfd}}$ is indicated by the solid black line. The green star marks the global best fit from experimental data.

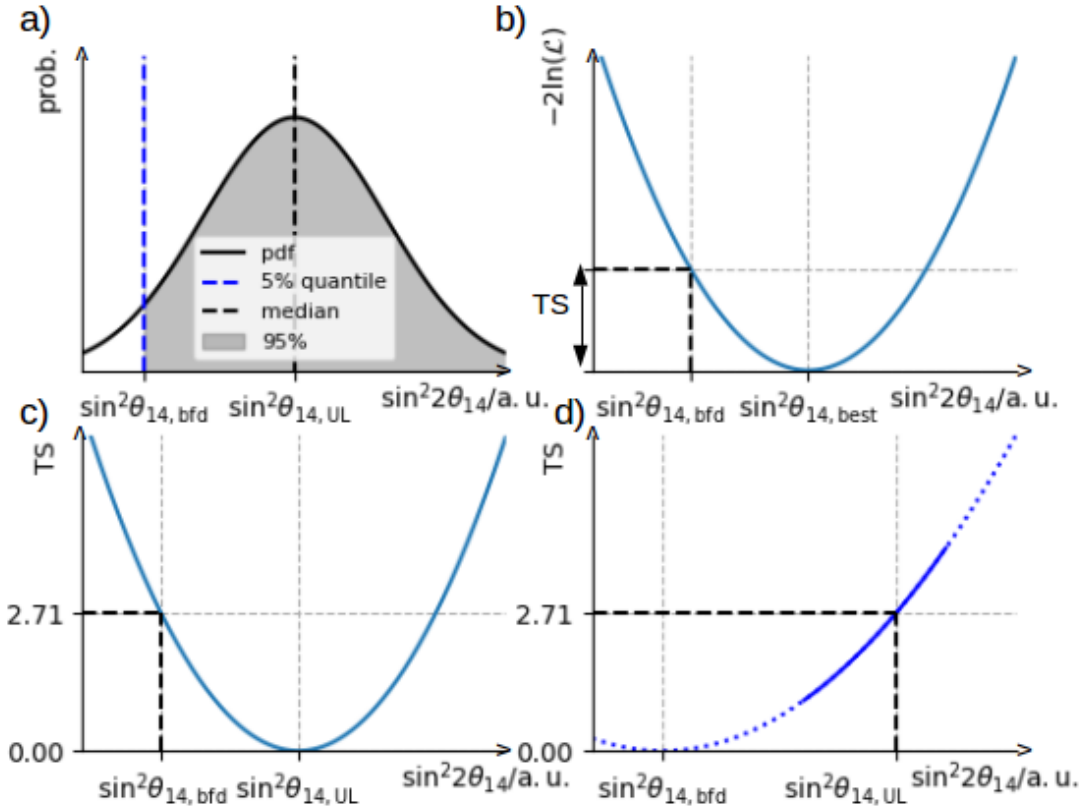

Figure 5.8: Sketches on the calculation of the upper limits: Δm^2_{41} is assumed to have the same fixed value in all subplots. $\sin^2 2\theta_{14,\mathrm{UL}}$ names the upper limit on $\sin^2 2\theta_{14}$ and $\sin^2 2\theta_{14,\mathrm{bfd}}$ the best fit $\sin^2 2\theta_{14}$ on experimental data for that given Δm^2_{41}[a].
a) Definition of the upper limit on $\sin^2 2\theta_{14}$[90]: Sketch of the pdf of best fit $\sin^2 2\theta_{14}$ for pseudo with true value $\sin^2 2\theta_{14,\mathrm{UL}}$; probability versus $\sin^2 2\theta_{14}$ in arbitrary units. The grey shaded area covers 95% of probability and the dashed blue line marks the 5% quantile which matches best fit $\sin^2 2\theta_{14}$ from experimental data $\sin^2 2\theta_{14,\mathrm{bfd}}$.
b) On the definition of the test statistics from equation (5.5): $-2\ln\mathcal{L}$ is plotted versus $\sin^2 2\theta_{14}$ in arbitrary units for pseudo data with median best fit value $\sin^2 2\theta_{14,\mathrm{best}}$. The definition of the test statistics is marked on the y-axis.
c) Illustration of how the upper limit can be obtained from the relation test statistics versus $\sin^2 2\theta_{14}$ (in arbitrary units); $\sin^2 2\theta_{14,\mathrm{UL}}$ is marked on the x-axis (see text).
d) Sketch on the final upper limit calculation. The test statistics TS (y-axis) is obtained for various $\sin^2 2\theta_{14}$ (x-axis, sketched in arbitrary units). A spline is used to describe the inverse function ($\sin^2 2\theta_{14}$ as a function of TS) and its value for TS=2.71 is given as $\sin^2 2\theta_{14,\mathrm{UL}}$. For efficiency reasons and to make the function unique not the whole range of $\sin^2\theta_{14}$ is scanned but only reasonable values $> \sin^2 2\theta_{14,\mathrm{med}}$ as $\sin^2 2\theta_{14,\mathrm{UL}}$ is larger than $> \sin^2 2\theta_{14,\mathrm{bfd}}$ by definition.

[a] i.e. $\sin^2 2\theta_{14,\mathrm{UL}}$ and $\sin^2 2\theta_{14,\mathrm{bfd}}$ are a functions of Δm^2_{41} which are evaluated at the same fixed point here. For reasons of readability the dependence on Δm^2_{41} is not written out.

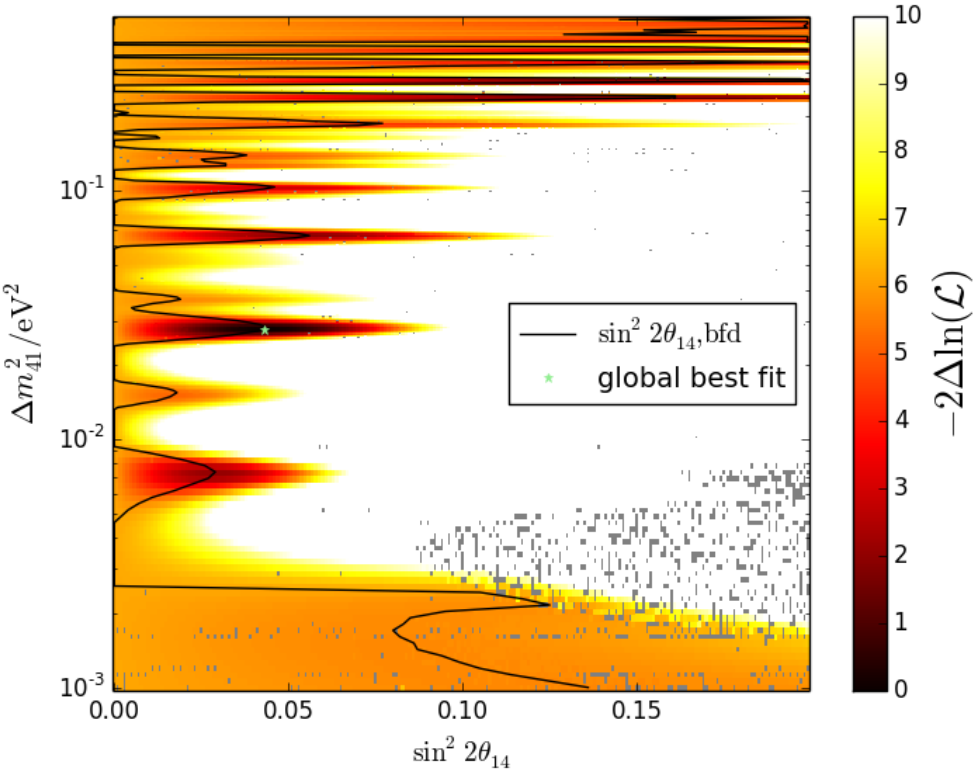

Figure 5.9: Scan of $-2\Delta\ln(\mathcal{L})$ for experimental data in $\sin^2 2\theta_{14}$ (x-axis) and $\Delta m^2_{41}/\mathrm{eV}^2$(y-axis). $-2\Delta\ln(\mathcal{L})$ is represented in the color bar where $\Delta\ln(\mathcal{L}) = \ln(\mathcal{L}) - \ln(\mathcal{L}_{\mathrm{max}})$ is the difference of the natural logarithm of the likelihood to the natural logarithm of the maximum likelihood from this scan. The green star marks the best fit point (i.e. the minimum of $-2\Delta\ln(\mathcal{L})$). The solid black line marks the experimental data best fit $\sin^2 2\theta_{14}$ as a function of Δm^2_{41}.

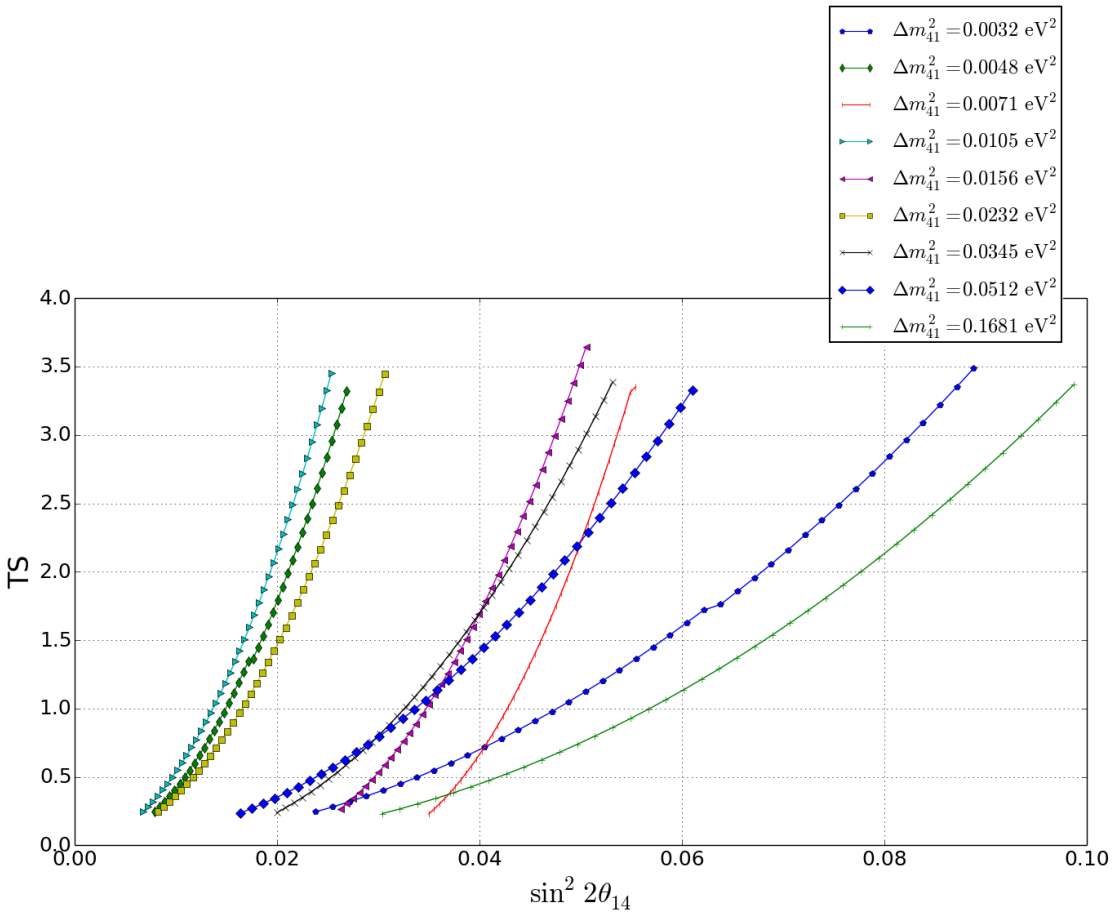

Figure 5.10: TS from equation (5.5)(illustrated in figure 5.8 b)) versus $\sin^2 2\theta_{14}$ for Asimov data with true value $\sin^2 2\theta_{14}$ and various Δm^2_{41} (see legend) as sketched in figure 5.8 d). The spline interpolation is indicated by the solid lines.

Figure 5.10 demonstrates the spline interpolation to describe the test statistics (cf. equation (5.5)) as a function of $\sin^2 2\theta_{14}$ (as illustrated in figure 5.8 d)) exemplary for a set of Δm^2_{41} values (see legend). The markers identify the points that have been calculated and the solid lines the spline interpolation. As explained already in figure 5.8 for a given Δm^2_{41} the $\sin^2 2\theta_{14}$ for which TS=2.71 is the upper limit on $\sin^2 2\theta_{14}$, $\sin^2 2\theta_{14,\mathrm{UL}}$. The upper limit calculated with this procedure has been confirmed with pseudo experiments for three data points [75].

Figure 5.11 presents the upper limit on $\sin^2 2\theta_{14}$ as a function of Δm^2_{41}. The upper limit at 95% confidence level is plotted with a solid black line. For comparison the median sensitivity is shown in solid green and its 1σ (2σ) uncertainty band is indicated in green (yellow) (cf. figure 4.38). The global best fit of experimental data is indicated with a blue diamond. As expected and natural for the approach used in this work, the upper limit is not better than the expected sensitivity (cf. section 4.4.2). Also, the upper limit is mostly in the 1σ and 2σ range of the sensitivity uncertainty and worst in the area around the global best fit.

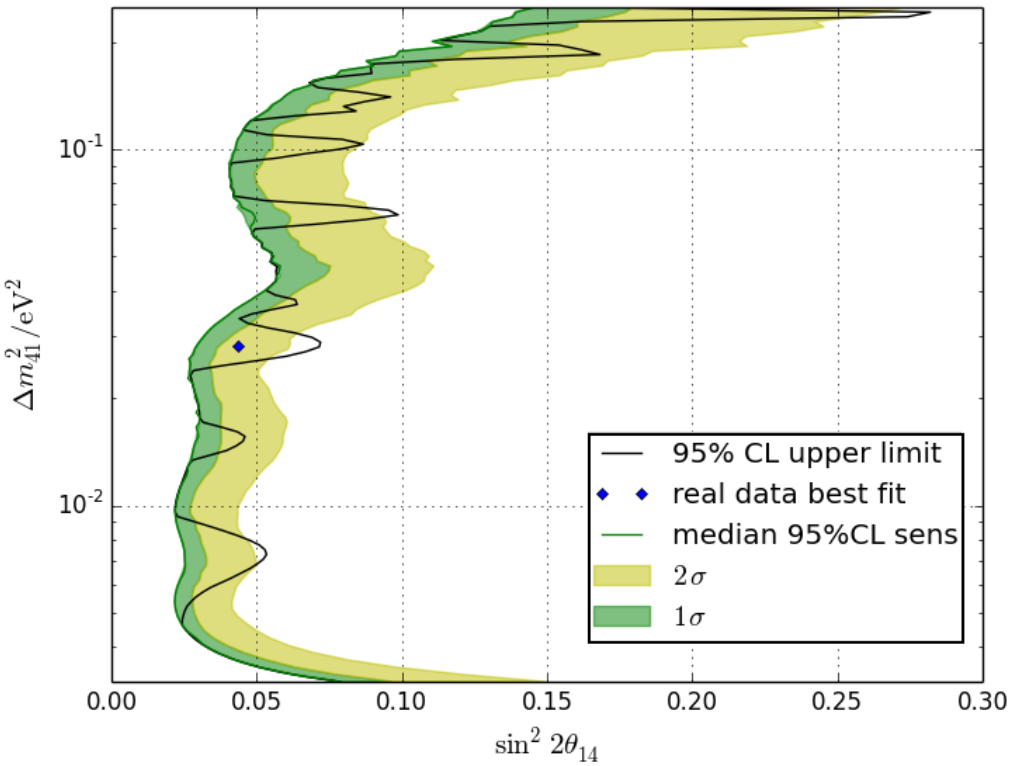

Figure 5.11: Upper limit at 95% confidence level on $\sin^2 2\theta_{14}$(x-axis) as a function of Δm^2_{41} (y-axis). The upper limit at 95% confidence level is indicated by the solid black line. The median sensitivity (also shown in figure 4.38) is plotted with a green solid line for comparison. Its 1σ uncertainty is shaded in green and its 2σ uncertainty is shaded in yellow. The best fit from experimental data is indicated with a blue diamond.

5.4 Comparison to RENO and Daya Bay

There are two other big reactor experiments designed to measure $\sin^2 2\theta_{13}$ that are similar to Double Chooz: RENO and Daya Bay. Both collaborations have published limits on (Δm^2_{41}, $\sin^2 2\theta_{14}$) [129] [21]. These limits are two dimensional limits on the combination of (Δm^2_{41}, $\sin^2 2\theta_{14}$) while the limits in this work are limits on $\sin^2 2\theta_{14}$ if Δm^2_{41} is given. In other words, Double Chooz does not provide a statement about likeliness of any Δm^2_{41}. RENO and Daya Bay give information about likeliness of values for Δm^2_{41} in combination with $\sin^2 2\theta_{14}$. This means that one can check the 95% excluded $\sin^2 2\theta_{14}$ for an external value of Δm^2_{41} directly from figure 5.11 but not directly from the plots provided by RENO and Daya Bay since the likeliness of Δm^2_{41} itself is included. Mathematically it means that 95% coverage corresponds to the two dimensional (Δm^2_{41}, $\sin^2 2\theta_{14}$) area for RENO and Daya Bay while it corresponds to one dimension ($\sin^2 2\theta_{14}$) for Double Chooz. Methodically, it means that Double Chooz uses a test statistics of general type $TS_{1\mathrm{D}}$ (cf. equation (4.37)) while RENO and Daya Bay use a test statistics of general type $TS_{2\mathrm{D}}$ (cf. equation (4.34) [129] [21].

Therefore, the limits from RENO, Daya Bay and Double Chooz do not have the identical physical meaning. However, the limited comparison of the provided by RENO, Daya Bay and Double Chooz is presented in figure 5.12. The upper limit from this work is plotted with a solid black line the upper limit from Daya Bay([21], full configuration, gadolinium selection) with a light grey line and from RENO([129], 500 days of lifetime, gadolinium selection) with a light green line. In most of the Δm^2_{41} area, the Daya Bay constraints are stronger than from Double Chooz which is expected to be due to the fact that Daya Bay detectors have a larger total target mass volume, their reactors provide more thermal power and that they collected more statistics (cf. figure 5.13). However, the Double Chooz constraints are in most of the Δm^2_{41} range stronger than RENO's. Adding inverse beta decay candidates in all detectors the RENO datasets used for their sterile analysis contains slightly more inverse beta decay candidates than the Double Chooz datasets together (cf. figure 5.13). In this work, it was decided to not calculate limits for $\Delta m^2_{41} \leq \Delta m^2_{ee}$ as for $\Delta m^2_{41} = \Delta m^2_{ee}$ the limits of $\sin^2 2\theta_{13}$ and $\sin^2 2\theta_{14}$ would be identical and for smaller Δm^2_{41} Double Chooz is barely sensitive. In contrast, RENO and Daya Bay analysis differ in terms of $\sin^2 2\theta_{13}$ handling, put constraints on it and published limits in $\Delta m^2_{41} \leq \Delta m^2_{ee}$ region. The nonexistence of constraints on $\sin^2 2\theta_{13}$ is an aspect for which limits provided in this work are more conservative. This effect is large for $\Delta m^2_{41} \approx \Delta m^2_{ee}$ and small for $\Delta m^2_{41} > \Delta m^2_{ee}$ (cf. section 4.3.6).

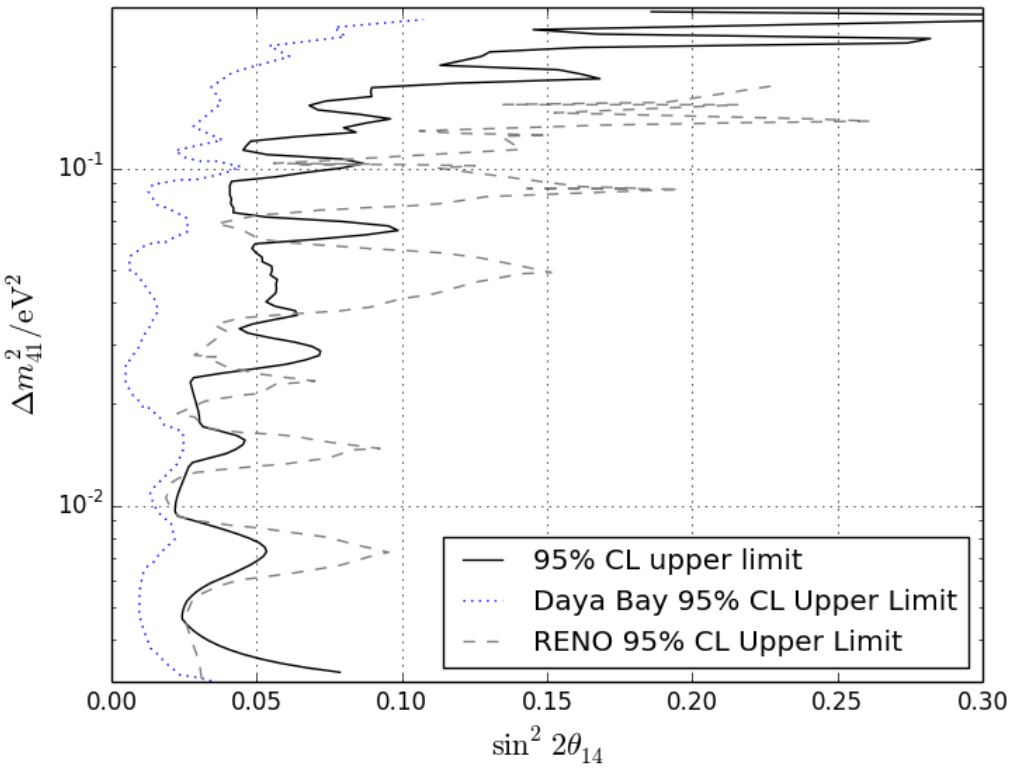

Figure 5.12: Upper limits at 95% confidence level provided by Double Chooz (this work), Daya Bay [21] and RENO [129] plotted Δm^2_{41} versus $\sin^2 2\theta_{14}$. The upper limit from Daya Bay is plotted with a dotted blue line, the upper limit from RENO with a dashed grey line and the upper limit from this work with a solid black line. The upper limit provided by Daya Bay and RENO are two dimensional limits, i.e. putting constraints on the combination of Δm^2_{41} versus $\sin^2 2\theta_{14}$. In contrast, the upper limit provided in this work is a one dimensional limit on $\sin^2 2\theta_{14}$ as a function of Δm^2_{41}. Thus, the limits by Daya Bay and RENO do not have the identical physical meaning (see text for details).

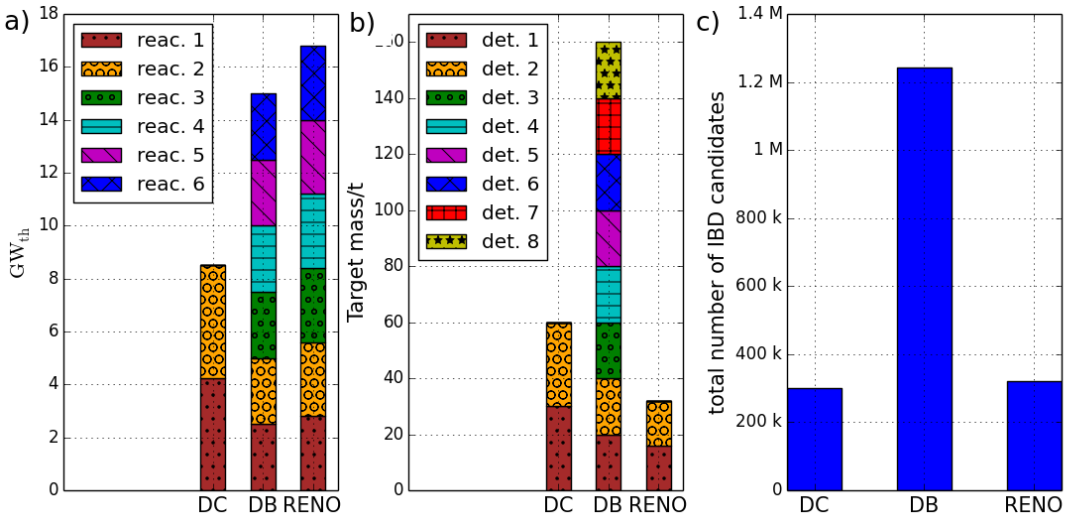

Figure 5.13: a) reactor power/GW$_{\text{th}}$(y-axis) available for Double Chooz (DC, left stack), Daya Bay (DB, middle stack) and RENO (right stack) experiments b) target mass/t (y-axis) of Double Chooz(left stack), Daya Bay(middle stack) and RENO (right stack) experimental setups used for sterile analyses c) total number of ibd candidates (y-axis) in datasets used for sterile analysis by Double Chooz (DC, left stack), DayaBay (DB, middle stack) and RENO (right stack).

5.5 Transfer to 3+2 model

Seven additional neutrino mixing angles exist in the 3+2 model (cf. section 1.2), namely θ_{14}, θ_{24}, θ_{34}, θ_{15}, θ_{25}, θ_{35}, θ_{45}. The PMNS-Matrix may be defined as

$$\mathrm{U} = \mathrm{R}_{45}\mathrm{R}_{35}\mathrm{R}_{34}\mathrm{R}_{25}\mathrm{R}_{24}\mathrm{R}_{23}\mathrm{R}_{15}\mathrm{R}_{14}\mathrm{R}_{13}\mathrm{R}_{12} = \mathrm{R}_{45}\mathrm{R}_{35}\mathrm{R}_{25}\mathrm{R}_{15}\mathrm{R}_{34}\mathrm{R}_{24}\mathrm{R}_{14}\mathrm{R}_{23}\mathrm{R}_{13}\mathrm{R}_{12} \quad (5.6)$$

in the 3+2 model, yielding

$$\mathrm{U}_{e1} = \cos\theta_{15}\cos\theta_{14}\cos\theta_{13}\cos\theta_{12} \quad (5.7)$$
$$\mathrm{U}_{e2} = \cos\theta_{15}\cos\theta_{14}\cos\theta_{13}\sin\theta_{12} \quad (5.8)$$
$$\mathrm{U}_{e3} = \cos\theta_{15}\cos\theta_{14}\sin\theta_{13} \quad (5.9)$$
$$\mathrm{U}_{e4} = \cos\theta_{15}\sin\theta_{14} \quad (5.10)$$
$$\mathrm{U}_{e5} = \sin\theta_{15} \quad . \quad (5.11)$$

Thus, with equation (1.17), the only non-standard mixing angles entering the anti-electron-neutrino survival probability are θ_{14} and θ_{15}. It is approximately given by:

$$P_{ee} \approx 1 - \sin^2 2\theta_{13}\sin^2(\Delta_{31}) - \sin^2 2\theta_{14}\sin^2(\Delta_{41}) - \sin^2 2\theta_{15}\sin^2(\Delta_{51}) \quad (5.12)$$

(see section E). Equation (5.12) tells that two sterile states with similar mass would be indistinguishable. Also, interference between oscillations related to both sterile states could occur depending on m_4^2, m_5^2. Figure 5.14 shows the far detectors neutrino events in 3+2 model and 3+1 model relative to the no-sterile model as a function of visible energy for ($\sin^2 2\theta_{14} = 0.043$, $\Delta m_{41}^2 = 0.029\,\mathrm{eV}^2$, $\sin^2 2\theta_{14} = 0.047$, $\Delta m_{51}^2 = 0.038\,\mathrm{eV}^2$, $\sin^2 2\theta_{14} = 0.091$). The same plot for the near detector may be found in figure E.1. One can see that the survival probability in the 3+2 model looks similar to a typical 3+1

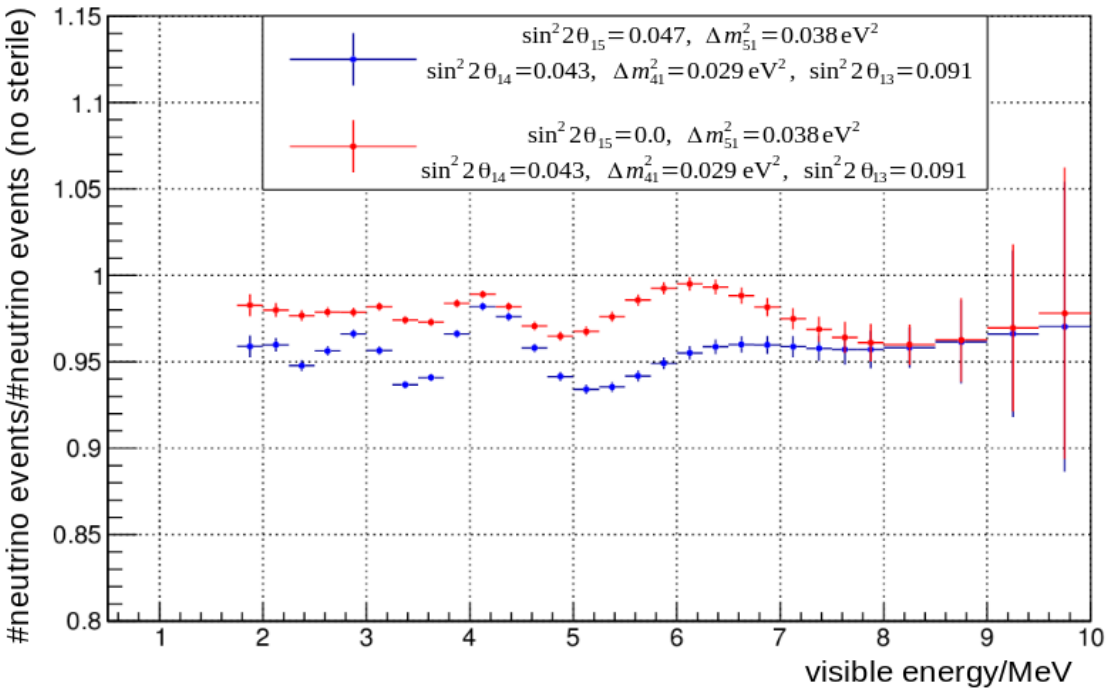

Figure 5.14: Far detector neutrino events in 3+2 model and 3+1 model relative to no-sterile model versus visible energy ($\sin^2 2\theta_{14} = 0.043$, $\Delta m^2_{41} = 0.029\,\mathrm{eV}^2$, $\sin^2 2\theta_{14} = 0.047$, $\Delta m^2_{51} = 0.038\,\mathrm{eV}^2$, $\sin^2 2\theta_{14} = 0.091$) [119]. This plot has been taken from [119] and modified.

model survival probability just with different Δm^2_{41}. Interference occurs in particular if $O\left(\left|\Delta m^2_{41}\right|\right) = O\left(\left|\Delta m^2_{51}\right|\right)$ where the signature will depend in detail on the two mass squared differences. As Double Chooz basically covers the sensitivity $0.005\,\mathrm{eV}^2 \leq \Delta m^2 \leq 0.2\,\mathrm{eV}^2$ (i.e. one order of magnitude) this makes giving limits in the 3+2 model even more non trivial and would require far too much computing effort at the current point in time. If $\Delta m^2_{41} << \Delta m^2_{51} \geq 0.3\,\mathrm{eV}^2$ oscillation signatures due to the fifth neutrino state get washed out and only lead to a smaller normalization in all detectors. An example is shown in figure E.2. Thus, the limits obtained in this work hold for models with $\Delta m^2_{51} \geq 0.3\,\mathrm{eV}^2$. More details on oscillation signatures in the 3+2 model can be found in [119].

Chapter 6

Summary

The search for so called light sterile neutrino with the Double Chooz reactor neutrino experiment was done for the first time in this work. Oscillation effects in the 3+1 model can be described by only two new parameters in very good approximation: θ_{14} and Δm^2_{41} (cf. chapter 1.2) where Double Chooz is sensitive to the new mixing angle θ_{14}. In contrast to earlier θ_{13}, data from both neutron capture on gadolinium and hydrogen has been selected to increase statistics. This is the current standard data selection applied in Double Chooz (see chapter 3 for details). A new Poisson likelihood fit technique, virtually relying only on the comparison of near and far detector data (i.e. independent from any reactor flux model), was used. The concept of this approach was developed in this work and based on the work by Stefan Schoppmann and described in detail in chapter 4. This work was done in close cooperation with Philipp Soldin who focused on the technical part and on the θ_{13} fit. In order to ensure consistency with the θ_{13} fit and as much crosschecking as possible, θ_{13} and sterile fit use the same software which was fully validated. Inter alia, by crosschecks with two other fit approaches doing the θ_{13} fit which were developed in the United States of America respectively Japan (cf. section 4.3.1). Moreover, data challenges have been done and systematics effects have been studied where it is found that the analysis is limited by statistics in most of the range where Double Chooz is sensitive (around $0.004\,\mathrm{eV}^2 \lesssim \Delta m^2_{41} \gtrsim 0.2\,\mathrm{eV}^2$). Also, it is demonstrated that the fit is indeed independent from the reactor flux model by adding artificial distortions (cf. section 4.3.4 and following). A huge challenge for this analysis is that there are always multiple solutions w.r.t. Δm^2_{41} and that any statistical fluctuation in data induces a best fit with $\sin^2 2\theta_{14} > 0$. Therefore, Wilks' theorem [127] does not hold and pseudo experiments are needed to obtain p-value, sensitivity and allowed regions. Each pseudo experiment needs to be scanned w.r.t. Δm^2_{41} to avoid problems due to local minima (see section 4.3.2). Finally, the analysis of the experimental data showed a p-value of 24.7% ± 2.2% i.e. fully consistence with the no-sterile hypothesis. Upper limits on $\sin^2 2\theta_{14}$ are given as a function of Δm^2_{41} after the best fit result has been carefully validated (cf. chapter 5). That is because two dimensional limits in (Δm^2_{41}, $\sin^2 2\theta_{14}$) space are computationally impossible at current point in time. The limits on $\sin^2 2\theta_{14}$ are presented in figure 5.11 and cover the region $0.004\,\mathrm{eV}^2 \lesssim \Delta m^2_{41} \gtrsim 0.2\,\mathrm{eV}^2$. As there is effort ongoing to further improve computation time, future analysis may be able to give limits in two dimensional space. Future analysis will be able to get higher statistics by running on the final Double Chooz dataset containing three years of exposure time with two detectors instead of the 18 month used in this work. Also, the final dataset will include around 25 exposure days of reactor off data including reactor off measurements for the near detector [50]. Analysis of this data is expected to

improve background constraints remarkably. Moreover, systematical limitations may be reduced by precise measurement of the detector volume during reconstruction suppressing dominant systematical uncertainty due to the so called proton number significantly.

Appendix A

Backgrounds

This chapter collects plots referring to the background processes mentioned in section 3.7.

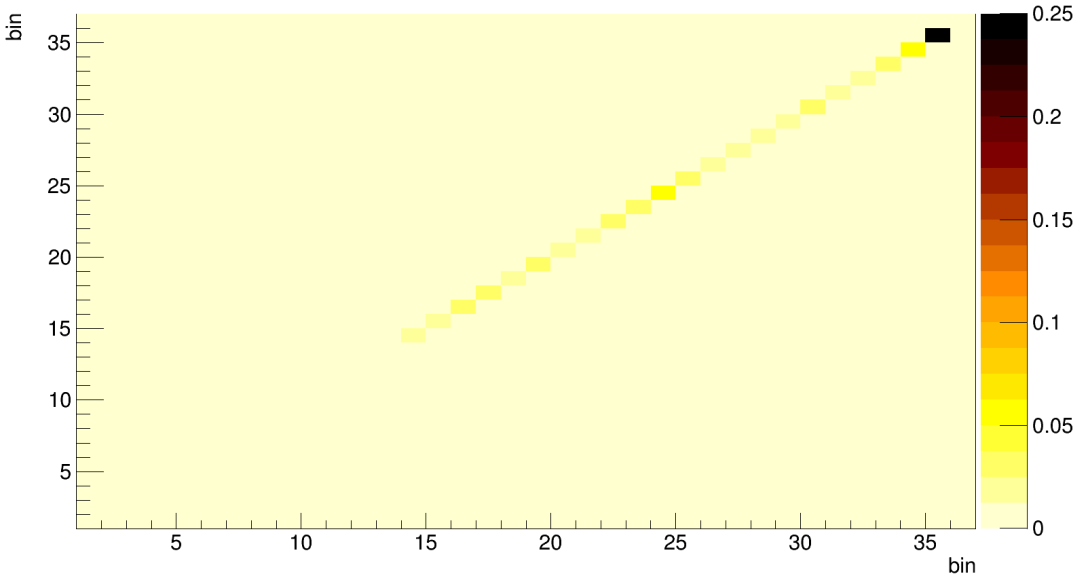

Figure A.1: Covariance matrix for the FD1 accidental background obtained with the offtime method as explained in section 3.7.1.

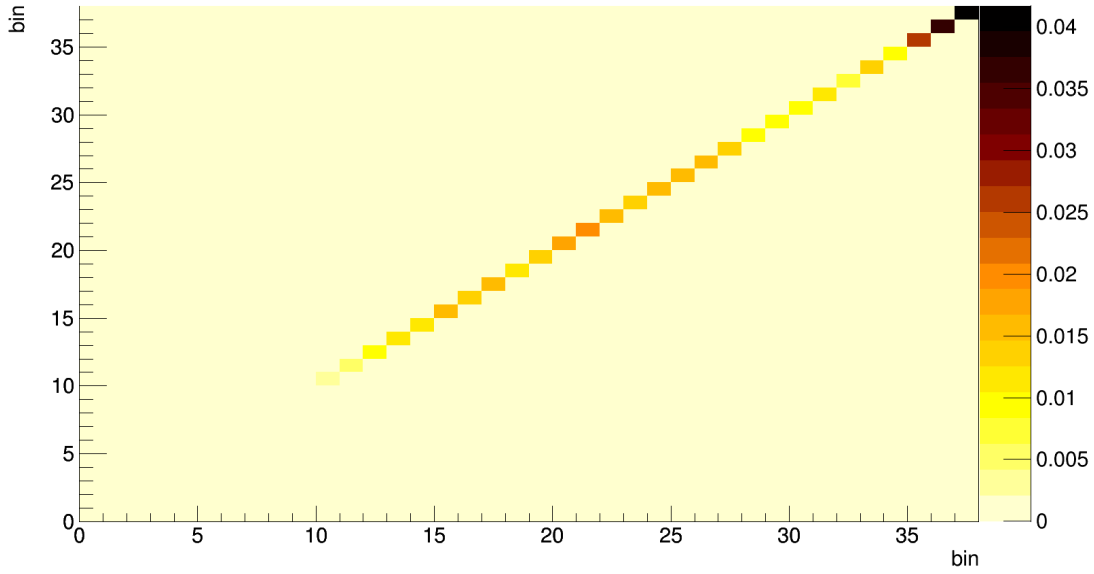

Figure A.2: Covariance matrix for accidental background in the near detector obtained with the offtime method as explained in section 3.7.1.

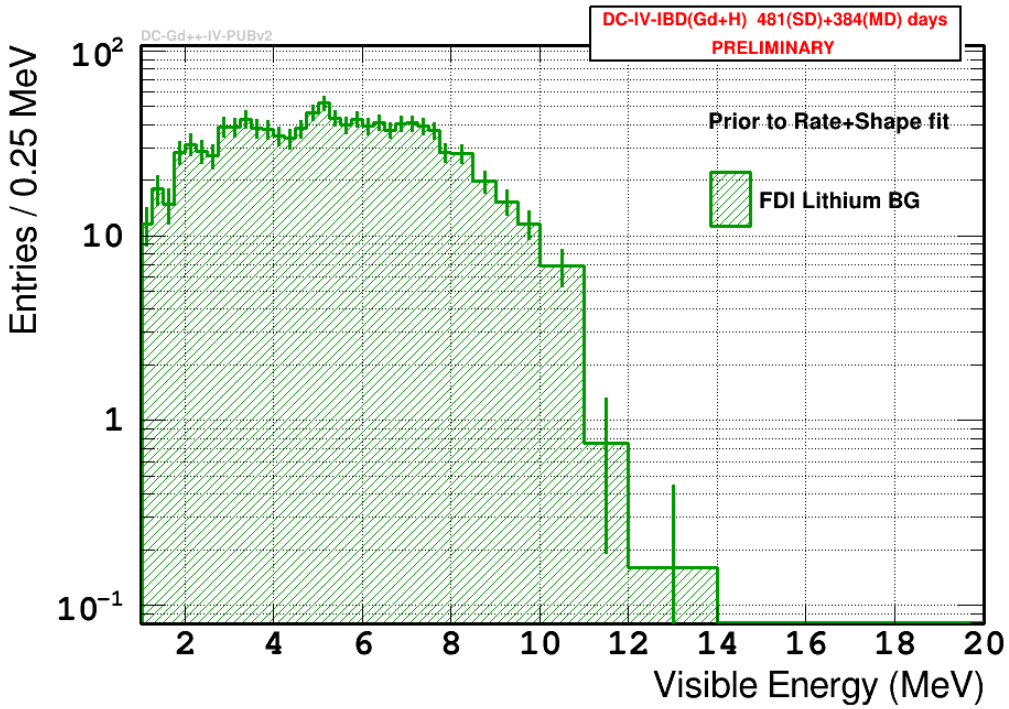

Figure A.3: FD1 lithium background data sample obtained based on the lithium likelihood as explained in the text [56]. Entries versus visible energy are shown.

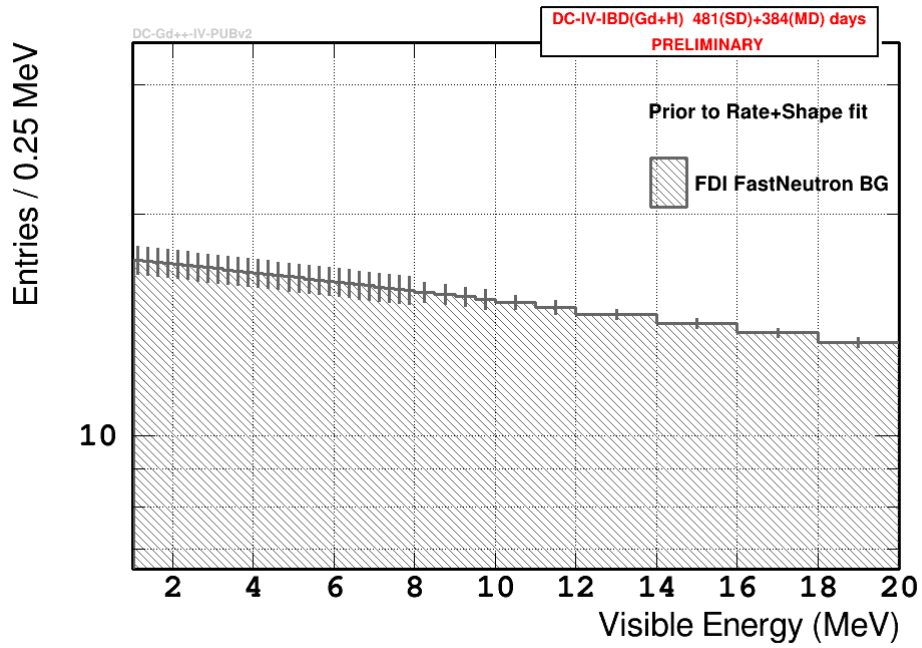

Figure A.4: FD1 fast neutron and stopping muon background data sample obtained from inner veto tagged events as explained in the text [56]. Entries versus visible energy are shown.

Appendix B

Input model

This chapter collects additional plots and tables referred to in section 4.2.

B.1 Oscillation probability

Figure B.1 provides comparison of oscillation formula approximation used in this work to the full four flavor oscillation for example parameters and is similar to figure 4.7.

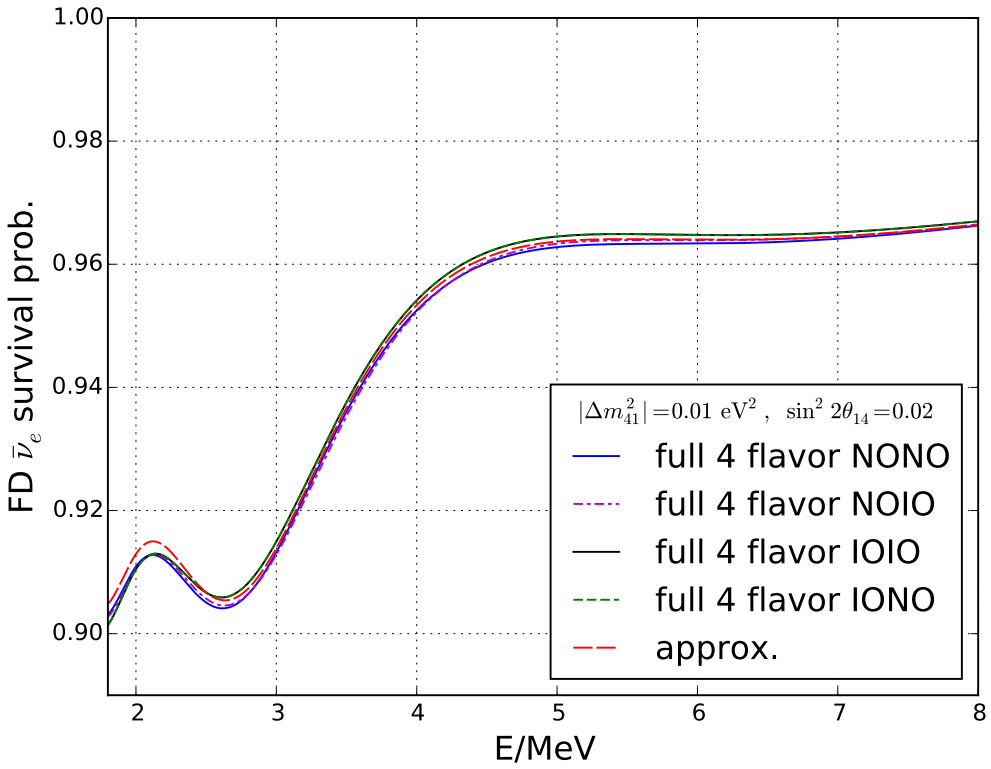

Figure B.1: Comparison of the approximation for the electron antineutrino survival probability used in this work to the full four flavor oscillation for example parameters of $\sin^2 2\theta_{14} = 0.02$ and $|\Delta m^2_{41}| = 0.02\,\mathrm{eV}^2$. The electron antineutrino survival probability versus true energy is shown. The approximation used in this work is plotted in dashed red. The full four flavor probability is shown in solid blue for scenario NONO, in dashed magenta for scenario NOIO in solid black, for scenario IOIO and in dashed green for scenario IONO. $\theta_{13} = 8.52\,^\circ$ ($\sin^2 2\theta_{13} = 0.086$) and Δm^2_{31}=0.00252 eV^2 has been used for all probabilities shown in this figure.

B.2 Energy and reactor flux

Table B.1 provides the correlations coefficients between energy calibration parameters in terms of physical cause (a_{LNL}, b_{LNL}, $b_{\mathrm{St/U}}$, b_{QNL} and c_{QNL}, cf. section 4.2.2). Central values and uncertainties of these parameters can be found in table B.2. Figures B.2 and B.3 show the covariance matrix of the reactor flux parameters for the FD1-On(FD2) dataset.

Table B.1: Correlations coefficients between energy calibration parameters in terms of physical cause. Correlations are assumed to be identical for FD1-On, FD2 and ND . The light non linearity parameters a_{LNL} and b_{LNL} are considered to be fully correlated between FD1-On, FD2 and ND while $b_{\mathrm{St/U}}$, b_{QNL} and c_{QNL} are considered to be fully uncorrelated between FD1, FD2 and ND. All correlations are identical to the correlations used in the θ_{13} fit [44].

parameter	a_{LNL}	b_{LNL}	$b_{\mathrm{St/U}}$	b_{QNL}	c_{QNL}
a_{LNL}	1	-1	0	0	0
b_{LNL}	-1	1	0	0	0
$b_{\mathrm{St/U}}$	0	0	1	0	0
b_{QNL}	0	0	0	1	-0.45
c_{QNL}	0	0	0	-0.45	1

Table B.2: Energy calibration parameters and uncertainties in terms of physical cause. All parameters are identical to the parameters in the θ_{13} fit [44].

parameter	FD1	FD2	ND
a_{LNL}		0.0091 ± 0.0157	
b_{LNL}		0.9959 ± 0.0071	
$b_{\mathrm{St/U}}$	1.0000 ± 0.0042	1.0000± 0.0045	1.0000± 0.0060
b_{QNL}	1.0000 ± 0.0012	1.0000 ± 0.0015	1.0000 ± 0.0011
c_{QNL}	0.00000 ± 0.00053	0.00000 ± 0.00069	0.00000 ± 0.00048

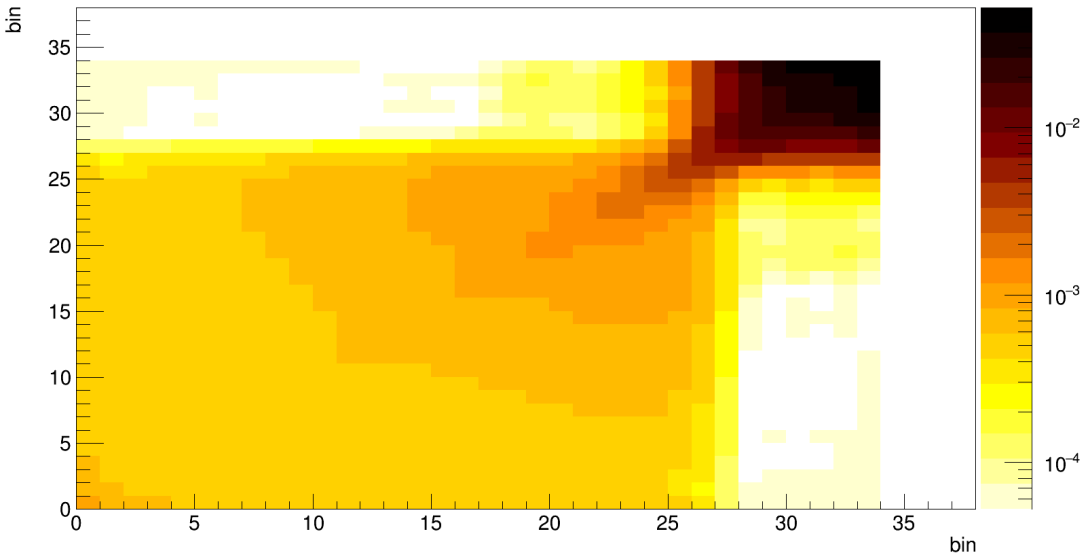

Figure B.2: Covariance matrix of the reactor flux parameters for the FD1-On dataset. This matrix has been generated without using the Bugey4 anchor point (cf. section 3.4).

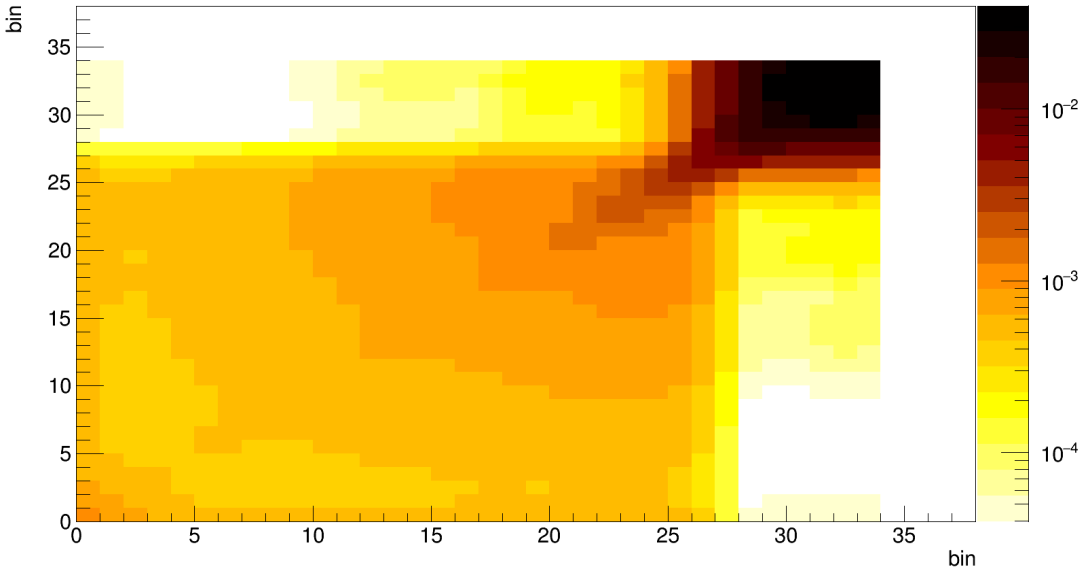

Figure B.3: Covariance matrix of the reactor flux parameters for the FD2 dataset. This matrix has been generated without using the Bugey4 anchor point (cf. section 3.4).

Appendix C

Validation of the algorithm

This section collects additional information regarding section 4.3. Figure C.1 shows a comparison of the LLH-FF fit and D2D Chi-square fit (Thiago) for a breakdown of the systematics for $\sin^2 2\theta_{13}$ from the N-1 test. The values can be found in table 4.9. Figure C.2 shows the post fit correlation matrix from the $\sin^2 2\theta_{13}$ fit for energy and correlated reactor flux parameters. Figure C.2 is intended to demonstrate that the correlations between reactor flux and energy parameters may significantly differ from zero. Particular values are not important.

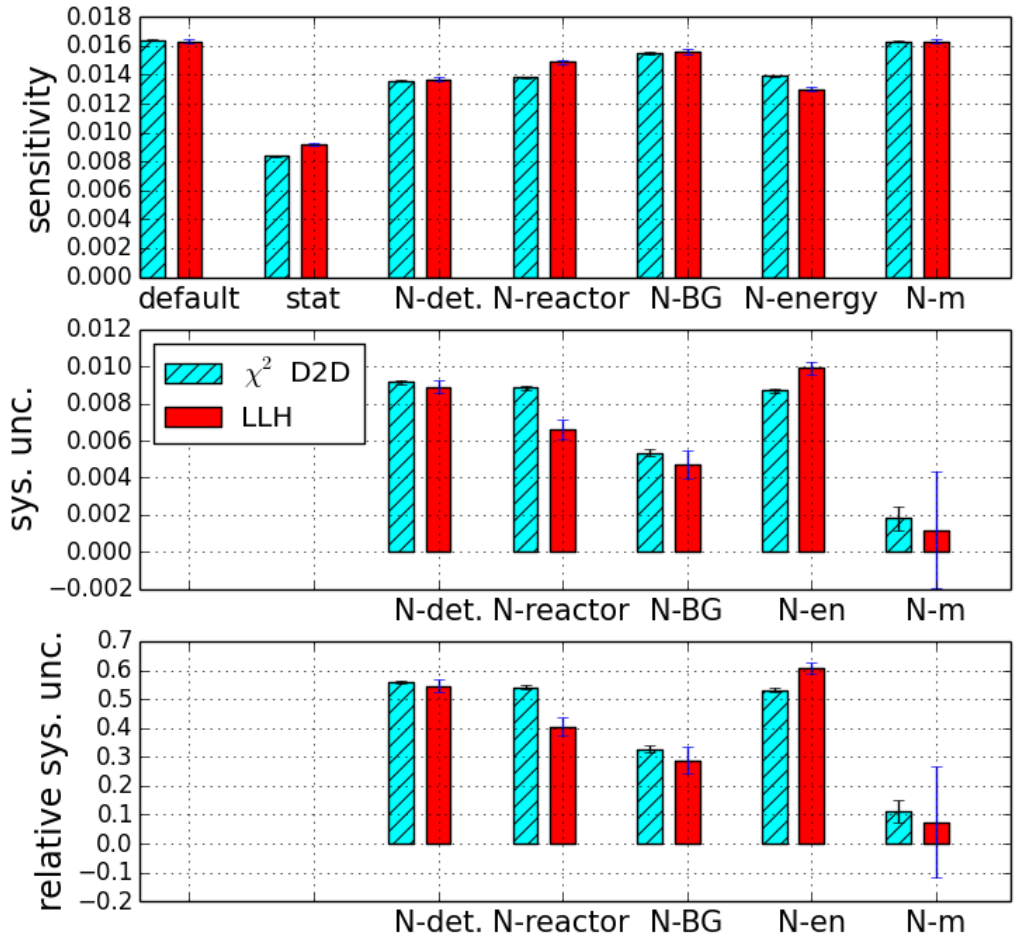

Figure C.1: Comparison of the LLH-FF fit and D2D Chi-square fit (Thiago) for a breakdown of the systematics for $\sin^2 2\theta_{13}$ from the N-1 test. The top plot shows the N-1 test sensitivity results, the plot in the middle shows $\sigma_{\mathrm{N-1,X}}$ (cf. equation (4.26)) and the plot in the bottom shows $r_{\mathrm{N-1,X}}$ (cf. equation (4.27)). The values can be found in table 4.9 The error bars correspond to a rounding uncertainty of 0.00005 for the Chi-square fit and to 1% of the N-1 test results for the likelihood fit.

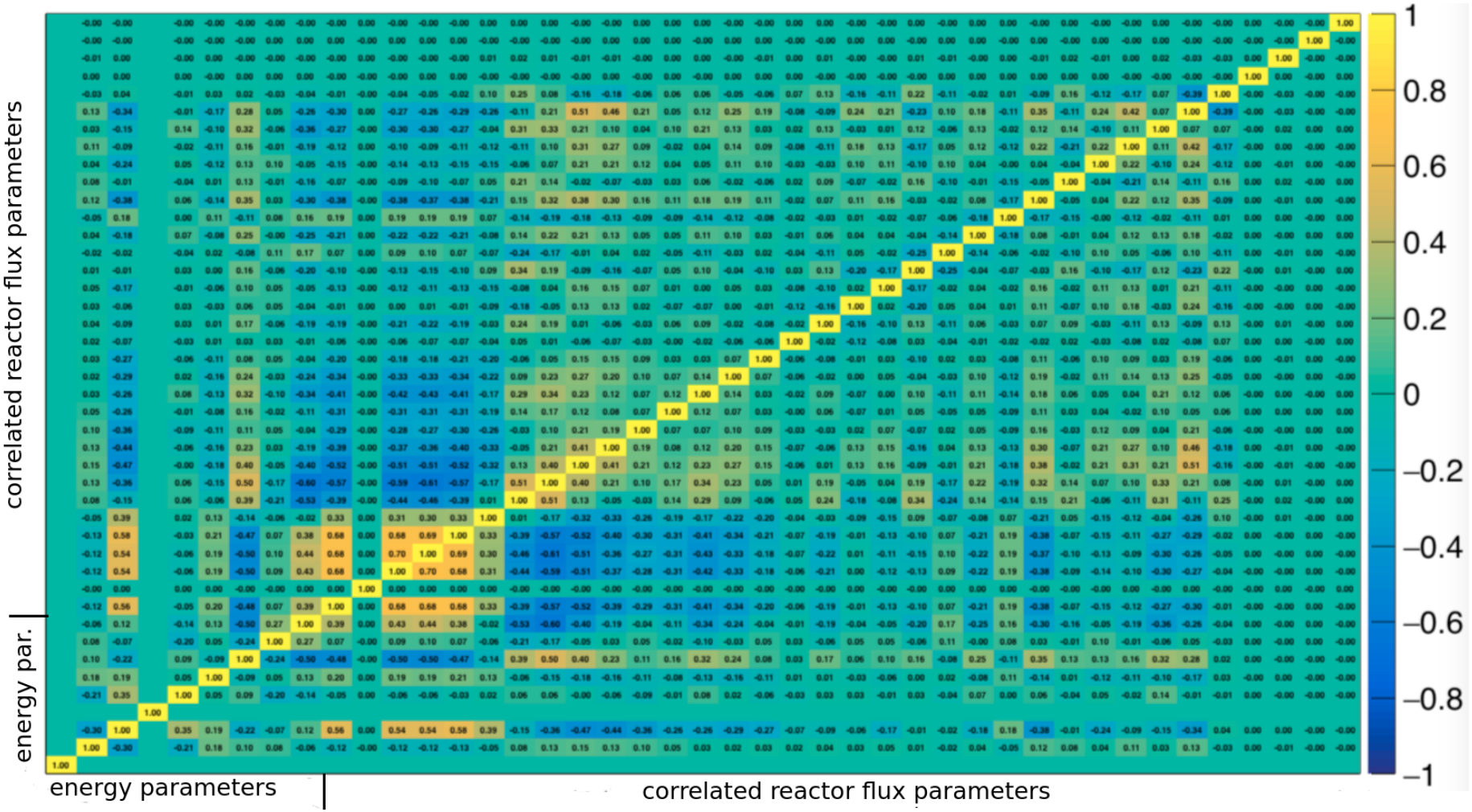

Figure C.2: $\sin^2 2\theta_{13}$ post fit correlation matrix for energy and correlated reactor flux parameters [118] (modified). This figure is intended to demonstrate that the correlations between reactor flux and energy parameters may significantly differ from zero. The first nine parameters are the energy parameters in the fit internal eigenbasis (cf. section 4.2.1). The other parameters are the correlated reactor flux parameters.

C.1 Data challenges

Figures C.3 - C.11 are two dimensional scan of $-2\ln(\mathcal{L})$ that were done during the data challenge described in section 4.3.4 and listed in table 4.12.

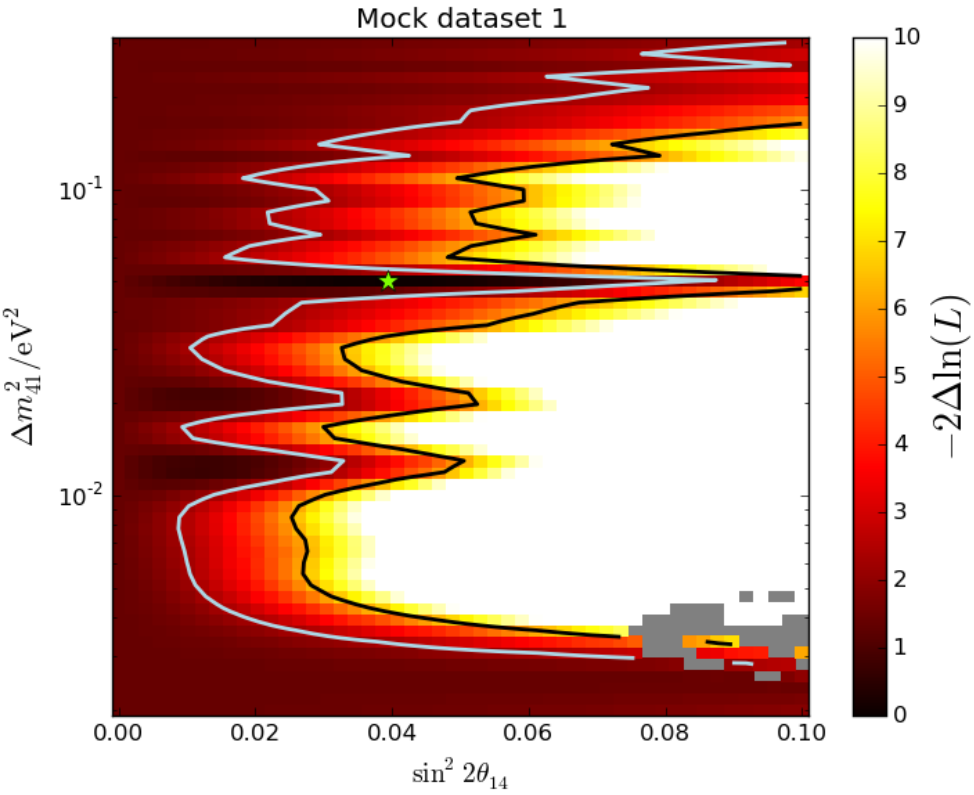

Figure C.3: Two dimensional scan of $-2\ln(\mathcal{L})$ in $\sin^2 2\theta_{14}$ (x-axis) and Δm^2_{41} (y-axis) of the first toy dataset from table 4.12. where $-2\Delta\ln(L)$ is represented by the color bar. $\Delta\ln(L) = \ln(\mathcal{L}) - \ln(\mathcal{L}_{\mathrm{max}})$ is the difference of the natural logarithm of the likelihood to the natural logarithm of the maximum likelihood. The 1σ (2σ) region for the local ($\sin^2 2\theta_{14}$, Δm^2_{41}) range in which Wilks' theorem holds is marked by the light blue (black) line. Gray areas indicate missing data. The same plot with an other z-axis (color bar) scaling is provided in figure C.4.

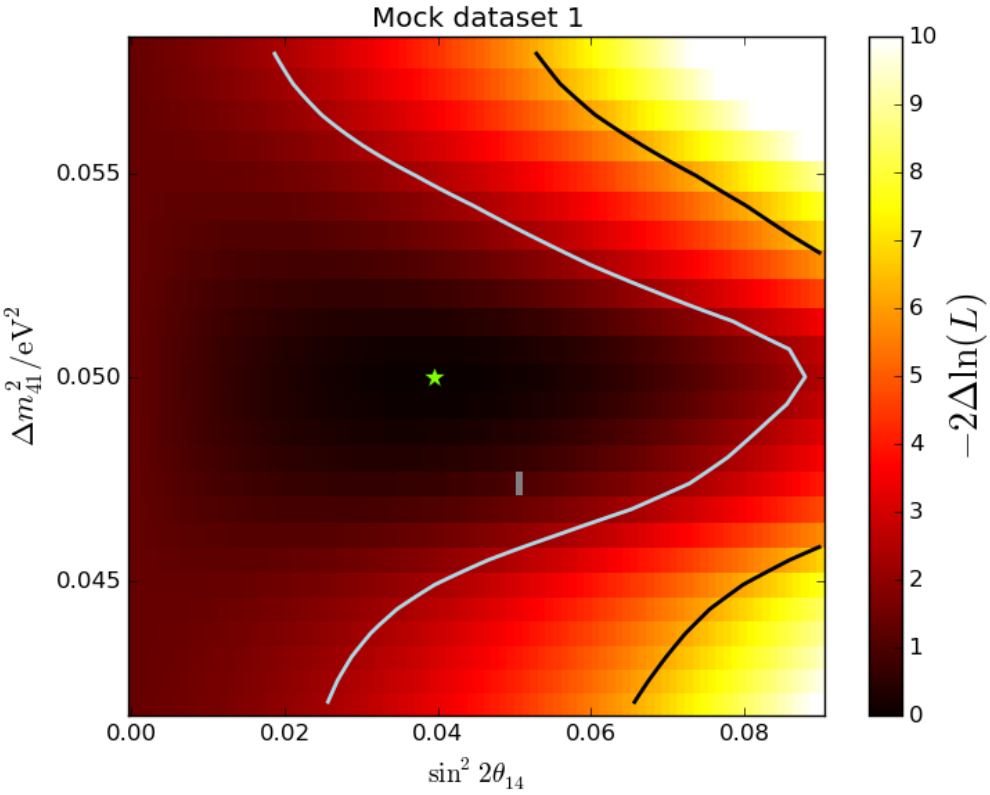

Figure C.4: Two dimensional scan of $-2\ln(\mathcal{L})$ in $\sin^2 2\theta_{14}$ (x-axis) and Δm^2_{41} (y-axis) of the first toy dataset from table 4.12. where $-2\Delta\ln(L)$ is represented by the color bar. $\Delta\ln(L) = \ln(\mathcal{L}) - \ln(\mathcal{L}_{\max})$ is the difference of the natural logarithm of the likelihood to the natural logarithm of the maximum likelihood. The 1σ (2σ) region for the local ($\sin^2 2\theta_{14}$, Δm^2_{41}) range in which Wilks' theorem holds is marked by the light blue (black) line. Gray areas indicate missing data. The same plot with an other z-axis (color bar) scaling is provided in figure C.3.

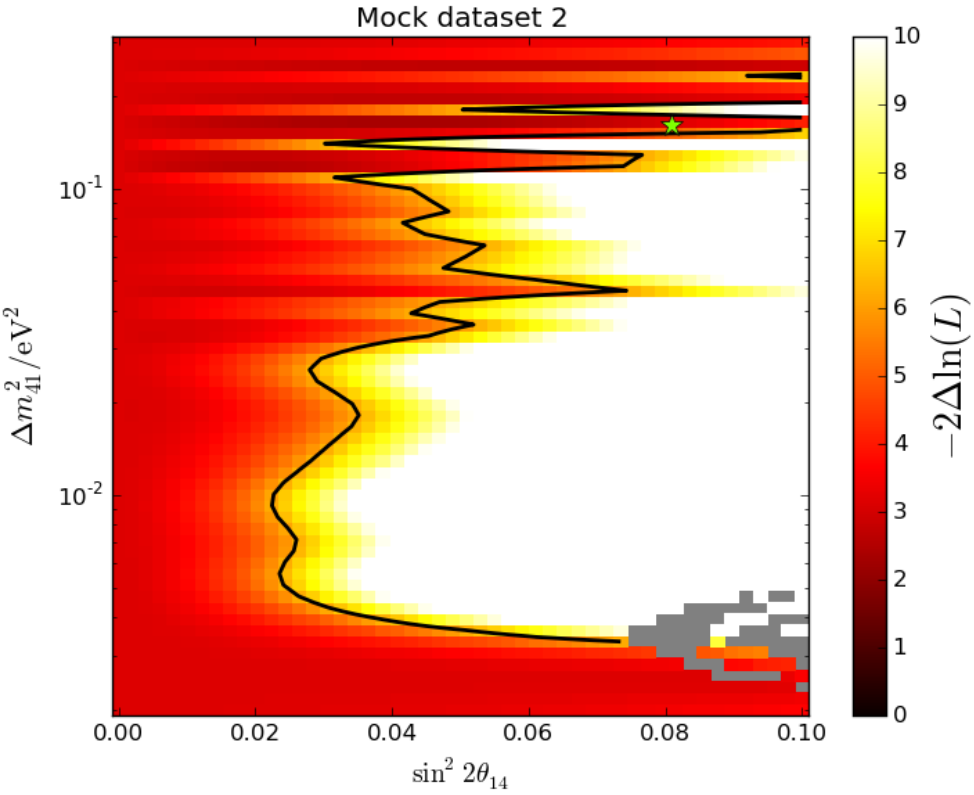

Figure C.5: Two dimensional scan of $-2\ln(\mathcal{L})$ in $\sin^2 2\theta_{14}$ (x-axis) and Δm^2_{41} (y-axis) of the second toy dataset from table 4.12. where $-2\Delta\ln(L)$ is represented by the color bar. $\Delta\ln(L) = \ln(\mathcal{L}) - \ln(\mathcal{L}_{\max})$ is the difference of the natural logarithm of the likelihood to the natural logarithm of the maximum likelihood. The 1σ (2σ) region for the local ($\sin^2 2\theta_{14}$, Δm^2_{41}) range in which Wilks' theorem holds is marked by the light blue (black) line. Gray areas indicate missing data. The same plot with an other z-axis (color bar) scaling is provided in figure C.6.

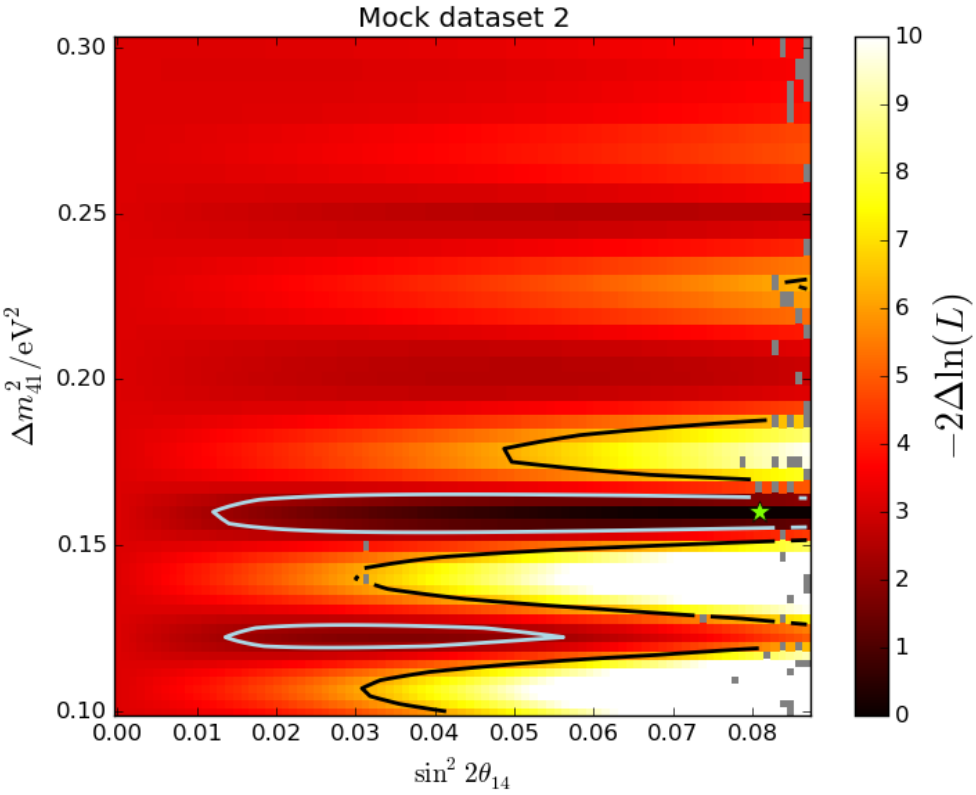

Figure C.6: Two dimensional scan of $-2\ln(\mathcal{L})$ in $\sin^2 2\theta_{14}$ (x-axis) and Δm^2_{41} (y-axis) of the second toy dataset from table 4.12. where $-2\Delta\ln(L)$ is represented by the color bar. $\Delta\ln(L) = \ln(\mathcal{L}) - \ln(\mathcal{L}_{\max})$ is the difference of the natural logarithm of the likelihood to the natural logarithm of the maximum likelihood. The 1σ (2σ) region for the local ($\sin^2 2\theta_{14}$, Δm^2_{41}) range in which Wilks' theorem holds is marked by the light blue (black) line. Gray areas indicate missing data. The same plot with an other z-axis (color bar) scaling is provided in figure C.5.

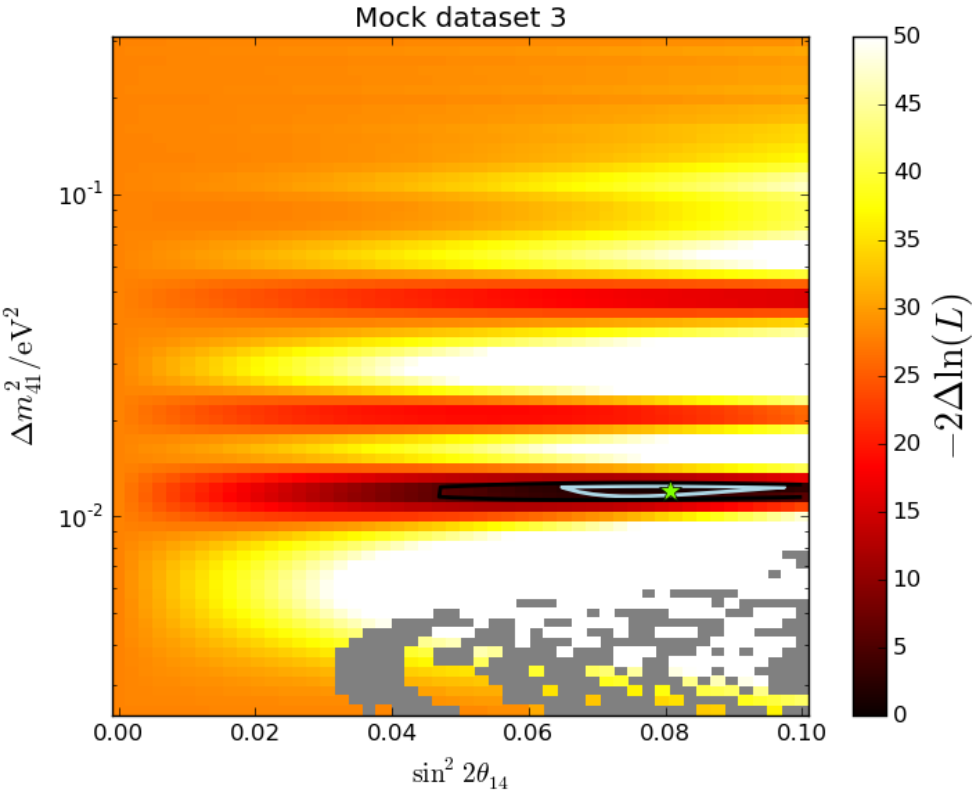

Figure C.7: Two dimensional scan of $-2\ln(\mathcal{L})$ in $\sin^2 2\theta_{14}$ (x-axis) and Δm^2_{41} (y-axis) of the third toy dataset from table 4.12. where $-2\Delta\ln(L)$ is represented by the color bar. $\Delta\ln(L) = \ln(\mathcal{L}) - \ln(\mathcal{L}_{\mathrm{max}})$ is the difference of the natural logarithm of the likelihood to the natural logarithm of the maximum likelihood. The 1σ (2σ) region for the local ($\sin^2 2\theta_{14}$, Δm^2_{41}) range in which Wilks' theorem holds is marked by the light blue (black) line. Gray areas indicate missing data. The same plot with an other z-axis (color bar) scaling is provided in figure 4.20.

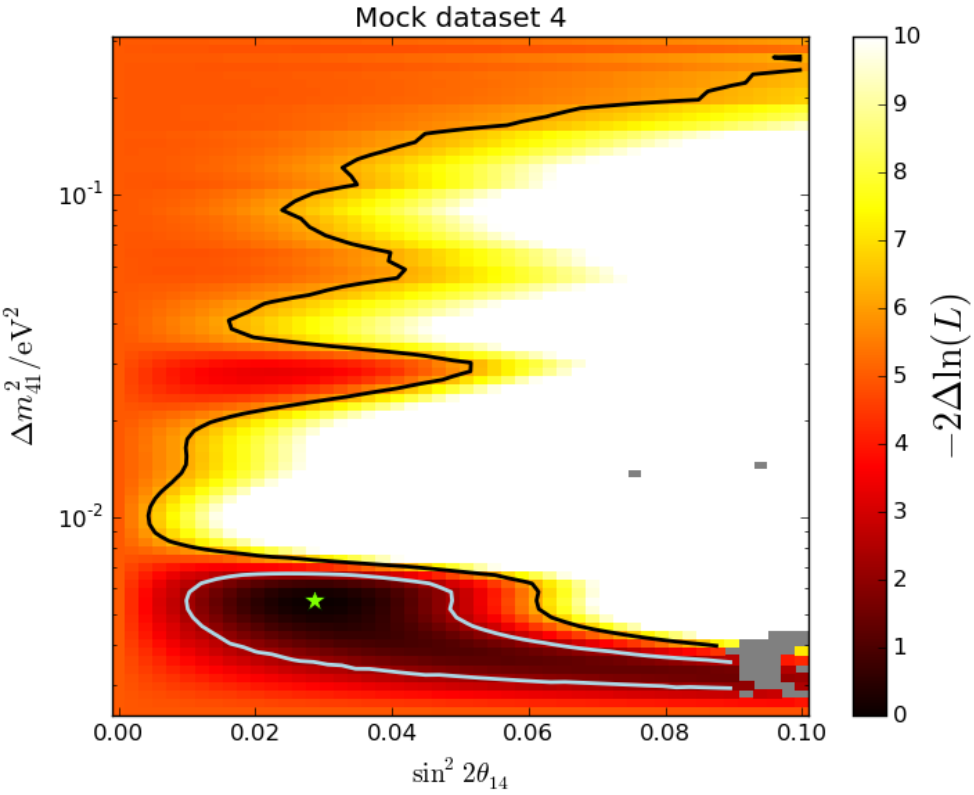

Figure C.8: Two dimensional scan of $-2\ln(\mathcal{L})$ in $\sin^2 2\theta_{14}$ (x-axis) and Δm^2_{41} (y-axis) of the fourth toy dataset from table 4.12. where $-2\Delta\ln(L)$ is represented by the color bar. $\Delta\ln(L) = \ln(\mathcal{L}) - \ln(\mathcal{L}_{\max})$ is the difference of the natural logarithm of the likelihood to the natural logarithm of the maximum likelihood. The 1σ (2σ) region for the local ($\sin^2 2\theta_{14}$, Δm^2_{41}) range in which Wilks' theorem holds is marked by the light blue (black) line. Gray areas indicate missing data. The same plot with an other z-axis (color bar) scaling is provided in figure C.9.

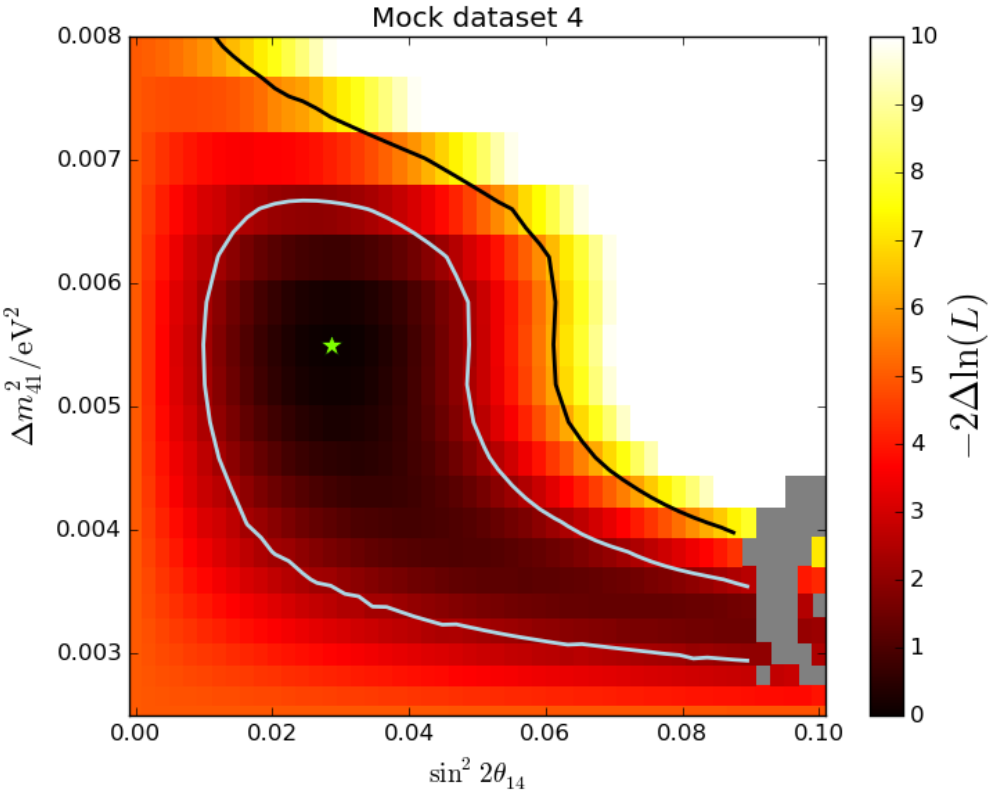

Figure C.9: Two dimensional scan of $-2\ln(\mathcal{L})$ in $\sin^2 2\theta_{14}$ (x-axis) and Δm^2_{41} (y-axis) of the fourth toy dataset from table 4.12. where $-2\Delta\ln(L)$ is represented by the color bar. $\Delta\ln(\mathcal{L}) = \ln(L) - \ln(\mathcal{L}_{\mathrm{max}})$ is the difference of the natural logarithm of the likelihood to the natural logarithm of the maximum likelihood. The 1σ (2σ) region for the local ($\sin^2 2\theta_{14}$, Δm^2_{41}) range in which Wilks' theorem holds is marked by the light blue (black) line. Gray areas indicate missing data. The same plot with an other z-axis (color bar) scaling is provided in figure C.8.

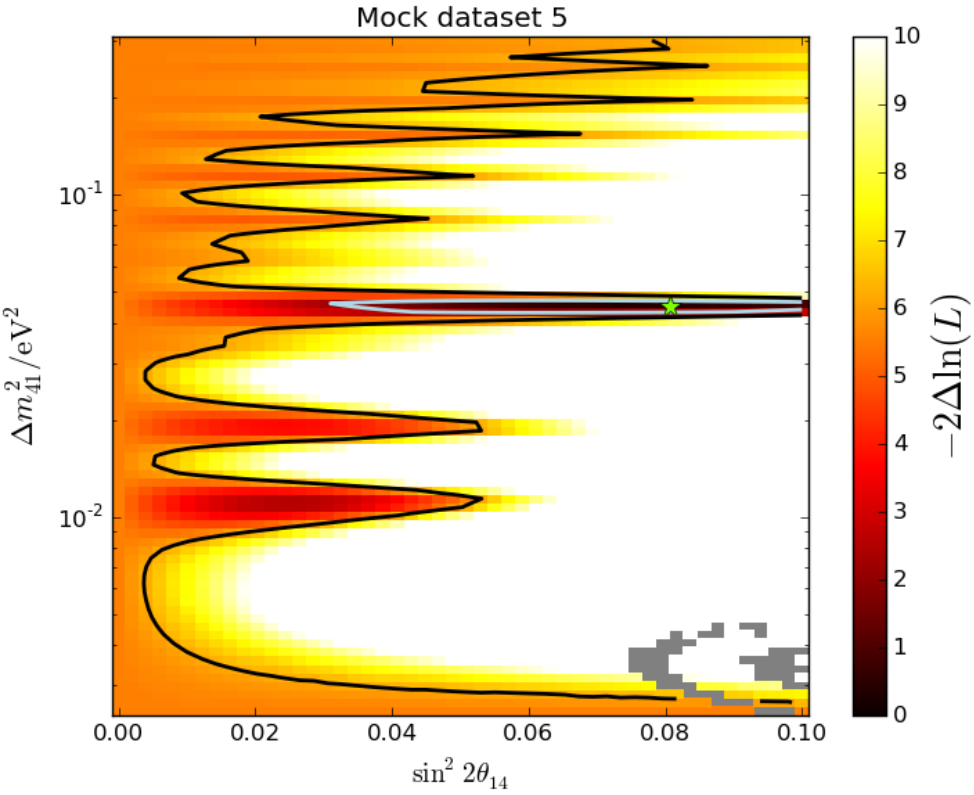

Figure C.10: Two dimensional scan of $-2\ln(\mathcal{L})$ in $\sin^2 2\theta_{14}$ (x-axis) and Δm^2_{41} (y-axis) of the fifth toy dataset from table 4.12. where $-2\Delta\ln(L)$ is represented by the color bar. $\Delta\ln(L) = \ln(\mathcal{L}) - \ln(\mathcal{L}_{\mathrm{max}})$ is the difference of the natural logarithm of the likelihood to the natural logarithm of the maximum likelihood. The 1σ (2σ) region for the local ($\sin^2 2\theta_{14}$, Δm^2_{41}) range in which Wilks' theorem holds is marked by the light blue (black) line. Gray areas indicate missing data. The same plot with an other z-axis (color bar) scaling is provided in figure C.11.

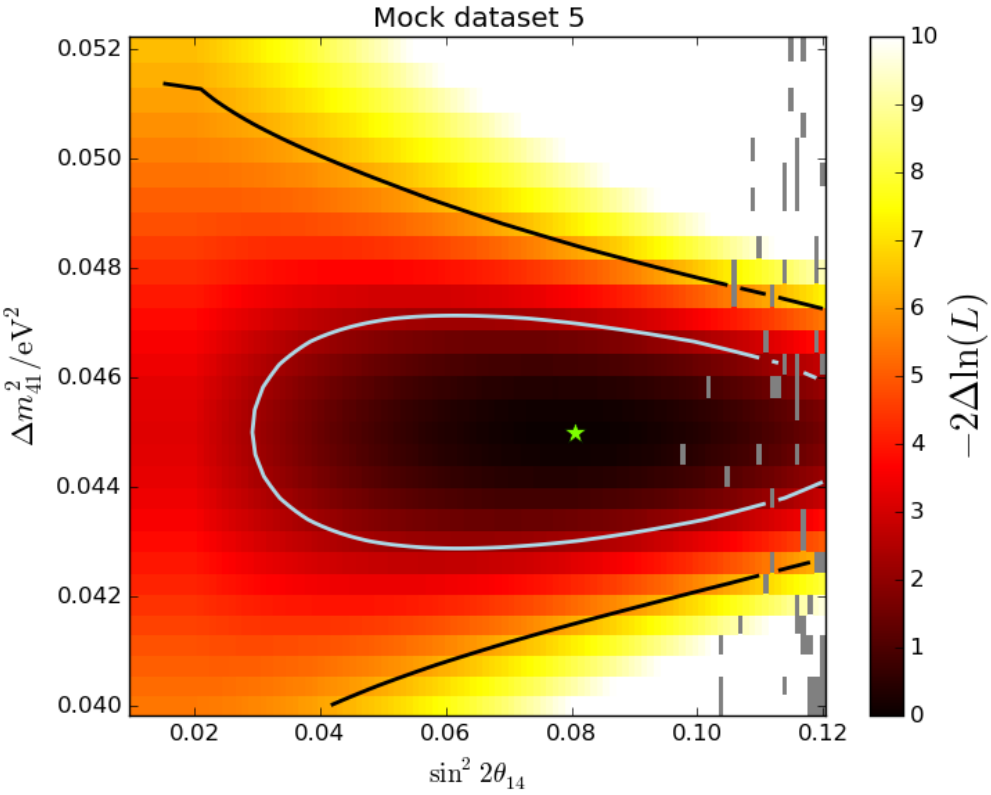

Figure C.11: Two dimensional scan of $-2\ln(\mathcal{L})$ in $\sin^2 2\theta_{14}$ (x-axis) and Δm^2_{41} (y-axis) of the fifth toy dataset from table 4.12. where $-2\Delta\ln(L)$ is represented by the color bar. $\Delta\ln(L) = \ln(\mathcal{L}) - \ln(\mathcal{L}_{\mathrm{max}})$ is the difference of the natural logarithm of the likelihood to the natural logarithm of the maximum likelihood. The 1σ (2σ) region for the local ($\sin^2 2\theta_{14}$, Δm^2_{41}) range in which Wilks' theorem holds is marked by the light blue (black) line. Gray areas indicate missing data. The same plot with an other z-axis (color bar) scaling is provided in figure C.10.

Appendix D

Results of the sterile analysis

D.1 Asimov dataset for sterile best fit parameters

Figure D.1 shows a scan of $-2\ln(\mathcal{L})$ for Asimov dataset with sterile best fit $\sin^2 2\theta_{14}$ and Δm^2_{41}

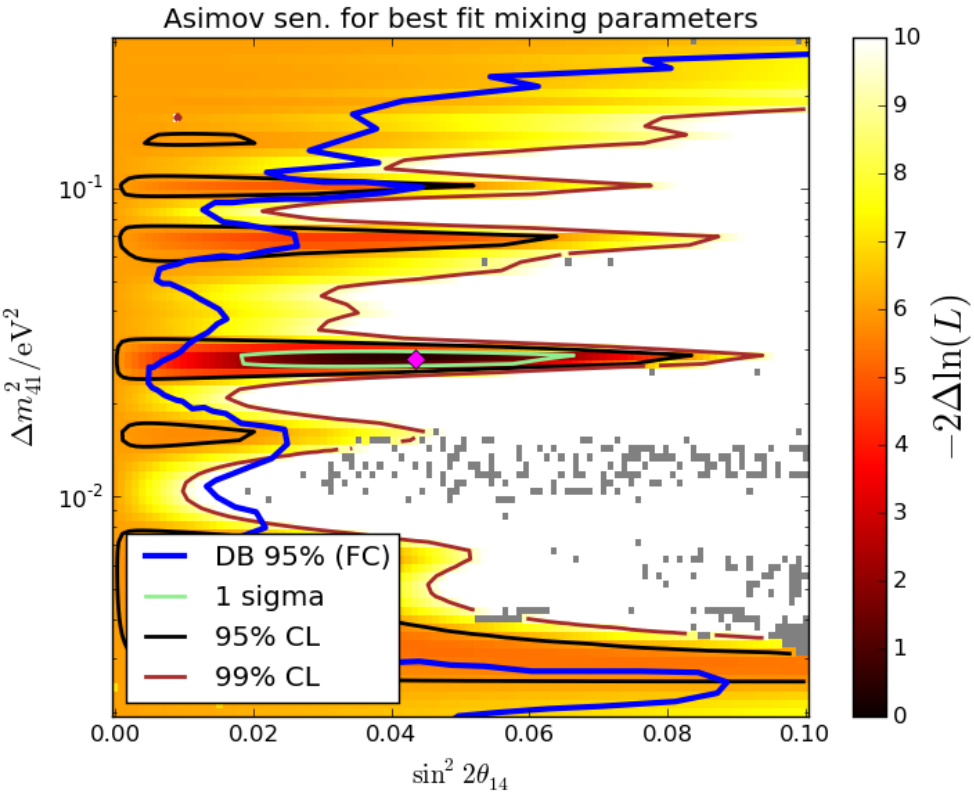

Figure D.1: Scan of $-2\ln(\mathcal{L})$ for Asimov dataset with best fit $\sin^2 2\theta_{14}$ and Δm^2_{41} found in experimental data as a function of $\sin^2 2\theta_{14}$(x-axis) and $\Delta m^2_{41}/\mathrm{eV}^2$(y-axis). The color scale shows the $-2\Delta\ln(L)$.

D.2 Residuen

Figures D.2- D.4 are additional plots of the residuen of sterile and no-sterile best fit for experimental data.

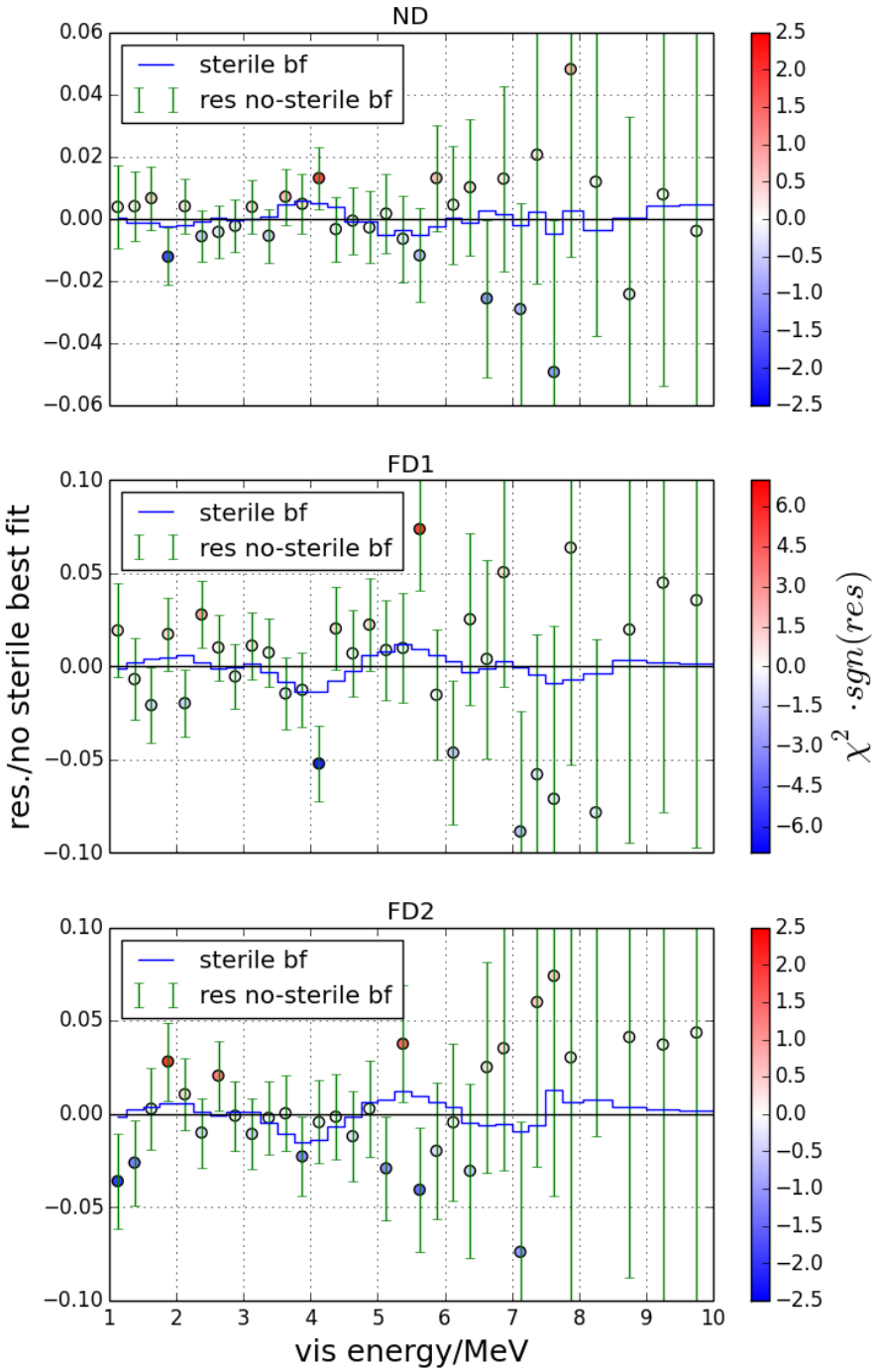

Figure D.2: Residuum of no-sterile best fit normalized to the no-sterile best fit versus visible energy compared to sterile best fit (blue line) for the ND(top), FD1 (middle) and FD2 (bottom) datasets. The color scale shows the χ^2 for each energy bin multiplied with the signum of the residuum.

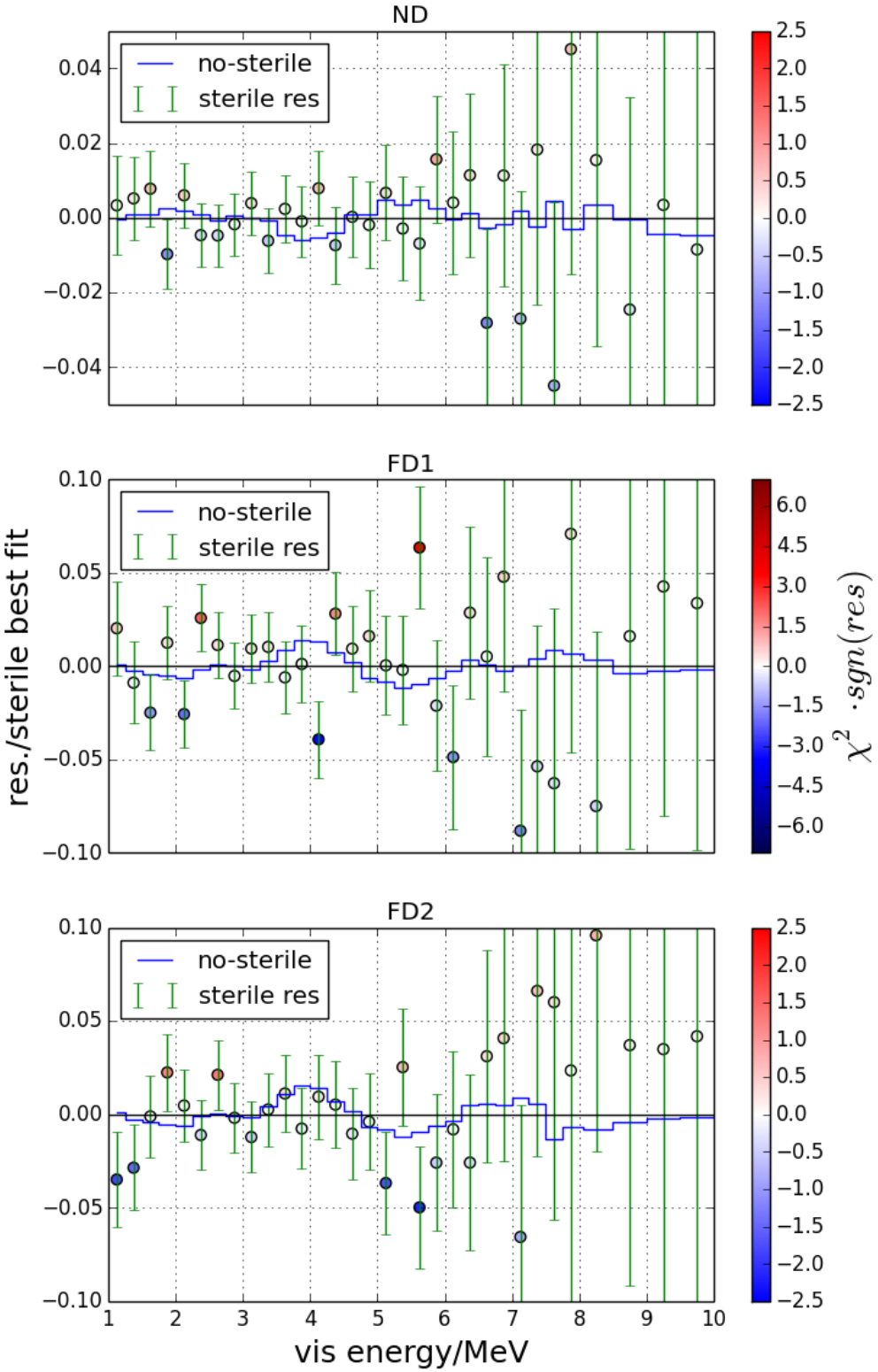

Figure D.3: Residuum of sterile best fit normalized to the sterile best fit versus visible energy compared to no-sterile best fit (blue line) for the ND (top), FD1 (middle) and FD2 (bottom) datasets. The color scale shows the χ^2 for each energy bin multiplied with the signum of the residuum.

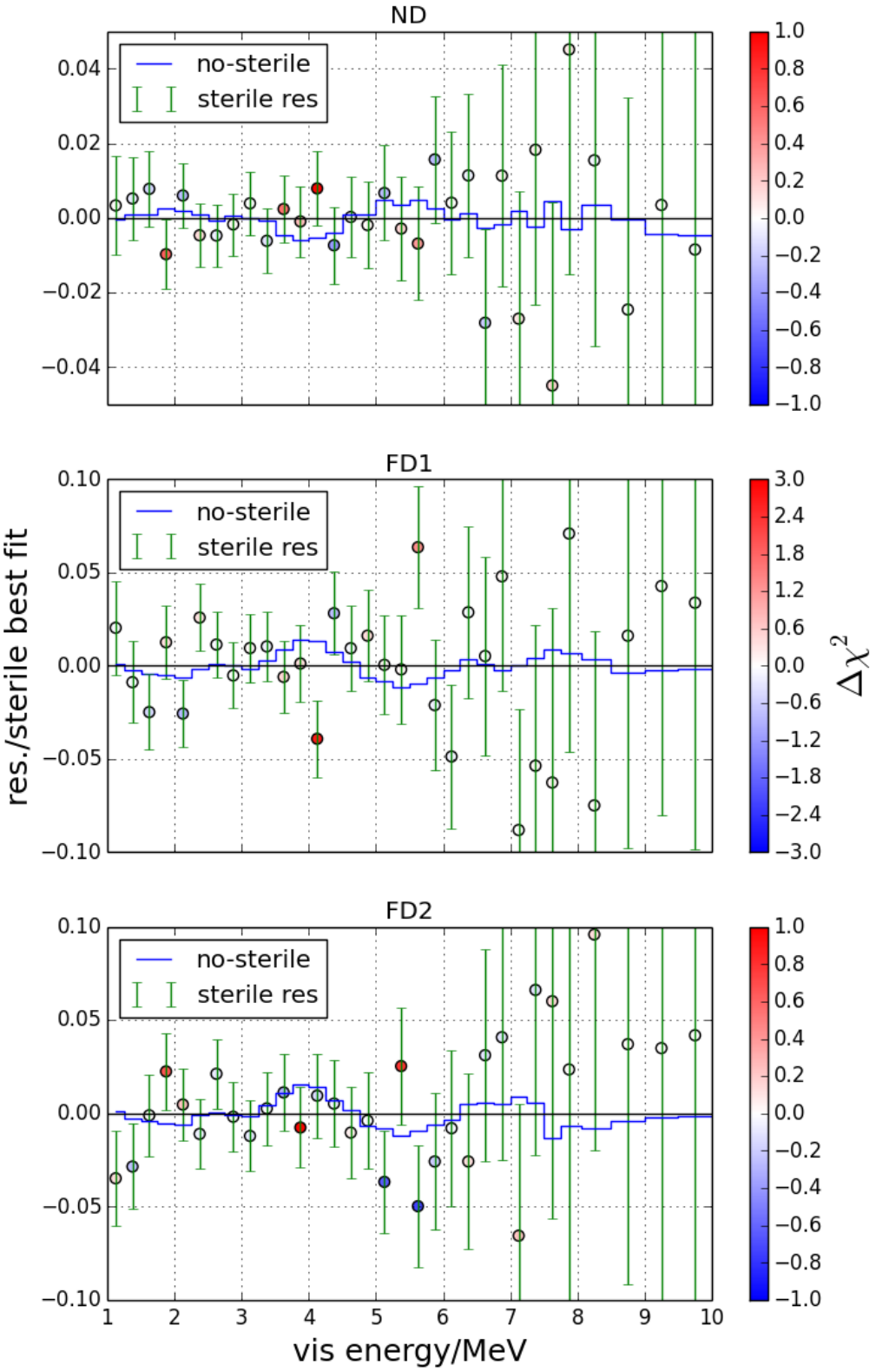

Figure D.4: Residuum of sterile best fit normalized to the sterile best fit versus visible energy compared to no-sterile best fit (blue line) for the ND(top), FD1-On(middle) and FD2 (bottom) datasets. The color scale shows the $\Delta\chi_i^2$ (cf. equation (5.4)) between sterile and no-sterile best fit for each energy bin.

Appendix E

3+2 model

Addition information related to chapter 5.5 is provided in the following.

E.1 Calculation of the electron antineutrino survival probability

This section provided more details on the calculation of the anti electron neutrino survival probability in the 3+2 model which is given in section 5.5 by equation (5.12). The matrix elements of the PMNS-matrix are given in equation (5.7) to (5.11). Several products of these matrix elements need to be calculated in order to use (1.17). These products are with equation (5.7) to (5.11):

$$\mathrm{U}_{e1}\mathrm{U}_{e1}\mathrm{U}_{e2}\mathrm{U}_{e2}\sin^2\Delta_{21} = c_{14}^4 c_{15}^4 c_{13}^4 \frac{\sin^2 2\theta_{12}}{4}\sin^2\Delta_{21} \overset{\sin^2\Delta_{21}\approx 0}{\approx} 0 \tag{E.1}$$

$$\mathrm{U}_{e1}\mathrm{U}_{e1}\mathrm{U}_{e3}\mathrm{U}_{e3} = c_{14}^4 c_{15}^4 c_{12}^2 \frac{\sin^2 2\theta_{13}}{4} \overset{c_{14}^4, c_{15}^4\approx 1}{\approx} c_{12}^2 \frac{\sin^2 2\theta_{13}}{4} \tag{E.2}$$

$$\mathrm{U}_{e1}\mathrm{U}_{e1}\mathrm{U}_{e4}\mathrm{U}_{e4} = c_{15}^4 c_{13}^2 c_{12}^2 \frac{\sin^2 2\theta_{14}}{4} \overset{c_{15}^4\approx 1}{\approx} c_{13}^2 c_{12}^2 \frac{\sin^2 2\theta_{14}}{4} \tag{E.3}$$

$$\mathrm{U}_{e1}\mathrm{U}_{e1}\mathrm{U}_{e5}\mathrm{U}_{e5} = c_{14}^2 c_{13}^2 c_{12}^2 \frac{\sin^2 2\theta_{15}}{4} \tag{E.4}$$

$$\mathrm{U}_{e2}\mathrm{U}_{e2}\mathrm{U}_{e3}\mathrm{U}_{e3} = c_{14}^4 c_{15}^4 s_{12}^2 \frac{\sin^2 2\theta_{13}}{4} \overset{c_{14}^4, c_{15}^4\approx 1}{\approx} s_{12}^2 \frac{\sin^2 2\theta_{13}}{4} \tag{E.5}$$

$$\mathrm{U}_{e2}\mathrm{U}_{e2}\mathrm{U}_{e4}\mathrm{U}_{e4} = c_{15}^4 c_{13}^2 s_{12}^2 \frac{\sin^2 2\theta_{14}}{4} \overset{c_{15}^4\approx 1}{\approx} c_{13}^2 s_{12}^2 \frac{\sin^2 2\theta_{14}}{4} \tag{E.6}$$

$$\mathrm{U}_{e2}\mathrm{U}_{e2}\mathrm{U}_{e5}\mathrm{U}_{e5} = c_{14}^2 c_{13}^2 s_{12}^2 \frac{\sin^2 2\theta_{15}}{4} \tag{E.7}$$

$$\mathrm{U}_{e3}\mathrm{U}_{e3}\mathrm{U}_{e4}\mathrm{U}_{e4} = c_{15}^4 s_{13}^2 \frac{\sin^2 2\theta_{14}}{4} \overset{c_{15}^4\approx 1}{\approx} s_{13}^2 \frac{\sin^2 2\theta_{14}}{4} \overset{s_{13}^2 \frac{\sin^2 2\theta_{14}}{4} << 1}{\approx} 0 \tag{E.8}$$

$$\mathrm{U}_{e3}\mathrm{U}_{e3}\mathrm{U}_{e5}\mathrm{U}_{e5} = c_{14}^2 s_{13}^2 \frac{\sin^2 2\theta_{15}}{4} \overset{s_{13}^2 \frac{\sin^2 2\theta_{15}}{4} << 1}{\approx} 0 \tag{E.9}$$

$$\mathrm{U}_{e4}\mathrm{U}_{e5}\mathrm{U}_{e5}\mathrm{U}_{e5} = s_{14}^2 \frac{\sin^2 2\theta_{15}}{4} \overset{s_{14}^2 \frac{\sin^2 2\theta_{15}}{4} << 1}{\approx} 0 \tag{E.10}$$

were

$$s_{ij} = \sin(\theta_{ij}) \quad \text{and} \quad c_{ij} = \cos(\theta_{ij}) \tag{E.11}$$

and

$$\Delta_{ij} := \frac{\Delta m^2_{ij} L}{4E} \approx 1.27 \frac{\Delta m^2_{ij}[\mathrm{eV}^2] L[\mathrm{km}]}{4E[\mathrm{GeV}]} \tag{E.12}$$

is used. Moreover, reasonable approximations have been done using $\sin^2 2\theta_{13}, \sin^2 2\theta_{14}, \sin^2 2\theta_{15} << 1$, $c^2_{13}, c^2_{14}, c^2_{15} << 1$ and $\sin^2 \Delta_{21} \approx 0$.

Inserting equations (E.1) to (E.10) into equation (1.17) yields

$$\begin{aligned} P_{ee} \approx\ & 1 - c^2_{12} \sin^2 2\theta_{13} \sin^2(\Delta_{31}) - c^2_{13} c^2_{12} \sin^2 2\theta_{14} \sin^2(\Delta_{41}) \\ & - c^2_{14} c^2_{13} c^2_{12} \sin^2 2\theta_{15} \sin^2(\Delta_{51}) - s^2_{12} \sin^2 2\theta_{13} \sin^2(\Delta_{32}) \\ & - c^2_{13} s^2_{12} \sin^2 2\theta_{14} \sin^2(\Delta_{42}) - c^2_{14} c^2_{13} s^2_{12} \sin^2 2\theta_{15} \sin^2(\Delta_{52}) \qquad \text{(E.13)} \\ \approx\ & 1 - \sin^2 2\theta_{13} \sin^2(\Delta_{31}) - \sin^2 2\theta_{14} \sin^2(\Delta_{41}) - \sin^2 2\theta_{15} \sin^2(\Delta_{51}) \qquad \text{(E.14)} \end{aligned}$$

E.2 Additional plots

Figure E.1 and E.2 show additional examples for near detector neutrino events in 3+2 model and 3+1 model relative to no-sterile model. They are mentioned in section 5.5.

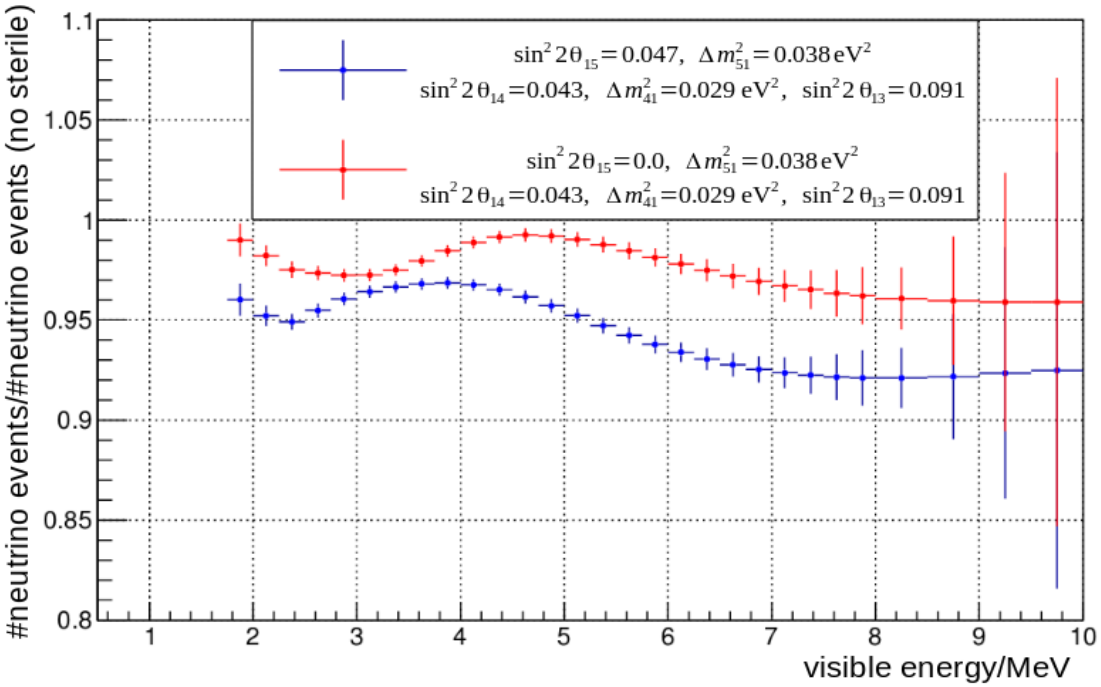

Figure E.1: Neutrino events in the near detector for the 3+2 model and the 3+1 model relative to no-sterile model versus visible energy ($\sin^2 2\theta_{14} = 0.043$, $\Delta m^2_{41} = 0.029\,\mathrm{eV}^2$, $\sin^2 2\theta_{14} = 0.047$, $\Delta m^2_{51} = 0.038\,\mathrm{eV}^2$, $\sin^2 2\theta_{14} = 0.091$) [119]. This plot has been taken from [119] and modified.

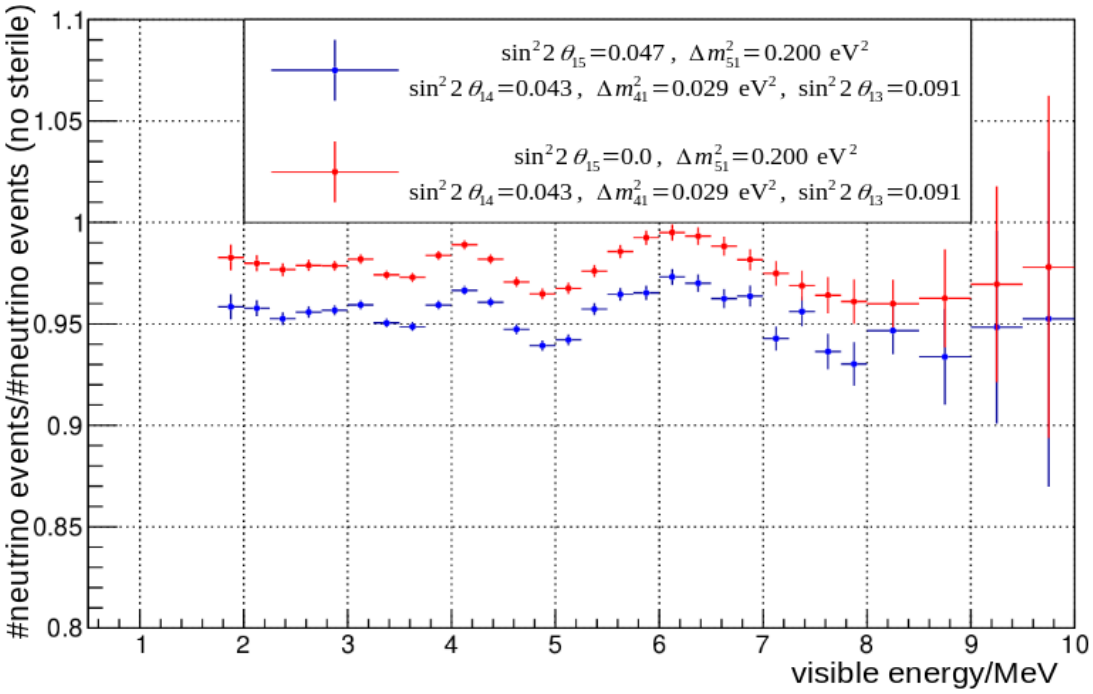

Figure E.2: Neutrino events in the far detector for the 3+2 model and the 3+1 model relative to no-sterile model versus visible energy ($\sin^2 2\theta_{14} = 0.043$, $\Delta m^2_{41} = 0.029\,\mathrm{eV}^2$, $\sin^2 2\theta_{14} = 0.047$, $\Delta m^2_{51} = 0.2\,\mathrm{eV}^2$, $\sin^2 2\theta_{14} = 0.091$) [119]. This plot has been taken from [119] and modified.

Bibliography

[1] J. N. Abdurashitov et al. Measurement of the response of the Russian-American gallium experiment to neutrinos from a Cr-51 source. *Phys. Rev.*, C59:2246–2263, 1999.

[2] J. N. Abdurashitov et al. Measurement of the response of a Ga solar neutrino experiment to neutrinos from an Ar-37 source. *Phys. Rev.*, C73:045805, 2006.

[3] Y. Abe et al. Indication of Reactor $\bar{\nu}_e$ Disappearance in the Double Chooz Experiment. *Phys. Rev. Lett.*, 108:131801, 2012.

[4] Y. Abe et al. Reactor electron antineutrino disappearance in the Double Chooz experiment. *Phys. Rev.*, D86:052008, 2012.

[5] Y. Abe et al. First Measurement of θ_{13} from Delayed Neutron Capture on Hydrogen in the Double Chooz Experiment. *Phys. Lett.*, B723:66–70, 2013.

[6] Y. Abe et al. The Waveform Digitiser of the Double Chooz Experiment: Performance and Quantisation Effects on PhotoMultiplier Tube Signals. *JINST*, 8:P08015, 2013.

[7] Y. Abe et al. Improved measurements of the neutrino mixing angle θ_{13} with the Double Chooz detector. *JHEP*, 10:086, 2014. [Erratum: JHEP02,074(2015)].

[8] Y. Abe et al. Characterization of the Spontaneous Light Emission of the PMTs used in the Double Chooz Experiment. *JINST*, 11(08):P08001, 2016.

[9] Y. Abe et al. Measurement of θ_{13} in Double Chooz using neutron captures on hydrogen with novel background rejection techniques. *JHEP*, 01:163, 2016.

[10] C. Aberle, C. Buck, F. Hartmann, and S. Schönert. Light yield and energy transfer in a new Gd-loaded liquid scintillator. *Chemical Physics Letters*, 516(4):257–262, 2011.

[11] C. Aberle, C. Buck, F. Hartmann, S. Schönert, and S. Wagner. Light output of Double Chooz scintillators for low energy electrons. *Journal of Instrumentation*, 6(11):P11006, 2011.

[12] P. A. R. Ade et al. Planck 2015 results. XIII. Cosmological parameters. *Astron. Astrophys.*, 594:A13, 2016.

[13] D. Adey et al. Measurement of the Electron Antineutrino Oscillation with 1958 Days of Operation at Daya Bay. *Phys. Rev. Lett.*, 121(24):241805, 2018.

[14] M. Agostini and B. Neumair. Statistical Methods for the Search of Sterile Neutrinos. *arXiv e-prints, arXiv:1906.11854*, Jun 2019.

[15] A. A. Aguilar-Arevalo et al. The MiniBooNE Detector. *Nucl. Instrum. Meth.*, A599:28–46, 2009.

[16] A. A. Aguilar-Arevalo et al. Significant Excess of ElectronLike Events in the MiniBooNE Short-Baseline Neutrino Experiment. *Phys. Rev. Lett.*, 121(22):221801, 2018.

[17] Q. R. Ahmad et al. Measurement of the rate of $\nu_e + d \rightarrow p + p + e^-$ interactions produced by ^8B solar neutrinos at the Sudbury Neutrino Observatory. *Phys. Rev. Lett.*, 87:071301, 2001.

[18] J. K. Ahn et al. Observation of Reactor Electron Antineutrino Disappearance in the RENO Experiment. *Phys. Rev. Lett.*, 108:191802, 2012.

[19] I. Alekseev et al. Search for sterile neutrinos at the DANSS experiment. *Phys. Lett.*, B787:56–63, 2018.

[20] F. An et al. Neutrino Physics with JUNO. *J. Phys.*, G43(3):030401, 2016.

[21] F. P. An et al. Improved Search for a Light Sterile Neutrino with the Full Configuration of the Daya Bay Experiment. *Phys. Rev. Lett.*, 117(15):151802, 2016.

[22] F. P. An et al. Measurement of the Reactor Antineutrino Flux and Spectrum at Daya Bay. *Phys. Rev. Lett.*, 116(6):061801, 2016. [Erratum: Phys. Rev. Lett.118,no.9,099902(2017)].

[23] F. P. An et al. Evolution of the Reactor Antineutrino Flux and Spectrum at Daya Bay. *Phys. Rev. Lett.*, 118(25):251801, 2017.

[24] F. P. An et al. Improved Measurement of the Reactor Antineutrino Flux and Spectrum at Daya Bay. *Chin. Phys.*, C41(1):013002, 2017.

[25] P. Anselmann et al. First results from the 51Cr neutrino source experiment with the GALLEX detector. *Physics Letters B*, 342(1):440 – 450, 1995.

[26] I. Antcheva et al. ROOT: A C++ framework for petabyte data storage, statistical analysis and visualization. *Comput. Phys. Commun.*, 180:2499–2512, 2009.

[27] M. Antonello et al. A Proposal for a Three Detector Short-Baseline Neutrino Oscillation Program in the Fermilab Booster Neutrino Beam. *arXiv:1503.01520*, 2015.

[28] M. Archidiacono, S. Hannestad, R. S. Hansen, and T. Tram. Cosmology with self-interacting sterile neutrinos and dark matter - A pseudoscalar model. *Phys. Rev.*, D91(6):065021, 2015.

[29] V. N. Aseev et al. An upper limit on electron antineutrino mass from Troitsk experiment. *Phys. Rev.*, D84:112003, 2011.

[30] J. Ashenfelter et al. First search for short-baseline neutrino oscillations at HFIR with PROSPECT. *Phys. Rev. Lett.*, 121(25):251802, 2018.

[31] C. Athanassopoulos et al. Evidence for neutrino oscillations from muon decay at rest. *Phys. Rev.*, C54:2685–2708, 1996.

[32] C. Athanassopoulos et al. Evidence for nu(mu) —> nu(e) neutrino oscillations from LSND. *Phys. Rev. Lett.*, 81:1774–1777, 1998.

[33] J. N. Bahcall and M. H. Pinsonneault. Standard solar models, with and without helium diffusion, and the solar neutrino problem. *Rev. Mod. Phys.*, 64:885–926, Oct 1992.

[34] V. Barinov, V. Gavrin, D. Gorbunov, and T. Ibragimova. BEST sensitivity to O(1) eV sterile neutrino. *Phys. Rev.*, D93(7):073002, 2016.

[35] C. Bauer et al. Qualification Tests of 474 Photomultiplier Tubes for the Inner Detector of the Double Chooz Experiment. *JINST*, 6:P06008, 2011.

[36] R. C. Baumann. Soft errors in advanced semiconductor devices-part I: the three radiation sources. *IEEE Transactions on device and materials reliability*, 1(1):17–22, 2001.

[37] R. E. Bell and L. G. Elliott. Gamma-Rays from the Reaction $H^1(n,\gamma)D^2$ and the Binding Energy of the Deuteron. *Phys. Rev.*, 79:282–285, Jul 1950.

[38] L. Bernard. Results from the STEREO Experiment with 119 days of Reactor-on Data. In *54th Rencontres de Moriond on Electroweak Interactions and Unified Theories (Moriond EW 2019) La Thuile, Italy, March 16-23, 2019*, 2019.

[39] T. J. C. Bezerra and T. Matsubara. Double Chooz χ^2 Fit Technote of DC-IV Data V0.2. *Double Chooz Document Database 7280-v2, Double Chooz internal note*, 2017.

[40] T. J. C. Bezerra and T. Matsubara. Chi2 Fit Results v41. *Double Chooz Document Database 7323-v8, talk at DC Analysis Meeting held on 06 Feb 2018*, 2018.

[41] J. B. Birks. Scintillations from organic crystals: specific fluorescence and relative response to different radiations. *Proceedings of the Physical Society. Section A*, 64(10):874, 1951.

[42] I. Bronstein, K. Semendjajew, G. Musiol, and H. Mühling. *Taschenbuch der Mathematik*. Wissenschaftlicher Verlag Harri Deutsch GmbH, 2008.

[43] A. Cabrera. Double Chooz Improved Multi-Detector Measurements. *Talk at CERN seminar on 20 Sep 2016,* `https://indico.cern.ch/event/548805/`, 2016.

[44] A. Cabrera. DC-IV FINAL TABLES. *Double Chooz Document Database 6780-v41, Double Chooz internal document*, 2017.

[45] E. Conover. 9Li Likelihood Technote. *Double Chooz Document Database 5160-v2, Double Choz internal technical note*, 2013.

[46] C. L. Cowan, F. Reines, F. B. Harrison, H. W. Kruse, and A. D. McGuire. Detection of the Free Neutrino: a Confirmation. *Science*, 124(3212):103–104, 1956.

[47] G. Cowan, K. Cranmer, E. Gross, and O. Vitells. Asymptotic formulae for likelihood-based tests of new physics. *Eur. Phys. J.*, C71:1554, 2011. [Erratum: Eur. Phys. J.C73,2501(2013)].

[48] G. Danby, J.-M. Gaillard, K. Goulianos, L. M. Lederman, N. Mistry, M. Schwartz, and J. Steinberger. Observation of High-Energy Neutrino Reactions and the Existence of Two Kinds of Neutrinos. *Phys. Rev. Lett.*, 9:36–44, Jul 1962.

[49] R. Davis, D. S. Harmer, and K. C. Hoffman. Search for Neutrinos from the Sun. *Phys. Rev. Lett.*, 20:1205–1209, May 1968.

[50] H. De Kerret et al. First Double Chooz θ_{13} Measurement via Total Neutron Capture Detection. *arXiv:1901.09445[hep-ex]*, 2019.

[51] Y. Declais et al. Study of reactor anti-neutrino interaction with proton at Bugey nuclear power plant. *Phys. Lett.*, B338:383–389, 1994.

[52] M. Dentler, A. Hernández-Cabezudo, J. Kopp, P. A. N. Machado, M. Maltoni, I. Martinez-Soler, and T. Schwetz. Updated Global Analysis of Neutrino Oscillations in the Presence of eV-Scale Sterile Neutrinos. *JHEP*, 08:010, 2018.

[53] Double Chooz Analysis Group. Internal note of DC-III neutrino oscillation analyses using energy spectrum. *Double Chooz Document Database 5162-v23, Double Chooz internal technical note*, 2014.

[54] Double Chooz Analysis Group. `http://doublechooz.in2p3.fr/Private/Working_Groups/Analysis/DC-IV/CATS_cern_pp/ALLNO.html`, Double Chooz internal documentation, 2016.

[55] Double Chooz Analysis Group. `http://doublechooz.in2p3.fr/Private/Working_Groups/Analysis/DC-IV/CATS_cern_pp/FinalPlots.html#final-energy-spectra`, Double Chooz internal documentation, 2016.

[56] Double Chooz Analysis Group. `http://doublechooz.in2p3.fr/Private/Working_Groups/Analysis/DC-IV/CATS_cern_pp/BGshapes.html`, Double Chooz internal documentation, 2016.

[57] Double Chooz Analysis Group. DC-IV Rate+Shape fit inputs for Neutrino. *Double Chooz Document Database 6760-v13, Double Chooz internal document*, 2017.

[58] Double Chooz Analysis Group, A. Onion et al. `http://doublechooz.in2p3.fr/Private/Working_Groups/Analysis/DC-IV/CATS_cern_pp/_images/Time_plot_ND_weekly.png`, Double Chooz internal document, 2016.

[59] Double Chooz Analysis Group, A. Onion et al. `http://doublechooz.in2p3.fr/Private/Working_Groups/Analysis/DC-IV/CATS_cern_pp/_images/Time_plot_FDII_weekly.png`, Double Chooz internal document, 2016.

[60] Double Chooz Collaboration. 2009 power plant site. *Double Chooz Document Database 1037-v1, Double Chooz internal document*, 2009.

[61] M. Dracos, J. Wurtz, and L. Kalousis. The Inner Veto Light Injection System. *Double Chooz Document Database 1772-v3*, 2010.

[62] D. A. Dwyer and T. J. Langford. Spectral Structure of Electron Antineutrinos from Nuclear Reactors. *Phys. Rev. Lett.*, 114(1):012502, 2015.

[63] R. L. Edwards, J. Chen, and G. Wasserburg. 238 U 234 U 230 Th 232 Th systematics and the precise measurement of time over the past 500,000 years. *Earth and Planetary Science Letters*, 81(2):175–192, 1987.

[64] S. Eidelman et al. Review of Particle Physics. *Physics Letters B*, 592(1):1 – 5, 2004.

[65] I. Esteban, M. C. Gonzalez-Garcia, M. Maltoni, I. Martinez-Soler, and T. Schwetz. Updated fit to three neutrino mixing: exploring the accelerator-reactor complementarity. *JHEP*, 01:087, see also NuFIT 3.1 (2017), www.nu–fit.org, 2017.

[66] I. Esteban, M. C. Gonzalez-Garcia, M. Maltoni, I. Martinez-Soler, and T. Schwetz. Updated fit to three neutrino mixing: exploring the accelerator-reactor complementarity. *JHEP*, 01:087, 2017.

[67] C. Giunti and M. Laveder. Statistical Significance of the Gallium Anomaly. *Phys. Rev.*, C83:065504, 2011.

[68] M. C. Gonzalez-Garcia and M. Maltoni. Phenomenology with Massive Neutrinos. *Phys. Rept.*, 460:1–129, 2008.

[69] E. Gross and O. Vitells. Trial factors for the look elsewhere effect in high energy physics. *Eur. Phys. J.*, C70:525–530, 2010.

[70] W. Hampel et al. Final results of the 51Cr neutrino source experiments in GALLEX. *Physics Letters B*, 420(1):114 – 126, 1998.

[71] S. Hannestad, R. S. Hansen, and T. Tram. How Self-Interactions can Reconcile Sterile Neutrinos with Cosmology. *Phys. Rev. Lett.*, 112(3):031802, 2014.

[72] S. Hannestad, I. Tamborra, and T. Tram. Thermalisation of light sterile neutrinos in the early universe. *JCAP*, 1207:025, 2012.

[73] D. Hellwig. Sterile Neutrino Search Using Data-Data Likelihood Approach. *Double Chooz Document Database 6693-v5, talk at Double Chooz Analysis Meeting held on 3 May 2016*, 2016.

[74] D. Hellwig. Technote on sterile neutrino hypothesis test. *Double Chooz Document Database 7339-v20, Double Chooz internal technical note*, 2018.

[75] D. Hellwig. Sterile Analysis Follow up. *Double Chooz Document Database 7508-v2, talk at Double Chooz Analysis Meeting held on 6 Jun 2019*, 2019.

[76] D. Hellwig and T. M. and. Sterile Neutrino Search with the Double Chooz Experiment. *Journal of Physics: Conference Series*, 888:012133, sep 2017.

[77] A. Hourlier. *Background Studies for Electron Antineutrino Oscillations Measurement at the Double Chooz Experiment*. PhD thesis, Université Paris Diderot (Paris VII), APC, 2016.

[78] A. Hourlier. Status of the Two-Detector Analysis of the Double Chooz Experiment. *Double Chooz Document Database 6869-v2, talk at NuFact held on 22 Aug 2016*, 2016.

[79] M. Ishitsuka. Double Chooz internal website, `http://doublechooz.in2p3.fr/Private/Working_Groups/Analysis/DC-IV/ibd.php`, last modified Jun 2016 accessed 9 Aug 2019.

[80] F. James et al. MINUIT reference manual. *CERN Program Library Long Writeup D506*, 94.1, 1998.

[81] F. James and M. Winkler. Minuit2 (ROOT documentation). website, `https://root.cern.ch/root/htmldoc/guides/minuit2/Minuit2.html`, accessed 11 May 2019.

[82] T. Kajita. Atmospheric neutrino results from super-kamiokande and kamiokande — evidence for ν_μ oscillations. *Nuclear Physics B - Proceedings Supplements*, 77(1):123 – 132, 1999.

[83] Y. J. Ko et al. Sterile Neutrino Search at the NEOS Experiment. *Phys. Rev. Lett.*, 118(12):121802, 2017.

[84] K. Kodama et al. Observation of tau neutrino interactions. *Phys. Lett.*, B504:218–224, 2001.

[85] J. Kostensalo, J. Suhonen, C. Giunti, and P. C. Srivastava. The gallium anomaly revisited. *Phys. Lett.*, B795:542–547, 2019.

[86] J. Lesgourgues and S. Pastor. Massive neutrinos and cosmology. *Phys. Rept.*, 429:307–379, 2006.

[87] J. Lesgourgues and S. Pastor. Neutrino mass from Cosmology. *Adv. High Energy Phys.*, 2012:608515, 2012.

[88] E. E. Lewis. *Fundamentals of nuclear reactor physics*. Academic Press, 2008.

[89] S. Lucht. Installation, Commissioning and Performance of the Trigger System of the Double Chooz Experiment and the Analysis of Hydrogen Capture-Neutrino Events. *PhD thesis*, RWTH Aachen University, 2013.

[90] L. Lyons et al. Open statistical issues in particle physics. *The Annals of Applied Statistics*, 2(3):887–915, 2008.

[91] G. Mention et al. The Reactor Antineutrino Anomaly. *Phys. Rev.*, D83:073006, 2011.

[92] A. Minotti. Exploitation of pulse shape analysis for correlated background rejection and ortho-positronium identification in the Double Chooz experiment. *PhD thesis*, Université de Strasbourg, NNT: 2015STRAE046. tel-01398615v1, 2015.

[93] T. A. Mueller et al. Improved Predictions of Reactor Antineutrino Spectra. *Phys. Rev.*, C83:054615, 2011.

[94] D. Navas. New MC ND and systematic studies for Gd++ and Gd analysis. *Double Chooz Document Database 6696-v2, talk at DC Analysis Meeting Nov 2016*, 2016.

[95] J. Neyman and E. S. Pearson. On the use and interpretation of certain test criteria for purposes of statistical inference: Part II. *Biometrika*, pages 263–294, 1928.

[96] NobelPrize.org. Nobel Media AB 2019. The Nobel Prize in Physics 1988. website, `https://www.nobelprize.org/prizes/physics/1988/summary/`, retrieved 29 May 2019.

[97] NobelPrize.org. Nobel Media AB 2019. The Nobel Prize in Physics 1995. website, `https://www.nobelprize.org/prizes/physics/1995/summary/`, retrieved 29 May 2019.

[98] NobelPrize.org. Nobel Media AB 2019. The Nobel Prize in Physics 2015. website, `https://www.nobelprize.org/prizes/physics/2015/summary/`, retrieved 31 May 2019.

[99] P. Novella. Double Chooz: Searching for θ_{13} with reactor neutrinos. In *Proceedings, 46th Rencontres de Moriond on Electroweak Interactions and Unified Theories: La Thuile, Italy, March 13-20, 2011*, pages 291–296, 2011.

[100] K. A. Olive et al. Review of Particle Physics. *Chin. Phys.*, C38:090001, 2014.

[101] A. Onion. Reactor errors tables & plots @Neutrino. *Double Chooz Document Database 6783-v5, talk at Double Chooz Analysis meeting held on 14 Jun 2016*, 2016.

[102] A. Onion. Crosscheck of Energy scale covariance matrices for the fit. *Double Chooz Document Database 7097-v2, talk at Double Chooz oscillation fit meeting held on 20 Mar 2017*, 2017.

[103] OpenStax CNX. *OpenStax, Chemistry.* `https://opentextbc.ca/chemistry/chapter/21-4-transmutation-and-nuclear-energy/`, 2016.

[104] A. Palazzo. Constraints on very light sterile neutrinos from θ_{13}-sensitive reactor experiments. *Journal of High Energy Physics*, 2013:172, Oct 2013.

[105] C. Palomares. Accidental background. *Double Chooz Document Database 1267-v1, talk at EU++ Analysis Cluster Meeting held on 10 Dec 2009 in Strasbourg, France*, 2009.

[106] C. Patrignani et al. Review of Particle Physics. *Chinese physics C*, 40(10):100001, 2016.

[107] C. Patrignani et al. Review of Particle Physics. *Chinese physics C*, 40(10):100001, 2016 (and 2017 update).

[108] Planck Collaboration, N. Aghanim, et al. Planck 2018 results. VI. Cosmological parameters. *arXiv e-prints, arXiv:1807.06209*, Jul 2018.

[109] G. Punzi. Sensitivity of searches for new signals and its optimization. *eConf*, C030908:MODT002, 2003. [,79(2003)].

[110] F. Reines. The neutrino: from poltergeist to particle. *Rev. Mod. Phys.*, 68:317–327, Apr 1996.

[111] S. P. Rosen and J. M. Gelb. Mikheyev-Smirnov-Wolfenstein enhancement of oscillations as a possible solution to the solar-neutrino problem. *Phys. Rev. D*, 34:969–979, Aug 1986.

[112] G. A. Sawyer and M. L. Wiedenbeck. Decay Constants of K^{40}. *Phys. Rev.*, 79:490–494, Aug 1950.

[113] S. Schoppmann. First Measurement of θ_{14} with the Final Two Detector Setup of the Double Chooz Experiment. *PhD thesis*, RWTH Aachen University, 2016.

[114] S. H. Seo et al. Spectral Measurement of the Electron Antineutrino Oscillation Amplitude and Frequency using 500 Live Days of RENO Data. *Phys. Rev.*, D98(1):012002, 2018.

[115] C. E. Shannon. Communication in the Presence of Noise. *Proceedings of the IRE*, 37(1):10–21, Jan 1949.

[116] V. Sibille. Mesure de l'angle de mélange θ_{13} avec les deux détecteurs de "Double Chooz" . *PhD thesis*, Paris-Saclay University prepared at Paris-Sud University, 2017.

[117] P. Soldin. Improved measurement of the neutrino mixing angle θ_{13} with the Double Chooz experiment. *Master thesis*, RWTH Aachen University, 2017.

[118] P. Soldin. private communication, 2018.

[119] Y. Sommer. Untersuchung zur Sensitivität des Double Chooz Neutrinooszillation Experiments zur Messung von Oszillation steriler Neutrinos im 3+2 Szenario. *Bachelor thesis*, RWTH Aachen University, 2017.

[120] M. Tanabashi et al. Review of Particle Physics. *Phys. Rev. D*, 98:030001, Aug 2018.

[121] The LEP Collaborations: ALEPH Collaboration, DELPHI Collaboration, L3 Collaboration, OPAL Collaboration, and the LEP Electroweak Working Group. A Combination of Preliminary Electroweak Measurements and Constraints on the Standard Model. *arXiv:0612034[hep-ex]*, Dec 2006.

[122] M. Vivier. Geodetic survey results. *Double Chooz Document Database 6286-v1, talk at Double Chooz Collaboration Meeting in Aachen*, 2015.

[123] P. Vogel and J. F. Beacom. Angular distribution of neutron inverse beta decay, anti-neutrino(e) + p —> e+ + n. *Phys. Rev.*, D60:053003, 1999.

[124] P. Wahnon et al. Absolute light level measurements of the Light Injection Calibration System (LICS). *Double Chooz Document Database 1652-v1, undergraduate project report*, 2010.

[125] M. Wallraff and C. Wiebusch. Calculation of oscillation probabilities of atmospheric neutrinos using nuCraft. *Comput. Phys. Commun.*, 197:185–189, 2015.

[126] wikipedia.org. `https://upload.wikimedia.org/wikipedia/commons/archive/e/e9/20171019134614%21France_location_map-Regions_and_departements-2016.svg`, created 2 Jan 2016.

[127] S. S. Wilks. The Large-Sample Distribution of the Likelihood Ratio for Testing Composite Hypotheses. *Annals Math. Statist.*, 9(1):60–62, 1938.

[128] K. Wisshak, F. Voss, F. Käppeler, K. Guber, L. Kazakov, N. Kornilov, M. Uhl, and G. Reffo. Stellar neutron capture cross sections of the Gd isotopes. *Physical Review C*, 52(5):2762, 1995.

[129] I. S. Yeo. Search for sterile neutrinos at RENO. *Journal of Physics: Conference Series*, 888:012139, Sep 2017.

Acknowledgements

I am indebted to my supervisors Prof. Dr. Christopher Wiebusch and Prof. Dr. Achim Stahl for their guidance and support throughout this dissertation. I am incredible thankful that they gave me the opportunity to work on the search for sterile neutrinos as this the topic I fell in love with when I did my bachelor thesis and agreed to be my supervisors. I am greatful to both of them for taking care for an excellent atmosphere in the group.
I am particularly grateful to my first supervisor Prof. Dr. Christopher Wiebusch who suggested me for the topic of this thesis. He provided guidance not only during this thesis but during my all my academic carrier starting from my bachelor thesis. He really cared for me more than I expected during all this times.
I would like to thank all members of the Aachen Double Chooz group, and the Aachen LAND group for the excellent atmosphere and for providing advice in every possible situation. They enabled me to benefit from their knowledge and expertise. In particular, I would like to thank Ilja Bekman, Dr. Sebastian Lucht and Dr. Stefan Schoppmann for warmly welcoming me and helping me to get started. Philipp Soldin and Thilo Birkenfeld have been great support in the time I finished my research and understood that I was struggling with it.
This work would not have been possible without the close cooperation with Aachen's θ_{13} fit people, Philipp Soldin, Dr. Stefan Schoppmann and Philipp Kampmann. In particular, I thank Philipp Soldin for the incredible amount of technical advice and improving the computing time of the fit framework by orders of magnitude by rewriting it. Without that, this work really would not have been possible. Also, it is out of question that Dr. Stefan Schoppmanns thesis was a necessary condition for this work. Philipp Kampmann pioneered the Gd++ analysis in Aachen and thus delivered significant input for this analysis. I can not thank the other θ_{13} fit people in the Double Chooz Collaboration enough either, in particular Dr. Thiago Bezerra and Dr. Tsunayuki Matsubara for providing support during the crosschecking process. Moreover, I thank Dr. Tsunayuki Matsubara and Dr. Anselmo for being Double Chooz internal reviewers of my analysis and enriched my thesis with their comments. Finally, I would like to thank Prof. Dr. Christopher Wiebusch, my sister Vanessa, Dr. Jochen Steinmann and Philipp Soldin for proofreading. Apart from the tremendous amount of work she spend on proofreading, my sister was always there for me whenever I needed her. I can not thank her enough. Last but not least I thank my family and my friends for supporting me in the not always easy time during my studies. I am indebted to my parents who always believed in me. I am extremely proud on my brother Christian who is playing golf in the German National Junior Team. I am greatful for the good relationship that we have and deeply appoligize for being rarely availible to support him.

Eidesstattliche Erklärung

Ich, Denise Hellwig erklärt hiermit, dass diese Dissertation und die darin dargelegten Inhalte die eigenen sind und selbstständig, als Ergebnis der eigenen originären Forschung, generiert wurden.
Hiermit erkläre ich an Eides statt

1. Diese Arbeit wurde vollständig oder größtenteils in der Phase als Doktorand dieser Fakultät und Universität angefertigt;
2. Sofern irgendein Bestandteil dieser Dissertation zuvor für einen akademischen Abschluss oder eine andere Qualifikation an dieser oder einer anderen Institution verwendet wurde, wurde diesklar angezeigt;
3. Wenn immer andere eigene- oder Veröffentlichungen Dritter herangezogen wurden, wurden diese klar benannt;
4. Wenn aus anderen eigenen- oder Veröffentlichungen Dritter zitiert wurde, wurde stets die Quelle hierfür angegeben. Diese Dissertation ist vollständig meine eigene Arbeit, mit der Ausnahme solcher Zitate;
5. Alle wesentlichen Quellen von Unterstützung wurden benannt;
6. Wenn immer ein Teil dieser Dissertation auf der Zusammenarbeit mit anderen basiert, wurde von mir klar gekennzeichnet, was von anderen und was von mir selbst erarbeitet wurde;
7. Kein Teil dieser Arbeit wurde vor deren Einreichung veröffentlicht.

Aachen, der 19. Mai 2020

Denise Hellwig